

Untargeted metabolomics and proteomics application of mass spectrometry: from biomarker identification within cells to their spatial localization on tissues

A thesis presented by

Domenica Berardi

Supervised by Dr Nicholas JW Rattray and Dr Zahra Rattray

In fulfilment of the requirement for the degree of

Doctor of Philosophy

2022

Strathclyde Institute of Pharmacy and Biomedical Science
University of Strathclyde

TABLE OF CONTENTS

ABSTRACT	V
ACKNOWLEDGEMENTS	VII
DECLARATION	VIII
COPYRIGHT STATEMENT	IX
LIST OF FIGURES	X
LIST OF TABLES	XVII
ABBREVIATIONS AND ACRONYMS	XIX
CHAPTER 1	- 1 -
1.1. Introduction	- 1 -
1.1.1. The central dogma	- 1 -
1.1.2. Technologies used in metabolomics and proteomics studies.....	- 3 -
1.1.3. <i>Study design for metabolomics and proteomics</i>	- 21 -
1.1.4. Metabolomics and proteomics in ageing and cancer research	- 33 -
1.1.5. Genomic instability	- 37 -
1.1.6. Metabolic reprogramming	- 41 -
1.2. References	- 47 -
1.3. Aims	- 54 -
CHAPTER 2	- 56 -
2.1. Abstract	- 56 -
2.2. Introduction	- 57 -
2.3. Materials	- 61 -
2.3.1. Cell line, chemical and treatment	- 61 -
2.4. Methods	- 62 -
2.4.1. Senescence associated β -galactosidase staining.....	- 62 -
2.4.2. Cell viability assay.....	- 62 -
2.4.3. Immunostaining for γ H2AX and Ki67	- 62 -
2.4.4. Sample preparation and metabolite extraction.....	- 63 -
2.4.5. Liquid Chromatography Tandem Mass Spectrometry (LC-MS/MS)	- 64 -
2.4.6. Mass Spectrometry Data Processing	- 65 -
2.4.7. Pathway Analysis with MetaboAnalyst	- 65 -
2.4.8. Statistical analysis.....	- 66 -
2.5. Results	- 67 -
2.5.1. Induction of senescence in normal human fibroblasts	- 67 -
2.5.2. Senescence results in the formation of γ H2AX and Ki-67 foci.....	- 69 -
2.5.3. Senescence-associated metabolic changes vary depending on the method of induction	- 72 -
2.5.4. Altered amino acid, lipids and carbohydrate metabolism in different senescence-induced cells.....	- 74 -

2.5.5.	Detection of extracellular inflammatory metabolites in different senescence-induced phenotypes.....	- 80 -
2.6.	Discussion	- 83 -
2.7.	Conclusion	- 89 -
2.8.	References	- 90 -
CHAPTER 3.....	- 93 -
3.1.	Abstract.....	- 93 -
3.2.	Introduction	- 94 -
3.3.	Materials	- 97 -
3.3.1.	Animals	- 97 -
3.3.2.	Reagents	- 97 -
3.4.	Methods	- 98 -
3.4.1.	Tissue collection.....	- 98 -
3.4.2.	Sample preparation for liquid chromatography – mass spectrometry (LC-MS)	- 98 -
3.4.3.	Liquid Chromatography tandem mass spectrometry (LC-MS/MS)	- 99 -
3.4.4.	Mass spectrometry data processing for metabolomics and proteomics	- 100 -
3.4.5.	Pathway Analysis with MetaboAnalyst	- 100 -
3.4.6.	Statistical Analysis	- 101 -
3.4.7.	Tissue preparation for MALDI Mass Spectrometry Imaging	- 101 -
3.4.8.	MALDI Matrix Application	- 101 -
3.4.9.	MALDI Mass Spectrometry Imaging	- 102 -
3.5.	Results	- 103 -
3.5.1.	Altered metabolic pathways in aged murine brain tissue	- 103 -
3.5.2.	Amino acid metabolism is significantly altered in aged murine brain tissue.....	104 -
3.5.3.	Altered protein content in murine brain tissue	- 105 -
3.5.4.	Combined metabolomics/proteomics network analysis of old murine brain tissues	- 107 -
3.5.5.	MALDI MSI reveals spatial localisation of putative lipids in the aged murine brain tissue	- 109 -
3.6.	Discussion	- 112 -
3.7.	Conclusion	- 115 -
3.8.	References	- 117 -
CHAPTER 4.....	- 120 -
4.1.	Abstract.....	- 120 -
4.2.	Introduction	- 121 -
4.3.	Materials	- 124 -
4.3.1.	Cell lines and chemicals	- 124 -
4.4.	Methods	- 125 -
4.4.1.	Cell Viability Assays.....	- 125 -
4.4.2.	Immunostaining for γ H2AX and p53BP1	- 126 -
4.4.3.	Sample preparation and metabolite extraction.....	- 126 -
4.4.4.	Liquid Chromatography Tandem Mass Spectrometry (LC-MS/MS)	- 127 -
4.4.5.	Mass Spectrometry Data Processing	- 128 -
4.4.6.	Pathway Analysis with MetaboAnalyst	- 129 -
4.4.7.	Statistical Analysis	- 129 -

4.5. Results	- 130 -
4.5.1. Olaparib sensitivity analysis	- 130 -
4.5.2. Exposure to olaparib induces dose-dependent formation of γ H2AX and 53BP1 foci in breast cancer cells.....	- 131 -
4.5.3. Biomolecular pathways altered in response to olaparib exposure vary across different cell lines.....	- 134 -
4.5.4. Amino acid and lipid metabolism are significantly altered in response to olaparib exposure.....	- 136 -
4.6. Discussion	- 142 -
4.7. Conclusion	- 148 -
4.8. References	- 150 -
CHAPTER 5	- 153 -
5.1. General discussion and conclusion	- 153 -
APPENDICES	- 159 -
6.1. Appendix 1	- 159 -
6.2. Appendix 2	- 184 -
6.3. Appendix 3	- 209 -
6.4. Appendix 4	- 229 -

ABSTRACT

Metabolomics is the newest omics science which studies the chemical changes of small molecules (metabolites) within cells and tissues of a living organism. Thanks to the implementation of liquid chromatography-mass spectrometry (LC-MS) and mass spectrometry imaging (MSI) analytical technologies, and the integration of multiple omics tools, metabolomics provides insight into the mechanisms underlying physiological and pathological conditions including ageing and cancer.

Time-dependent accumulation of DNA damage has been observed during senescence, the state of cell cycle arrest and resistance to death which has been recognised as a driver of the ageing process. Similarly, genomic instability can initiate cancer and influence the overall prognosis of affected patients. Metabolomics has shown that metabolic reprogramming is another key characteristic of both ageing and cancer, necessary to sustain their survival in adverse conditions. Genomic instability and metabolic reprogramming contribute to the highly heterogeneous and dynamic phenotype of ageing and cancer, therefore predisposing patients to inferior clinical outcomes and resistance to treatments.

Due to their heterogeneous and dynamic nature, isolating and effectively analysing the different phenotypes of both ageing and cancer is still a challenge. Owing to the implementation of mass spectrometry and its combination with microscopy technologies it is now possible to identify and spatially localise the distribution of new reliable and specific biomarkers for each individual phenotype.

In this thesis, molecular assays coupled to mass spectrometry-based global metabolomics and proteomics techniques were employed to examine the changes occurring during cellular senescence upon induction of DNA damage, brain ageing in mice, and different breast cancer subtypes in response to DDR inhibition. The results presented show that at the cellular level senescence can be induced through replication stress, irradiation and DNA damage-inducing

chemicals (hydroxyurea and etoposide), which share similar molecular features (growth arrest, flattened shape, expression of β -galactosidase, DNA damage foci and cell cycle alteration), but different intra and extracellular metabolic components specific for each phenotype. At the tissue level, integration of global metabolomics and proteomics analysis allowed to design a putative metabolic map of the changes in the metabolites and proteins that were altered in the aged brain of mice. Moreover, the employment of mass spectrometry imaging (MSI) enabled the spatial localization of metabolites within specific regions of the brain. Finally, changes in cellular metabolism (glutamine and lipids metabolism) were observed in different breast cancer sub-phenotypes in response to DDR inhibition through Olaparib treatment.

Overall, this thesis presents metabolomics – combined with molecular, proteomics studies and the high-resolution spatial determination of metabolites – as a powerful tool to reveal novel therapeutic targets for the treatment of ageing and age-related diseases (including cancer) and to comprehensively stratify different phenotypes relative to their tissue localization and based on their altered genetic alterations. When transferred into clinical diagnostics, this approach has future potential design personalised therapeutic approaches.

ACKNOWLEDGEMENTS

I would like to express my deep gratitude to my supervisor, Dr Nicholas JW Rattray for the continuous guidance and support in this PhD study. Thank you for the patience, motivation and enthusiasm you gave me. Thank you for your immense knowledge, humility and encouragement in thinking outside the box. I feel privileged and I could not have imagined having a better supervisor and mentor for my PhD study.

I feel a deep sense of gratitude to Dr Zahra Rattray for her dedication and caring attitude to support and help me. Your timely advice, meticulous scrutiny and professional approach have been fundamental to accomplishing this beautiful journey. Your determination and ambition have been inspiring for me and triggered my willingness in aiming high for new challenges.

I thank profusely all my colleagues who have been at my side in these years, and who I have had the pleasure to work with: Karim for your tender support, Abdullah for your deep sensibility, Layla for your sweet care, Tricia for your inspirational tenacity, and Jene for being an example of commitment to responsibilities. I am very grateful to Gillian for her exemplary resilience and bright sense of humour. Thank you to Yasmin who has been a great support during my final year. Thank you Lisa for being always there with your strong empathy and smart advice.

On a personal level, I owe an immense thanks to Cristina for having been a pillar in this journey as a friend and scientist. I could not thank you enough! Thank you Valeria and thank you to all the friends who never left me alone despite the distance, especially Giulia and Claudia.

Last but not least, thanks to my Mum and Dad for the reality checks and Antonio, Maria and Mariangela for having taken my side.

DECLARATION

This thesis is the result of the author's original research. It has been composed by the author and has not been previously submitted for examination which has led to the award of a degree

COPYRIGHT STATEMENT

The copyright of this thesis belongs to the author under the terms of the United Kingdom Copyright Acts as qualified by University of Strathclyde Regulation 3.5. Due to acknowledgement must always be made of the use of any material contained in, or derived from, this thesis.

Signed: 

Date: 30/09/2022

LIST OF FIGURES

CHAPTER 1

Figure 1. 1 The central dogma of molecular biology. Biochemical information contained in a cell is translated from the DNA to the RNA and proteins, including enzymes. Enzymatic reactions lead to the production of metabolites which are the molecules closely associated with organism phenotype. Created in Biorender. _____ - 1 -

Figure 1. 2 Example of a Liquid Chromatography – Mass Spectrometry (LC-MS) system. Example of the Exploris 240 MS system. The LC apparatus consists of an autosampler, pump and column compartment. The samples held in the autosampler are injected into the column through the needle injector. The mobile phases flow through the column after being mixed in the pump system. Eluted analytes are then introduced in the ion source where the liquid phase is evaporated and the analyte is ionised. Ions in the gas-phase are transported through the MS apparatus from the low to high vacuum regions. Thus, they pass through a transfer and electrodynamic tube where the internal calibrant (IC) ion, fluoranthene (202.0777 m/z), is delivered to the sample by the EASY-IC component. Ions are then transported along the advanced active beam guide (AABG) to the quadrupole component (AQT) for an initial ion selection. Ions in a C-trap will be injected in to the orbitrap, the second mass analyser. During fragmentation, ions pass through the ion routing multipole before being re-introduced in the orbitrap analyser. Created in Biorender. _____ - 4 -

Figure 1. 3 Graphical representation of HILIC column composition and the general principle of separation. The column is composed of a solid polar stationary phase (e.g., silica). The mobile phase is generally ACN with a low percentage of water. During separation the analyte is partitioned between the mobile phase and a water enriched layer that forms on the hydrophilic stationary phase. The more hydrophilic the analyte is, the more its partitioned equilibrium is shifted towards the water layer in the stationary phase, resulting in more retention of the analyte. This principle of separation is only based on circumstantial evidence and is still debated. _____ - 8 -

Figure 1. 4 Van Deemter equation and Theoretical plates. a) Plot of the Van Deemter equation describing the efficiency of the column in terms of plate height (equivalent to theoretical plate) in relation with linear velocity. A term indicates the particle size; B/u term is the axial diffusion, while the Cu is the molecular diffusion of the analyte between the mobile and stationary phase. At the lowest HETP (arrow) corresponds to the optimum plate count. HETP: Height Equivalent of a Theoretical Plate. A: Eddy diffusion factor. u: Speed. B/u: Longitudinal molecular diffusion term. Cu: Mass transfer term. b) Summary of the rationale behind the Van Deemter equation describing that the highest separation efficiency of a column is reached at the minimum plate heights (h). _____ - 10 -

Figure 1. 5 The mechanism of electrospray ionization. Under high voltage, a current passes a wire filament to produce electrons for ionization. An electric field (i) is imposed into the liquid leading to an enrichment of positive ions at the meniscus of the spray needle. Consequently, a cone of positive ions (Taylor cone) is generated. The resulting droplets will have an excess of positive ions. During evaporation, the charges will get closer therefore increasing the Coulombic repulsion between charges of the same sign. This destabilises the droplets leading to the formation of free gas-phase ions. Created in Biorender. _____ - 12 -

Figure 1. 6 Resolution and mass accuracy in mass spectrometry. A) To determine peak resolution, the m/z value of an ion is related to its $\Delta m/z$ (the difference between the first and second highest m/z value of that ion) at 50% intensity or width. B) Mass accuracy is the difference between the observed (experimental) and the calculated (exact) value of the mass, expressed in ppm. _____ - 14 -

Figure 1. 7 MS1 and MS2 chromatogram. A) MS1 chromatogram with identified precursor ion of 147.0764 m/z (z=1) corresponding to glutamine (mm=146.14 g/mol). B) MS2 chromatogram where the precursor ion (red arrow) has been fragmented into its smaller components are represented through the chemical structures. _____ - 17 -

Figure 1. 8 Workflow of MALDI-MSI analysis. Image acquisition involves sample preparation by mounting the tissue section on a conductive slide and matrix application. A laser beam is employed to allow the desorption/ionization of the analyte. Ions are transferred in the MS system for mass analysis and generation of MS spectra. After MS analysis, immunohistochemical analysis is performed visualising the distribution of multiple molecules

within the tissue. Data analysis includes classification of the images and database searching for the identification of molecules. Adapted from Norris, JL., et al., 2013 [40]. _____ - 19 -

Figure 1. 9 QTOF-MS. Ions from the ion source are first focused into a beam and transmitted into the quadrupole (Q). Then they are accelerated by a high-voltage field – via a pusher pulse. The kinetic energy associated with each ion is converted into unidirectional velocity or time-of-flight. The mass of each ion is then assigned based on its “flight time”. Created in Biorender. _____ - 21 -

Figure 1. 10 Sample preparation workflow for metabolomics. 1) washing and solvent extraction, 2) scraping and transfer into an Eppendorf tube, 3) quenching in liquid nitrogen, 4) three cycles of liquid nitrogen, vortex and sonication, 5) centrifugation, 6) separation of supernatant and pelleting, 7) drying of the supernatant and reconstitution. The pellet is retained for protein quantification. Created in Biorender. _____ - 25 -

Figure 1. 11 Sample preparation for MALDI-MSI analysis. Frozen tissues are cryo-sectioned and tissue slides deposited onto an indium-tin oxide (ITO) coated metal slide. Next, a matrix is applied through sublimation gradually progressing upon heat application from the bottom and condensation onto the tissue. After equilibration at room temperature, the MALDI slide is ready for MS analysis. Created in Biorender. _____ - 26 -

Figure 1. 12 Sample preparation workflow for proteomics. 1) lysis, 2) reduction/alkylation, 3) digestion, 4) washing hydrophilic contaminants, 5) washing hydrophobic contaminants, 6) clean-up of the peptide solution, 7) drying and reconstitution. Created in Biorender. _____ - 27 -

Figure 1. 13 An example sequence order for a LC-MS analysis run. _____ - 28 -

Figure 1. 14 An example of a MS metabolomics workflow analysis. _____ - 29 -

Figure 1. 15 Graphical representation of Principal Component Analysis (PCA) and Partial Least Square (PLS) analysis. a) PCA theoretical model, b) PCA score plot, c) PCA loading plot, d) combination of PCA score and loading plot, e) PLS analysis, and f) plot of PLS– Discriminant Analysis (PLS-DA). Y= known variable. W=weight contribution of the known variable. C=component. F=latent variable. b=weight contribution of the latent variable. u=error terms. The theoretical models of PCA and PLS analysis are adapted from <https://www.theanalysisfactor.com>. Created in Biorender. _____ - 33 -

Figure 1. 16 Representation of different DNA repair mechanisms. 8-Oxoguanine DNA Glycosylase (OGG1), Poly(ADP-Ribose) Polymerase (PARP), X-Ray Repair Cross Complementing 1 (XRCC1), polymerase (Pol), Proliferating cell nuclear antigen (PCNA), Flap Structure-Specific Endonuclease 1 (FEN1), Xeroderma pigmentosum (XP), DNA damage-binding (DDB), Cockayne syndrome (CS), MutS Homolog (MSH), MutL Homologous (MLH), Exonuclease 1 (EXO1), Replication factor C (RFC), Ataxia telangiectasia mutated (ATM), Mre11-Rad50-Nbs1 (MRN) complex, Replication protein (RPA), Breast cancer gene (BRCA), FA Complementation group (FANC). _____ - 39 -

Figure 1. 17 Key metabolic changes occurring in cancer and senescent cells. The picture describes key metabolic pathways known to be rewired in cancer (blue arrows) and senescent cells (red arrows). Altered metabolic pathways include glycolysis (green), amino acids (purple), nucleotides (orange), and lipids metabolism (light blue). Glucose transporter 1 (GLUT1), Monocarboxylate transporter 4 (MCT4), Fatty acid binding protein (FABP), Peroxisome proliferator-activated receptor (PPAR), Lactate dehydrogenase A (LDHA), Pyruvate dehydrogenase (PDH), Isocitrate dehydrogenase (IDH), Succinate dehydrogenase (SDH), Carnitine palmitoyl transferase 1 (CPT1). _____ - 42 -

CHAPTER 2

Figure 2. 1 Subtypes of senescence based on their method of induction. The general features of senescence include: high lysosomal activity through increased β -galactosidase (β -Gal) expression, high expression of p16, p21 and p53 and consequent cell cycle arrest and decreased proliferation, telomere shortening, generation of senescence associated heterochromatin foci (SAHF), increased ROS, reduced energy production, metabolic reprogramming, and the senescence associated secretory phenotype (SASP). _____ - 58 -

Figure 2. 2 β -Gal in senescence-induced HFF-1 cells. Representative phase contrast images of β -Gal staining (grey), DAPI (blue) and composite (β -Gal (grey) and DAPI (blue)) in cells at passage 20, 1 week post irradiation at 12 Gy, 800 μ M hydroxyurea for two weeks and 10 μ M etoposide for one week (a). Corresponding β -Gal levels expressed as a percentage of cell count relative to the number of nuclei counted using ImageJ (b). 9 repeats from 3

independent replicates with on average >50 cells per each sample. p-values have been determined through t-test and represented as $\leq 0.00005 = ****$. _____ - 68 -

Figure 2. 3 γ H2AX foci immunodetection in senescence-induced HFF-1 cells.

Representative images of γ H2AX immunostaining (green), DAPI (blue) and composite (γ H2AX (green) and DAPI (blue)) in cells at passage 20, 12 Gy IR for 1 week, 800 μ M hydroxyurea for two weeks and 10 μ M etoposide for one week (a). Corresponding γ H2AX foci count per cell as measured in Cell Profiler. 9 repeats from 3 independent replicates with on average >50 cells per each sample. Pairwise comparison was performed, and p-values have been determined using a t-test and represented as: $0.0005 = ***$, $\leq 0.00005 = ****$. ____ - 70 -

Figure 2. 4 Ki-67 positive nuclei immunodetection in senescence-induced normal human fibroblasts.

Representative images of Ki-67 immunostaining (red), DAPI (blue) and composite (Ki-67 (red) and DAPI (blue)) in cells at passage 20, 12 Gy IR for one week, 800 μ M hydroxyurea for two weeks and 10 μ M etoposide for one week (a). Corresponding Ki-67 expression levels representative of positive nuclei count (b). 9 repeats from 3 independent replicates with on average >50 cells per each sample. p-values have been determined through t-test and represented as: $0.0005 = ***$, $\leq 0.00005 = ****$, and non-significant = ns. _ - 71 -

Figure 2. 5 Statistical analysis of the metabolic features identified in HFF-1 cells. Cells at passage 20, and following 12 Gy IR for one week, 800 μ M hydroxyurea for two weeks and 10 μ M etoposide for one week. A) PCA score plots and B) PCA loading plots for pairwise analysis of metabolites altered in the different senescence-induced cells. For each treatment group, five replicates were used. Data points in the two-dimensional PCA score plot were central scaled. C) volcano plots displaying enriched (gray) and depleted (blue) metabolic features by representing the \log_2 fold change in altered features and the $-\log_{10}$ adjusted p-values (two-tailed t-test) with cut off values selected at >1.5 and <0.05 , respectively. The first 20 features mostly contributing to the separation between non-treated and treated samples correspond to the PLS-DA components (**Figure S1. 6**, and **Table S1. 3**), and have been highlighted in orange. _____ - 73 -

Figure 2. 6 Pathway enrichment analysis of HFF-1 cells. Cells at passage 20 in culture, following 12 Gy IR for one week, 800 μ M hydroxyurea for two weeks and 10 μ M etoposide for one week. Numbering for each metabolic pathway is kept consistent across the different plots. Pathway analysis was based on the hypergeometric test. Topological analysis was based on betweenness centrality. A FDR $p < 0.05$, and pathway impact > 0.1 were deemed significant. Asterisks (*) indicate non-significant pathways for FDR > 0.05 , but Fisher's p-value < 0.05 . _____ - 75 -

Figure 2. 7 Heatmap cluster analysis. Study of relevant metabolites associated with the pathways altered upon the induction of senescence through multiple passages ($P=20$), irradiation (12 Gy), hydroxyurea (800 μ M) and etoposide (10 μ M). Column dendrogram (Euclidean distance function) reflects the separation of the different senescent models. - 77 -

Figure 2. 8 Summary of putatively identified metabolic pathways altered upon induction of senescence. Enriched metabolic pathways are represented in the coloured boxes: Glycerophospholipids (red), Pentose phosphate pathway (PPP) and histidine (green), glutamine, glutamate aspartate and glutathione (blue), amino/nucleotide sugar (yellow), arginine biosynthesis (purple), and taurine, butanoate metabolism (grey). _____ - 79 -

Figure 2. 9 Statistical analysis of the metabolic features identified in the growth media of HFF-1 cells. Cells at passage 20, and following 12 Gy IR for one week, 800 μ M hydroxyurea for two weeks and 10 μ M etoposide for one week. A) PCA score plots and B) PCA loading plots for pairwise analysis of metabolites altered in the different senescence-induced cells. For each treatment group, five replicates were used. Data points in the two-dimensional PCA score plot were central scaled. C) volcano plots displaying enriched (brown) and depleted (blue) metabolic features by representing the \log_2 fold change in altered features and the $-\log_{10}$ adjusted p-values (two-tailed t-test) with cut off values selected at >1.5 and <0.05 , respectively. The first 10 features mostly contributing to the separation between non-treated and treated samples correspond to the PLS-DA components (**Figure S1. 10** and **Table S1. 6**), and have been highlighted in orange. ____ - 81 -

Figure 2. 10 Venn diagram. The diagram represents the enriched class of extracellular and intracellular metabolites in late passaged, irradiated, hydroxyurea and etoposide treated cells. Data have been processed in MetaboAnalyst 5.0. _____ - 82 -

Figure 3. 1 Statistical analysis of the metabolic content of aged murine brain tissues. Graphical representation of the PCA statistical analysis and differentially expressed metabolites in aged murine brain tissue relative to control. For each sample group, five biological replicates were used. a) Data points in the two-dimensional PCA score plot and b) loading plot were central scaled. Ellipses are indicators of the clustered samples. C) Volcano plots display enriched (blue) and depleted (yellow) metabolic features by representing the log₂ fold change in altered features and the -log₁₀ adjusted p-values (two-tailed t-test) with cut off values selected at >1.5 and <0.05, respectively. The first 20 features mostly contributing to the separation between young and old samples correspond to the PLS-DA components (**Figure S2. 3**), and have been highlighted as orange data points. _____ - 103 -

Figure 3. 2 Pathway enrichment analysis of metabolites occurring the aged murine brain tissue. A) Metabolite enrichment analysis of aged murine brain tissue. Enrichment analysis was based on a hypergeometric test. Topological analysis was based on betweenness centrality. B) The list of significant metabolites (p≤0.05) altered in murine brain tissue with ageing. Variance of metabolite expression levels between old and young murine tissue is expressed as a Log₂ fold change. _____ - 104 -

Figure 3. 3 Proteins altered in murine brain tissue as a function of age. A) PCA statistical analysis score plot and b) loading plot. Data points in the two-dimensional PCA plots were central scaled. c) volcano plot-based differential study of proteins in old vs young mice. Data display enriched (blue) and depleted (yellow) protein features by representing the log₂ fold change in altered features and the -log₁₀ adjusted p-values (two-tailed t-test) with cut off values selected at >1.5 and <0.05, respectively. For each sample group, five biological replicates were used. d) Significantly altered protein genes in old mice relative to the young controls. Variance of the expression levels of proteins is represented with the Log₂Fold change. _____ - 106 -

Figure 3. 4 Enriched metabolic pathways altered in aged murine brain tissue. Enrichment analysis resulted from the integration of identified putative protein genes and metabolites. _____ - 108 -

Figure 3. 5 Graphical summary representation of the putatively identified metabolic pathways in the brain tissues of old mice. Enriched and depleted metabolic/protein features are in green and red, respectively. In bold are represented significant metabolites. - 109 -

Figure 3. 6 MALDI-MSI analysis of the left-brain hemisphere of aged (10-months) and young (5-months) mice. a) Frontal and temporal lobe of wild type (WT) old and young mice. Fatty acid (FA) 16:0 (m/z 255.231), FA 18:1 (m/z 281.246), FA 18:0 (m/z 283.261), and FA 20:4 (m/z 303.231). b) Frontal, temporal and parietal lobe of young (5-months) mice wild-type (WT) and deficient in glutathione (GSH) synthesis (Gclm -/-). FA 16:0 (m/z 255.231), FA 18:1 (m/z 281.246), FA 18:0 (m/z 283.261), phosphatidylinositol (PI) 38:4 (m/z 885.543), and phosphatidylethanolamine (PE) 46:7:0 (m/z 888.616). _____ - 110 -

CHAPTER 4

Figure 4. 1 Corresponding MTS dose-response curves for MCF7, HCC1937 and MDA-MB-231 cells treated with ascending doses of olaparib (0.1-500 μM) for seven days. The corresponding R² values for fitted dose-response curves in MCF7 (IC₅₀= 10 μM), MDA-MB-231 (IC₅₀= 14 μM), and HCC1937 (IC₅₀= 150 μM) cells were 0.89, 0.91 and 0.85, respectively. The equation for the non-linear regression curve is $Y = \text{Bottom} - (\text{Top} - \text{Bottom}) / (1 + (X / \text{IC}_{50}))$. IC₅₀ is the concentration of drug that gives a response halfway between Bottom and Top. This is not the same as the response at Y=50. _____ - 130 -

Figure 4. 2 The formation of p53BP1 foci in response to treatment with either growth medium or medium containing olaparib. Representative images of immunolabelled P53BP1 foci (red), DAPI (blue) nuclear counterstain and composite (p53BP1 (red) and DAPI (blue)) in MCF-7, MDA-MB-231, and HCC1937 cells treated with olaparib for seven days (a, c, e). Corresponding p53BP1 foci counts determined using Cell Profiler (b, d, f). 9 repeats with on average >100 cells per each sample. p-values have been determined through ANOVA test. Dunnett's multiple comparison test was used as a follow up to ANOVA test and the p-values were represented as: non-significant=ns, 0.05=*, 0.005=**, 0.0005=***, >0.00005=****. _____ - 132 -

Figure 4. 3 The formation of γH2AX foci formation in response to treatment with either growth medium or medium containing olaparib. Representative images of immunolabelled γH2AX foci (green), DAPI (blue) nuclear counterstain and composite

(γ H2AX and DAPI) in MCF-7, MDA-MB-231, and HCC1937 cells treated with for seven days (a, c, e). Corresponding γ H2AX foci counts determined using Cell Profiler (b, d, f). (>100 cells per sample). Dunnett's multiple comparison test was used as a follow up to ANOVA and corresponding p-values were represented as: non-significant=ns, 0.05=*, 0.005=**, 0.0005=***, >0.00005=****.

Figure 4. 4 Statistical analyses of global metabolic features identified in MCF7, MDA-MB-231 and HCC1937 upon exposure to IC₁₀, IC₂₅ and IC₅₀ olaparib doses for seven days. Data acquired in positive and negative ionization mode. For each treatment group, five replicates were used. Data points in the two-dimensional PCA score plot were central scaled. a) PCA pairwise analysis and differential analysis of metabolites altered in IC₅₀-treated cells, ellipses represent the 95% confidence interval. b) Volcano plots displaying enriched (blue) and depleted (grey) metabolic features by representing the log₂ fold change in altered features and the -log₁₀ adjusted p-values with cut off values selected at >1.5 and <0.05, respectively.

Figure 4. 5 Pathway enrichment analysis of MCF7 (10 μ M), MDA-MB-231 (14 μ M) and HCC1937 (150 μ M) cells following a seven-day exposure to olaparib. Enrichment analysis was based on the hypergeometric test. Topological analysis was based on betweenness centrality. The tight integration method was used by combining genes and metabolites into a single query. A p<0.05, and pathway impact >0.1 were deemed significant.

Figure 4. 6 Heatmap cluster analysis of relevant metabolites associated with the pathways altered upon exposure to olaparib in MCF7 (10 μ M), MDA-MB-231 (14 μ M) and HCC1937 (150 μ M) cells for seven days. Clustering and distance function are Ward and Canberra, respectively. Normalised areas indicate chromatographic peaks areas that have been normalised based on the QC samples to compensate for batch effects.

Figure 4. 7 A summary of putatively identified metabolic pathways altered in response to olaparib exposure. Significantly altered features with a Log₂ fold change of >1.5 (blue-enriched and grey-depleted). Fitness effect score of metabolic enzymes (light-blue boxes) in relation to PARP expression in each cell line. Positive and negative scores are in green and red, respectively. MCF-7 (■), MDA-MB-231 (▨), and HCC1937 (▩). Fitness effect score is based on the Chronos algorithm.

APPENDIX 1

Figure S1. 1 Sample batch order. 2 blanks were injected at the beginning and at the end of the run. 10 QCs were injected before injections of the samples. Then QCs were injected after every 5 samples. QCs have been prepared by pooling together all the sample after drying and reconstitution with water:acetonitrile (50:50, v/v).

Figure S1. 2 Viability response of HFF-1 cells at different passages, different doses of X-Ray, hydroxyurea and etoposide. Passaged, irradiated and etoposide-treated cells were kept in culture for 1 week, while hydroxyurea cells were treated for 2 weeks. After the incubation time, cells were stained with crystal violet, subsequently solubilised in ethanol, and absorbance was read at 600 nm. p-values have been determined through ANOVA test. Dunnett's multiple comparison test was used as a follow up to ANOVA test and the p-values were represented as: non-significant=ns, 0.05=*, 0.005=**, 0.0005=***, 0.00005=****.

Figure S1. 3 The expression of β -Gal in senescence-induced HFF-1 cells. Representative phase contrast images of β -Gal staining (grey), DAPI immunolabelled nuclei (blue) and composite (β -Gal (grey) and DAPI (blue)) in cells at different passages (a), increasing irradiation doses for 1 week (b), treatment with increasing concentrations of hydroxyurea for 2 weeks (c) and etoposide for 1 week (d). For each condition, corresponding β -Gal expression levels expressed have been reported as a percentage of manually counted stained cells relative to the number of counted nuclei using ImageJ. 9 repeats with on average >50 cells per each sample. p-values have been determined ANOVA test.

Figure S1. 4 Measurements of width and length of HFF-1 cells. Cells at late passage (P20), 12 Gy irradiation, for 1 week, 800 μ M hydroxyurea for 2 weeks, and 10 μ M etoposide for 1 week. Cells stained for β -Gal expression have been analysed to measure width and length of individual cells. A total number of 45 cells have been analysed per each passage and dosage. Width and length have been measured through the line tool in ImageJ and expressed as μ m. Dunnett's multiple comparison test was used as a follow up to ANOVA and corresponding p-values were represented as: non-significant=ns, 0.05=*, 0.005=**, 0.0005=***, 0.00005=****.

Figure S1. 5 Statistical analysis of global metabolomics features identified in different induced senescence models. These include replicative senescence at passage 20, 12 Gy irradiation for 1 week, 800 μ M hydroxyurea for 2 weeks, and 10 μ M etoposide for 1 week. A) Workflow used in this study to perform pathway analysis from metabolomics analyses. b) Global PCA score plots of the analysed senescent cells for data acquired in positive/negative switching mode. For each treatment group, five replicates were used. Data points in the two-dimensional PCA score plot were central scaled. _____ - 168 -

Figure S1. 6 Pairwise partial least square-discriminant analysis (PLS-DA) of different senescence-induced cells. The orange circles represent the first 20 discriminating compounds that allow to differentiate between non-treated and treated cells. _____ - 169 -

Figure S1. 7 Venn diagram. The diagram represents the metabolic pathways of normal human fibroblast at late passaged cells, and cells treated with irradiation, hydroxyurea, and etoposide. _____ - 172 -

Figure S1. 8 Known and predicted protein-protein interactions. Analysis performed through STRING Data Sources. Input data are represented by the list of senescence genes (Table S 3) and the enzymatic genes in the metabolic pathway model of Figure 8. ____ - 177 -

Figure S1. 9 PCA analysis of growth media samples collected from HFF-1 cells. Cells at passage 20, and after treatment with 12 Gy irradiation, 800 μ M hydroxyurea and 10 μ M etoposide. For each treatment group, five replicates were used. Data points in the two-dimensional PCA score plot were central scaled. Ellipses represent 95% confidence interval. _____ - 178 -

Figure S1. 10 Pairwise partial least square-discriminant analysis (PLS-DA) of the media collected from different senescence-induced cells. The orange circles represent the first 10 discriminating compounds that allow to differentiate between non-treated and treated cells. - 178 -

APPENDIX 2

Figure S2. 1 Sample batch order. 2 blanks were injected at the beginning and at the end of the run and after every 5 samples. _____ - 191 -

Figure S2. 2 Workflow used in this study to perform pathways analysis from metabolomics analyses _____ - 192 -

Figure S2. 3 Pairwise partial least square-discriminant analysis (PLS-DA) of old vs young brain tissues. The orange circles represent the first 20 discriminating compounds that allow to differentiate between young and old murine brain tissues. _____ - 192 -

Figure S2. 4 Workflow used in this study to perform pathway analysis from proteomics analyses. _____ - 197 -

APPENDIX 3

Figure S3. 1 Sample batch order. 2 blanks were injected at the beginning and at the end of the run. 10 QCs were injected before injections of the samples. Then QCs were injected after every 5 samples. QCs have been prepared by pooling together all the sample after drying and reconstitution with water:acetonitrile (50:50, v/v). _____ - 209 -

Figure S3. 2 The formation of p53BP1 foci in response to treatment with either growth medium or medium containing olaparib. Representative images of immunolabelled P53BP1 foci (red), DAPI (blue) nuclear counterstain and composite (p53BP1 (red) and DAPI (blue)) in MCF-7, MDA-MB-231, and HCC1937 cells treated with olaparib for seven days (a-c)._ - 214 -

Figure S3. 3 The formation of γ H2AX foci formation in response to treatment with either growth medium or medium containing olaparib. Representative images of immunolabelled γ H2AX foci (green), DAPI (blue) nuclear counterstain and composite (γ H2AX and DAPI) in MCF-7, MDA-MB-231, and HCC1937 cells treated with for seven days (a-c). _____ - 215 -

Figure S3. 4 Global metabolic features identified in MCF7, MDA-MB-231 and HCC1937 upon exposure to IC₁₀, IC₂₅ and IC₅₀ olaparib doses for seven days acquired in positive and negative ionization mode. a) Workflow used in this study to perform pathway analysis from metabolomics analyses. b) Global PCA score plots of the analysed breast cancer cell lines for data acquired in positive and negative ionization mode. For each treatment group, five replicates were used. Data points in the two-dimensional PCA score plot were central scaled. Ellipses represent 95% confidence interval. _____ - 215 -

Figure S3. 5 PCA pairwise analysis of untargeted metabolomics data collected, in both positive and negative mode, from MCF7, MDA-MB-231, and HCC1937 cells treated with IC₁₀, IC₂₅ and IC₅₀ olaparib treatment doses. Data points in the two-dimensional PCA score

plot were central scaled. The plot was designed on R through the ggplot2 graphical package (n=5). Ellipses represent 95% confidence interval. _____ - 216 -

Figure S3. 6 Volcano plots showing the log₂ fold change and the -log₁₀ adjusted p-values in metabolite levels induced by treatment with different doses of Olaparib (IC₁₀, IC₂₅, and IC₅₀) in MCF7, MDA-MB-231 and HCC1937 cells. Data were selected at the cut off values adjusted p<0.05 and fold change >1.5. Blue and grey boxes indicate metabolites significantly enriched and depleted in the different samples, respectively. _____ - 216 -

Figure S3. 7 Statistical analysis with new data processing method using 70% of annotation threshold and more ion adducts ([M+H]⁺+1; [M-H]⁻-1; [M+ACN+H]⁺+1; [M+FA-H]⁻-1; [M+ACN+Na]⁺+1; [M+H+Na]⁺+2; [M+H+NH₄]⁺+2; [M+Na]⁺+1; [M+NH₄]⁺+1). A) PCA pairwise analysis of untargeted metabolomics data collected, in both positive and negative mode, from MCF7, MDA-MB-231, and HCC1937 cells treated with IC₁₀, IC₂₅ and IC₅₀ olaparib treatment doses. Data points in the two-dimensional PCA score plot were central scaled. The plot was designed on R through the ggplot2 graphical package (n=5). Ellipses represent 95% confidence interval. B) Volcano plots showing the log₂ fold change and the -log₁₀ adjusted p-values in metabolite levels induced by treatment with different doses of Olaparib (IC₁₀, IC₂₅, and IC₅₀) in MCF7, MDA-MB-231 and HCC1937 cells. Data were selected at the cut off values adjusted p<0.05 and fold change >1.5. Blue and grey boxes indicate metabolites significantly enriched and depleted in the different samples, respectively. The first 20 features mostly contributing to the separation between young and old samples are indicated as orange data points and correspond to the PLS-DA components highlighted in the c) loading plot and d) PLS-DA analysis. _____ - 218 -

Figure S3. 8 Enrichment analysis of non-treated MCF7, MDA-MB-231 and HCC1937 cells. - 218 -

Figure S3. 9 Venn diagram representing the metabolic pathways in MCF7, MDA-MB-231 and HCC1937 cells .a) Baseline metabolic pathways and b) following a seven day treatment with olaparib at IC₅₀ doses. _____ - 219 -

Figure S3. 10 Pearson's correlation analysis between the relevant metabolites identified within each different breast cancer cell line. Pearson's coefficient is set in a range of 1 to -1, indicative of a positive and negative correlation, respectively. _____ - 226 -

LIST OF TABLES

CHAPTER 1

Table 1. 1 List of the most common additives used in HPLC and UHPLC analysis _____	- 6 -
Table 1. 2 Strategies employed in chromatography during separation of analytes. _____	- 6 -
Table 1. 3 Description of different HILIC column stationary phases, their base particles, functional groups and application for separation of specific compounds _____	- 9 -
Table 1. 4 Typical Features of the mass analysers, quadrupole and orbitrap. Compared to the quadrupole, the orbitrap mass analyser is characterised by higher resolution and mass accuracy. _____	- 15 -
Table 1. 5 MALDI matrices used for the analysis of specific classes of analytes. Adapted from Norris, JL., et al., 2013 [40]. _____	- 20 -
Table 1. 6 Key features of untargeted and targeted approaches in metabolomics and proteomics _____	- 21 -
Table 1. 7 Extraction solvents commonly used for the extraction of metabolites. _____	- 25 -
Table 1. 8 List of FDA approved biomarkers for clinical use. In bold are indicated the metabolic targets [116]. _____	- 35 -
Table 1. 9 Class of gene mutations and their association with abnormal protein synthesis and age-related diseases including cancer. _____	- 37 -

CHAPTER 2

Table 2. 1 Thresholding parameters applied in Cell Profiler for the detection of foci and labelled nuclei. _____	- 63 -
-------------------------------------------------------------------------------------------------------------------------	--------

APPENDIX 1

Table S1. 1 Elution gradient used for the chromatographic separation of metabolite extracts - 159 -	
Table S1. 2 Setting for LC-MS data analysis and processing _____	- 160 -
Table S1. 3 Table with a list of the first 20 PLS-DA compounds for all the conditions. m/z value, Log ₂ Fold change and p-values have been reported. _____	- 169 -
Table S1. 4 Output tables of pathway enriched analysis performed with MetaboAnalyst and Mummichog software in different cell treatment conditions (multiple passages, irradiation, hydroxyurea, and etoposide). P values are FDR = False Discovery Rate. _____	- 170 -
Table S1. 5 List of metabolites identified in normal human fibroblasts. Cells at passage 20, after 12 Gy X-ray treatment for 1 week, 800 μ M hydroxyurea and 10 μ M etoposide treatment for 2 and 1 week, respectively. Class, name, Log ₂ fold change, and p-value (p) is represented for each compound. In bold are the significant compounds. _____	- 173 -
Table S1. 6 Table with a list of the first 10 PLS-DA compounds for all the conditions. m/z value, Log ₂ Fold change and p-values have been reported. _____	- 179 -
Table S1. 7 List of metabolites identified in the media of normal human fibroblasts. Cells at passage 20, after 12 Gy X-ray treatment for 1 week, 800 μ M hydroxyurea and 10 μ M etoposide treatment for 2 and 1 week, respectively. Class, Name, Log ₂ fold change, and p-value (p) is represented for each compound. In bold are significant compounds. _____	- 180 -

APPENDIX 2

Table S2. 1 Corresponding elution gradient used for the chromatographic separation of metabolites and protein extracts _____	- 184 -
Table S2. 2 LC-MS/MS method summary for metabolomics and proteomics _____	- 184 -
Table S2. 3 Data processing workflows for metabolomics analysis through Compound Discoverer 3.3 _____	- 186 -
Table S2. 4 Data processing workflows (processing and consensus) for proteomics analysis through Proteome Discoverer 3.0 _____	- 189 -
Table S2. 5 Table with a list of the first 20 PLS-DA compounds for all the conditions. m/z value, Log ₂ Fold change and p-values have been reported. _____	- 193 -
Table S2. 6 Classes of enriched metabolites in the brain tissues of old mice relative to the young mice. Analysis performed through MetaboAnalyst and Mummichog software. _____	- 193 -

Table S2. 7 Classification of putative metabolites identified in the brain tissues of old and young mice. Variation of metabolite expression in old/young mice is represented with the Log₂ fold change, while P is the p-value associated with each metabolite. Significant metabolites are highlighted in Bold. _____ - 194 -

Table S2. 8 List of genes encoding proteins/enzymes involved in certain metabolic pathways. Name, pathways, role and location for each gene have been reported, which were acquired from UniProt. _____ - 198 -

Table S2. 9 Metabolic pathways enriched in the brain tissues of aged mice after integrative analysis with metabolomics and proteomics data. FDR = False discovery rate. _____ - 204 -

Table S2. 10 List of lipids identified from MALDI-MSI analysis. For each m/z value peak intensity is reported in Young-wild type (Young-WT), Old-WT, and Young-knocked out (Young-KO) samples. _____ - 205 -

APPENDIX 3

Table S3. 1 Cell lines used in this study and their corresponding clinicopathologic profiles (ER: estrogen receptor, PR: progesterone receptor, and HER2: Human epidermal growth factor 2 receptor) _____ - 209 -

Table S3. 2 Corresponding elution gradient used for the chromatographic separation of metabolite extracts _____ - 210 -

Table S3. 3 Normality test for cell viability and immunofluorescence quantification data. The Shapiro-Wilk test has been performed with R software. p-values of >0.05 were considered as normally distributed. P-value (p). _____ - 210 -

Table S3. 4 Setting for LC-MS data analysis and processing _____ - 210 -

Table S3. 5 ANOVA analysis of olaparib dose-dependent DNA DSB immunofoci formation - 215 -

Table S3. 6 Global differential number of altered metabolites for samples treated with IC₁₀, IC₂₅ and IC₅₀ of Olaparib and their relative control (non-treated) samples. Metabolites identified in both positive and negative mode with p-value = <0.05 and Log₂ Fold Change = >1.5. _____ - 218 -

Table S3. 7 Metabolic pathways in different breast cancer cells (MCF7, MDA-MB-231, and HCC1937) before and after treatment with IC₅₀ dose of Olaparib. FDR = False Discovery Rate. _____ - 219 -

Table S3. 8 Comparison analysis between MetaboAnalyst and Mummichog software. FDR = False discovery rate. Gamma = Gamma p-value. FET = Fisher's Exact test. _____ - 220 -

Table S3. 9 Classification of the metabolites identified in MCF7, MDA-MB-231 and HCC1937 at all Olaparib doses (IC₁₀, IC₂₅ and IC₅₀) after seven days treatment. Class, name, Log₂ fold change, and the p-value (p) is represented for each compound. PC: phosphocholine; PE: phosphoethanolamine; PUFA: poly unsaturated fatty acid; SM: Sphingomyelin. _____ - 221 -

Table S3. 10 Effect scores of enriched metabolic genes in MCF-7, MDA-MB-231 and HCC1937 cells evaluated through the Dependency Map Portal (DepMap) database. Fitness effect score is based on the Chronos algorithm. Fitness Effect Score (FES). _____ - 227 -

ABBREVIATIONS AND ACRONYMS

2,4-DNPH: 2,4-dinitrophenylhydrazine
3-HPA: 3-hydroxypicolinic acid
AA: Acrylamide
Ahcy11: adenosylhomocysteine hydrolase-like protein 1
AMP: adenosine monophosphate
AMPK: AMP-activated protein kinase
ANOVA: Analysis Of Variance
APCI: Atmospheric-Pressure Chemical Ionization
APPI: Atmospheric-Pressure Photoionization
ASNS: asparagine synthetase
ATM: Ataxia Telangiectasia Mutant gene
ATP: Adenosine Triphosphate
BCAA: Branched-Chain Amino Acids
BCL-2: B Cell Lymphoma 2
BRCA: breast cancer susceptibility gene
C-trap: Curved linear trap
CDP: cytidine diphosphate
CHCA: α -cyano-4-hydroxycinnamic acid
ChEBI: Chemical Entities of Biological Interest
CI: Chemical Ionization
CPT1: Carnitine Palmitoyltransferase 1
DAN: 1,5-Diaminonaphthalene
DC: Direct Current
DDA: Data Dependent Acquisition
DDR: DNA Damage Response
DepMap: Dependency Map Portal
DESI: Desorption Electrospray Ionization
DHA: 2,6-dihydroxyacetophenone
DHB: 2,5-Dihydroxybenzoic acid
DIA: Data Independent Acquisition
DODE: 9,12-dioxo-10-dodecenoic acid
DSB: Double Strand Break
DTT: Dithiothreitol
EDE: 4,5-epoxy-2-decenal
EI: Electron Ionization
ESI: Electrospray Ionization
FA: Fatty Acid
FAB: Fast Atom Bombardment
FABP: Fatty Acid Binding Protein

FDA: Food and Drug Administration
FDR: False Discovery Rate
FWHM: Full Width at Half Maximum
GC-MS: Gas Chromatography-Mass spectrometry
GCN2: General Control Nondepressible 2
GenAge: The Ageing Gene Database
GlcM: glutamate-cysteine ligase modifier
Glud1: glutamate dehydrogenase 1
GLUT1: Glucose transporter 1
Got1/2: aspartate aminotransferase
GSH: Glutathione
HDR: homology-dependent repair
HER2: human epidermal growth factor receptor 2
HESI: heated electrospray ionisation
HHE: 4-hydroxy-2-hexenal
HIF1: Hypoxia-inducible factor
HILIC: Hydrophilic Interaction Chromatography
HMDB: Human Metabolome Database
HNE: 4-hydroxy-2nonenal
HPLC: High-Pressure Liquid Chromatography
HPNE: 4-hydroperoxy-2-nonenal
HR: Homologous Recombination
IACUC: Institutional Animal Care and Use Committee
ICR: Ion Cyclotron Resonance
IDH: Isocitrate Dehydrogenase
IR: Ionization Radiation
IT: Ion Trap
ITO: indium tin oxide
KDM: lysine (K)-specific demethylase
KEGG: Kyoto Encyclopedia of Genes and Genomes
LC-MS: Liquid Chromatography-Mass Spectrometry
LC-MS/MS: Liquid Chromatography tandem Mass Spectrometry
LDHA: Lactate dehydrogenase A
LPO: Lipid peroxide
MALDI: Matrix-Assisted Laser Desorption/Ionization
MCT4: Monocarboxylate transporter 4
MDA: Malondialdehyde
MiDAS: Mitochondrial Dysfunction Associated Senescence
MSEA: Metabolite Set Enrichment Analysis
MSI: Mass Spectrometry Imaging
MTS: 3-(4,5-dimethylthiazol-2-yl)-5-(3-carboxymethoxyphenyl)-2-(4-sulfophenyl)-2H-tetrazolium

NAD: Nicotinamide Adenine Dinucleotide
Nd:YAG: Neodymium-doped Yttrium Aluminum Garnet
NEAA: Non Essential Amino Acid
NF-Kb: Nuclear Factor Kappa B
NMR: Nuclear Magnetic Resonance
ODC: ornithine decarboxylase
OHE: 4-oxo-2-hexenal
ONE: 4-oxo-2-nonenal
OXPHOS: Oxidative phosphorylation
p53BP1: p53-binding protein 1
PARP: Poly (ADP Ribose) Polymerase
PARylation: Poly-ADP-Ribosylation
PC: Principal Component
PCA: Principal Component Analysis
PCoA: Principal Coordinate Analysis
PDH: Pyruvate dehydrogenase
PE: phosphoethanolamines
PGF: Prostaglandine
PI: Phosphatidylinositol
PI3K: phosphatidylinositol-4,5-bisphosphate 3-kinase
PLS-DA: PLS-Discriminant Analysis
PLS: Partial Least Square
PPAR: Peroxisome Proliferator-Activated Receptor
PPi: pyrophosphate
PPP: pentose phosphate pathway
PTM: Post-translational modification
PUFA: Polyunsaturated Fatty Acid
Q: Quadrupole
QC: Quality Control
RF: Radiofrequency
ROS: Reactive Oxygen Species
RT: Retention Time
SA: 3,5-Dimethoxy-4-hydroxycinnamic acid
SAHF: Senescence associated heterochromatin foci
SAM: S-adenosylmethionine
SASP: Senescence Associated Secretory Phenotype
SDH: Succinate Dehydrogenase
SIPS: Stress-Induced Premature Senescence
SLP: Substrate-Level Phosphorylation
TAGs: triacylglycerols
TCA: Tricarboxylic acid

TET: Ten-Eleven Translocation
TFA: Trifluoroacetic acid
THAP: 2,4,6-trihydroxyacetophenone
TNBC: Triple negative breast cancer
TOF: Time of Flight
TP53BP1: Tumour Protein P53 Binding Protein 1
UDP: Uridine diphosphate
UHPLC: Ultra-High-Performance Liquid Chromatography
WT: Wild type
β-Gal: β-galactosidase
γH2AX: Phosphorylated histone H2 variant

CHAPTER 1

1.1. Introduction

1.1.1. The central dogma

The central dogma of molecular biology was introduced in the 1927 by Francis Crick [1] who stated that in a living organism the information contained in the DNA is transcribed into RNA and translated into proteins, including enzymes (**Figure 1. 1**). In 2005, metabolites, the product of endogenous enzymatic reactions and processing of external sources (food, drugs, microbiome, environment), were described as a key missing link in the central dogma of biology [2].

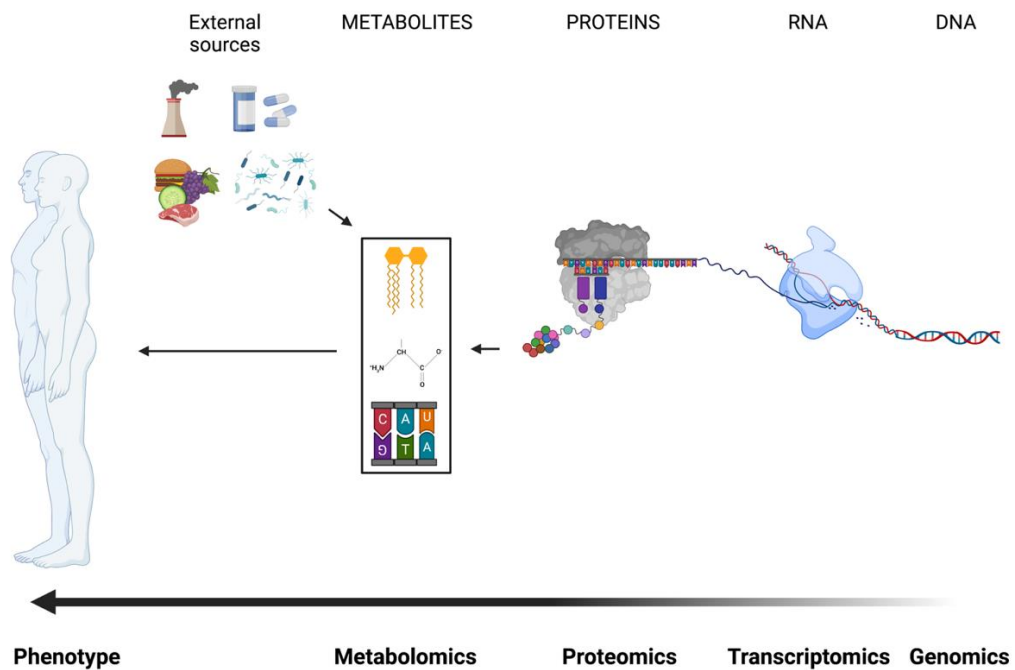


Figure 1. 1 The central dogma of molecular biology. Biochemical information contained in a cell is translated from the DNA to the RNA and proteins, including enzymes. Enzymatic reactions lead to the production of metabolites which are the molecules closely associated with organism phenotype. Created in Biorender.

For decades the unidirectionality of the central dogma has led to consider genes as the blueprint for life, and since the publication of the whole human genome sequence (2004) [3], genomics has represented the main tool

researchers have employed to understand the mechanisms of disease pathogenesis. However, it is now clear that information flows multi-directionally between the tiers (genomics, transcriptomics, proteomics, and metabolomics) of biological information, and that genes do not provide enough information to profile the whole phenotype of an organism. One gene can be translated into more than one protein which can in turn undergo a series of post-translational modifications (PTMs), therefore increasing the complexity of gene function.

Proteomics is a postgenomic discipline (1990s) aiming not only at identifying and quantifying all the proteins in an organism, but also at studying their functions, localization, interactions, PTMs and turnover [4]. In humans, there are an estimated 80,000 proteins [5] encoded by approximately 20,000 – 25,000 genes [6]. Following the PTMs the number of proteins is over 1 million [7]. Proteins have various functions in cell signalling, immune response, DNA replication and DNA repair, but also structural and mechanical functions. Importantly, many proteins are enzymes crucial to catalysing the set of life-sustaining biochemical reactions referred to as metabolism.

Metabolomics is the comprehensive study of metabolites – small molecules (50 – 1,500 Da) intermediate and end products of the metabolism. Metabolites are present in biofluids, cells and tissues at a specific time, therefore providing an immediate snapshot of the physiological state of a biological system. Of particular note, metabolites serve to generate the building blocks of macromolecules such as DNA, RNA and proteins, so that any changes occurring at the level of metabolites will reflect changes at the genomic, transcriptomic and proteomic levels. This peculiarity makes metabolomics a promising tool for understanding mechanisms driving the development of disease. Cells and tissues have unique metabolic features which are sensitive to various genetic and environmental stimuli and vary with time. This heterogeneous and dynamic nature of metabolism makes it difficult to characterise, but a powerful predictive, prognostic and diagnostic tool for precision medicine [8]. Considering their constitutive role in the metabolism of living organisms, metabolites are key regulators of energy production,

consumption and storage, signal transduction, inflammatory response, viability and death [9]. Therefore, regulating metabolic homeostasis is essential to guarantee the correct functionality of biological systems. Such homeostatic control can be compromised with age and diseases such as cancer, leading to chronic structural and functional dysfunctions [10]. Given these premises, it is not surprising that there is a growing interest in better understanding the specific functions of metabolites and identifying the pathways in which they are involved that associate with specific phenotypes.

1.1.2. Technologies used in metabolomics and proteomics studies

Analytical tools for metabolomics and proteomics research include nuclear magnetic resonance (NMR), gas chromatography – mass spectrometry (GC-MS), liquid chromatography – mass spectrometry (LC-MS), and mass spectrometry imaging (MSI) [11]. Despite extensive NMR use in metabolomics for the identification of unknown compounds, its low sensitivity has led to the preferential use of MS-based techniques which allow tens of thousands of m/z features to be captured for each sample [12]. Among the MS technologies, LC-MS is the preferred analytical tool used in metabolomics. The popularity of LC-MS use is due to the rapid and efficient separation of species contained within samples [12]. One of the limitations of LC-MS is the inability to provide information on spatial metabolite distribution. This information is provided by MSI which has been successfully and extensively applied to various human and animal tissues.

1.1.2.1. Liquid Chromatography – Mass Spectrometry

In general, LC-MS is an analytical technique coupling the physical separation of the components present in a sample with their mass analysis by means of liquid chromatography and mass spectrometry devices, respectively. A schematic representation of LC-MS components is given in **Figure 1. 2**.

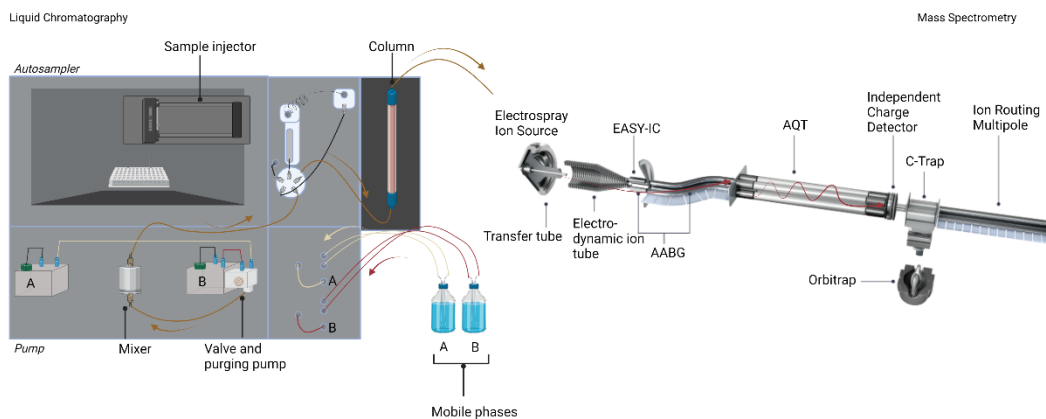


Figure 1. 2 Example of a Liquid Chromatography– Mass Spectrometry (LC-MS) system. Example of the Exploris 240 MS system. The LC apparatus consists of an autosampler, pump and column compartment. The samples held in the autosampler are injected into the column through the needle injector. The mobile phases flow through the column after being mixed in the pump system. Eluted analytes are then introduced in the ion source where the liquid phase is evaporated and the analyte is ionised. Ions in the gas-phase are transported through the MS apparatus from the low to high vacuum regions. Thus, they pass through a transfer and electrodynamic tube where the internal calibrant (IC) ion, fluoranthene (202.0777 m/z), is delivered to the sample by the EASY-IC component. Ions are then transported along the advanced active beam guide (AABG) to the quadrupole component (AQT) for an initial ion selection. Ions in a C-trap will be injected in to the orbitrap, the second mass analyser. During fragmentation, ions pass through the ion routing multipole before being re-introduced in the orbitrap analyser. Created in Biorender.

The LC system separates the components of a sample in a liquid fluid known as the mobile phase, which is passed through a column filled with a stationary phase. In a high-pressure liquid chromatography (HPLC) apparatus, the mobile phase is pumped at high pressure (50 – 400 bar) through a column filled with a granular material (silica, polymers, etc.) of small particles (2-50 μm), an internal diameter of 4.6 mm and a length of 50-250 mm [13]. In 2003, ultra-high-performance liquid chromatography (UHPLC) was introduced as an alternative to HPLC [14]. The UHPLC system is characterised by a shorter column (internal diameter <2.1 mm and length of ~100 mm) whose particle size is <2 μm . Consequently, the backpressure can go up to 1500 bar. Considering its features, UHPLC allows a faster separation, better peak resolution, and a relatively lower cost compared to HPLC. In addition to its technical advantages, UHPLC is environmental-friendly because of the

reduced solvent needed to run an analysis [15]. However, most methods have been developed for the HPLC system, thus a higher investment in time and resources should be considered when adapting those methods to UHPLC [16]. The mobile phase is generally a miscible combination of water and organic solvents (e.g., methanol, acetonitrile, IPA). Controlling the pH of the mobile phase is crucial when weak acids or bases are added like the polar molecules that constitute part of the human metabolome [17]. Weak acids and bases are ionizable analytes. Mobile phase pH affects the ionization of an analyte, and consequently its retention time on a stationary phase (time measured from the point of injection to the maximum point of retained peak), selectivity and peak shape [18]. Indeed, when the analyte is ionised, it becomes more polar and therefore it will be more likely to participate in hydrophilic rather than hydrophobic interactions [18]. Assuming a non-polar stationary phase, this translates into reduced retention of the ionised analyte and a faster elution through the hydrophilic mobile phase. If both ionised and neutral forms of an analyte are present within a sample, they will elute at different retention times thus resulting in asymmetric peaks and poor peak shape. To avoid this issue, the mobile phase pH can be controlled and adjusted by supplementation with additives which form neutral ion-pairs with the basic groups of the analyte therefore enhancing its hydrophobic properties. However, solely considering the chromatographic performance of an additive is not sufficient and its MS sensitivity should also be considered. For example, strong acids such as trifluoroacetic acids (TFA), used as a gold standard mobile phase additive, are also a strong suppressor of ion formation in the electrospray source. This is a result of ion-pair resistance to fragmentation, which prevents their detection in MS conditions [19]. Thus, weaker ion-pairing additives such as formic acid should be considered. Some known additives and their properties have been listed in **Table 1. 1**.

Table 1. 1 List of the most common additives used in HPLC and UHPLC analysis

NAME	pKa	pKb	Formula
Acetic acid	4.7		CH ₃ COOH
Formic acid	3.7		HCOOH
Trifluoroacetic acid	0.5		CF ₃ COOH
Triethylammonium acetate	4.7	11.0	(CH ₃ CH ₂) ₃ N:CH ₃ COONH ₄
Triethylammonium formate	3.7	11.0	(CH ₃ CH ₂) ₃ N:NH ₄ COOH
Ammonium acetate	4.7	9.2	CH ₃ COONH ₄
Ammonium formate	3.8	9.2	NH ₄ COOH
Ammonium bicarbonate	6.3	10.3	NH ₄ HCO ₃

Both water and organic solvents are combined in a mixing chamber before entering the column. During isocratic elution the composition of the mobile phase is maintained, while in gradient elution the mobile phase composition changes so that a weak elution solvent is used at the start of the run, and then increasing proportions of a strong elution solvent is added during separation. In a complex sample made of a mixture of polar and non-polar compounds, gradient elution is preferable as it allows the separation of a wider range of molecules.

Mobile phase components are selected depending on the nature of the analytical column and the chemistry of the targets of interest. In turn, analytical columns are chosen based on the type of mixture being separated and the type of interaction with the stationary phase. To analyse polar mixtures, columns composed of polar stationary phase are used (normal phase chromatography), while non-polar mixtures require a non-polar stationary phase (reverse phase chromatography) [20]. The characteristics of the two types of chromatographic analyses are described in **Table 1. 2**.

Table 1. 2 Strategies employed in chromatography during separation of analytes.

	Normal phase	Reverse phase
--	--------------	---------------

Mixture	Polar	Non-polar
Stationary phase	Polar (Silica, polymer, etc.)	Non-polar (hydrocarbons: C8, C18)
Mobile phase	Non-polar or less polar	Polar
	(Non-aqueous solvents, chloroform)	(water, methanol, acetonitrile)
Application	Separation of polar compounds	Separation of non-polar compounds
Principle	Analytes are eluted by increasing the polarity of the mobile phase	Analytes are eluted by decreasing the polarity of the mobile phase

At present most validated methods have been developed based on reverse phase chromatography because, in contrast to the normal phase approach it allows the analysis of a wider range of compounds and provides more reproducible retention times for most organic molecules. Thus, efforts have been attempted to adapt reverse phase chromatography to more polar (hydrophilic) and uncharged compounds. For example, hydrophilic interaction chromatography (HILIC) is a variant of both normal and reverse phase chromatography [21]. The mechanism of separation associated with HILIC is based on the differential distribution of the analyte between the organic mobile phase (typically acetonitrile) and the water layer that is adsorbed onto the polar stationary phase **Figure 1. 3**.

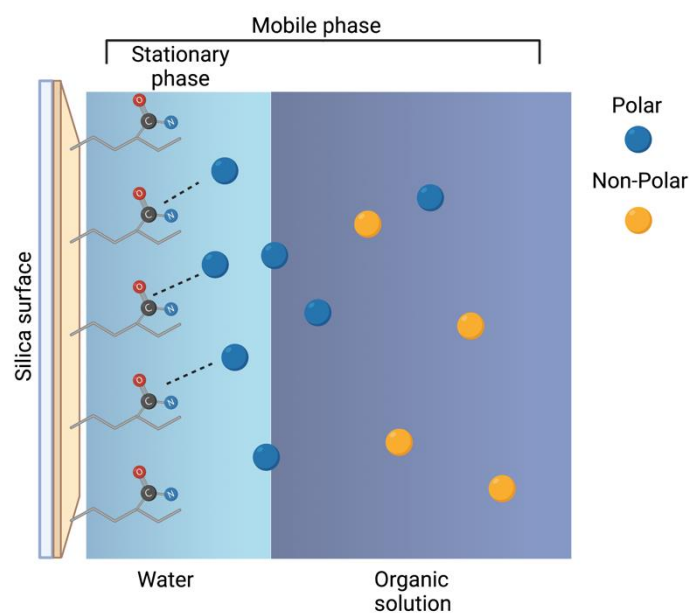


Figure 1. 3 Graphical representation of HILIC column composition and the general principle of separation. The column is composed of a solid polar stationary phase (e.g., silica). The mobile phase is generally ACN with a low percentage of water. During separation the analyte is partitioned between the mobile phase and a water enriched layer that forms on the hydrophilic stationary phase. The more hydrophilic the analyte is, the more its partitioned equilibrium is shifted towards the water layer in the stationary phase, resulting in more retention of the analyte. This principle of separation is only based on circumstantial evidence and is still debated.

During HILIC separation, different surfaces can be used as stationary phases whose properties make them suitable for the separation of specific compounds [22]. **Table 1. 3** Description of different HILIC column stationary phases, their base particles, functional groups and application for separation of specific compounds summarises some of the most common HILIC surfaces.

Table 1. 3 Description of different HILIC column stationary phases, their base particles, functional groups and application for separation of specific compounds

Column	Base particle	Functional group	Application
ZIC-HILIC	Silica	Sulfobetaine	Small polar compounds, metabolomes, glucosinolates, aminoglycosides, peptides, glycopeptides, purine and pyrimidine bases and nucleosides
ZIC-cHILIC	Silica	Phosphorylcholine	Peptides, amino acids, carboxylic acids
ZIC-pHILIC	Polymer	Sulfobetaine	Proteins, glycopeptides
Amine	Silica	Aminopropyl	Sugars, amino acids, peptides, carboxylic acids, nucleosides
Hybrid	Silica-polymer	Ethylene bridges	Metabolomes
Diol	Silica	2,3-dihydroxypropyl	Proteins
Amide	Silica	Amide or carbamoyl	Oligosaccharides, glycoproteins, glycosides
Cyclodextrin	Silica	Cyclic oligosaccharides	sugar alcohols, monosaccharides, oligosaccharides

When selecting a column for liquid chromatography, it is important to evaluate its efficiency in the separation of sample components. This can be achieved through the Van Deemter equation [23, 24] that represents the relationship between peak height and linear velocity **Figure 1. 4**.

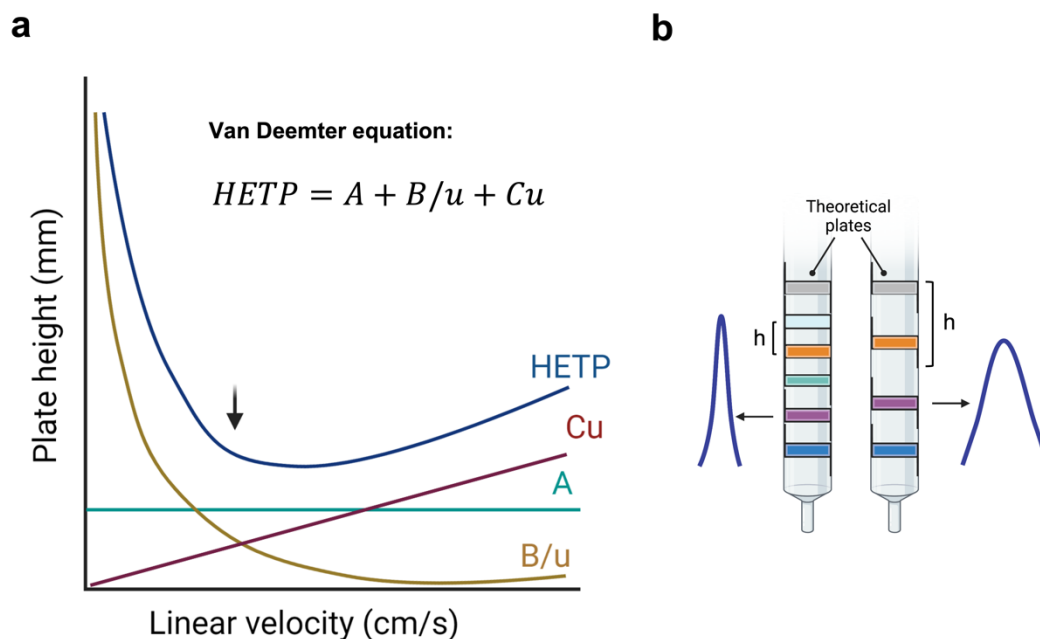


Figure 1. 4 Van Deemter equation and Theoretical plates. a) Plot of the Van Deemter equation describing the efficiency of the column in terms of plate height (equivalent to theoretical plate) in relation with linear velocity. A term indicates the particle size; B/u term is the axial diffusion, while the Cu is the molecular diffusion of the analyte between the mobile and stationary phase. At the lowest HETP (arrow) corresponds to the optimum plate count. HETP: Height Equivalent of a Theoretical Plate. A: Eddy diffusion factor. u: Speed. B/u: Longitudinal molecular diffusion term. Cu: Mass transfer term. b) Summary of the rationale behind the Van Deemter equation describing that the highest separation efficiency of a column is reached at the minimum plate heights (h).

To explain the rationale behind the Van Deemter equation, one should imagine a column as divided into several sections known as theoretical plates. When a sample component is introduced into the column, it spends a finite time in each plate necessary to accomplish every adsorption-desorption step. This migration of a component from one plate to another across the column length is influenced by different parameters including the physicochemical properties of the stationary phase, the flow rate of the mobile phase, and the nature of the analyte.

Columns are composed of particles of different sizes such that with larger particles, the path length of the sample component through the column will be longer. These properties influence the so-called Eddy diffusion based on the concept that big sample component will spend more time in the theoretical

plate and the resulting peak will be broader. Conversely, smaller particles will spend less time in the theoretical plate resulting in sharper/narrower peaks. To understand how flow rate affects the migration of a component, it is necessary to introduce the concept of molecular diffusion. It describes the migration of a molecule from a place of high concentration to a place of lower concentration. At the beginning of a chromatography run, all the particles contained within the sample are packed together (high concentration) and will separate throughout the elution process (low concentration) leading to peak broadening. Therefore, it is important to reduce the elution time to reduce molecular diffusion and sharpen the resulting peak. This can be achieved by increasing the flow rate of the mobile phase, which is then critical to increasing the separation efficiency of the column. There is not a defined flow rate optimal for all conditions. Thus, it should be optimised considering that the flow rate cannot be increased in excess because there are particles that – due to their physicochemical properties – interact and strongly adsorb to the column stationary phase requiring more time to re-enter the mobile phase. This last case is examined through the mass transfer factor which refers to the particles “left behind” during the run, ultimately leading to a phenomenon called tailing where a peak is smeared in the chromatogram with some analyte components of the peak eluting first while others have a longer retention time on the stationary phase.

In summary, the Van Deemter equation states that to achieve the highest separation efficiency of a column, the plate heights should be minimised by reducing the column particle size and finding a balance between molecular diffusion and mass transfer factors [23, 24].

Following the chromatographic separation of the analyte components, sample species are introduced to the MS system and measured based on their mass-to-charge (m/z) ratio.

Of note, LC and MS systems are incompatible because the high pressurised liquid mobile phase present in the LC device cannot be directly injected into the MS analyser that operates under a vacuum. The presence of a source interface helps bypass this issue. Thus, it dries the mobile phase before

entering the vacuum environment of the mass analyser. Different types of source interfaces exist including fast atom bombardment (FAB), chemical ionization (CI), atmospheric-pressure chemical ionization (APCI), atmospheric-pressure photoionization (APPI), electrospray ionization (ESI), desorption electrospray ionization (DESI), and matrix-assisted laser desorption/ionization (MALDI). The sources used in this thesis are ESI and MALDI. The mechanism of ESI is described in **Figure 1. 5**, while MALDI is described in the section dedicated to *Mass spectrometry imaging (MSI)*.

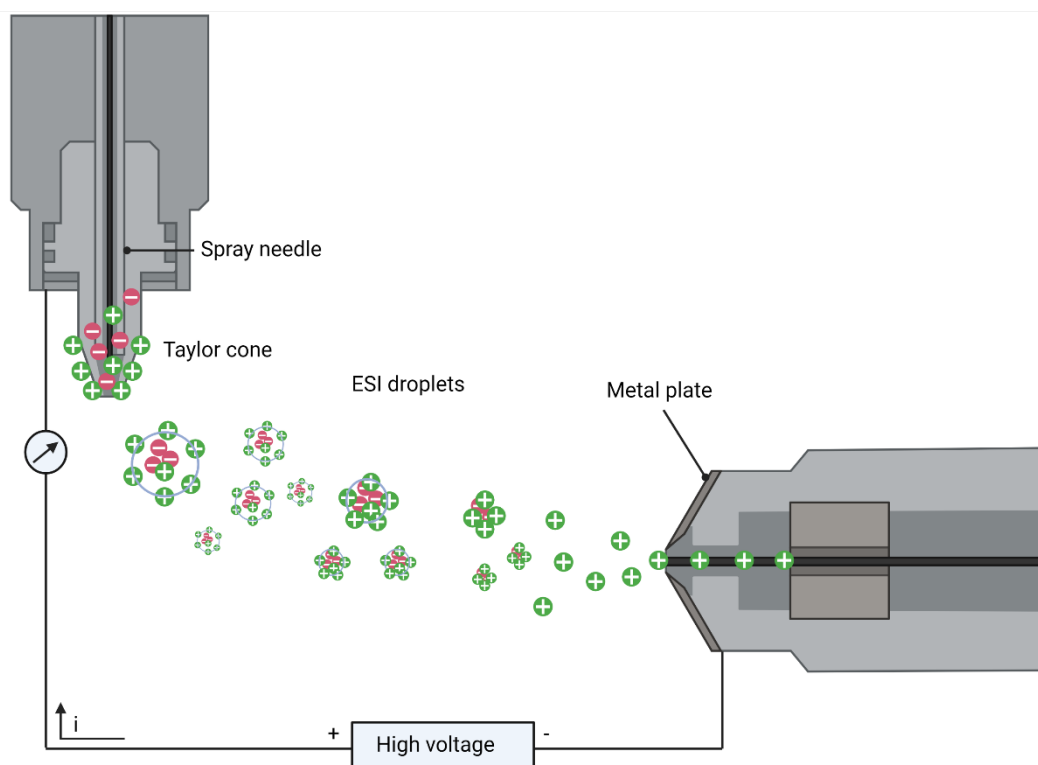


Figure 1. 5 The mechanism of electrospray ionization. Under high voltage, a current passes a wire filament to produce electrons for ionization. An electric field (i) is imposed into the liquid leading to an enrichment of positive ions at the meniscus of the spray needle. Consequently, a cone of positive ions (Taylor cone) is generated. The resulting droplets will have an excess of positive ions. During evaporation, the charges will get closer therefore increasing the Coulombic repulsion between charges of the same sign. This destabilises the droplets leading to the formation of free gas-phase ions. Created in Biorender.

The main advantage of the ESI source interface is its ability to produce multiple-charged ions therefore amplifying the mass range of molecules that can be detected in the analyser (kDa-mDa) [25, 26]. Of note, ionization

depends on the pKa of the functional groups contained within each molecule and the pH of the solvent that they are contained within [18]. In general, if the molecule's pKa is the same as the pH of the solvent it is dissolved in, then 50% of the molecule exists ionised and 50% exists non-ionised. This means that during a mass spectrometry analysis absolute ion currents do not linearly correlate with the absolute amount of the analyte. On this basis, absolute quantitative measurements of an ion of interest (or more ions) can be performed by monitoring the intensity of structurally similar compounds (standards) [27]. In practice, a calibration curve is designed from the relationship between the signal intensity observed for the standard compound and the amount introduced into the system. On the other hand, in an untargeted study – as the one presented in this thesis - relative peak areas are used to follow trends in metabolomics therefore providing a relative quantification of the detected metabolites.

Considering these premises, ionization is easy on functional groups with pKa that is $<$ or $>$ than the pH of the solvent (polar compounds), and it is difficult on functional groups with a pKa similar to the pH of the solvent (low polar or neutral compounds). Ionised functional groups are easier to protonate or deprotonate therefore creating positively or negatively charged ions, respectively.

The collection of multiple charged ions is helpful especially for high mass molecular species like proteins, where the phenomenon is referred as charge state distribution and is helpful for characterising intact proteins [28]. However, in metabolomics singly charged species are primarily observed, while neutral metabolites (those species that don't ionize) are virtually impossible to detect using LC-MS. Moreover, ESI provides very little fragmentation (soft-ionization) which is useful for preserving the structure of the molecular ion – an ion formed by removing or adding one or more electrons from a molecule (M) to form a positive (M⁺) or negative ion (M⁻), respectively. The mass of this ion is the sum of the masses of the various isotopes of the atoms that make up the molecule, with a correction for the masses of the electron(s) lost or gained.

After ionization, ions are accelerated into the vacuum chamber of the mass spectrometer and directed towards the mass analysers. Different types of mass analysers exist such as quadrupole (Q), Ion Trap (IT), Time of Flight (TOF), Orbitrap, and Ion cyclotron resonance (ICR). Each mass analyzer has a different resolution and mass accuracy, which are the parameters commonly used to represent the efficiency of a mass analyser [29]. Resolution refers to the ability of a system to resolve/separate two m/z peaks and is generally indicated as Full Width at Half Maximum (FWHM). FWHM describes the width of a peak measured at half of its maximum amplitude **Figure 1. 6a**, thus it indicates the ability to distinguish ion peaks with a similar m/z [30]. Mass accuracy represents the deviation of an experimental mass measurement to the true or exact mass of an ion [31]. Given the very small deviation offered by modern instrumentation, this is usually expressed as parts-per-million (ppm). Based on its general formula **Figure 1. 6b**, mass accuracy can be defined as the difference between the observed and calculated m/z value as a fraction of the calculated m/z .

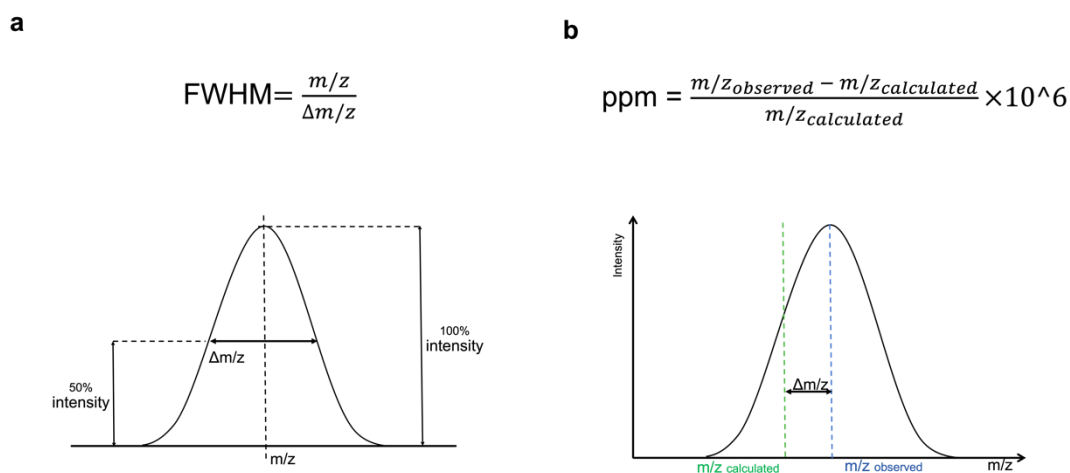
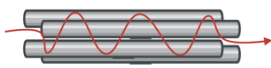
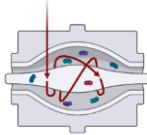


Figure 1. 6 Resolution and mass accuracy in mass spectrometry. A) To determine peak resolution, the m/z value of an ion is related to its $\Delta m/z$ (the difference between the first and second highest m/z value of that ion) at 50% intensity or width. B) Mass accuracy is the difference between the observed (experimental) and the calculated (exact) value of the mass, expressed in ppm.

Among the mass analysers of interest there are the quadrupole, and the orbitrap analysers whose characteristics are shown in **Table 1. 4**.

Table 1. 4 Typical Features of the mass analysers, quadrupole and orbitrap. Compared to the quadrupole, the orbitrap mass analyser is characterised by higher resolution and mass accuracy.

	Quadrupole	Orbitrap
		
Mass Range	10-2000 m/z	40-6000 m/z
Resolution	≤ 0.1 FWHM	$>500K$ FWHM
Scan speed	20 000 Da/s	22-40 Hz
Mass accuracy	<100 ppm	<1 ppm

A quadrupole consists of four cylindrical rods corresponding to electrodes positioned in parallel to each other and with opposite charges (two positives and two negatives) [32]. Its ability to scan ions of a certain m/z ratio depends on a direct current (DC) and radiofrequency (RF) potential that is applied to the quadrupole. When both potentials are combined, an electric field with rapidly varying phases is generated, which causes oscillation of ions as they pass through the quadrupole. Only ions with certain m/z values will have stable trajectories and pass through the mass analyser, while the ions with unstable trajectories will collide into the rods and be filtered out. The major advantages of quadrupoles are their low cost, fast duty cycle, and stability. Therefore, they are suitable for most laboratories and do not require continuous maintenance. However, they have a limited mass range and poor resolution, which makes it difficult to analyse ions with large and similar masses. In the Exploris 240, this limitation is bypassed by the presence of a second mass analyser, the orbitrap. The orbitrap mass analyser is characterised by an inner spindle electrode covered by two concave electrodes facing each other, which are separated by a thin ring of dielectric material [33]. Generally, mass spectrometers equipped

with an orbitrap mass analyser, use a curved linear trap (C-trap) for ion injection. Ions from the C-trap pass through a hole in one of the concave electrodes tangential to the inner spindle electrode. The electric field between the inner and outer electrodes creates a potential that allows the ions to continuously spin (back and forward) around the inner electrode. The outer electrodes detect the oscillation of the ions transforming their time domain into the frequency domain (Fourier transform). The frequencies of ions are proportional to the m/z of the ions.

More than one analyser can be incorporated into a MS/MS instrument. In a MS/MS technology, the first mass analyser (MS1) separates the ions based on their m/z ratio, then selected and dissociated into smaller fragments (**Figure 1. 7**). These fragments are further separated and detected in a second mass analyser (MS2), therefore allowing discrimination between ions with similar m/z ratios [34].

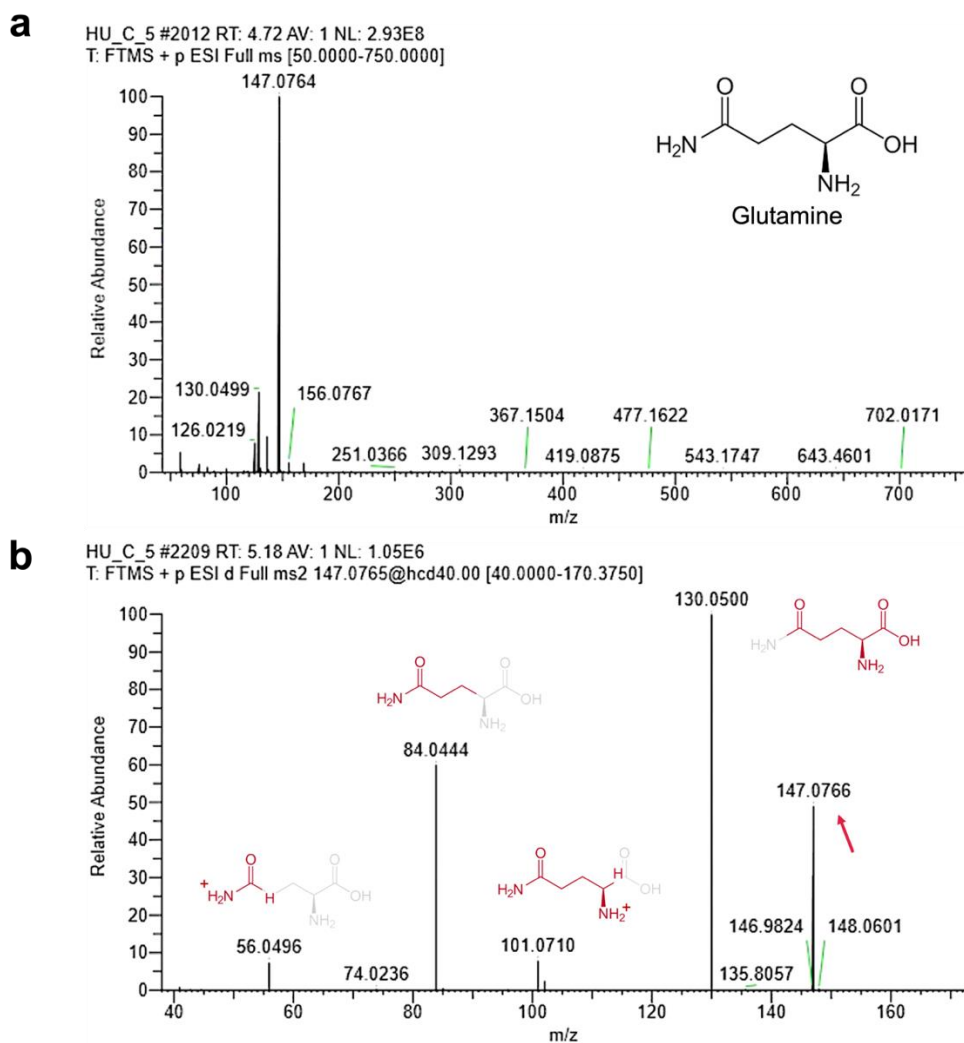


Figure 1. 7 MS1 and MS2 chromatogram. A) MS1 chromatogram with identified precursor ion of 147.0764 m/z ($z=1$) corresponding to glutamine ($m=146.14$ g/mol). B) MS2 chromatogram where the precursor ion (red arrow) has been fragmented into its smaller components are represented through the chemical structures.

In the Exploris 240, the MS1 is represented by a first stage analysis for ion precursor detection involving ion filtering through the Q and mass analysis in the orbitrap. The MS2 is a second stage analysis involving the ion routing multipole where ions are fragmented and redirected to the orbitrap mass analyser. Other tandem instruments include the QQQ and a combination of Q-TOF, IT-TOF, and FT-ICR-MS [35-37]. The advantage of combining multiple mass analysers is that they provide a high resolving power and a consequent high-quality data set because of the combination of high speed and high mass accuracy.

1.1.2.2. Mass spectrometry imaging (MSI)

MSI is one of the recent advanced technologies in mass spectrometry that combines the analytical potential of mass spectrometry with the microscopic and spatial histologic information of the analyte [38]. With this regard, MSI aims to localise and visualise selected metabolites and proteins within a biological sample. This is not possible with the canonical mass spectrometry tools where the extraction process involves the disintegration of samples.

The general principle for MSI on tissue samples is shown in **Figure 1. 8**, and can be generally divided into image acquisition, data analysis and data interpretation. During image acquisition, samples are first prepared by mounting frozen tissue sections on an indium tin oxide (ITO) slide and applying a matrix to the biological specimen. A pulsed laser is then applied which leads to the desorption and ionisation of the analyte into the gas-phase at each lasered spot [39]. A neodymium-doped yttrium aluminum garnet (Nd:YAG) laser or UV laser can be used which operate at different wavelength, 355 nm and 266 nm, respectively [40]. The resulting ionised molecules are transferred to the mass analyser where separation and fragmentation occur generating a mass spectrum for each spot. Through the process of rastering the laser across the area of a sample, an image can be generated. Data analysis and interpretation are subsequently performed through appropriate software.

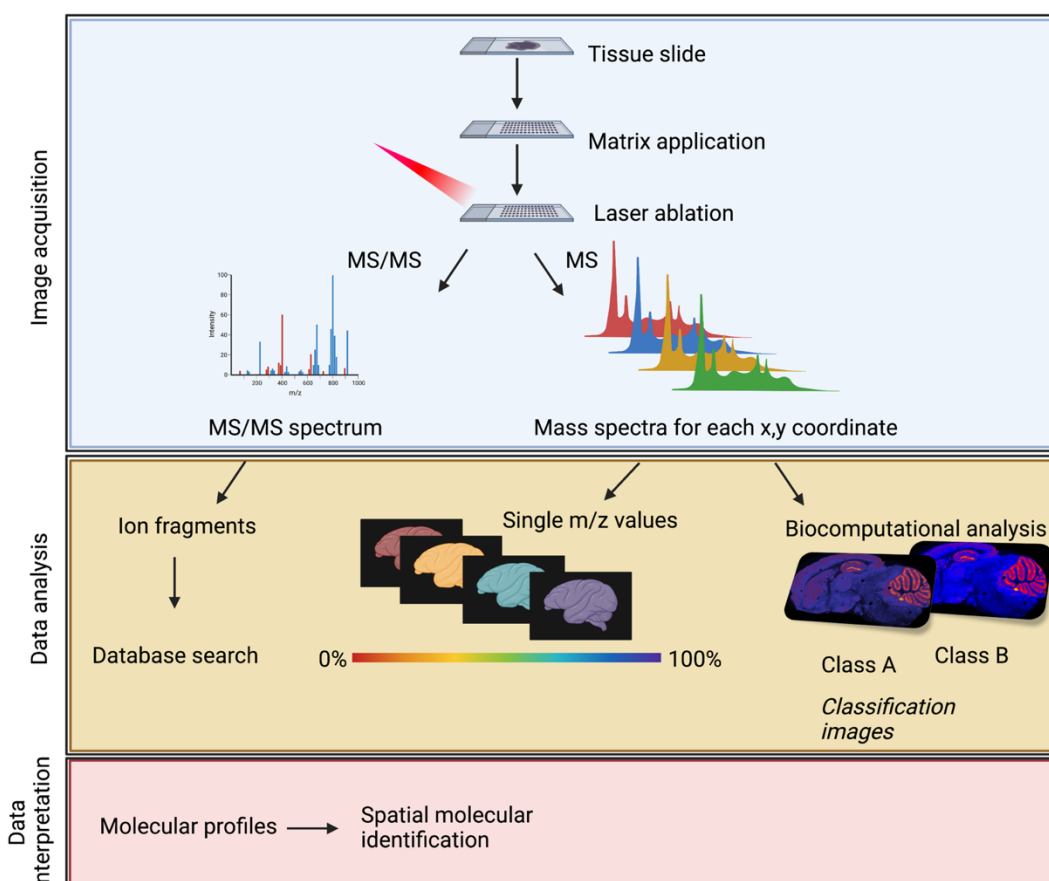
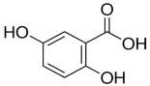
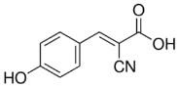
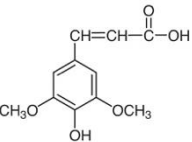
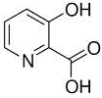
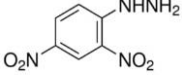
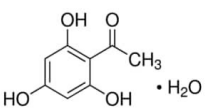
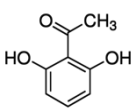
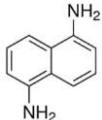


Figure 1. 8 Workflow of MALDI-MSI analysis. Image acquisition involves sample preparation by mounting the tissue section on a conductive slide and matrix application. A laser beam is employed to allow the desorption/ionization of the analyte. Ions are transferred in the MS system for mass analysis and generation of MS spectra. After MS analysis, immunohistochemical analysis is performed visualising the distribution of multiple molecules within the tissue. Data analysis includes classification of the images and database searching for the identification of molecules. Adapted from Norris, JL., et al., 2013 [41].

Analyte detection by MSI is strongly affected by the application of the matrix, which is selected based on absorption characteristics at the wavelength of the irradiation laser, the class of analyte and spatial resolution required (**Table 1. 5**) [42, 43]. The matrix is generally applied with an organic solvent at a concentration of 50-70%, which can be methanol, ethanol or acetonitrile. Adjusting the amount of solvent as well as the pH of the solution is fundamental to promoting the mixing of the matrix/analyte and recrystallization of the matrix.

Table 1. 5 MALDI matrices used for the analysis of specific classes of analytes. Adapted from Norris, JL., et al., 2013 [41].

MATRIX	CLASS OF ANALYTE	CHEMICAL STRUCTURE
2,5-Dihydroxybenzoic acid (DHB)	Peptides, lipids, drugs	proteins, 
α-cyano-4-hydroxycinnamic acid (CHCA)	Peptides, lipids, drugs	proteins, 
3,5-Dimethoxy-4-hydroxycinnamic acid (SA)	Proteins	
3-hydroxypicolinic acid (3-HPA)	Peptides, oligonucleotides	
2,4-dinitrophenylhydrazine (2,4-DNPH)	Peptides	
2,4,6-trihydroxyacetophenone (THAP)	Lipids, oligonucleotides, drugs	
2,6-dihydroxyacetophenone (DHA)	Lipids	
1,5-Diaminonaphthalene (DAN)	Lipids	

Similar to LC-MS, the choice of mass spectrometer for MALDI-MSI is mainly based on resolution, mass accuracy and scan speed. Among the most common mass analysers used in MALDI-MSI is MALDI-TOF [38], generally applied in tandem with a second mass analyser. High-resolution mass spectrometers include MALDI-FT-ICR [44] and MALDI-FT-Orbitrap [45]. In this thesis, the (MALDI)-Synapt-G2Si instrument, a tandem MALDI-Q-TOF system

(**Figure 1. 9**) was employed which is a good compromise between resolution (10K-60K FWHM), mass accuracy (1 ppm), and cost.

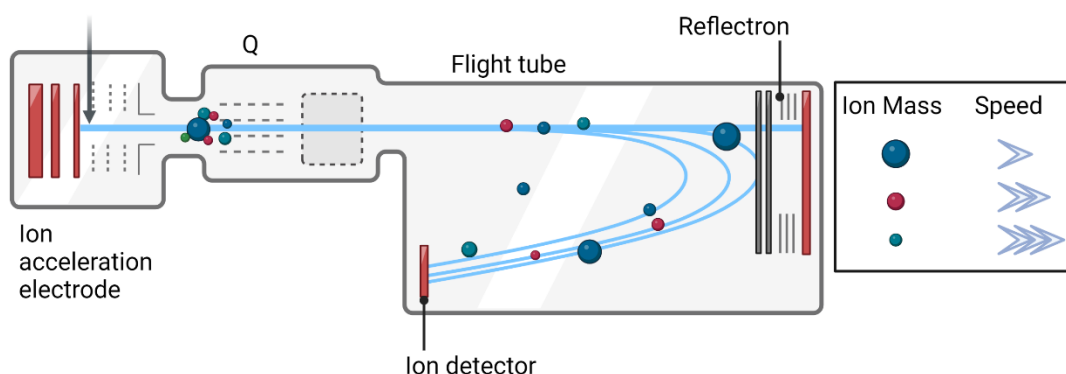


Figure 1. 9 QTOF-MS. Ions from the ion source are first focused into a beam and transmitted into the quadrupole (Q). Then they are accelerated by a high-voltage field – via a pusher pulse. The kinetic energy associated with each ion is converted into unidirectional velocity or time-of-flight. The mass of each ion is then assigned based on its “flight time”. Created in Biorender.

MALDI-MSI systems are generally accompanied by software designed for the acquisition, visualization and analysis of imaging data [46, 47]. Through these software, m/z intensities are visualised as colour signals therefore providing information on the spatial distribution of the molecule of interest within samples. The advantage of this method – in comparison to traditional immunohistochemistry – is that the spatial location of a huge range of molecules can be examined at the same time in one single measurement.

1.1.3. Study design for metabolomics and proteomics

Untargeted and targeted mass spectrometry-based metabolomics and proteomics are the main methods employed for the identification and study of the metabolome and proteome of biological systems, respectively (**Table 1. 6**).

Table 1. 6 Key features of untargeted and targeted approaches in metabolomics and proteomics

	Untargeted	Targeted
Features	Biomarker discovery, hypothesis generating, global metabolomics/proteomics profiling, qualitative analysis,	Validation, Hypothesis driven, Absolute quantification, Chemical standard required

	relative quantification, >1000s metabolites measured	
Sample preparation	Global metabolites/proteins extraction, derivatization (optional)	Extraction procedure for specific metabolites/proteins
Data acquisition	Chromatographic separation, MS ionization (negative and positive), mass detection	Chromatographic separation, MS ionization (negative and positive), Mass detection
Data processing	Noise filtering, retention time correction, peak detection, chromatogram alignment, unknown features identification, data preparation: data integrity checking, normalization, compound name identification, statistical analysis	Data processing, Statistical analysis, Absolute quantification of metabolite/protein concentration
Data interpretation	Bioinformatics, integrative OMICS, enrichment analysis, pathway analysis, metabolic network	Bioinformatics, Integrative OMICS, Enrichment analysis, Pathway analysis, Metabolic network

1.1.3.1. Untargeted and targeted proteomics and metabolomics

Untargeted metabolomics and proteomics aim to comprehensively investigate the near-complete set of metabolites or proteins present in a biological sample without *a priori* knowledge of its content [48]. The main advantage of this method is its unbiased strategy to identify metabolites/proteins (known and unknown) from different biomolecular pathways. However, the identification process is one of its main limitations because there are no existing instruments and methods capable of identifying and quantifying all the metabolites and proteins present in a biological sample [48]. In MS/MS analysis there are currently two mass spectrometry based approaches employed to identify features in a sample, and they are known as data-dependent acquisition (DDA)

and data-independent acquisition (DIA) [49]. DDA selects the ions with the highest signal intensity (generally the top-5 precursors) in the first MS stage. The selected ions are further fragmented in the second MS stage, and the resulting data are used to search an existing database (online or in-house). On the other hand, in DIA there is no prior selection of ions, instead they are selected and fragmented in the second MS stage. The resulting data are much larger than DDA, thus more difficult to process and interpret.

Relative quantification of metabolites/proteins is available for untargeted metabolomics/proteomics which may limit precision and accuracy. Hence, the implementation of quality control (QC) measures in the analytical workflow is essential to increase the quality of data and reliability of this technology [50]. A complex data set is generated from untargeted metabolomics that requires downstream computational tools for data post-processing and analysis.

In proteomics the untargeted approach is also referred to as “Bottom-up” or “Shotgun” proteomics where a mixture of peptides is digested in solution and the resulting fragments are analysed by mass spectrometry [51].

Targeted metabolomics and proteomics aim to investigate the selected metabolites/proteins based on *a priori* information [52]. Methods and analysis are optimised for the detection of specific metabolites/proteins of interest that have been chemically characterised and biochemically annotated. For this reason, DDA is more generally applied to targeted analyses than DIA, making it more selective and sensitive than the untargeted method. Targeted analysis is hypothesis-driven – compared to untargeted analysis which is hypothesis generating – and generally follows untargeted analysis to validate its results. Accurate absolute quantification of specific features can be obtained using internal and chemical standards to generate a standard curve for a concentration range of the metabolite or protein of interest.

In proteomics the targeted approach is referred to as “Top-Down” proteomics, where intact proteins of interest are readily fragmented in the MS providing a complete description of their primary structure and modifications [53].

DDA has been also utilised to acquire MS/MS data in untargeted metabolomics/proteomics to enhance the confidence of compounds

identification [54]. Specifically, a list of target precursor ions can be generated and used as inclusion (or exclusion) list for subsequent DDA analysis, therefore increasing selectivity and experimental efficiency. If using different injection volumes of the selected precursor ions, then a calibration curve can be generated and embedded onto the untargeted data [55].

1.1.3.2. Sample preparation for LC-MS and MALDI-MSI analysis

Sample preparation is a crucial and challenging step to generate high-quality data [56]. For both proteomics and metabolomics sample preparation is time critical, thus a quick handling procedure must be adopted to avoid altering the chemistry of the analytical sample. For both metabolomics and proteomics, sample preparation varies depending on the strategy employed including untargeted and targeted, the instrumentation (LC-MS or MALDI-MSI), and the sample type (urine, blood, faeces, tissues or cells) [57]. In this thesis, we optimize cell and tissue sample preparation for downstream metabolomics and proteomics analysis as described below. In both cases, prior to metabolite/protein collection, the number of cells and tissues amount need to be optimised to obtain enough signal in MS to be able to detect low abundance small metabolites. Depending on the purpose of the study, the composition of cell culture media is also important to consider. Cell culture media used during experiment incubations can be aspirated from cells and stored at -80 °C following cellular debris removal for future analyses.

1.1.3.3. Sample preparation in metabolomics

As previously stated, timings for sample preparation is a limiting factor in metabolomics analysis, because metabolic processes are rapidly-occurring (< 1 s), thus rapid inhibition of enzymatic processes is required by freeze quenching metabolism before extraction [58]. For LC-MS analysis, this procedure is performed through liquid nitrogen or ice-cold extraction solvents followed by cell scraping (or tissue homogenization) and metabolite extraction (**Figure 1. 10**).

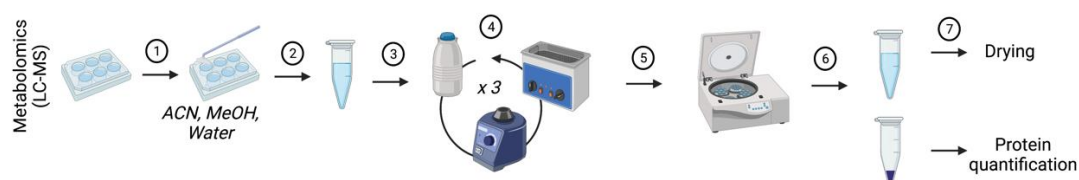


Figure 1. 10 Sample preparation workflow for metabolomics. 1) washing and solvent extraction, 2) scraping and transfer into an Eppendorf tube, 3) quenching in liquid nitrogen, 4) three cycles of liquid nitrogen, vortex and sonication, 5) centrifugation, 6) separation of supernatant and pelleting, 7) drying of the supernatant and reconstitution. The pellet is retained for protein quantification. Created in Biorender.

The solvents used for metabolite extraction vary depending on the class of metabolites of interest (polar e.g., nucleotides, some amino acids and peptides versus non-polar e.g., lipids, certain amino acids and peptides) (**Table 1. 7**).

Table 1. 7 Extraction solvents commonly used for the extraction of metabolites.

Extraction solvent (ratio)	Metabolic classes	Reference
CH ₃ OH (100%, v/v)	Sugars, sugar alcohols, organic acids, fatty acids, few amino acids	[59]
CH ₃ OH:H ₂ O (80:20, v/v)	Nucleotides, few amino acids, sugar alcohols, carboxylic acids	[60]
CH ₃ OH:CHCl ₃ (50:50, v/v)	Nucleotides, amino acids, phospholipids	[61, 62]
CH ₃ OH:CH ₃ CN:H ₂ O (50:30:20, v/v)	Amino acids, fatty acids, nucleotides, sugars	[63-65]
CH ₃ CN:H ₂ O (70:30, v/v)	Amines, amino acids	[66]
CH ₃ OH:CHCl ₃ (50:50, v/v) + CHCl ₃ : CH ₃ OH: H ₂ O (57:23:20, v/v)	Lipids	Folch extraction [67, 68]
CHCl ₃ : CH ₃ OH: H ₂ O (26:53:21, v/v) + CHCl ₃ : CH ₃ OH: H ₂ O (34:34:32, v/v)	Lipids	Bligh and Dyer [69]

In this study, for metabolomics extraction we employed the use of methanol, acetonitrile and water (50:30:20, v/v), as it has been documented to increase the efficiency of extracting a large range of metabolites [63-65]. Following quenching and extraction, samples are centrifuged, and the supernatant is lyophilized to preserve the quality of metabolites and increase their shelf-life for subsequent analyses. Metabolite samples are reconstituted in solvents

suitable for LC-MS analysis that include acetonitrile, methanol or water, or combinations at different ratios, depending on the column and mobile phase selection.

In MALDI-MSI, cryo-sectioning is used to prepare tissue sections and quench their metabolism. The thickness of the specimen is 5-20 μm [70], and tissue slices are mounted onto a conductive surface slide that can be a metal or a glass slide. A matrix is then applied manually (through a nebuliser or airbrush), or with automated strategies [41]. The strategy employed in this thesis for matrix application is the manual method of sublimation described in **Figure 1. 11**. In metabolomics and proteomics, the matrix is homogeneously applied to the entire surface of the specimen. For targeted analysis, the matrix can be applied to the specimen regions of interest [44]. In order to maximise information on the spatial distribution of molecules within a tissue with MALDI-MSI, the same tissue section can be stained for histological inspection with hematoxylin for visualising the nuclei and eosin for the extracellular matrix and cytoplasm [71].

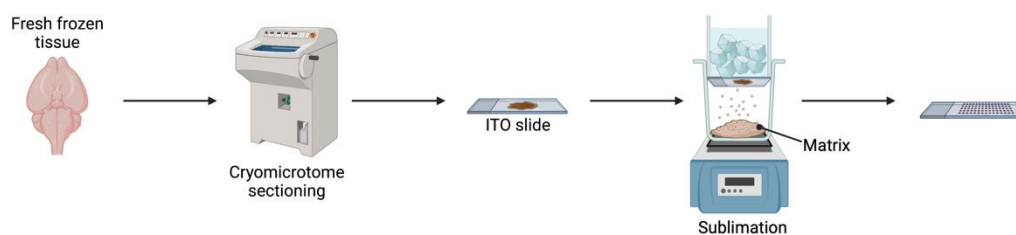


Figure 1. 11 Sample preparation for MALDI-MSI analysis. Frozen tissues are cryo-sectioned and tissue slides deposited onto an indium-tin oxide (ITO) coated metal slide. Next, a matrix is applied through sublimation gradually progressing upon heat application from the bottom and condensation onto the tissue. After equilibration at room temperature, the MALDI slide is ready for MS analysis. Created in Biorender.

1.1.3.4. Sample preparation for proteomics

In contrast to metabolomics, sample preparation for untargeted proteomics (Bottom-Up) requires multiple sample-preparation steps prior to mass analysis [72] (**Figure 1. 12**). During sample preparation, proteins need to be extracted, denatured, digested and cleaned from readily ionizable lipids, detergent and

salts which may compete for charge with proteins and ultimately affect their detection [73].

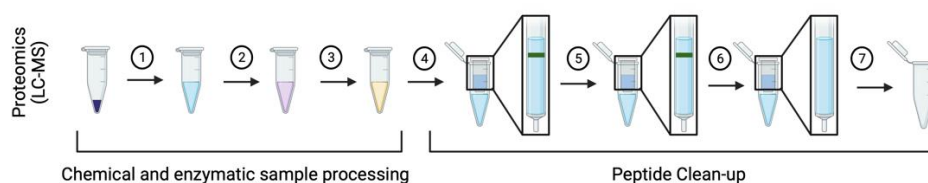


Figure 1. 12 Sample preparation workflow for proteomics. 1) lysis, 2) reduction/alkylation, 3) digestion, 4) washing hydrophilic contaminants, 5) washing hydrophobic contaminants, 6) clean-up of the peptide solution, 7) drying and reconstitution. Created in Biorender.

Cell lysis is generally the first step, which can be accomplished mechanically or using pre-formulated lysis buffers. These last are generally preferred as they are more reproducible and time effective. These lysis buffer usually contain protease and phosphatase inhibitors to prevent protein degradation. Next, proteins are reduced into peptides. Thus, they are denatured through reduction of disulfide bridges, and alkylated to modify cysteine SH-groups, therefore preventing free cysteines to form novel disulfide bonds and loss of cysteine containing peptides [74]. Different reagents can be used for protein denaturation/alkylation. For in solution denaturation, dithiothreitol (DTT) and acrylamide (AA) give the best yield of protein denaturation [75]. In shotgun proteomics, proteins are digested into peptides by a protease enzyme (e.g., trypsin). Trypsin is one of the most used digest proteins for MS-based proteomics as it generates a positively charged C-terminus by cleaving the protein arginine and lysine residues [76]. Following digestion, peptides have been isolated but salts and buffers removal, and peptide concentration steps are required for sample preparation. An efficient strategy for peptide clean-up is using spin columns [77]. Briefly, the peptides bind to the column, while salts and buffer are washed off. In the last step, peptides are eluted with a high organic mobile phase, and concentration is achieved by drying the eluted peptides.

Such purified peptides can then be separated and analysed using LC-MS, or spatially detected on tissues through MALDI-MSI. Top-Down proteomics does not require protein digestion as intact proteins are required for structural composition analysis [78].

In untargeted and targeted LC-MS based metabolomics, QC samples need to be applied prior to sample analysis and data processing to demonstrate analytical accuracy, precision and data repeatability [50]. For cellular and tissue samples, pooled QC samples can be prepared by combining equal aliquots of the extracted samples before the drying process or after the reconstitution of dried extracts [50]. Of notice, the pooled QC samples and the biological samples must be identically processed. Moreover, it is important to consider how many times each QC sample is analysed and at which position in the run they are placed. An example of sample ordering for LC-MS analysis is shown in **Figure 1. 13**. Generally, it is recommended i) to analyse a pooled QC no more than every 10 samples, ii) that at least five QCs are evenly distributed across the batch, iii) to have at least two QCs at the beginning and the end of the batch [50].

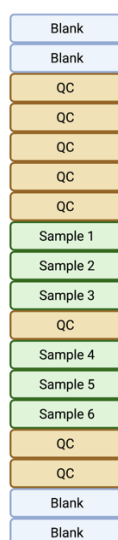


Figure 1. 13 An example sequence order for a LC-MS analysis run.

1.1.3.5. Data processing and analysis in metabolomics and proteomics

Following MS analysis, the output data for each sample is an ion chromatogram containing thousands of features that require reliable identification and quantification. Therefore, a common metabolomics data processing workflow includes baseline correction, noise reduction, alignment, integration, and peak normalization steps (**Figure 1. 14**) [79].

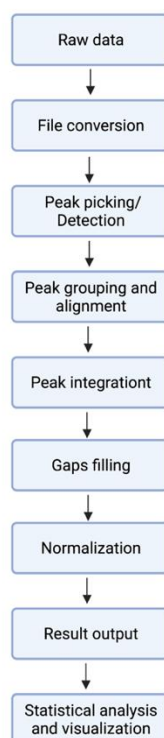


Figure 1. 14 An example of a MS metabolomics workflow analysis.

Several open-source software packages are available for the analysis of LC-MS metabolomics data [80-84], which follow a general stepwise processing workflow starting with the conversion of raw files from the proprietary vendor formats into open file formats (i.e., mzXML, mzData).

Subsequent data analysis and post-processing steps are summarized as follows:

Peak picking identifies legible m/z peaks within a mass spectrum. Thus, baseline correction and noise reduction of data are performed to filter out background ions and solvent impurities. A further challenge in LC-MS is the elution of two or more analytes with similar retention times resulting in overlapping chromatographic peaks. **Deconvolution** is necessary to separate these ions based on different features (e.g. peak shape) [85]. At this stage, for each sample there is a data file with independent lists of ions. To determine among individual ions, which are the same across different samples, **peak grouping** and **alignment** are performed. This aligns ions extracted with close retention times and close m/z values in the different classes of samples [86]. Therefore, it is important to establish *a priori* what kind of classes are present

in the sample. This grouping step is important because the data matrix that is generated is used for statistical analyses.

Gap filling can be performed on the aligned features to cope with missing features that are absent in the given sample, or that might be an artifact of the features-detection process [87]. The fill gaps algorithm used in this work can search for the missing ion with the expected m/z and retention time parameters against all detected ions while ignoring the assigned adduct type (filling by matching ion); or it can detect the peak at a lower intensity threshold then using the integrated peak area to fill the gap (Re-detected peak); or it can fit a Gaussian peak for the expected m/z range (filled by simulated peak).

The detected peaks are integrated to enable the comparison of relative metabolite or peptide abundances and enable the identification of differences between sample groups. Generally, **peak integration** is performed by peak area or peak height. **Normalization** is used to reduce the systematic errors arising from technical or analytical variations (sample type or size, column composition and instrumentation), therefore improving the performance of downstream statistical analysis [88]. Normalization applies prior and/or post data acquisition. In this thesis, both pre- and post-acquisition normalization have been used. Pre-acquisition normalization allows to equalize the total sample concentration for all samples. As a result, similar instrumental responses can be obtained from all samples and more accurate quantitative analysis of changes in metabolites concentrations can be evaluated. Strategies to perform pre-acquisition normalization of cell extracts include cell count, measurement of total protein content, and dry weight [89].

Post-acquisition normalization is applied during data processing, and it can be performed through the utilization of QC samples or internal/external standard (known) metabolites. In this work QC samples have been used to create a regression curve of area versus acquisition time for each detected compound to compensate for time-dependent batch effect. Alternatively, the intensity drift of specific metabolites in the QC samples can be used to build a regression model and correct the peak intensities of the same metabolite in the sample of interest [90].

Another post-acquisition normalization strategy is the addition of internal or external standards (known metabolites) prior or after extraction, respectively [91]. Through this method normalization can be obtained by subtracting the average abundance of internal/external standards from the abundance of the metabolites in each sample. After normalization, and before statistical analysis, data should be centered and scaled. Centering means that the averages of concentrations are subtracted from the data to centre it on 0, thus only the relevant variations between the samples are considered. Not scaled data focus on metabolite features with high intensities which are likely to show higher variance than variables with low intensities. However, relevant metabolites are not necessarily the most abundant, thus scaling can be advantageous as it gives equal weights to the variables. Scaling can be performed by dividing each variable by a factor which can be the standard deviation, the square root of the standard deviation (Pareto scaling), or the average concentration of metabolites.

From data post-processing, the output result is a large data matrix containing information on thousands of m/z features (variables) that can be correlated or anti-correlated against each other. For this reason, ***multivariate statistical analyses*** are applied to metabolomics and proteomics data to analyse multiple variables simultaneously. Multivariate techniques can be divided into *unsupervised* and *supervised* approaches. Unsupervised multivariate analysis does not require prior knowledge of the features representing each sample group, providing a robust tool to identify group clustering in datasets. Principal component analysis (PCA) is among the common unsupervised approaches used in metabolomics, but principal coordinate analysis (PCoA) can also be used for proteomics. PCA and PCoA are similar in representing similarities and differences between sample groups, but PCoA geometrically visualises the distance between two groups through a vector line [92]. In this thesis we focus on PCA analysis as it is extensively used in the metabolomics and proteomics analyses.

PCA is a useful tool that allows data dimensionality reduction by approximating the complex data matrix to a few orthogonal principal components (PCs) [93]. These components are a combination of the original variables and the weights

of their contributions to explain the maximum amount of variance possible (**Figure 1. 15a**). PCA serves to better visualise large datasets and detect similarities/differences in the features characterising different sample groups. Upon conversion of data according to PCs, the results can be represented by score and loading plots. The score plot represents the coordinates of the samples in the PCA model (**Figure 1. 15b**), where variables distant from the origin are relevant to the model, while variables proximal to the origin have little effect on the model. Moreover, PCA score plots can be useful for investigating the presence of either analytical or technical variation. In this regard, QCs are extremely helpful as clustering of the last QC injection with periodical QC injections during the run ensures that the system has achieved stability. The loading plot shows the contribution of the original variables to generate the scores (**Figure 1. 15c**). Thus, following the vectors from the origin ($PC1=0$, $PC2=0$), their Cartesian coordinates reveal how much weight they have on the PC1 or PC2 component. The angles between the vectors represent the correlation between features. The combination of the score and loading plot can be useful to understand how strongly each vector (feature) influences the separation (**Figure 1. 15d**).

As aforementioned, PCA separates sample groups based on their principal components, but does not give information about the specific contribution of features to separation. The supervised multivariate analysis can be used to obtain this type of information because knowledge of the features within a dataset, allows models to be developed to predict latent variables (i.e., information that is not included in the initial data matrix). The most commonly used supervised tool is the Partial Least Square (PLS- **Figure 1. 15e**) [94]. PLS is based on one latent variable (F) that influences the known variables (Y). The weight of this contribution (b) is different for each known variable Y that, in the original data matrix, corresponds to the identified metabolite/protein. In a complex dataset there are multiple latent variables affecting metabolites/proteins, and a new algorithm suitable for their multiple measurement is the PLS-discriminant analysis (PLS-DA). Thus, PLS-DA – within each PC – measures the correlation of the different metabolites/proteins

as a function of their covariation (**Figure 1. 15f**), which is derived from their differential response to multiple latent variables.

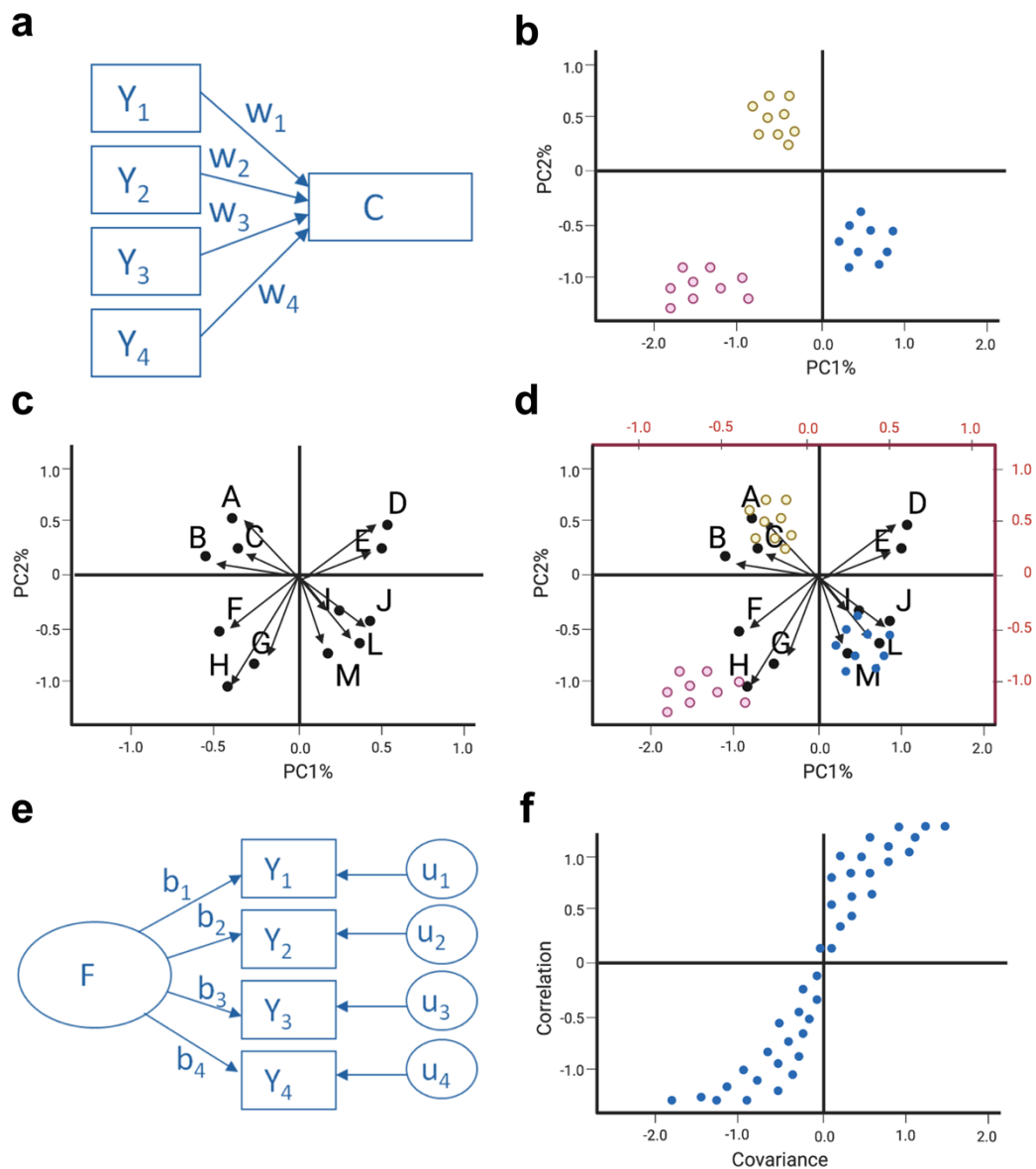


Figure 1. 15 Graphical representation of Principal Component Analysis (PCA) and Partial Least Square (PLS) analysis. a) PCA theoretical model, b) PCA score plot, c) PCA loading plot, d) combination of PCA score and loading plot, e) PLS analysis, and f) plot of PLS– Discriminant Analysis (PLS-DA). Y= known variable. W=weight contribution of the known variable. C=component. F=latent variable. b=weight contribution of the latent variable. u=error terms. The theoretical models of PCA and PLS analysis are adapted from <https://www.theanalysisfactor.com>. Created in Biorender.

1.1.4. Metabolomics and proteomics in ageing and cancer research

Ageing is a progressive dysfunctional process generated from the gradual accumulation of cellular damage [95]. Some of this damage (e.g., somatic mutations on oncogene or tumour suppressor genes) confer a selective advantage to cells which may ultimately result in carcinogenesis [96]. On this basis, estimates present a burden in the incidence of cancer (> 50%) in people aged over 65 which is not only driven by the passage of time, but also defined biomolecular mechanisms [97]. Emerging evidences shows that the accumulation of senescent cells – the gold standard model of cellular ageing [98-100]– establishes a microenvironment that promotes tumorigenesis because of the dramatic increase in the recruitment of inflammatory cells and extracellular matrix deposition [101]. Age-associated chronic inflammation (or inflammageing) is at present a widely accepted risk factor for cancer development [102-104].

The senescent state is an adaptive mechanism that cells activate to prevent the proliferation of damaged cells and promote their recognition and removal by the immune system [105]. Some senescent cells may prevent cancer development through the activation of the immune surveillance [106-108]. The role of senescence in cancer has not yet been elucidated, thus these enigmas remain unsolved. Campisi, et al. (2014) have hypothesised that the pro- or anti-tumour activity of senescent cells may depend on when and where they develop and accumulate [109]. The senescent state [110] and cancer [111] are dynamic and heterogeneous processes harbouring different features that determine their aggressivity and resistance to therapies.

Assessing senescence and tumour heterogeneity is currently based on the detection of a specific biomarker that by definition is a “*biological molecule found in blood, other body fluids, or tissues that is a sign of [...] a condition or disease*” [112].

Metabolites and proteins can be used as biomarkers in living organisms, such that they can be helpful targets in developing new diagnostics and guiding the drug discovery and development process.

Prior to the growth of proteomics and metabolomics, genomics has been extensively applied to biomarker discovery and the drug developmental process [113, 114]. Proteomics has since expanded the knowledge on protein function, modification, regulation, and interaction [115]. Metabolomics has gained attention in biomarker discovery in recent years as it has revealed significant biochemical changes influencing the state and activity of genes and proteins. Additionally, thanks to the increased sensitivity of the modern technologies (e.g., MS), untargeted metabolomics has enabled a more comprehensive understanding of the metabolic composition of living organisms [116, 117]. Hence, a wider number of small molecules has been revealed which are not catalogued in databases.

Despite the great efforts of these “omics” tools in the field of biomarker discovery, the number of markers approved by the Food and Drug Administration (FDA) in current clinical use remains limited in scope (**Table 1. 8**), and metabolic targets are scarcely represented [118]. This can be attributed to several factors such as the small number of metabolic samples analysed to-date, the lack of information on the background of the sample, lack of age and gender-match between cases and controls, the low number of metabolites included within metabolite databases [119], and importantly the absence of clear harmonized and standardised operating procedures in metabolomics for sample collection, storage, handling, analysis, and data interpretation [117].

Table 1. 8 List of FDA approved biomarkers for clinical use. In bold are indicated the metabolic targets [120].

Therapeutic Area	Biomarker
Gastroenterology	ABCB11, CPOX, HMBS, PPOX, CYB5R, CYP2C19, CYP2D6, G6PD , IL12A, IL12B, IL23A, JAG1
Inborn Errors of Metabolism	ACADVL, CPT2, HADHA, HADHB, AMACR, AKR1D1, CYP7A1, CYP27A1, DHCR7, HSD3B2, ASS1 , CPS1, OTC , CASR, CYP2D6, GAA, GALNS, GLA, LMNA, NAGS, TPP1, ZMPSTE24
Neurology	ACHR, ALDH5A1, APOE, AQP4, CYP2C19, CYP2D6, DMD, HLA-A, HLA-B, MOCS1, NAT2, POLG, SMN1, SMN2, TTR
Urology	AGXT, CYP2D6
Oncology	ALK, BCR-ABL1, BRAF, BRCA, CCDC6-RET, KIF5B-RET, RET, CD19, CD274 (PD-L1), CD33, Chromosome 11q, Chromosome 14q;16q, Chromosome 17p, Chromosome 4p;14q, CYB5R, CYP1A2, CYP2C19, CYP2D6, DPYD, EGFR, ERBB2 (HER2), ESR, PGR, F2,

	<i>FCGR2A (CD32A), FGFR, FGFR2, FIP1L1-PDGFR, FLT3, G6PD, HLA-A, HLA-B, HLA-DQA1, HLA-DRB1, IDH1, IDH2, IGH, IL2RA, KIT, KRAS, MET, MKI67, MS4A1, MYCN, MYD88, NECTIN4, NPM1, NTRK, NUDT15, PDGFRA, PDGFRB, PIK3CA, PML-RARA, PPP2R2A, RAS, RET, ROS1, SSTR, TNFRSF8 (CD30), TP53, TPMT, UGT2B17, UGT1A1, VHL</i>
Anesthesiology	<i>BCHE, CYP2C9, CYP2D6, G6PD, RYR1</i>
Pulmonary	<i>CFTR, CYP2C19, UGT1A1</i>
Hematology	<i>Chromosome 13, Chromosome 5q, Chromosome 7, CYP2C9, F2, G6PD, HBB, JAK2, PRF1, RAB27A, SH2D1A, STXBP2, STX11, UNC13D, XIAP, PROC, PROS1, SERPINC1, VKORC1</i>
Cardiology	<i>CYB5R, CYP2B6, CYP2C19, CYP2D6, CYP3A5, TTR</i>
Infectious Diseases	<i>CYB5R, CYP2B6, CYP2C19, CYP2D6, G6PD, HLA-B, IFNL3 (IL28B), UGT1A1</i>
Gynecology	<i>CYP2B6, CYP2C19, CYP2D6, PROC, PROS1, SERPINC1, SLC01B1</i>
Psychiatry	<i>CYP2C19, CYP2D6, SLC01B1</i>
Rheumatology	<i>CYP2C19, CYP2D6, G6PD, NLRP3, NUDT15, TPMT</i>
Endocrinology	<i>CYP2C9, G6PD, LDLR, LEP, LEPR, PCSK1, POMC, SLC01B1</i>
Dental	<i>CYP2D6</i>
Dermatology	<i>DPYD, G6PD, IL12A, IL12B, IL23A</i>
Toxicology	G6PD
Transplantation	<i>HPRT1</i>

Referring to **Table 1. 8**, not all the listed therapeutic areas refer to diseases with a genetic basis and most have a strong metabolic basis. Moreover, several biomarkers are genes and enzymes regulating key metabolic pathways. This suggests that abnormal metabolite levels lie beneath altered gene expression and function, signal transduction pathways, epigenetic modifications, and other hallmark alterations observed in chronic conditions. For example, genomic instability and metabolic reprogramming are among the most prominent hallmarks of many chronic age-related disabilities including neurologic diseases, diabetes, cardiovascular diseases and cancer [121, 122]. The mutual dependencies of these two hallmarks are described in subsequent sections.

1.1.5. Genomic instability

Genomic instability represents the accumulation of DNA damage and mutations. These abnormalities play a significant role in ageing and cancer as they are responsible for genomic alterations [123], aberrant protein synthesis and activity [124], increased levels of reactive oxygen species (ROS) [125] and altered cell cycle activity, which is blocked in ageing [126] and increased in cancer eventually leading to metastatic burden [127].

Genomic instability can be caused by endogenous and exogenous factors. Among endogenous factors there are DNA replication errors such as base substitutions, single base insertions, and deletions which are introduced at a frequency of 10^{-6} to 10^{-8} per cell cycle [128, 129]. Endogenous DNA damage is also a consequence of aberrant functions of topoisomerase enzymes – nuclear enzymes that catalyse changes in the topological structure of DNA, therefore regulating its replication and transcription [130]. Other endogenous sources of DNA damage include spontaneous base deamination [131], formation of abasic sites [132], lesions (or modifications) induced by reactive oxygen species (ROS) [133], and DNA methylation [134]. Exogenous agents responsible for DNA damage include ionization radiation (IR) [135], chemicals [136], toxins [137], and environmental stresses [138].

Different types of genetic lesions exist including point mutations, translocations, chromosome gain or loss, and telomere shortening [139, 140]. They affect gene expression and their transcriptional pathways, consequently leading to the synthesis of dysfunctional proteins (**Table 1. 9**).

Table 1. 9 Class of gene mutations and their association with abnormal protein synthesis and age-related diseases including cancer.

Gene mutation	Protein mutation	Disease
Point mutation	Missense mutation (change in one amino acid - protein variant). Non-sense mutation (a codon is changed with a premature stop codon - shorter protein). Non-stop mutation (lack of a stop codon - longer protein)	Breast and ovarian cancer [141], neurological diseases [142, 143], Progeroid syndrome [144], Werner syndrome [145]

Chromosomal mutation	<p>Inversion (a region of a chromosome is flipped and reinserted).</p> <p>Deletion (loss of a chromosome region).</p> <p>Duplication (a region of a chromosome is repeated).</p> <p>Translocation (a region of a chromosome is moved onto another region or another chromosome)</p>	Turner syndrome [146], Down syndrome [147], solid tumours [148]
Copy number variation	<p>Gene amplification (several copies of a gene on a locus).</p> <p>Expanding trinucleotide repeat (several repeated trinucleotide sequences)</p>	Ageing[149, 150], cancer [151, 152], spinal muscular atrophy [153]

Cells have evolved various DNA damage repair (DDR) strategies to repair these lesions and ensure the structural and functional integrity of DNA (**Figure 1. 16**). Homologous recombination (HR) and non-homologous end joining (NHEJ) are only two of the various repair mechanisms activated upon DNA damage and refer specifically to double-strand breaks (DSBs) which are responsible for several human disorders and cancer. Upon DSB formation, a cascade of events occur, including activation of the Ataxia telangiectasia mutated gene (ATM), phosphorylation of the histone γ H2AX, chromatin Poly-ADP-Ribosylation (PARylation), recruitment of the Mediator of DNA Damage Checkpoint 1 (MDC1), Tumour Protein P53 Binding Protein 1 (TP53BP1) and finally the Breast Cancer 1 encoded protein BRCA1 [154].

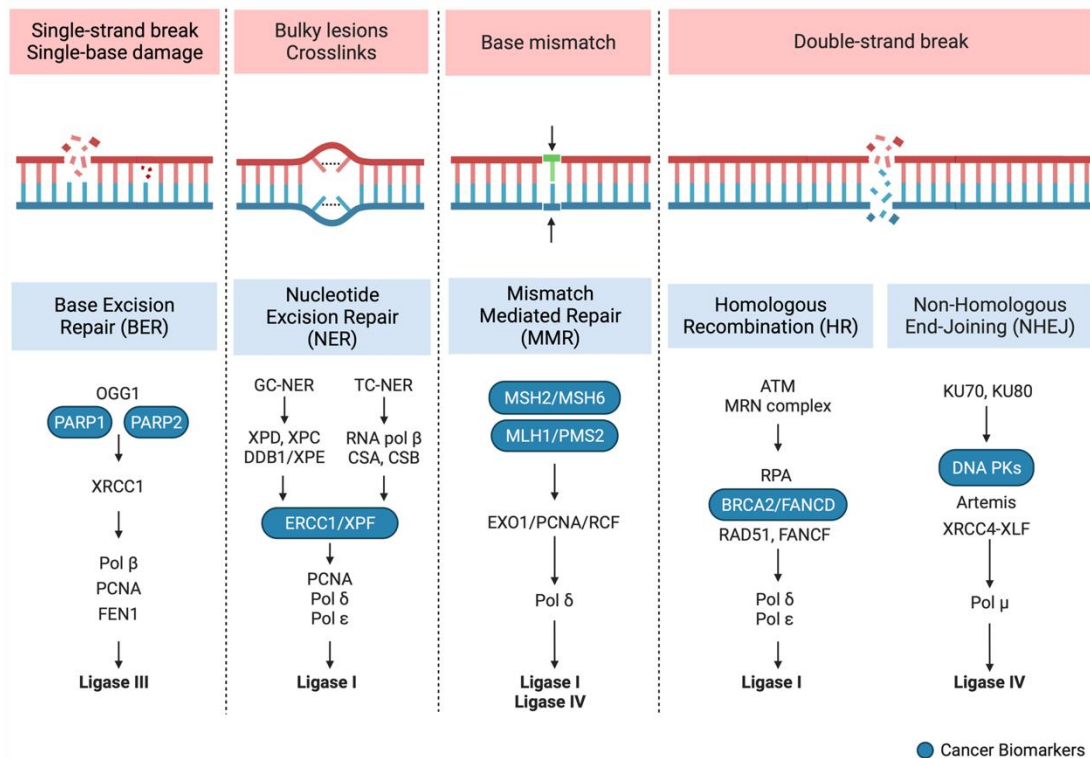


Figure 1. 16 Representation of different DNA repair mechanisms. 8-Oxoguanine DNA Glycosylase (OGG1), Poly(ADP-Ribose) Polymerase (PARP), X-Ray Repair Cross Complementing 1 (XRCC1), polymerase (Pol), Proliferating cell nuclear antigen (PCNA), Flap Structure-Specific Endonuclease 1 (FEN1), Xeroderma pigmentosum (XP), DNA damage-binding (DDB), Cockayne syndrome (CS), MutS Homolog (MSH), MutL Homologous (MLH), Exonuclease 1 (EXO1), Replication factor C (RCF), Ataxia telangiectasia mutated (ATM), Mre11-Rad50-Nbs1 (MRN) complex, Replication protein (RPA), Breast cancer gene (BRCA), FA Complementation group (FANC).

Of notice, DDR proteins such as ATM, poly (ADP-Ribose) polymerase (PARP), and BRCA1, have important roles in maintaining telomere functionality. Hence, their defect is responsible for telomere shortening and dysfunction in ageing [155]. In cancer cells where these DDR proteins are enhanced, telomere length is maintained supporting proliferation. Telomere shortening occurs at each cell division until the telomeres reach a limited length when they are recognised as DSBs and lead to the chronic activation of DDR [156]. At this stage cells can enter the programmed cell death (apoptosis), or senescence which is a state of cell cycle arrest and resistance to apoptosis. In addition to short telomeres, the increased expression of DBSs markers has been reported in senescent cells [157]. ATM has a key role in the sensing and signalling of DSBs, mediating their repair mechanisms through the recruitment of DNA-repair

proteins onto the site of damage [158]. Among its targets, ATM cascade response involves activation of p53, p21 and p16 which are inhibitors of the cell cycle and markers of senescence.

Activated oncogenes and DNA replication stress with DSB formation are responsible for chromosomal instability that has been observed in several solid tumours [159]. Carcinogens and hereditary DDR defects also contribute to cancer development and may induce an adaptive response that promotes tumour survival and proliferation despite the accumulation of mutations.

Although genomic instability is associated with genetic alterations at the DNA level, there is increasing evidence linking genomic instability to cellular metabolism. For example, a feature of patients lacking ATM expression (Ataxia telangiectasia patients) is a reduced activity of the insulin-signalling pathway that regulates protein synthesis through the activation of the components of the translational machinery (e.g., eIFs and eEFs) [160], since insulin is known to regulate the levels of the energy metabolite glucose in cells [161], this suggests a role for ATM in the regulation of cellular energy metabolism.

Another example is increased histone and DNA methylation associated with high levels of S-adenosylmethionine (SAM) and serine [162].

Conversely, metabolites can also influence gene expression and the DNA status. As in the case of α -ketoglutarate, a key metabolite in several metabolic and cellular pathways including hydroxylation reactions, where it serves as a substrate for specific dioxygenases like Lysine demethylase (KDMs) and ten-eleven translocation (TET) responsible for DNA demethylation [163-165]. In certain cancer types, the overexpression of 2-hydroxyglutarate – an antagonist of α -ketoglutarate [166] – inhibits the activity of α -ketoglutarate-dependent dioxygenases, promoting hypermethylation of the DNA and regulation of gene expression [167, 168]. A recent study reported that in people aged over 60 years, high levels of glycerophospholipids, and low levels of methionine, and tyrosine, are associated with reduced leukocyte telomere length, therefore suggesting a role for lipid metabolism in the regulation of genome stability [169].

In conclusion, the focus of this section was on the genomic alterations representing key features of disrupted cells. We explored some connections between DNA lesions and cellular metabolism, showing the impact that metabolic changes may have on the regulation of gene expression. The focus of the next section will be on the metabolic alterations that influence cellular growth and functionality.

1.1.6. Metabolic reprogramming

Metabolic reprogramming refers to the ability of cells to alter their normal metabolism in order to adapt to adverse conditions and support their growth and survival [170]. Metabolic reprogramming is a key hallmark of both cancer and senescence (**Figure 1. 17**).

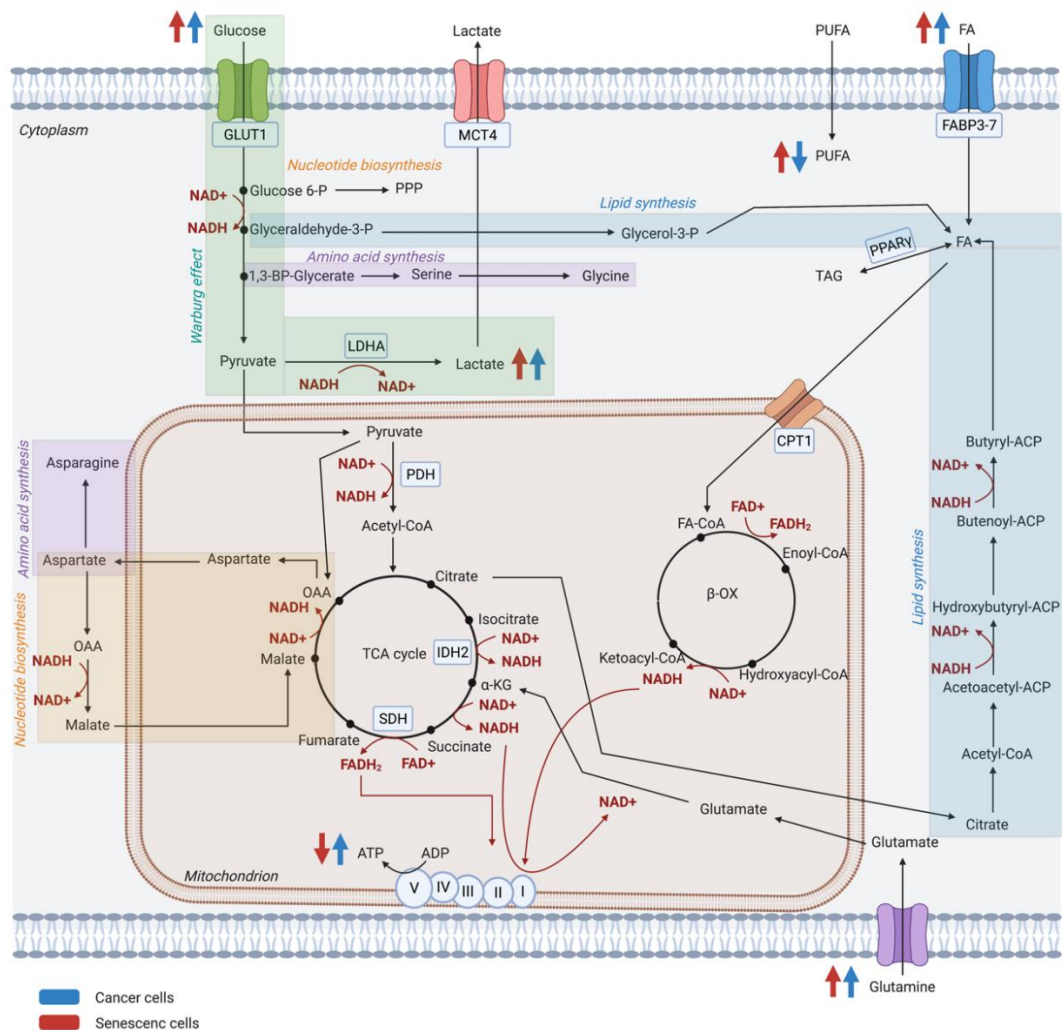


Figure 1. 17 Key metabolic changes occurring in cancer and senescent cells. The picture describes key metabolic pathways known to be rewired in cancer (blue arrows) and senescent cells (red arrows). Altered metabolic pathways include glycolysis (green), amino acids (purple), nucleotides (orange), and lipids metabolism (light blue). Glucose transporter 1 (GLUT1), Monocarboxylate transporter 4 (MCT4), Fatty acid binding protein (FABP), Peroxisome proliferator-activated receptor (PPAR), Lactate dehydrogenase A (LDHA), Pyruvate dehydrogenase (PDH), Isocitrate dehydrogenase (IDH), Succinate dehydrogenase (SDH), Carnitine palmitoyl transferase 1 (CPT1).

Cellular metabolism is the sum of biochemical reactions that occur in a living organism. They are described by two opposing processes: catabolism and anabolism. Catabolism is the oxidative degradation of molecules aimed to produce adenosine triphosphate (ATP), whereas anabolism refers to the reductive and energy-consuming reactions triggering the synthesis of biomolecules such as proteins, lipids, nucleic acids and carbohydrates. The

activity of both processes is generally regulated in such a way that they can supply the bioenergetic requirement of cells, underpinning their proliferation rate.

Cellular proliferation requires a source of nutrients supporting energy and biomass production. Glucose is the major energy source for ATP production through the concerted activity of glycolysis, the tricarboxylic acid (TCA) cycle, and oxidative phosphorylation (OXPHOS). About 89% of ATP is produced through OXPHOS, while the remaining 11% derives from substrate-level phosphorylation (SLP) reactions occurring either in the cytosol or in mitochondria [171]. The latter involves the transfer of a phosphate to ADP from a metabolic substrate to form ATP. Glutamine is the second critical nutrient in cells as it represents an alternative source of carbon for the TCA cycle (anaplerotic reactions), plays a role in several signal transduction pathways and is a required precursor for the synthesis of amino acids, proteins, nucleotides and lipids. Moreover, glutamine is required for the synthesis of glutathione (GSH), an important antioxidant molecule protecting cells from oxidative stress.

In cancer and senescent cells, glucose metabolism is one of the key reprogrammed metabolic pathways [172]. In both cases there is a high rate of glucose uptake, which is then converted into lactate (fermentation) despite the presence of oxygen. Consequently, senescent cells present low levels of ATP. In addition to glucose, reduced NAD⁺/NADH ratios that inhibit the glycolytic enzyme GAPDH are also impacted in senescent cells [173].

Conversely, cancer cells keep a balanced ATP turnover despite glucose fermentation. Of notice, fermentation does not provide sufficient ATP molecules to satisfy the energy demand of cancer cells for their high proliferation rate [171]. Thus, it remains to be established which alternate energy sources are used by cancer cells to generate ATP. A potential ATP compensatory pathway has been proposed, which is based on SLP reactions driven by glutamine metabolism through α -ketoglutarate [174]. Glucose metabolism also has a role in apoptosis resistance which is a common feature

of both cancer and senescent cells [175]. Considering that cancer and senescent cells are in sub-optimal oxygen conditions, they are both characterised by increased expression of Hypoxia-inducible factor (HIF) [176, 177]. In addition to enhancing glycolytic factors, HIF directly suppresses the pro-apoptotic protein, B cell lymphoma 2 (BCL-2) [178]. Enhanced glycolysis has also been demonstrated to activate Nuclear Factor Kappa B (NF- κ B) pathways as a response to DNA damage, therefore promoting pro-inflammatory changes as observed during senescence [179].

As anticipated, glutamine is an essential metabolite for tumour cell growth, and several cancers exhibit glutamine addiction- evidenced by their inability to survive under glutamine-deprived conditions [180]. DDR activation diminishes glutamine anaplerosis while favouring glutamine redirection toward biosynthetic pathways [181]. Thus, glutamine metabolic rewiring exhibits a significant influence on the DNA damage response. Glutamine utilization in *de novo* biosynthetic pathways is a feature of cancer and senescent cells [182]. As for the biosynthesis of nucleotides where glutamine metabolism, through α -KG, sustain branched-chain amino acids (BCAA) as nitrogen donors [183]. Moreover, in senescent cells, the elevated glutaminolysis processes lead to high production of nitrogen, which has the potential to neutralise the cytosolic acidity caused by lysosomal dysfunction represented by β -galactosidase enzyme (β -gal) [184].

In addition to amino acid and glucose metabolism, metabolic reprogramming is also associated with changes in lipid metabolism. Lipids (sterols, mono/di/triglycerides, phospholipids and glycolipids) serve as an energy source, membrane components and signalling molecules under homeostatic conditions. In senescent cells phospholipids, triglycerides and polyunsaturated fatty acids (PUFA) accumulate due to their increased extracellular uptake [185]. The sphingomyelin-ceramide pathways have been found to be upregulated in senescent and cancer cells [186, 187]. These pathways upregulate p21, therefore inducing cell cycle arrest [188]. Moreover, the

upregulation of ceramide metabolism promotes the production of sphingolipids that protect cells against apoptosis therefore promoting their survival [189].

A consequence of lipid *de novo* lipogenesis and internalisation is their accumulation in lipid droplets where they serve as an energy source, and maintenance of lipid and membrane homeostasis. Accumulation of lipid droplets has been observed in both senescent and cancer cells [190, 191].

Similar to the TCA cycle, lipids are intracellularly oxidised via β -oxidation which is a source of NADH reducing power for the synthesis of the OXPHOS-derived ATP. Whether β -oxidation is relevant to produce ATP in senescent and cancer cells still needs to be established as very few studies have focused on this area of research. However, the increased expression of β -oxidation enzymes has been reported in both senescent and cancer cells [192, 193].

β -oxidation is also responsible for the accumulation of ROS, therefore its altered activity creates a redox imbalance that consequently leads to lipid peroxidation [194]. This is a biological process whose primary products are unstable lipid peroxides (LPOs) that easily decompose into more stable but reactive secondary compounds such as Malondialdehyde (MDA), 4-hydroxy-2-nonenal (HNE), 4-hydroxy-2-hexenal (HHE), 4-hydroperoxy-2-nonenal (HPNE), 4-oxo-2-nonenal (ONE), 4-oxo-2-hexenal (OHE), 4,5-epoxy-2-decenal (EDE), 9,12-dioxo-10-dodecenoic acid (DODE) [195]. These are highly toxic compounds since they exert mutagenic activity by directly interacting with guanine in DNA [196]. They also have epigenetic effects by binding histones regulating chromatin condensation [197]. LPOs are responsible for the oxidative modifications of proteins and membrane phospholipids, therefore affecting protein function and membrane stability, respectively [198]. Lipid peroxidation also potentiates cellular damage at distant sites, thereby propagating the response and injury initiated by ROS, including the induction of cell senescence in neighbouring cells [199].

This thesis presents different studies where, through the combined application of molecular biology approaches, and LC-MS based metabolomics, proteomics and MSI, we explored the metabolic changes occurring during ageing and cancer development. Thanks to the advent of highly sensitive

instruments in the field of mass spectrometry, it is now possible to collect new and more accurate information on the molecular and metabolic composition of biological systems (cells and tissues). However, alone these data are not sufficient to understand the genetic, physiologic and metabolic complexity of ageing and cancer. Thus, the integration of all the “omics” information of the central dogma (genomics, transcriptomics, proteomics and metabolomics) is required to uncover the pathways and regulatory networks that are at the basis of ageing and cancer development and/or progression.

1.2. References

1. Crick, F., *On protein synthesis*. Symposia of the Society for Experimental Biology, 1958. **12**: p. 138-163.
2. Schreiber, S., *Small molecules: the missing link in the central dogma*. Nature Chemical Biology, 2005. **1**(2): p. 64-66.
3. Consortium, I.H.G.S., *Finishing the euchromatic sequence of the human genome*. Nature, 2004. **431**: p. 931-945.
4. Blackstock, W., et al, *Proteomics: quantitative and physical mapping of cellular proteins*. Trends in Biotechnology, 1999. **17**(3): p. 121-127.
5. Schröder, T., *The protein puzzle*, in *Biology & medicine cell research*. p. 54-59.
6. Willyard, C., *New human gene tally reignites debate*, in *Nature*. 2018. p. 354-355.
7. Khoury, G., et al, *Proteome-wide post-translational modification statistics: frequency analysis and curation of the swiss-prot database*. Science Reports, 2011. **1**(90).
8. Beger, R., *Metabolomics enables precision medicine: "A White Paper, Community Perspective"*. Metabolomics, 2016. **12**(10): p. 149.
9. Lieberman, M., et al, *Energy Production and Metabolism*. Cell physiology source book 2001. **Third edition**: p. 119-138.
10. Tidwell, T., et al, *Aging, Metabolism, and Cancer Development: from Peto's Paradox to the Warburg Effect*. Aging Disease, 2017. **8**(5): p. 662-676.
11. Azad, R., *Metabolomics technology and bioinformatics for precision medicine*. Briefings in Bioinformatics, 2019. **20**(6): p. 1957-1971.
12. Edison, A., et al, *NMR: Unique Strengths That Enhance Modern Metabolomics Research*. Analytical Chemistry, 2021. **93**(1): p. 478-499.
13. Robards, K., et al., *High performance liquid chromatography: Instrumentation and techniques*, in *Principles and Practice of Modern Chromatographic Methods*. 2022. p. 247-282.
14. Jerkovich, A., et al., *The use of micrometer-sized particles in ultrahigh pressure liquid chromatography: capillary columns packed with 1-[micro]m particles can provide separations far superior to those of conventional high performance liquid chromatography (HPLC) columns and maintain normal HPLC analysis times. (Column Watch)*. LC-GC North America, 2003. **21**(7).
15. Piotek, J., et al., *UHPLC: The Greening Face of Liquid Chromatography*. Chromatographia, 2013. **76**(21): p. 1429-1437.
16. Fekete, S., et al., *Current and future trends in UHPLC*. Trends in analytical chemistry, 2014. **63**: p. 2-13.
17. Manallack, D., et al., *The Acid/Base Profile of the Human Metabolome and Natural Products*. Molecular informatics, 2013. **32**(5-6): p. 505-515.
18. Liigang, J., et al., *pH Effects on Electrospray Ionization Efficiency*. Journal of American Society for Mass Spectrometry, 2017. **28**(3): p. 461-469.
19. Apffel, A., et al., *Enhanced sensitivity for peptide mapping with electrospray liquid chromatography-mass spectrometry in the presence of signal suppression due to trifluoroacetic acid-containing mobile phases*. Journal of Chromatography A, 1995. **712**(1): p. 177-190.
20. Jandera, P., *Liquid chromatography | Normal Phase*, in *Encyclopedia of Analytical Science*. 2005. p. 142-152.
21. Buszewski, B. et al., *Hydrophilic interaction liquid chromatography (HILIC)—a powerful separation technique*. Analytical and Bioanalytical Chemistry, 2011. **402**(1): p. 231-247.
22. Jandera, P., *Stationary and mobile phases in hydrophilic interaction chromatography: a review*. Analytica Chimica Acta, 2011. **692**(1-2): p. 1-25.
23. Gritti, F., et al., *The van Deemter equation: Assumptions, limits, and adjustment to modern high performance liquid chromatography*. Journal of Chromatography A, 2013. **1302**: p. 1-13.
24. Kaplitz, A., et al., *High-Throughput and Ultrafast Liquid Chromatography*. Analytical Chemistry, 2020. **92**(1): p. 67-84.
25. Kebarle, P., *Electrospray: From ions in solution to ions in the gas phase, what we know now*. Mass Spectrometry Review, 2009. **28**(6): p. 898-917.

26. Fenn, J., et al., *Electrospray ionization for mass spectrometry of large biomolecules*. Science, 1989. **246**(4926): p. 64-71.
27. Krueve, A., *Strategies for Drawing Quantitative Conclusions from Nontargeted Liquid Chromatography–High-Resolution Mass Spectrometry Analysis*. Analytical Chemistry, 2020. **92**(7): p. 4691-4699.
28. Hamdy, O., et al., *Reflections on Charge State Distributions, Protein Structure, and the Mystical Mechanism of Electrospray Ionization*. Journal of American Society for Mass Spectrometry, 2011. **23**(1-6).
29. Perez de Souza, L., et al., *Ultra-high-performance liquid chromatography high-resolution mass spectrometry variants for metabolomics research*. Nature, 2021. **18**: p. 733-754.
30. McNaught, A., et al., *IUPAC. Compendium of Chemical Terminology*. 2nd Edition ed. 1997: Blackwell Scientific Publications, Oxford.
31. Brenton, A., et al., *Accurate Mass Measurement: Terminology and Treatment of Data*. Journal of American Society for Mass Spectrometry, 2010. **21**(11): p. 1821-1835.
32. Glauser, G., et al., *Ultra-high pressure liquid chromatography-mass spectrometry for plant metabolomics: a systematic comparison of high-resolution quadrupole-time-of-flight and single stage Orbitrap mass spectrometers*. Journal of Chromatography A, 2013. **1292**: p. 151-159.
33. Zubarev, R., et al., *Orbitrap mass spectrometry*. Analytical Chemistry, 2013. **85**(11): p. 5288-5296.
34. Mellon, F., *Mass spectrometry | Principles and Instrumentation*, in *Encyclopedia of Food Sciences and Nutrition* 2003. p. 3739-3749.
35. Allen, D., et al., *Quadrupole Time-of-Flight Mass Spectrometry: A Paradigm Shift in Toxicology Screening Applications*. Australasian Association for Clinical Biochemistry and Laboratory Medicine, 2019. **40**(3): p. 135-146.
36. Lloyd, J., et al., *An IT-TOF mass spectrometer for the analysis of organic aerosol*. International Journal of Mass Spectrometry, 2009. **281**(1-2): p. 8-14.
37. Thompson, A., et al., *Fourier transform ion cyclotron resonance mass spectrometry (FT-ICR-MS) peak intensity normalization for complex mixture analyses*. Rapid Communications in Mass Spectrometry, 2021. **35**(9): p. e9068.
38. Caprioli, M., et al., *Molecular imaging of biological samples: localization of peptides and proteins using MALDI-TOF MS*. Analytical Chemistry, 1997. **69**(23): p. 4751-4760.
39. Jaskolla, T. et al., *Compelling evidence for Lucky Survivor and gas phase protonation: the unified MALDI analyte protonation mechanism*. Journal of the American Society for Mass Spectrometry, 2011. **22**(6): p. 976-988.
40. Dreisewerd, K., *Recent methodological advances in MALDI mass spectrometry*. Analytical and Bioanalytical Chemistry, 2014. **406**: p. 2261-2278.
41. Norris, J., et al., *Analysis of tissue specimens by matrix-assisted laser desorption/ionization imaging mass spectrometry in biological and clinical research*. Chemical Reviews, 2013. **113**(4): p. 2309-2342.
42. Thomas, A., et al., *Sublimation of new matrix candidates for high spatial resolution imaging mass spectrometry of lipids: enhanced information in both positive and negative polarities after 1,5-diaminonaphthalene deposition*. Analytical Chemistry, 2012. **84**(4): p. 2048-2054.
43. Meriaux, C., et al., *Liquid ionic matrixes for MALDI mass spectrometry imaging of lipids*. Journal of Proteomics, 2010. **73**(6): p. 1204-1218.
44. Cornett, D., et al., *MALDI-FTICR Imaging Mass Spectrometry of Drugs and Metabolites in Tissue*. Analytical Chemistry, 2008. **80**(14): p. 5648-5653.
45. DeLaney, K., et al., *Advances in high-resolution maldi mass spectrometry for neurobiology*. Mass Spectrometry Review, 2022. **41**(2): p. 194-214.
46. Römpp, A., et al., *imzML: Imaging Mass Spectrometry Markup Language: A Common Data Format for Mass Spectrometry Imaging*, in *Methods in Molecular Biology*. 2010. p. 205-224.
47. Nilsson, A., et al., *Fine mapping the spatial distribution and concentration of unlabeled drugs within tissue micro-compartments using imaging mass spectrometry*. PloS One, 2010. **5**(7): p. e11411.
48. Schrimpe-Rutledge, A., et al., *Untargeted metabolomics strategies – Challenges and Emerging Directions*. Journal of the American Society for Mass Spectrometry, 2016. **27**(12): p. 1897–1905.

49. Guan, S., et al., *Data Dependent–Independent Acquisition (DDIA) Proteomics*. Journal of Proteome Research, 2020. **19**(8): p. 3230–3237.
50. Broadhurst, D., et al., *Guidelines and considerations for the use of system suitability and quality control samples in mass spectrometry assays applied in untargeted clinical metabolomic studies*. Metabolomics, 2018. **14**(72).
51. Chait, B., *Mass Spectrometry: Bottom-Up or Top-Down?* Science, 2006. **314**(5796): p. 65-66.
52. Roberts, L., et al., *Targeted metabolomics*. Current Protocols in molecular biology, 2012.
53. Cui, W., et al., *Top-Down Mass Spectrometry: Recent Developments, Applications and Perspectives*. Analyst, 2011. **136**(19): p. 3854–3864.
54. Wang, Y., et al., *Enhanced MS/MS coverage for metabolite identification in LC-MS-based untargeted metabolomics by target-directed data dependent acquisition with time-staggered precursor ion list*. Analytica Chimica Acta, 2017. **992**: p. 67-75.
55. Bowen, T., et al., *An Extensive Metabolomics Workflow to Discover Cardiotoxin-Induced Molecular Perturbations in Microtissues*. Metabolites, 2021. **11**(9): p. 644.
56. Vuckovic, D., *Sample Preparation in Global Metabolomics of Biological Fluids and Tissues*, in *Proteomic and Metabolomic Approaches to Biomarker Discovery*. 2013. p. 51-75.
57. Smith, L., et al., *Important Considerations for Sample Collection in Metabolomics Studies with a Special Focus on Applications to Liver Functions*. Metabolites, 2020. **10**(3): p. 104.
58. Sillas, G., et al., *Metabolome analysis: an introduction*. 2007: John Wiley & Sons, Inc.
59. Kapoore, R., et al., *Influence of washing and quenching in profiling the metabolome of adherent mammalian cells: a case study with the metastatic breast cancer cell line MDA-MB-231*. Analyst, 2017. **142**: p. 2038-2049.
60. Munger, J., et al., *Dynamics of the Cellular Metabolome during Human Cytomegalovirus Infection*. PLoS Pathog, 2006. **2**(12): p. e132.
61. Chong, W., et al., *LC-MS-based metabolic characterization of high monoclonal antibody-producing Chinese hamster ovary cells*. Biotechnology and bioengineering, 2012. **109**(12): p. 3103-3111.
62. Sheikh, K., et al., *Small Molecule Metabolite Extraction Strategy for Improving LC/MS Detection of Cancer Cell Metabolome*. Journal of Biomolecular techniques, 2011. **22**(1): p. 1-4.
63. Alamri, A., et al., *Untargeted Metabolic Profiling Cell-Based Approach of Pulmonary Artery Smooth Muscle Cells in Response to High Glucose and the Effect of the Antioxidant Vitamins D and E*. Metabolites, 2018. **8**(87).
64. Alonezi, S., et al., *Metabolomic Profiling of the Synergistic Effects of Melittin in Combination with Cisplatin on Ovarian Cancer Cells*. Metabolites, 2017. **7**(2).
65. Edwards-Hicks, J., et al., *MYC sensitises cells to apoptosis by driving energetic demand*. Nature communications, 2022. **13**(4674).
66. Yuan, W., et al., *Subsecond Absolute Quantitation of Amine Metabolites Using Isobaric Tags for Discovery of Pathway Activation in Mammalian Cells*. Analytical Chemistry, 2012. **84**(6): p. 2892-2899.
67. Ulmer, C., et al., *A Robust Lipidomics Workflow for Mammalian Cells, Plasma, and Tissue Using Liquid-Chromatography High-Resolution Tandem Mass Spectrometry*. Methods Molecular biology, 2017. **1609**: p. 91-106.
68. Folch, J., et al., *A simple method for the isolation and purification of total lipids from animal tissues*. Journal of Biological Chemistry, 1956. **226**(1): p. 497-509.
69. Bligh, E., et al., *A rapid method of total lipid extraction and purification*. Canadian Journal of Biochemistry and Physiology, 1959. **37**(8): p. 911-917.
70. Sugiura, Y., et al., *Thin Sectioning Improves the Peak Intensity and Signal-to-Noise Ratio in Direct Tissue Mass Spectrometry*. J-Stage, 2006. **54**(2): p. 45-48.
71. Chaurand, P., et al., *Integrating histology and imaging mass spectrometry*. Analytical Chemistry, 2004. **76**(4): p. 1145-1155.
72. Wither, M., et al., *Mass Spectrometry-Based Bottom-Up Proteomics: Sample Preparation, LC-MS/MS Analysis, and Database Query Strategies*. Current Protocols in Protein Science, 2016. **86**(16.4.1-16.4.20).
73. Manza, L., et al., *Sample preparation and digestion for proteomic analyses using spin filters*. Proteomics, 2005. **5**(7): p. 1742-1745.

74. Wu, X., et al., *Reduction and Alkylation of Proteins in 2D Gel Electrophoresis: Before or after Isoelectric Focusing?* *Frontiers in Chemistry*, 2017. **5**(59).
75. Müller, T., et al., *Systematic Evaluation of Protein Reduction and Alkylation Reveals Massive Unspecific Side Effects by Iodine-containing Reagents.* *Molecular & Cellular proteomics*, 2017. **16**(7): p. 1173-1187.
76. Huang, Y., et al., *Statistical characterization of the charge state and residue dependence of low-energy CID peptide dissociation patterns.* *Analytical Chemistry*, 2005. **77**(18): p. 5800-5813.
77. Naldrett, M., et al., *Concentration and Desalting of Peptide and Protein Samples with a Newly Developed C18 Membrane in a Microspin Column Format.* *Journal of Biomolecular techniques*, 2005. **16**(4): p. 423-428.
78. Smith, L., et al., *Proteoform: a single term describing protein complexity.* *Nature*, 2013. **10**: p. 186-187.
79. Hendriks, M., et al., *Data-processing strategies for metabolomics studies.* *Trends in analytical chemistry*, 2011. **30**(10): p. 1685-1698.
80. Mahieu, N., et al., *A roadmap for the XCMS family of software solutions in metabolomics.* *Current Opinion in Chemical Biology*, 2016. **30**: p. 87-93.
81. Lommen, A., et al., *MetAlign 3.0: performance enhancement by efficient use of advances in computer hardware.* *Metabolomics*, 2012. **8**(4): p. 719-726.
82. Tsugawa, H., et al., *MS-DIAL: data-independent MS/MS deconvolution for comprehensive metabolome analysis.* *Nature Methods*, 2015. **12**(6): p. 523-526.
83. Chong, J., et al., *MetaboAnalyst 4.0: towards more transparent and integrative metabolomics analysis.* *Nucleic Acids Research*, 2018. **46**(1): p. 486-494.
84. Blaženović, I., et al., *Software Tools and Approaches for Compound Identification of LC-MS/MS Data in Metabolomics.* *Metabolites*, 2018. **8**(2): p. 31.
85. Smith CA., et al., *XCMS: Processing Mass Spectrometry Data for Metabolite Profiling Using Nonlinear Peak Alignment, Matching, and Identification.* *Analytical Chemistry*, 2006. **78**(3): p. 779-787.
86. Burton, L., et al., *Instrumental and experimental effects in LC-MS-based metabolomics.* *Journal of Chromatography B*, 2008. **871**(2): p. 227-235.
87. Benton HP., et al., *Correction of mass calibration gaps in liquid chromatography-mass spectrometry metabolomics data* *Bioinformatics*, 2010. **26**(19): p. 2488-2489.
88. Want, E., et al., *Processing and Analysis of GC/LC-MS-Based Metabolomics Data, in Metabolic profiling. Methods in molecular biology*, T. Metz, Editor. 2010, Humana press. p. 277-298.
89. Kapoore, R., et al., *Towards quantitative mass spectrometry-based metabolomics in microbial and mammalian systems.* *Philosophical Transactions of the Royal Society A*, 2016. **374**(2079): p. 20150363.
90. Van der Kloet, F., et al., *Analytical error reduction using single point calibration for accurate and precise metabolomic phenotyping.* *Journal of proteome research*, 2009. **8**(11): p. 5132-5141.
91. De Livera, A., et al., *Statistical Methods for Handling Unwanted Variation in Metabolomics Data.* *Analytical chemistry*, 2015. **87**(7): p. 3606-3615.
92. Palmer, M. *Ordination Methods - an overview.* 11-09-2022]; Available from: <http://ordination.okstate.edu/overview.htm>.
93. Ivosev, G., et al., *Dimensionality reduction and visualization in principal component analysis.* *Analytical Chemistry*, 2008. **80**(13): p. 4933-4944.
94. Gromski, P., et al., *A tutorial review: Metabolomics and partial least squares-discriminant analysis – a marriage of convenience or a shotgun wedding.* *Analytica Chimica Acta*, 2015. **16**: p. 10-23.
95. Kirkwood, T., et al., *Understanding the odd science of aging.* *Cell*, 2005. **120**(4): p. 437-447.
96. Olafsson, S., et al., *Somatic mutations provide important and unique insights into the biology of complex diseases.* *Trends in Genetics*, 2021. **37**(10): p. 872-881.
97. Laconi, E., et al., *Cancer as a disease of old age: changing mutational and microenvironmental landscapes.* *British Journal of Cancer*, 2020. **122**: p. 943-952.
98. Dimri GP., et al., *A biomarker that identifies senescent human cells in culture and in aging skin in vivo.* *Proceedings of the National Academy of Sciences of the United States of America*, 1995. **92**(20): p. 9363-9367.

99. Ressler, S., et al., *p16INK4A is a robust in vivo biomarker of cellular aging in human skin*. *Aging Cell*, 2006. **5**(5): p. 379-389.
100. Velarde, M., et al., *Mitochondrial oxidative stress caused by Sod2 deficiency promotes cellular senescence and aging phenotypes in the skin*. *Aging* (Albany NY), 2012. **4**(1): p. 3-12.
101. Ruhland, M., et al., *Stromal senescence establishes an immunosuppressive microenvironment that drives tumorigenesis*. *Nature Communications*, 2016. **7**(11762).
102. Zinger, A., et al., *Cancer and Aging - the Inflammatory Connection*. *Aging and Disease*, 2017. **8**(5): p. 611-627.
103. Fane, M., et al., *How the ageing microenvironment influences tumour progression*. *Nature*, 2019. **20**: p. 89-106.
104. Leonardi, G., et al., *Ageing: from inflammation to cancer*. *Immunity & Ageing*, 2018. **15**(1).
105. van Deursen, J., et al., *The role of senescent cells in ageing*. *Nature*, 2014. **509**(7501): p. 439-446.
106. Krizhanovsky, V., et al., *Senescence of activated stellate cells limits liver fibrosis*. *Cell*, 2008. **134**(4): p. 657-667.
107. Chien, Y., et al., *Control of the senescence-associated secretory phenotype by NF- κ B promotes senescence and enhances chemosensitivity*. *Genes & Development*, 2011. **25**(20): p. 2125-2136.
108. Kang, T., et al., *Senescence surveillance of pre-malignant hepatocytes limits liver cancer development*. *Nature*, 2011. **479**(7374): p. 547-551.
109. Campisi, J., *Aging, Cellular Senescence, and Cancer*. *Annual Review of Physiology*, 2014. **75**: p. 685-705.
110. Lee, S., et al., *The dynamic nature of senescence in cancer*. *Nature*, 2019. **21**: p. 94-101.
111. Jack, I., et al., *Tumour heterogeneity and resistance to cancer therapies*. *Nature*, 2017. **15**: p. 81-94.
112. NIH, *Biomarker*. p. <https://www.cancer.gov/publications/dictionaries/cancer-terms/def/biomarker>.
113. Stranger BE., et al., *Progress and promise of genome-wide association studies for human complex trait genetics*. *Genetics*, 2011. **187**(2): p. 367-383.
114. Botstein, D., et al., *Discovering genotypes underlying human phenotypes: past successes for mendelian disease, future approaches for complex disease*. *Nature Genetics*, 2003. **33**: p. 228-237.
115. Savino, R., et al., *The Proteomics Big Challenge for Biomarkers and New Drug-Targets Discovery*. *International Journal of Molecular Sciences*, 2012. **13**(11): p. 13926–13948.
116. Patti, G., et al., *Metabolomics: the apogee of the omic trilogy*. *Nature Reviews Molecular Cell Biology*, 2012. **13**(4): p. 263-269.
117. Baker, M., *Metabolomics: from small molecules to big ideas*. *Nature*, 2011. **8**: p. 117-121.
118. Bains, W., *Failure rates in drug discovery and development: will we ever get any better?* *Drug discovery world fall*, 2004: p. 9-18.
119. Sindelar, M., et al., *Chemical Discovery in the Era of Metabolomics*. *Journal of American Chemical Society*, 2020. **142**(20): p. 9097-9105.
120. administration, F.D., *Table of Pharmacogenomic Biomarkers in Drug Labeling*. 2022: Online.
121. López-Otín, C., et., *The Hallmarks of Aging*. *Cell*, 2013. **153**(6): p. 1194-1217.
122. Hanahan, D., et al., *Hallmarks of Cancer: The Next Generation*. *Cell*, 2011. **144**(5): p. 646-674.
123. Tucker, J., et al., *Frequency of spontaneous chromosome aberrations in mice: effects of age*. *Mutation Research*, 1999. **425**(1): p. 135-141.
124. Ainslie, A., et al., *Genome instability and loss of protein homeostasis: converging paths to neurodegeneration?* *Open Biology*, 2021. **11**(4): p. 200296.
125. D'Errico, M., et al., *The role of CSA and CSB protein in the oxidative stress response*. *Mechanisms of ageing and development*, 2013. **134**(5-6): p. 261-269.
126. Vijg, J., et al., *Genome instability and aging: Cause or effect?* *Translational Medicine of Aging*, 2017. **1**: p. 5-11.

127. Bakhoun, S., et al., *Chromosomal instability drives metastasis through a cytosolic DNA response*. Nature, 2018. **553**(7689): p. 467-472.
128. Viguera, E., et al., *Replication slippage involves DNA polymerase pausing and dissociation*. EMBO Journal, 2001. **20**(10): p. 2587-2595.
129. Kunkel, T., *Evolving views of DNA replication (in)fidelity*. Cold Spring Harbor Symposia on Quantitative Biology, 2009. **74**: p. 91-101.
130. Wang, J., *Cellular roles of DNA topoisomerases: a molecular perspective*. Nature Reviews Molecular Cell Biology, 2002. **3**(6): p. 430-440.
131. Lindahl, T., *Instability and decay of the primary structure of DNA*. Nature, 1993. **362**(6422): p. 709-715.
132. Lindahl, et al., *Repair of endogenous DNA damage*. Cold Spring Harbor Symposia on Quantitative Biology, 2000. **65**: p. 127-133.
133. Henle, E., et al., *Formation, prevention, and repair of DNA damage by iron/hydrogen peroxide*. Journal of Biological Chemistry, 1997. **272**(31): p. 19095-8.
134. Zhao, C., et al., *Endogenous and background DNA adducts by methylating and 2-hydroxyethylating agents*. Mutation Research, 1999. **424**(1-2): p. 117-125.
135. Vignard, J. et al., *Ionizing-radiation induced DNA double-strand breaks: a direct and indirect lighting up*. Radiotherapy and Oncology, 2013. **108**(3): p. 362-369.
136. Lawley, P., *Effects of some chemical mutagens and carcinogens on nucleic acids*. Progress in Nucleic Acid Research and Molecular Biology, 1966. **5**: p. 89-131.
137. Smela, M., et al., *The chemistry and biology of aflatoxin B(1): from mutational spectrometry to carcinogenesis*. Carcinogenesis, 2001. **22**(4): p. 535-545.
138. Chatterjee, N., et al., *Environmental stress induces trinucleotide repeat mutagenesis in human cells*. Proceedings of the National Academy of Sciences of the United States of America, 2015. **112**(12): p. 3764–3769.
139. Broustas, C. et al., *DNA Damage Response Genes and the Development of Cancer Metastasis*. Radiation Research, 2014. **181**(2): p. 111-130.
140. Bohlander, S. et al., *DNA Repair and Chromosomal Translocations*. Recent Results in Cancer Research, 2015. **200**: p. 1-37.
141. Alnoumas, L., et al., *Evaluation of the role of KPNA2 mutations in breast cancer prognosis using bioinformatics datasets*. BMC Cancer, 2022. **22**(874).
142. Sherrington, R., et al., *Alzheimer's Disease Associated with Mutations in Presenilin 2 is Rare and Variably Penetrant*. Human Molecular Genetics, 1996. **5**(7): p. 985-988.
143. Lelieveld, S., et al., *Spatial Clustering of de Novo Missense Mutations Identifies Candidate Neurodevelopmental Disorder-Associated Genes*. American Journal of Human Genetics, 2017. **101**(3): p. 478-484.
144. Spear, E., et al., *ZMPSTE24 Missense Mutations that Cause Progeroid Diseases Decrease Prelamin A Cleavage Activity and/or Protein Stability*. Disease Models & Mechanisms, 2018. **11**(7).
145. Agrelo, R., et al., *A novel Werner Syndrome mutation: pharmacological treatment by read-through of nonsense mutations and epigenetic therapies*. Epigenetics, 2015. **10**(4): p. 329-341.
146. Zhao, C., et al., *Mapping the effect of the X chromosome on the human brain: Neuroimaging evidence from Turner syndrome*. Neuroscience & Biobehavioral Reviews, 2017. **80**: p. 263-275.
147. Gardiner, K., et al., *The sequence of human chromosome 21 and implications for research into Down syndrome*. Genome Biology, 2000. **1**(2).
148. Albertson, D., et al., *Chromosome aberrations in solid tumors*. Nature, 2003. **34**: p. 369-376.
149. Villela, D., et al., *Increased DNA Copy Number Variation Mosaicism in Elderly Human Brain*. Neural Plasticity during Aging, 2018. **2018**(2406170).
150. Arlt, M., et al., *Copy number variants are produced in response to low-dose ionizing radiation in cultured cells*. Environmental and Molecular Mutagenesis, 2013. **55**(2): p. 103-113.
151. Dennis, J., et al., *Rare germline copy number variants (CNVs) and breast cancer risk*. Nature, 2022. **5**(65).
152. Beroukhim, R., et al., *The landscape of somatic copy-number alteration across human cancers*. Nature, 2010. **463**: p. 899-905.
153. Kolb, S., et al., *Spinal Muscular Atrophy*. Neurologic Clinics, 2015. **33**(4): p. 831-846.

154. Chatterjee, N., et al., *Mechanisms of DNA damage, repair and mutagenesis*. Environmental and Molecular Mutagenesis, 2017. **58**(5): p. 235-263.
155. d'Adda di Fagagna, F., et al., *Functional links between telomeres and proteins of the DNA-damage response*. Genes Development, 2004. **18**(15): p. 1781-1799.
156. Longhese, M., *DNA damage response at functional and dysfunctional telomeres*. Genes Development, 2008. **22**(2): p. 125-140.
157. Jackson, S., et al., *The DNA-damage response in human biology and disease*. Nature, 2009. **461**: p. 1071-1078.
158. Lee, J., et al., *Cellular functions of the protein kinase ATM and their relevance to human disease*. Nature, 2021. **22**: p. 796-814.
159. Lengauer, C., et al., *Genetic instabilities in human cancers*. Nature, 1998. **396**(6712): p. 643-649.
160. Yand, D., et al., *Participation of ATM in insulin signalling through phosphorylation of eIF-4E-binding protein 1*. Nature Cell Biology, 2000. **2**: p. 893-898.
161. Pineda, W., et al., *The regulatory role of insulin in energy metabolism and leukocyte functions*. Journal of leukocyte Biology, 2021. **111**(1): p. 197-208.
162. Chiang, E., et al., *Effects of insulin and glucose on cellular metabolic fluxes in homocysteine transsulfuration, remethylation, S-adenosylmethionine synthesis, and global deoxyribonucleic acid methylation*. The Journal of Clinical Endocrinology and Metabolism, 2008. **94**(3): p. 1017-1025.
163. Hausinger, R., *Fell/alpha-ketoglutarate-dependent hydroxylases and related enzymes*. Critical Reviews in Biochemistry and Molecular Biology, 2004. **39**(1): p. 21-68.
164. Tsukada, Y., et al., *Histone demethylation by a family of JmjC domain-containing proteins*. Nature, 2006. **439**(7078): p. 811-816.
165. Tahiliani, M., et al., *Conversion of 5-methylcytosine to 5-hydroxymethylcytosine in mammalian DNA by MLL partner TET1*. Science, 2009. **324**(5929): p. 930-935.
166. Xu, W., et al., *Oncometabolite 2-Hydroxyglutarate Is a Competitive Inhibitor of α -Ketoglutarate-Dependent Dioxygenases*. Cancer Cell, 2011. **19**(1): p. 17-30.
167. Xiao, M., et al., *Inhibition of α -KG-dependent histone and DNA demethylases by fumarate and succinate that are accumulated in mutations of FH and SDH tumor suppressors*. Genes Development, 2012. **26**(12): p. 1326-1338.
168. Noshmehr, H., et al., *Identification of a CpG Island Methylator Phenotype that Defines a Distinct Subgroup of Glioma*. Cancer Cell, 2011. **17**(5): p. 510-522.
169. van der Spek, A., et al., *Metabolomics reveals a link between homocysteine and lipid metabolism and leukocyte telomere length: the ENGAGE consortium*. Scientific Reports, 2019. **9**(11623).
170. Carvalho-Santos, Z., et al., *Cellular metabolic reprogramming controls sugar appetite in Drosophila*. Nature Metabolism, 2020. **2**(9): p. 958-973.
171. Seyfried, T., et al., *On the Origin of ATP Synthesis in Cancer*. iScience, 2020. **23**(11): p. 101761.
172. Warburg, O., *The Metabolism of Carcinoma Cells*. The Journal of Cancer Research, 1925. **9**(1): p. 148-163.
173. Wiley, C., et al., *Mitochondrial Dysfunction Induces Senescence with a Distinct Secretory Phenotype*. Cell Metabolism, 2016. **23**(2): p. 303-314.
174. Chinopoulos, C., et al., *Mitochondrial Substrate-Level Phosphorylation as Energy Source for Glioblastoma: Review and Hypothesis*. ASN Neuro, 2018. **10**: p. 1-27.
175. Vaughn, A., et al., *Glucose Metabolism Inhibits Apoptosis in Neurons and Cancer Cells by Redox Inactivation of Cytochrome c*. Nature Cell Biology, 2009. **10**(12): p. 1477-1483.
176. Jun, J., et al., *Hypoxia-Inducible Factors and Cancer*. Current Sleep Medicine Reports, 2017. **3**(1): p. 1-10.
177. Alique, M., et al., *Hypoxia-Inducible Factor-1 α : The Master Regulator of Endothelial Cell Senescence in Vascular Aging*. Cells, 2020. **9**(1): p. 195.
178. Sermeus, A., et al., *Hypoxia-Induced Modulation of Apoptosis and BCL-2 Family Proteins in Different Cancer Cell Types*. PlosOne, 2012. **7**(11): p. e47519.
179. Mauro, C., et al., *NF- κ B controls energy homeostasis and metabolic adaptation by upregulating mitochondrial respiration*. Nature Cell Biology, 2011. **13**(10): p. 1272-1279.
180. Krall, A., et al., *Rethinking glutamine addiction*. Nature, 2015. **17**: p. 1515-1517.

181. Jeong, S., et al., *SIRT4 Has Tumor-Suppressive Activity and Regulates the Cellular Metabolic Response to DNA Damage by Inhibiting Mitochondrial Glutamine Metabolism*. *Cancer Cell*, 2013. **23**(4): p. 450-463.
182. Kodama, M., et al., *A second Warburg-like effect in cancer metabolism: The metabolic shift of glutamine-derived nitrogen*. *BioEssays*, 2020. **42**(12).
183. Holeček, M., *Branched-chain amino acids in health and disease: metabolism, alterations in blood plasma, and as supplements*. *Nutrition & Metabolism*, 2018. **15**(33).
184. Johmura, Y., et al., *Senolysis by glutaminolysis inhibition ameliorates various age-associated disorders*. *Science*, 2021. **371**(6526): p. 265-270.
185. Wiley, C., et al., *Secretion of leukotrienes by senescent lung fibroblasts promotes pulmonary fibrosis*. *JCI insight*, 2019. **4**(24): p. e130056.
186. Ogretmen, B., *Sphingolipid metabolism in cancer signalling and therapy*. *Nature*, 2017. **18**: p. 33-50.
187. Venable, M., et al., *Role of ceramide in cellular senescence*. *Journal of Biological Chemistry*, 1995. **270**(51): p. 30701-30708.
188. Lee, J., et al., *Regulation of cyclin-dependent kinase 2 activity by ceramide*. *Experimental Cell Research*, 2000. **261**(2): p. 303-311.
189. Modrak, D., et al., *Ceramide regulates gemcitabine-induced senescence and apoptosis in human pancreatic cancer cell lines*. *Molecular Cancer Research*, 2009. **7**(6): p. 890-896.
190. Petan, T., et al., *Lipid Droplets in Cancer: Guardians of Fat in a Stressful World*. *Molecules*, 2018. **23**(8): p. 1941.
191. Maeda, M., et al., *Regulation of fatty acid synthesis and Delta9-desaturation in senescence of human fibroblasts*. *Life Science*, 2009. **84**(3-4): p. 119-124.
192. Flor, A., et al., *A signature of enhanced lipid metabolism, lipid peroxidation and aldehyde stress in therapy-induced senescence*. *Cell Death Discovery*, 2017. **3**(17075).
193. Snaebjornsson, M., et al., *Greasing the Wheels of the Cancer Machine: The Role of Lipid Metabolism in Cancer*. *Cell Metabolism*, 2020. **31**(1): p. 62-76.
194. Wong-Ekkabut, J., et al., *Effect of lipid peroxidation on the properties of lipid bilayers: a molecular dynamics study*. *Biophysical Journal*, 2007. **93**(12): p. 4225-4236.
195. Guéraud, F., et al., *Chemistry and biochemistry of lipid peroxidation products*. *Free Radical Research*, 2010. **44**(10): p. 1098-1124.
196. Nair, J., et al., *Ethno DNA-base adducts from endogenous reactive species*. *Mutation Research*, 1999. **424**(1-2): p. 59-69.
197. Drake, J., et al., *4-Hydroxynonenal oxidatively modifies histones: implications for Alzheimer's disease*. *Neuroscience Letters*, 2004. **356**(3): p. 155-158.
198. Suzuki, Y., et al., *Protein carbonylation*. *Antioxidants & Redox Signaling*, 2010. **12**(3): p. 323-325.
199. Ramana, K., et al., *Lipid Peroxidation Products in Human Health and Disease 2016*. *Oxidative Medicine and Cellular Longevity*, 2017. **2017**.

1.3. Aims

Mass spectrometry-based metabolomics and proteomics represent efficient technologies to characterise biochemical events that underpin physiological and pathological processes. Ageing and cancer research are two scientific areas that are benefitting from the utilisation of these high throughput approaches as there is an evolving demand for appropriate and sensitive diagnostic strategies to predict and identify new biomarkers specific for different pathological phenotypes.

The overall aim of this thesis is to advance the application of mass spectrometry-based metabolomics/proteomics methods to give more insights into pathological mechanisms such as ageing and cancer. By coupling molecular, proteomics and metabolomics approaches alongside the determination of the spatial distribution of metabolites, we hope that the methods proposed in this research can contribute to improve the current clinical diagnostic strategies.

The specific aim of this thesis is to:

- Apply combined analysis of senescence associated β -galactosidase expression, DNA damage foci formation and cell cycle impairment with untargeted mass-spectrometry-based metabolomics to determine the intra- and extracellular metabolic changes occurring following induction of senescence (Chapter 2);
- Apply combined global mass-spectrometry-based metabolomics and proteomics analysis to design a putative map of the metabolic pathways that change during ageing of murine brain tissues. In this context we also aimed to determine the spatial localization of metabolites within the same tissue section through mass-spectrometry imaging (Chapter 3);

Apply combined analysis of DNA damage foci formation with global mass-spectrometry-based global metabolomics to profile the molecular and metabolic changes of different breast cancer cell lines in response to various DDR inhibition treatment doses of olaparib (Chapter 4).

CHAPTER 2

Measurement of molecular, metabolic, and inflammatory changes in different cellular senescence phenotypes

Domenica Berardi¹, Gillian Farrell¹, Ashley McCulloch¹, Zahra Rattray^{1*}, and Nicholas JW Rattray^{1*}

1. Strathclyde Institute of Pharmacy and Biomedical Science, University of Strathclyde, Glasgow, G4 0RE.

Corresponding authors: nicholas.rattray@strath.ac.uk and zahra.rattray@strath.ac.uk

2.1. Abstract

Cellular senescence has been widely accepted as a key driver of ageing, poorly ageing phenotypes and age-related disease. Thus, targeting and eliminating senescent cells to predict and/or ameliorate age-related malady is a major focus in biogerontological research. Targeting senescent cells is aided by the identification of novel biomarkers of cellular senescence. While many studies have focused on the identification of molecular biomarkers of senescence, there remains a baseline biomolecular profiling of senescence and its diverse phenotypes. Here we report the development of a model of replicative, chemical and x-ray induced senescence with assessment of DNA damage, ROS production, and metabolic profile.

Following induction of senescence, we measured the extent of DNA damage and replication index through detection of γ H2AX and Ki-67 molecular markers in the different senescence-like phenotypes. We subsequently evaluated intra- and extracellular metabolism using untargeted mass spectrometry-based metabolomics analysis. Altered metabolic changes were identified followed by pathway and metabolite enrichment analysis in cells and their growth media. We found that key intracellular metabolic changes predominantly in amino acid metabolism (histidine, arginine, alanine, aspartate and glutamate), occurring upon induction of senescence which was dependent on the stress stimulus type. The intracellular metabolic changes that we observed were consistent

with the presence of pro-inflammatory metabolites in the senescent cell growth media of each specific phenotype.

Our work shows the advantage of combining phenotypic, molecular and metabolomics studies for the detailed analysis of senescence and its heterogeneous phenotypes. Future studies are required to further validate the senescence-induced changes in metabolic pathways. Integration with genomics, transcriptomics and proteomics data will help understand the mechanisms that underpin ageing, providing insights into the pathophysiology of many age-related diseases.

KEYWORDS: Ageing, senescence, biomarker, metabolic reprogramming, mass spectrometry

2.2. Introduction

Currently, more than 12% (900 million) of the global population are over 60 years old and by 2050 this estimate will raise up to 22% (2 billion) [1]. This demographic change will lead to increased medical care and social needs, therefore having a radical impact on the structure and function of society, the global economy and health systems [2].

Human ageing is a temporal process of structural and functional accrument of damage at the molecular, cellular and tissue level which leads to the state of disease development, that can turn into a chronic condition and ultimately leading to death [3]. Accordingly, ageing represents the primary risk factor in the majority of diseases like diabetes, cancer [4], neurological [5], cardiovascular, and immune disorders [6]. For this reason, strategies to improve human health span, through the prevention and amelioration of age-related disease, have been extensively studied [7]. A better understanding of the biology of ageing is needed to develop diagnostics and therapies capable of tracking and targeting features of ageing.

Among the primary feature of ageing there is the accumulation of senescent cells, which have been observed in several age-related diseases and in the elderly [8]. Senescence is a hallmark of ageing characterised by the arrest of cell proliferation and resistance to death [9]. At present, induction of the senescence phenotype in normal human cells is the widest accepted strategy in ageing research to better understand its biological mechanisms and role in pathological conditions [10-12].

Cellular senescence was first reported in normal human fibroblasts where replication-associated telomere shortening was observed, which has widely been used as a prototype model for senescence known as replicative senescence [13, 14]. Stress-induced premature senescence (SIPS) is another type of senescence which includes DNA damage-induced senescence, Oncogene induced senescence, mitochondrial dysfunction-induced senescence, epigenetically induced senescence, and reactive oxygen species (ROS) induced senescence [15-17] (**Figure 2. 1**).

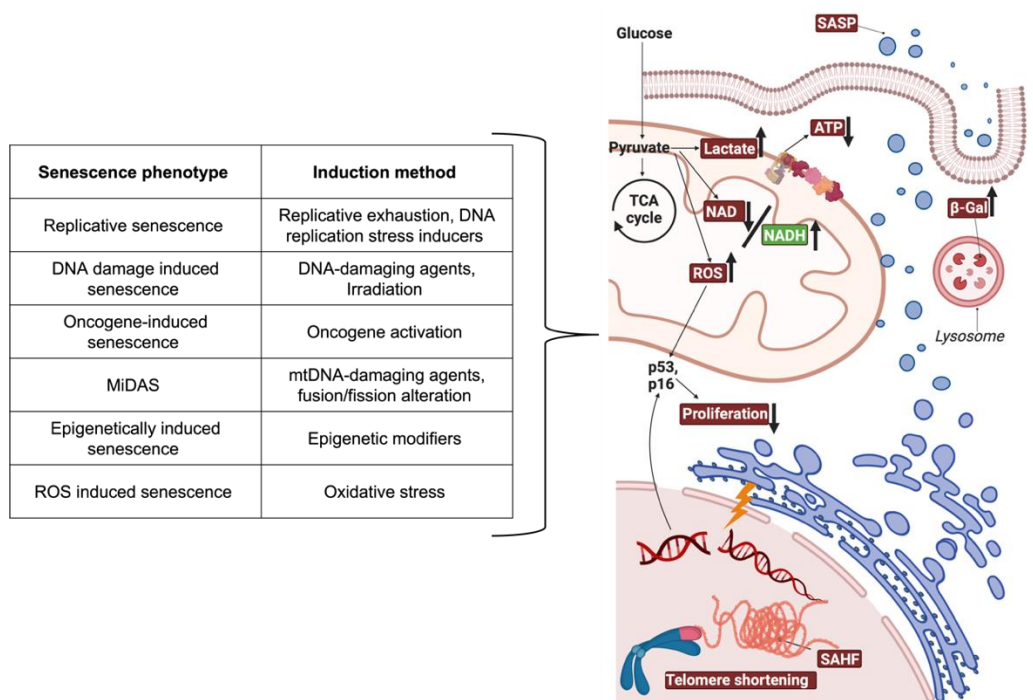


Figure 2. 1 Subtypes of senescence based on their method of induction. The general features of senescence include: high lysosomal activity through increased β -galactosidase (β -Gal) expression, high expression of p16, p21 and p53 and consequent cell cycle arrest and decreased proliferation, telomere shortening, generation of senescence associated heterochromatin foci (SAHF), increased ROS, reduced energy production, metabolic reprogramming, and the senescence associated secretory phenotype (SASP).

Several SIPS have been reported that differ based on the expression of specific senescence features, which include DNA damage, telomere attrition, cell cycle arrest, resistance to apoptosis, endoplasmic reticulum stress, increased lysosomal content of β -galactosidase (β -Gal), mitochondrial dysfunction, senescence-associated heterochromatin foci (SAHF), flattened morphology, larger cell surface, senescence-associated secretory phenotype (SASP), and metabolic reprogramming [17, 18] However, these features are facultative in the senescence phenotype and dependent on senescence-inducing stimuli and the cell type impacted.

Ionizing radiation (including X-rays) induce DNA damage and mutations directly by secondary electrons emission and/or indirectly by ROS formation [19], therefore resulting in DNA breaks (single or double stranded), DNA-protein crosslinks, oxidation of bases, and formation of abasic sites [20]. Hydroxyurea is an inhibitor of ribonucleotide reductase [21] by removing tyrosine free radicals that are required for the reduction of nucleoside diphosphates and DNA synthesis, consequently resulting in DNA single - strand breaks [22]. Etoposide is a chemotherapy agent that inhibits DNA topoisomerase II (TopII) therefore preventing the re-ligation of broken DNA strands [23].

The heterogeneity of the senescence phenotype and lack of sensitive selective markers of senescence pose a significant challenge for the identification of senescent cells in culture, tissues and *in vivo* [24]. Combining the measurement of multiple molecular biomarkers is the current strategy used for the identification of senescent cells.

Metabolomics is the comprehensive analysis of small molecule metabolites, which are downstream by-products of gene, RNA, and protein function [25]. Metabolomics can provide an integrated portrayal of biological pathways and how changes in biochemistry are associated with human disorders and disease. Considering that the application of metabolomics to ageing research

is relatively new, it is still lacking an exhaustive annotated metabolic dataset describing the complexity of senescence phenotypes.

Here we report the study of molecular and metabolic markers of different senescence phenotypes through measuring the expression of β -Gal, DNA damage foci, cell cycle activity, morphology, and global intracellular and extracellular metabolites to analyse changes in the phenotype of senescent cells in response to different methods of induction in normal human fibroblasts.

2.3. Materials

2.3.1. Cell line, chemical and treatment

All cell culture reagents were obtained from Gibco (Thermo Fisher Scientific). Human Foreskin Fibroblasts cell line (HFF-1, ATCC® SCRC-1041) was purchased and maintained in Dulbecco's Modified Eagle's Medium (DMEM, high glucose) supplemented with 10% v/v FBS (high glucose, Invitrogen), 1% v/v non-essential amino acids (NEAA), and 1% v/v penicillin-streptomycin (Invitrogen). Cells were maintained in a pre-humidified atmosphere containing 5% v/v CO₂ at 37°C.

Hydroxyurea (Sigma Fisher Scientific) was prepared as a 10 mM stock in water. Etoposide was prepared as a 1 mM stock solution in DMSO. All drug stocks were aliquoted and stored at -20°C until use.

Crystal violet (Sigma Fisher Scientific) stain was prepared with 20% methanol (Alfa Aesar by Fisher Scientific) and 2% sucrose (VWR Life science) and stored at ambient temperature. Primary antibodies for γ H2AX and Ki67 (Cell Signalling Technologies) were used for foci immunostaining alongside Alexa Fluor® 488-conjugated secondary antibody (Fisher Scientific).

Cells were passaged multiple times in culture (up to 20 passages) and were either treated with ascending doses of irradiation (1-12 Gy for 1 week), hydroxyurea (0-1,000 μ M for 2 weeks), or etoposide (0-50 μ M for 1 week) until markers of senescence appeared (growth arrest, increase in cell size, β -Gal expression).

2.4. Methods

2.4.1. Senescence associated β -galactosidase staining

Cells were seeded in a 96-well plate at a density of 4,000 per well and incubated for a pre-defined period for each specific treatment type. Following incubation, senescence associated β -Gal activity was assessed using a senescence detection kit (ab65351, Abcam) as per the manufacturer's recommendations. Subsequently cells were counterstained with DAPI to stain their nuclei. Image acquisition was carried out using an Invitrogen EVOS Auto Imaging System (AMAFD1000-Thermo Fisher Scientific) with a minimum of 100 cells imaged per treatment condition. β -Gal-stained cells were manually counted with ImageJ software. The number of β -Gal-stained cells was normalized with the number of counted nuclei.

2.4.2. Cell viability assay

The crystal violet assay was used to determine the viability of human fibroblasts following the induction of senescence. HFF-1 cells were plated in 96 well plates at 4,000 cells per well, treated and incubated for pre-defined times depending on the mechanism of senescence. Following treatment, the culture medium was removed, and the treated cells were washed once with PBS and stained with the crystal violet staining solution for 30 min at ambient temperature. Subsequently, the staining solution was removed, cells were gently rinsed with tap water and left to dry for 24 hours at ambient temperature. Subsequently, the stain was solubilized with 100% Ethanol and quantified at 600 nm using a GM3500 Glomax® Explorer Multimode Microplate Reader (Promega).

2.4.3. Immunostaining for γ H2AX and Ki67

Foci immunodetection for γ H2AX and Ki67 was performed in low and high passage cells seven days after seeding for non-irradiated cells and for cells irradiated at 12Gy for seven days, in non-treated and treated cells with hydroxyurea (800 μ M) and etoposide (10 μ M) for 14 and seven days, respectively. Briefly, cell monolayers were fixed in chilled 4% w/v

formaldehyde containing 2% w/v sucrose in PBS, followed by fixation in ice-cold methanol (100% v/v). Subsequently, cells were permeabilized in 0.25% v/v Triton X-100 in PBS, blocked with 5% v/v goat serum/5% w/v BSA, immunoprobed with either a primary rabbit anti- γ H2AX (1:1000) or primary mouse anti-Ki67 (1:1000) antibody overnight at 4°C. Cell monolayers were treated with goat, anti-rabbit and anti-mouse Alexa Fluor® 488 conjugated secondary antibody and counterstained with DAPI. Image acquisition was carried out using an Invitrogen EVOS Auto Imaging System (AMAFD1000-Thermo Fisher Scientific) with a minimum of 100 cells imaged per treatment condition. Resultant γ H2AX foci and Ki-67 labelled nuclei images were analysed in Cell Profiler (v.4.2.1.) using a modified version of the “speckle counting” and “percent positive” pipeline, respectively. Further thresholding setting for nuclei, γ H2AX foci and Ki-67 labelled nuclei are indicated in **Table 2. 1.**

Table 2. 1 Thresholding parameters applied in Cell Profiler for the detection of foci and labelled nuclei.

	DAPI	γH2AX	Ki-67
Diameter of objects (in pixel units)	Min: 8 Max:80	Min: 1 Max: 40	Min: 5 Max:200
Distinguish objects by	Shape	Intensity	Intensity
Thresholding method	Minimum Cross-Entropy	Minimum Cross-Entropy	Minimum Cross-Entropy
Lower and upper bounds on threshold	0.05, 1.00	0.00, 1.00	0.00, 1.00

2.4.4. Sample preparation and metabolite extraction

HFF-1 cells were seeded at a density of 2×10^6 cells per well in 6-well plates, at passage 20 and before exposure to either 12 Gy irradiation, or growth medium containing 800 μ M hydroxyurea or 10 μ M etoposide. Following senescence induction, the growth medium was aspirated from each well, centrifuged to remove cell debris, aliquoted and stored at -80°C. Next, treated cells were washed with pre-chilled PBS, with the metabolites quenched and extracted in a final volume of 1.5 ml pre-chilled (-80°C) methanol:acetonitrile:water solvent (50:30:20, v/v). Resultant cell pellets were

collected, and flash frozen in liquid nitrogen, vortexed and sonicated for three min in an ice-water bath. This process was performed in triplicate. Resultant extracts were centrifuged at 13,000 x g for 10 min at 4°C and the pellets retained for protein quantification using the Bradford assay (Pierce™ Coomassie Plus Bradford assay kit, Thermo Scientific™). The resultant supernatant was collected, and dried with a Speed vac centrifuge for 10 h (Savant-SPD121P). Dried metabolite pellets were subsequently reconstituted in acetonitrile:water (50:50, v/v) at volumes normalised to the relative protein content. Quality control (QC) samples were prepared by pooling samples across all control and treatment groups. Solvent blank (reconstitution buffer) and QC samples were inserted in the analytical batch (**Figure S1. 1**).

2.4.5. Liquid Chromatography Tandem Mass Spectrometry (LC-MS/MS)

Metabolite separation was performed on a binary Thermo Vanquish ultra-high-performance liquid chromatography system where 10 µl of the reconstituted cellular extract was injected onto a Thermo Accucore HILIC column (100 mm x 2.1 mm, particle size 2.6 µm). QC samples were injected after every five samples to assess the stability of the detecting system. The temperature of the column oven was maintained at 50°C while the autosampler temperature was set at 5°C. For chromatographic separation, a consistent flow rate of 500 µl/min was used where the mobile phase in positive and negative heated electrospray ionisation mode (HESI+/-) was composed of buffer A (100% acetonitrile with 0.1% formic acid) and buffer B (20 mM ammonium acetate in water with 0.1% formic acid). The elution gradient used for the chromatographic separation of metabolites is included in supplementary information (**Table S1. 1**).

A high-resolution Exploris 240-Orbitrap mass spectrometer (Thermo Fisher Scientific) was used to perform a full scan and fragmentation analyses. Global operating parameters were set as follows: spray voltages of 3900V in HESI +ve mode, and 2500V in HESI -ve mode. The temperature of the transfer tube was set at 320°C with a vaporiser temperature of 300°C. Sheath, aux gas and sheath gas flow rates were set at 40, 10 and 1 Arb, respectively. A top-5 Data-

dependent acquisition (DDA) was performed using the following parameter: survey scan range was 50-750 m/z with MS1 resolution of 60,000. Subsequent MS/MS scans were processed with a resolution of 15,000. High-purity nitrogen was used as nebulising and as the collision gas for higher energy collisional dissociation. Further details are included in the supplementary information (**Table S1. 2**).

2.4.6. Mass Spectrometry Data Processing

Raw data files obtained from Thermo Scientific Xcalibur TM software v4.2 were imported into Compound Discoverer™ 3.3 software where the “Untargeted Metabolomics with Statistics Detect Unknowns with ID Using Online Databases and mzLogic” feature was selected (all settings are provided in **Table S1. 2**). The workflow analysis performed retention time alignment, unknown compound detection, predicted elemental compositions for all compounds, hid chemical background (using Blank samples). For the detection of compounds, mass and retention time (RT) tolerance were set to 3 ppm and 0.3 min, respectively. The library search was conducted against the mzCloud, Human Metabolome Database (HMDB) and Chemical Entities of Biological Interest (ChEBI) database. A compound table was generated with a list of MSI2 level putative metabolites (known and unknown). Among them, we selected all the known compounds fully matching at least two of the annotation sources and with MS2 data (DDA for preferred ion). The selected metabolites were then used to perform pathway and statistical analysis.

2.4.7. Pathway Analysis with MetaboAnalyst

Prior to the analysis of the intracellular and extracellular metabolic pathways with MetaboAnalyst 5.0 (<http://www.metaboanalyst.ca/>), a HMDB identification code was assigned to each MSI2 annotated metabolite. For intracellular metabolites, pathway analysis was performed by mapping the significant altered metabolic features and their associated Log₂ Fold change values. The pathway analysis parameters included a scatter plot visualization method and enrichment analysis based on a hypergeometric test. The hypergeometric test

allows to define the significance of the association between two sets of data (genes and metabolites) [26]. Finally, important nodes (compounds) were scored based on their betweenness centrality, and pathway analysis results were generated. Homo sapiens (KEGG) metabolome was used as reference. For the extracellular metabolites Metabolite Set Enrichment Analysis (MSEA) was applied by uploading a list of ID metabolites entered as one-column data followed by a hypergeometric test to evaluate whether a particular metabolite set is represented more than expected by chance within the given compound list.

2.4.8. Statistical analysis

All data are presented as mean \pm standard deviation ($n \geq 5$). For metabolomics analysis, Principal Component Analysis (PCA) (score plot and loading plot) was performed to test the analytical reproducibility of QC injections, reduce the dimensionality of data, and visualise the presence of any clustering differences between sample groups. Differential analysis was used to compare differences between control and treatment groups and plotted as a Volcano plot (\log_2 -fold change vs. $-\log_{10}$ p-value). Peak areas were \log_{10} transformed. P values were calculated by two-tailed t-test in the pairwise analysis between control and treatment. A p value < 0.05 and a fold-change > 1.5 was deemed to be statistically significant.

2.5. Results

2.5.1. Induction of senescence in normal human fibroblasts

The initial focus of this work was to design and classify the biomolecular differences of functional models of replicative and stress-induced senescence. To achieve this, we passaged cells multiple times in culture and treated them with different doses of X-rays, hydroxyurea and etoposide as previously outlined (see methods). The state of senescence was optimised for each condition with a target cell viability of ~ 50% (**Figure S1. 2**), > 50% β -galactosidase (β -Gal) expression in sub-optimal conditions (pH<6) (**Figure S1. 3;Figure 2. 2**), and an increased surface area of treated cells compared to their relative controls (**Figure S1. 4**). The rationale behind this optimisation, was to ensure an adequate number of cells (biomass) for subsequent imaging and metabolomics experiments.

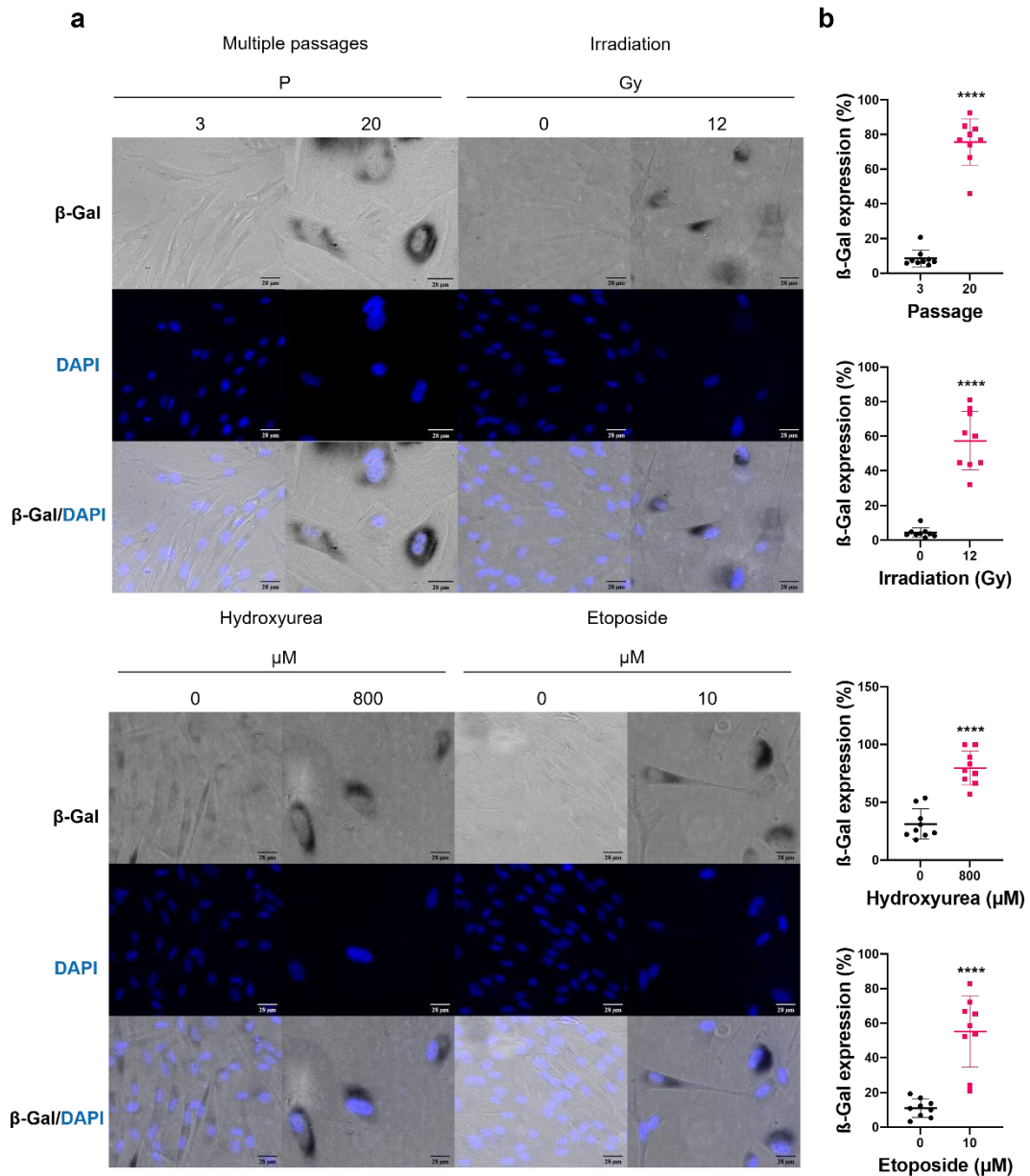


Figure 2. 2 β -Gal in senescence-induced HFF-1 cells. Representative phase contrast images of β -Gal staining (grey), DAPI (blue) and composite (β -Gal (grey) and DAPI (blue)) in cells at passage 20, 1 week post irradiation at 12 Gy, 800 μ M hydroxyurea for two weeks and 10 μ M etoposide for one week (a). Corresponding β -Gal levels expressed as a percentage of cell count relative to the number of nuclei counted using ImageJ (b). 9 repeats from 3 independent replicates with on average >50 cells per each sample. *p*-values have been determined through *t*-test and represented as ≤ 0.00005 =****.

Based on our results, senescence was induced across all the conditions examined at a late passage (P=20) and higher ionizing radiation dose and chemical treatment compared to control. We observed ~ 80% of cells were β -

Gal-positive after 20 passages and treatment with 800 μ M hydroxyurea, while cells treated with 12 Gy IR and 10 μ M etoposide resulted in >60% β -Gal-positive cells. Of notice, the control samples for each condition (passage 3, 0 Gy IR, and 0 μ M of hydroxyurea and etoposide) had a baseline percentage of β -Gal-positive cells which corresponds to <20% in the passaged, irradiated and etoposide-treated cells after a one week incubation, while ~30% in the hydroxyurea-treated cells following a two week incubation. These results show a baseline number of senescent cells exist under normal cell culture conditions and that β -Gal expression is influenced also by the experiment incubation time.

2.5.2. Senescence results in the formation of γ H2AX and Ki-67 foci

Senescent cells are characterised by accumulation of DNA damage and cell cycle arrest [27]. Therefore, we next analysed the extent to which late passages in culture (P=20), exposure to 12 Gy IR, 800 μ M hydroxyurea and 10 μ M etoposide promotes the accumulation of DNA double-strand breaks (DSBs) and cell cycle arrest. Phosphorylated histone H2 variant γ H2AX (γ H2AX) is a key marker of DNA DSBs [28], while Ki-67- a marker of cellular proliferation- is progressively expressed during the S phase of the cell cycle (replication phase) [29]. To measure the formation of DNA DSBs and cell cycle arrest in senescence-induced cells we performed γ H2AX (**Figure 2. 3**).

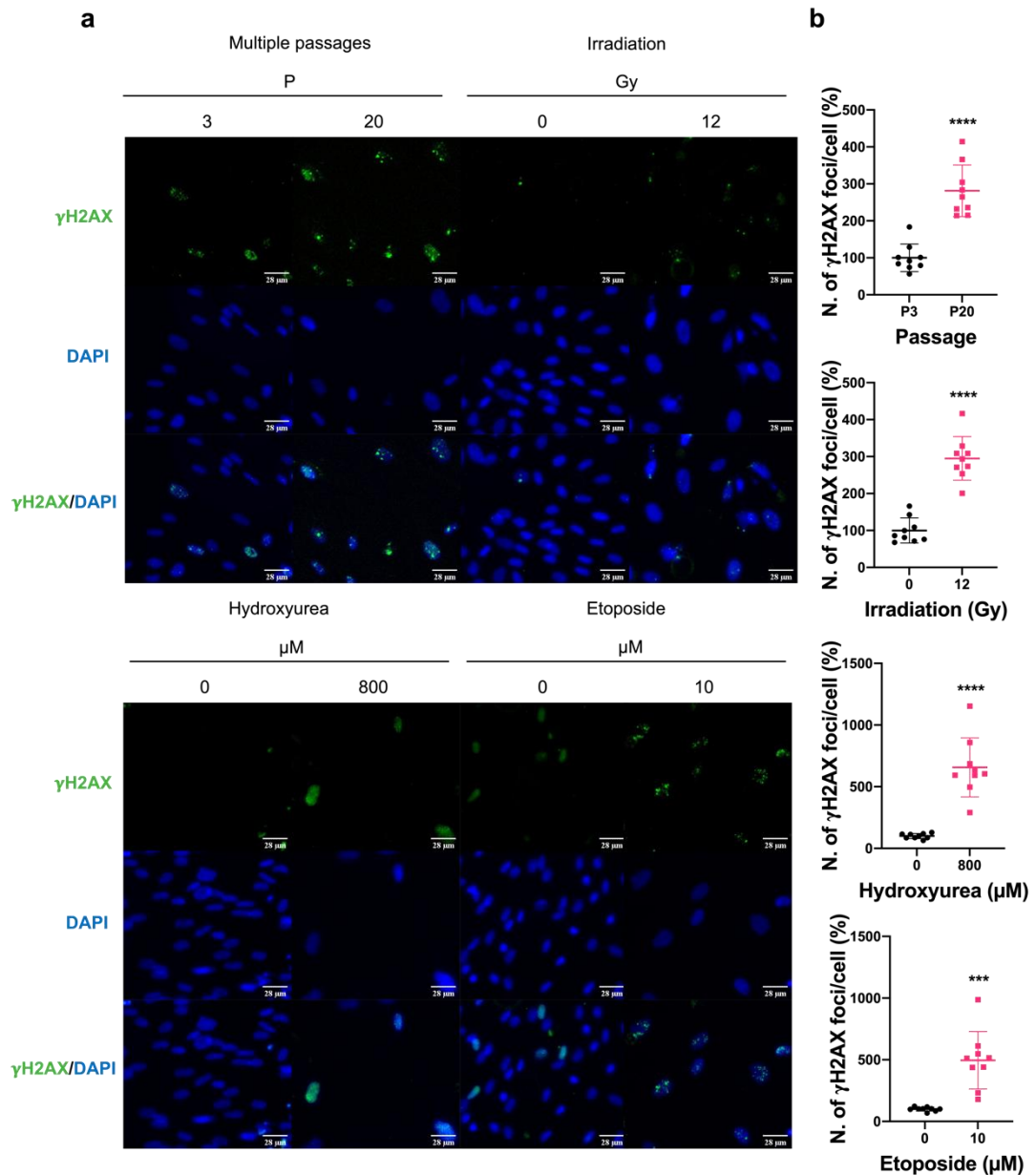


Figure 2. 3 γH2AX foci immunodetection in senescence-induced HFF-1 cells. Representative images of γH2AX immunostaining (green), DAPI (blue) and composite (γH2AX (green) and DAPI (blue)) in cells at passage 20, 12 Gy IR for 1 week, 800 μM hydroxyurea for two weeks and 10 μM etoposide for one week (a). Corresponding γH2AX foci count per cell as measured in Cell Profiler. 9 repeats from 3 independent replicates with on average >50 cells per each sample. Pairwise comparison was performed, and p-values have been determined using a t-test and represented as: 0.0005=***, ≤ 0.00005 =****.

Based on our results, γH2AX foci levels increased in HFF-1 cells at later passages (i.e., P=20) and following treatment with 12 Gy IR, 800 μM hydroxyurea and 10 μM etoposide (**Figure 2. 3a,b**). Next, cell cycle activity was analysed via Ki-67 immunocytochemistry (**Figure 2. 4**).

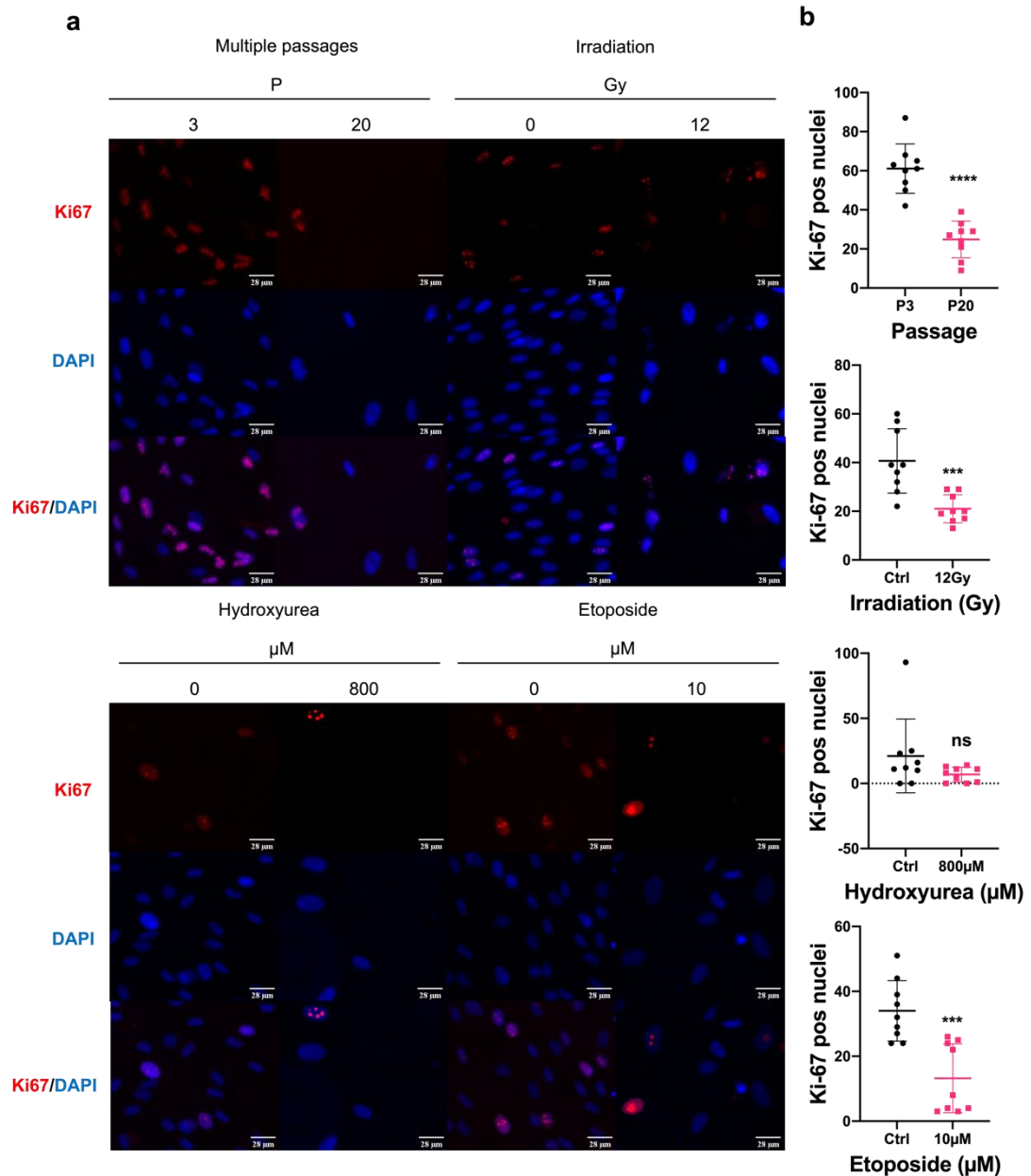


Figure 2. 4 Ki-67 positive nuclei immunodetection in senescence-induced normal human fibroblasts. Representative images of Ki-67 immunostaining (red), DAPI (blue) and composite (Ki-67 (red) and DAPI (blue)) in cells at passage 20, 12 Gy IR for one week, 800 μM hydroxyurea for two weeks and 10 μM etoposide for one week (a). Corresponding Ki-67 expression levels representative of positive nuclei count (b). 9 repeats from 3 independent replicates with on average >50 cells per each sample. *p*-values have been determined through *t*-test and represented as: 0.0005=***, ≤ 0.00005 =****, and non-significant=ns.

Regarding Ki-67 expression, we observed that the number of Ki-67-positive nuclei were reduced in all our samples with a significant reduction in the late passaged, irradiated and etoposide treated cells (**Figure 2. 4a,b**). An increase

of γ H2AX foci is consistent with the accumulation of DNA damage in senescence cells both in vitro and in vivo. Reduced levels of Ki-67 foci in the senescence-induced cells reflect their reduced proliferation.

2.5.3. Senescence-associated metabolic changes vary depending on the method of induction

To investigate the variation among different senescence models, their metabolic content was profiled using the untargeted liquid chromatography-mass spectrometry pipeline illustrated in **Figure S1. 5a**. Briefly, after data acquisition, data were processed and analysed in Compound Discoverer 3.3. Principal component analysis (PCA) was performed to reduce the global dataset of features from all the conditions, and to cluster and easily visualise the differences between the senescent models (**Figure S1. 5b**). Pairwise PCA analysis allowed to better discriminate the differences in the components between controls and treated samples (see score plot in **Figure 2. 5a**), and highlight the features mostly contributing to the separations between the two conditions (see loading plot in **Figure 2. 5b**). Differential analysis through volcano plot provided information on the differential number of significant metabolites altered (enriched or depleted) upon induction of senescence through multiple passages, ionizing radiation, and incubation with drugs (i.e., hydroxyurea, and etoposide) (**Figure 2. 5c**).

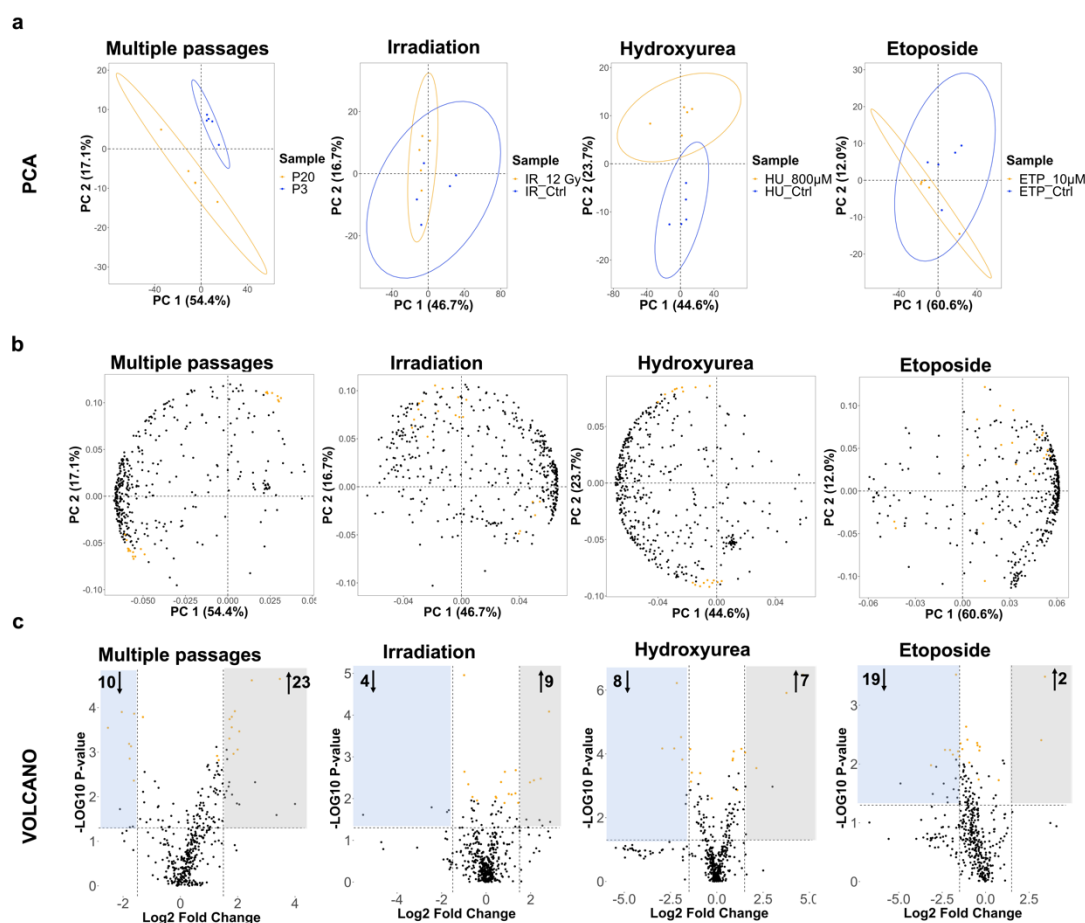


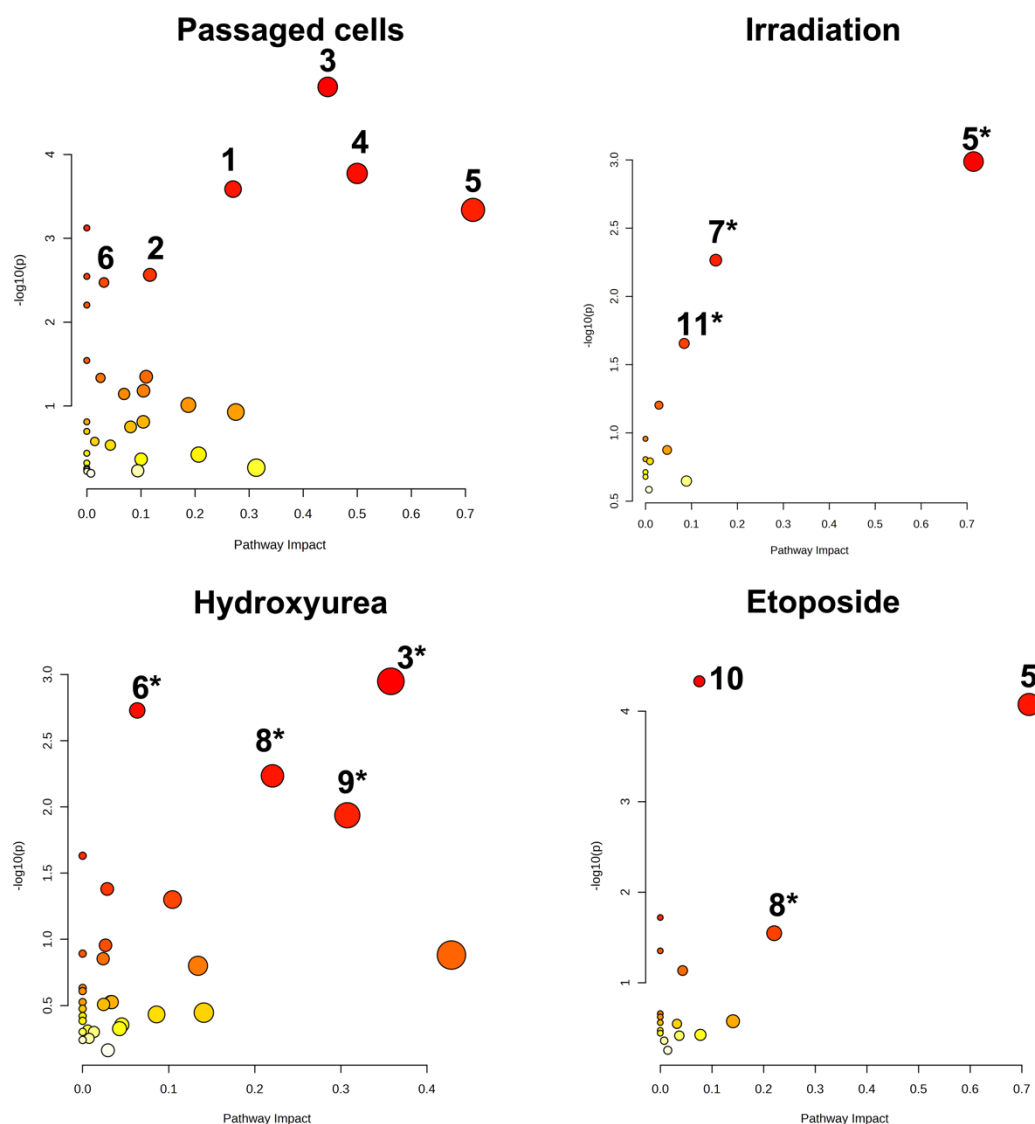
Figure 2. 5 Statistical analysis of the metabolic features identified in HFF-1 cells. Cells at passage 20, and following 12 Gy IR for one week, 800 μ M hydroxyurea for two weeks and 10 μ M etoposide for one week. A) PCA score plots and B) PCA loading plots for pairwise analysis of metabolites altered in the different senescence-induced cells. For each treatment group, five replicates were used. Data points in the two-dimensional PCA score plot were central scaled. C) volcano plots displaying enriched (gray) and depleted (blue) metabolic features by representing the log₂ fold change in altered features and the $-\log_{10}$ adjusted p-values (two-tailed t-test) with cut off values selected at >1.5 and <0.05 , respectively. The first 20 features mostly contributing to the separation between non-treated and treated samples correspond to the PLS-DA components (Figure S1. 6, and Table S1. 3), and have been highlighted in orange.

Pooled quality control (QC) data confirmed the stability of data acquisition across all the measurements performed in positive/negative switching mode (Figure S1. 5b). Feature separation was observed between treated samples and their controls (Figure 2. 5a,b). Volcano plots indicate the differential number of metabolic features that are significantly altered following senescence induction (Figure 2. 5c, Table S1. 3). From our results, we observed that in cells at late passage (p=20) and cells treated with irradiation (12 Gy), and hydroxyurea (800 μ M) most of the metabolic features were

enriched with respect to their relative control. Conversely, in the etoposide-treated cells (10 μ M) the number of depleted metabolic features was higher (n.=19) compared to the enriched features (n.=2) (**Figure 2. 5c**). Together, these findings show a differential metabolic response of normal human fibroblasts to different stress stimuli inducing different senescence phenotypes.

2.5.4. Altered amino acid, lipids and carbohydrate metabolism in different senescence-induced cells

To analyse the chemical and biomolecular changes in response to the induction of senescence, we used MetaboAnalyst to identify specific metabolic pathways altered at later passages in culture (P=20), following 12 Gy IR, and treatment with 800 μ M hydroxyurea and 10 μ M etoposide. Thus, we performed pathway analysis for all the conditions (**Figure 2. 6**). Among the pathways ranked in the top 10, we selected altered pathways with a corresponding pathway impact >0.1, and FDR p-value <0.05 (**Table S1. 4**). Mummichog software was also employed to putatively design metabolic pathways. Based on our results, only a few pathways matched the ones revealed from MetaboAnalyst. Considering that our data have a MSI2 level of metabolites annotation, while Mummichog is better suited for MSI level 3 putative IDs, we decided to continue the analysis using MetaboAnalyst.



- | | |
|------------------------------------------------|-------------------------------------------------|
| 1. Histidine metabolism | 6. Butanoate metabolism |
| 2. Arginine biosynthesis | 7. Starch and sucrose |
| 3. Alanine, aspartate and glutamate metabolism | 8. Pentose phosphate |
| 4. Glutamine metabolism | 9. Glutathione metabolism |
| 5. Taurine and hypotaurine metabolism | 10. Glycerophospholipid metabolism |
| | 11. Amino sugar and nucleotide sugar metabolism |

Figure 2. 6 Pathway enrichment analysis of HFF-1 cells. Cells at passage 20 in culture, following 12 Gy IR for one week, 800 μM hydroxyurea for two weeks and 10 μM etoposide for one week. Numbering for each metabolic pathway is kept consistent across the different plots. Pathway analysis was based on the hypergeometric test. Topological analysis was based on betweenness centrality. A $FDR\ p < 0.05$, and pathway impact > 0.1 were deemed significant. Asterisks (*) indicate non-significant pathways for $FDR > 0.05$, but Fisher's $p\text{-value} < 0.05$.

Across the senescence model examined, the top putative pathways significantly altered in MetaboAnalyst were based on amino acid, lipids and

carbohydrates metabolism for replicative senescence (histidine, arginine, alanine, aspartate, glutamate, glutamine, taurine and butanoate), irradiation-induced senescence (Taurine, starch, sucrose, amino and nucleotide sugars), hydroxyurea (alanine, butanoate, pentose phosphate and glutathione), and etoposide (taurine, glycerophospholipids and pentose phosphate). Following the identification of metabolic pathways altered upon senescence induction, we constructed a Venn diagram (**Figure S1. 7**) to outline common altered metabolic features.

Alteration in taurine metabolism is common to passaged cells and cells treated with irradiation and etoposide. Butanoate, alanine, aspartate and glutamate pathways are common to late passaged and hydroxyurea-treated cells. Changes in pentose phosphate metabolism are relevant for hydroxyurea and etoposide treated cells. Peculiar metabolic pathways were also identified for late passaged cells (glutamine, arginine and histidine), irradiated cells (starch, sucrose, amino and nucleotide sugar metabolism), hydroxyurea (glutathione) and etoposide treated cells (glycerophospholipids).

Next, we evaluated the relative changes in the levels of the individual metabolites that are representative of the altered metabolic pathways in the different senescence-induced models. The results were presented through a heatmap clustering analysis (**Figure 2. 7**). A wider list of compounds specific to each model of senescence is provided in **Table S1. 5**.

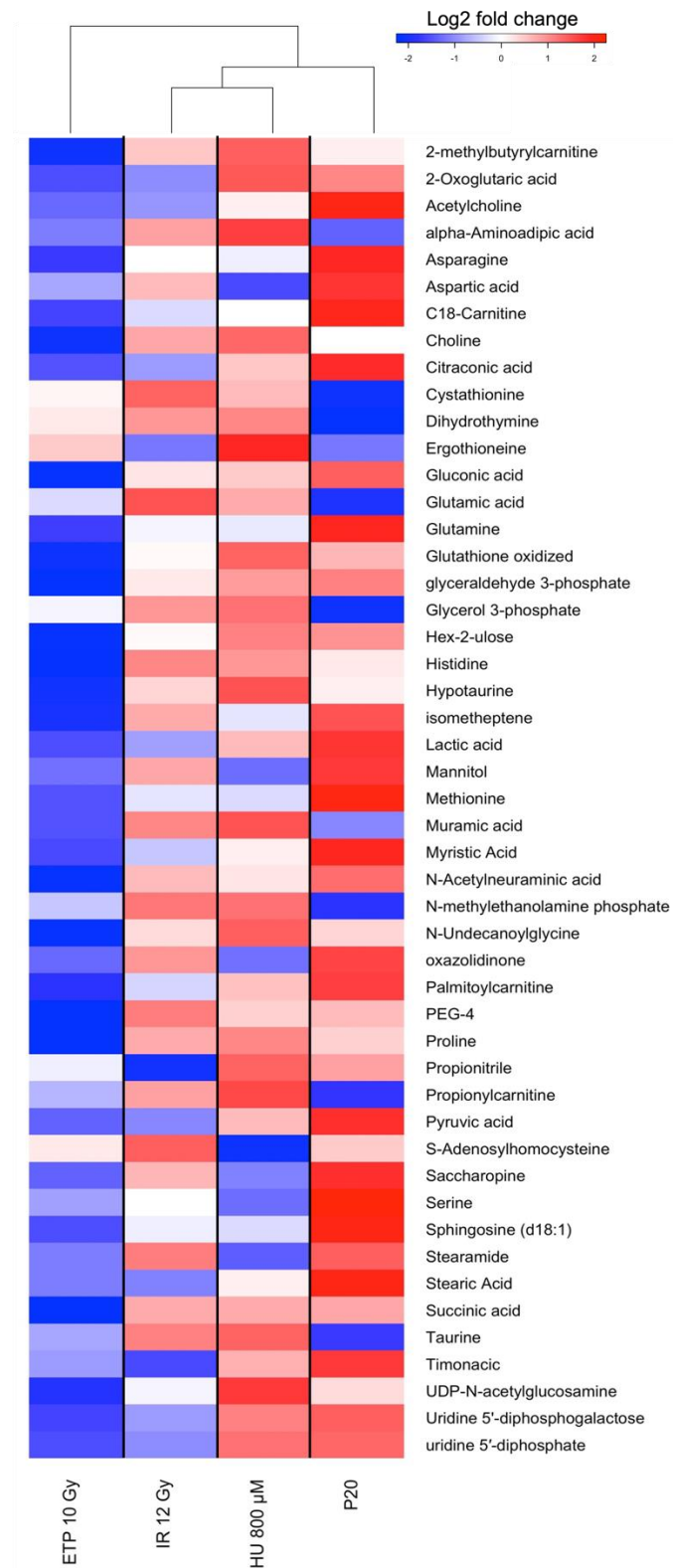


Figure 2. 7 Heatmap cluster analysis. Study of relevant metabolites associated with the pathways altered upon the induction of senescence through multiple passages (P=20), irradiation (12 Gy), hydroxyurea (800 μM) and etoposide (10 μM). Column dendrogram (Euclidean distance function) reflects the separation of the different senescent models.

Analysis of the heatmap cluster (**Figure 2. 7**) indicates significantly high levels of serine and hypoxanthine were detected in cells at late passage in culture and following treatment with 12 Gy IR. High levels of serine were detected also in the hydroxyurea and etoposide-treated cells although the enrichment was not significant relative to the control. Significant depletion of taurine and hypotaurine was a commonly observed feature of all the senescent cells in this study, accompanied by a high ratio of GSSG/GSH calculated for replicative senescent cells (0.64), hydroxyurea (1.34) and etoposide-treated cells (1.25). Enrichment of alpha-ketoglutarate (α -KG) was a common feature of late passaged cells and hydroxyurea treated cells. Enriched methionine was also a feature of cells treated with ionizing radiation. These features were depleted in cells treated with etoposide. Depletion of proline, glutamate and aspartate have been observed in all the senescence-induced cells although not at significant levels. Significantly depleted levels of acetylcholine have been shown in cells treated with irradiation and etoposide, except in cells at late passage and irradiated.

Taken together, these results highlight the prevalence of depleted metabolites upon treatment with etoposide compared to the passaged, irradiated and hydroxyurea-treated cells.

An overview of the metabolic features altered in response to senescence induction is provided in **Figure 2. 8**, where we mapped the differences in metabolite levels of the various senescence models using the Kyoto Encyclopaedia of Genes and Genomes (KEGG) database.

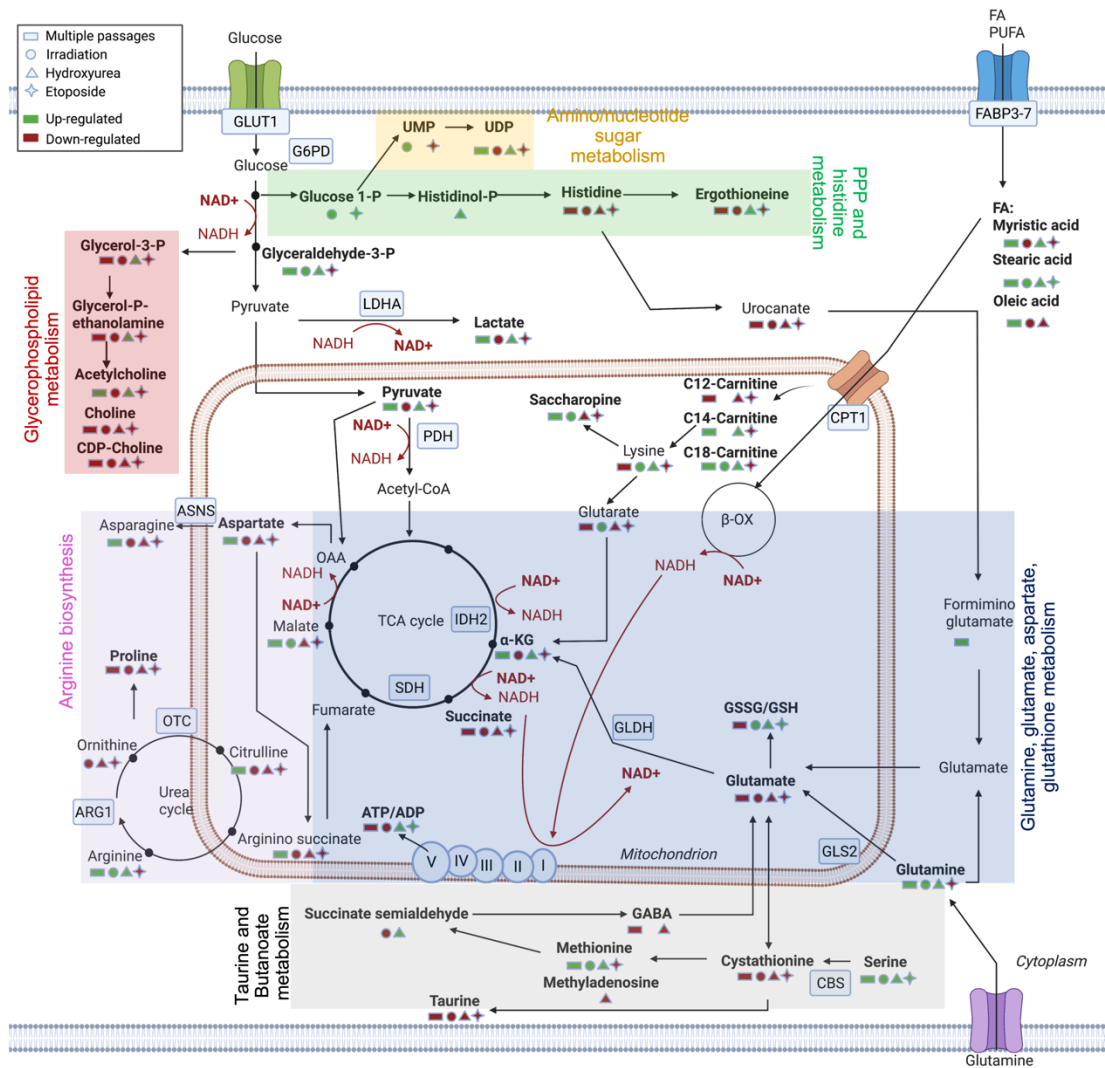


Figure 2. 8 Summary of putatively identified metabolic pathways altered upon induction of senescence. Enriched metabolic pathways are represented in the coloured boxes: Glycerophospholipids (red), Pentose phosphate pathway (PPP) and histidine (green), glutamine, glutamate aspartate and glutathione (blue), amino/nucleotide sugar (yellow), arginine biosynthesis (purple), and taurine, butanoate metabolism (grey).

The enzymatic genes associated with the metabolic reactions have been represented in the map, followed by network analysis with relevant senescence genes (**Figure S1. 8**). We distinguished among the metabolic changes occurring for each different senescence-induced phenotype. In the replicative senescence model we observed the enrichment of glutamine metabolism paralleled by enriched metabolites associated with TCA cycle (α -ketoglutarate) and urea cycle (arginine). In the senescence model induced

through irradiation, enriched glucose-1phosphate and uridine monophosphate was detected indicating a redirection of glucose metabolism towards the pentose phosphate pathway. Regarding hydroxyurea-induced senescence, we identified enhanced expression of methionine and succinate semialdehyde involved in glutathione metabolism. Common to all the senescence models was the high ratio of oxidised/reduced glutathione. Finally, in the etoposide-induced senescence phenotype, most of the metabolic pathways were depleted but we measured enrichment of serine and saturated fatty acids similarly to the other senescence phenotypes.

Overall, through the joint metabolic study of the different senescence-induced models we computed similarities and differences in their intracellular metabolic response to different stress stimuli.

2.5.5. Detection of extracellular inflammatory metabolites in different senescence-induced phenotypes

To analyse the extracellular composition of metabolites, we next applied the metabolomics pipeline to the study of growth media collected from all the senescence-induced cells of this study. We used PCA analysis and volcano plots to examine the differences between growth media aspirated from senescence-induced cells and their relative controls (**Figure 2. 9**).

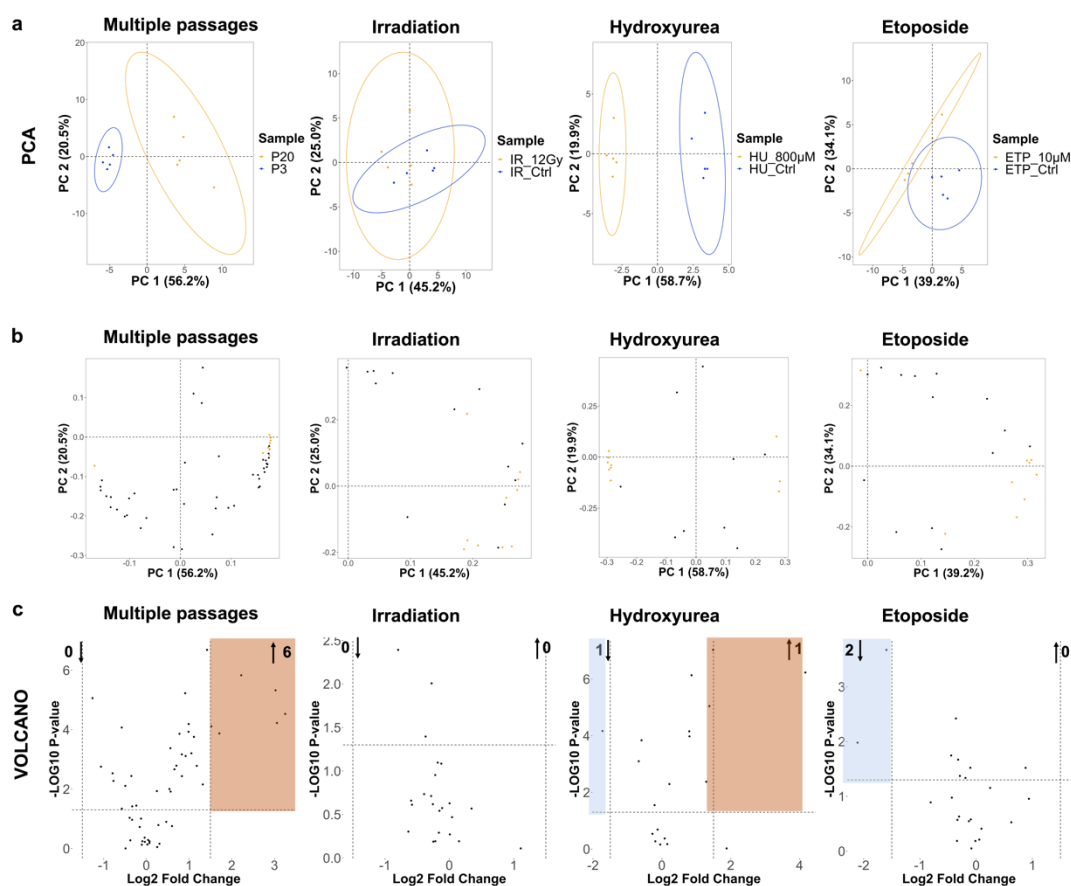


Figure 2. 9 Statistical analysis of the metabolic features identified in the growth media of HFF-1 cells. Cells at passage 20, and following 12 Gy IR for one week, 800 µM hydroxyurea for two weeks and 10 µM etoposide for one week. A) PCA score plots and B) PCA loading plots for pairwise analysis of metabolites altered in the different senescence-induced cells. For each treatment group, five replicates were used. Data points in the two-dimensional PCA score plot were central scaled. C) volcano plots displaying enriched (brown) and depleted (blue) metabolic features by representing the log₂ fold change in altered features and the -log₁₀ adjusted p-values (two-tailed t-test) with cut off values selected at >1.5 and <0.05, respectively. The first 10 features mostly contributing to the separation between non-treated and treated samples correspond to the PLS-DA components (Figure S1. 10 and Table S1. 6), and have been highlighted in orange.

LC-MS stability was confirmed by the analysis of QC samples (Figure S1. 9). Grouping of different features was observed across all the conditions (Figure 2. 9a,b). Using volcano plots we analysed the differential expression between the metabolites significantly altered in the senescence-induced cells (enrichment and depletion) relative to their controls (Figure 2. 9c). Next, we performed enrichment analysis through MetaboAnalyst with the global list of metabolites and ranked them based on their class (Table S1. 7).

Through a Venn diagram we presented the differences between the enriched metabolites within the growth media and cells of the late passaged cells and those treated with IR, hydroxyurea and etoposide (**Figure 2. 10**).

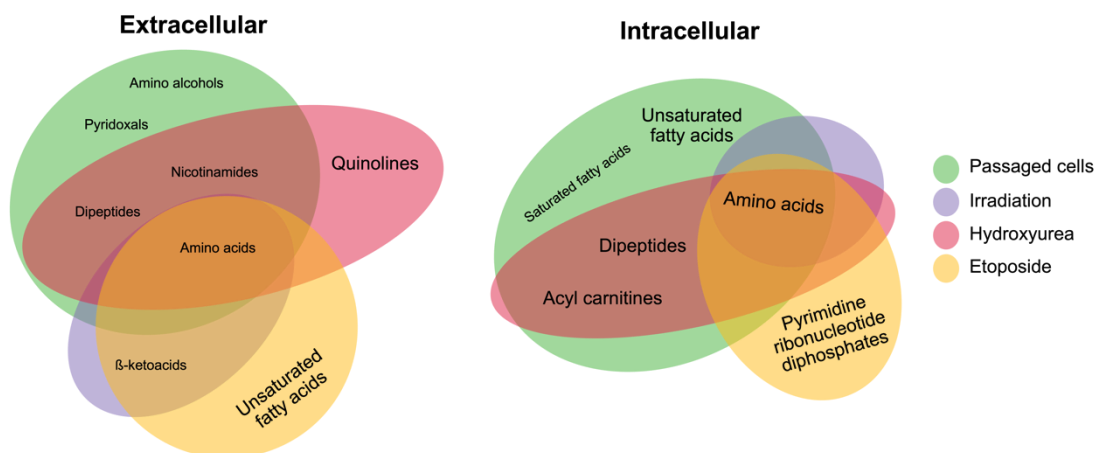


Figure 2. 10 Venn diagram. The diagram represents the enriched class of extracellular and intracellular metabolites in late passaged, irradiated, hydroxyurea and etoposide treated cells. Data have been processed in MetaboAnalyst 5.0.

From analysis of metabolic features altered in the growth media of senescence-induced models (passage, IR and chemically-induced) we observed that amino acids represented the most commonly enriched class of metabolite across the senescence-induced models. Amino alcohols and pyridoxals were mostly enriched in the replicative senescence model (high passage). β -ketoacids were enriched in irradiated samples, and cells treated with etoposide. In the hydroxyurea-treated cells, we detected an enrichment of quinolines. Of notice, in the media of the late passaged cells we detected significant high levels of prostaglandin E1, in the irradiated cells we observed enrichment of phenylalanine while in the hydroxyurea treated cells we detected depleted levels of threonine-phenylalanine, although not at significant levels (**Table S1. 7**).

Regarding the intracellularly detected metabolites, among the different senescence-induced models we identified common classes of amino acids. Unsaturated and saturated fatty acids were representative of cells at late passage ($P=20$). Acyl carnitines and dipeptides were also measures in the hydroxyurea-treated cells. While pyrimidine ribonucleotides diphosphates were representative of cells treated with etoposide.

2.6. Discussion

Identifying senescent cells for the treatment of age-related disease is a primary unresolved challenge in ageing research. Thus, the development of cell models to understand senescent phenotypes with the aim of developing biomarkers is of huge importance. Heterogeneity of the senescence phenotype represents a significant barrier to studying the mechanisms underpinning the phenotypes of ageing, the consequences of which include the lack of a universal model of senescence and a universal marker for the identification of senescent cells [30].

In this study we generated different models of senescence based on replication stress (replicative senescence), genotoxic and oxidative stress (stress-induced senescence) stimuli. The rationale behind the selection of these models was to explore how different stress stimuli influence the development of senescence through the accumulation of various biomolecular and metabolic alterations.

High β -Gal expression, reduced proliferation, cell enlargement and flattening are primary characteristics of senescent cells. Initially we evaluated the presence of those phenotypic markers in cells at multiple passages and treated them with multiple dosages of irradiation, hydroxyurea or etoposide (**Figure 2. 2, Figure 2. 3, Figure 2. 4**). From our results, cells at a late passage (P = 20) showed a higher level of β -Gal expression, in line with other studies [8]. Ionizing radiation (IR)-induced senescence has been extensively studied showing induction by exposure to moderate IR doses [31]. Our study further confirms this evidence of senescence induction at 12 Gy irradiation. Hydroxyurea induced senescence-like changes in normal human fibroblasts after long-term treatment with higher drug concentrations (400-800 μ M) [32]. Conversely, etoposide is known to induce senescence at a low dosage (<50 μ M) [33]. Accordingly, our results showed a global increase of β -Gal expression at 800 μ M of hydroxyurea and 10 μ M of etoposide. At the morphological level, senescent cells present a characteristic enlarged and flattened morphology [34]. According to this, the human fibroblasts of this study

at late passage (p=20), and at dosage of 12 Gy irradiation, 800 μ M hydroxyurea and 10 μ M etoposide, increased their length and width compared to the early passaged cells and cells treated at lower radiation and chemical dosage (**Figure S1. 4**). Of notice, in the chemical treated cells higher concentrations of hydroxyurea (1000 μ M) and etoposide (25-50 μ M) resulted in reduction of the cell size (width and length) which might be associated with the treatment toxicity and the induction of programmed cell death or apoptosis. Shrinkage of the cell is indeed a hallmark of apoptosis [35], however, specific molecular markers are needed to verify this assumption.

From analysis of γ H2AX foci DSB immunolabelled foci (**Figure 2. 3**), higher DNA damage foci were observed in drug-treated cells (hydroxyurea and etoposide) compared to cells undergoing replication-induced senescence and treatment with IR. While the analysis of the Ki-67 replication marker showed a significant reduction of Ki-67-positive cells in the late passaged and etoposide treated cells (**Figure 2. 4**). This reduction was not significant in cells exposed to IR or absent in hydroxyurea-treated cells. Based on these results we observed that accumulation of DNA damage and reduction of proliferation index are common traits of the stress-induced phenotypes of this study, therefore confirming their effective senescence-like phenotype.

Genetic and molecular biomarkers – including proteins – have been extensively used for the identification of senescent cells both in vitro and in vivo. They have been useful in underlying key biological features of senescence and identifying its major drivers during natural ageing and in age-related diseases. However, genetic and molecular biomarkers are generally nonspecific and non-reproducible across all cell/tissue types [36]. These limitations represent an obstacle for the effective detection of senescence and a proper understanding of its mechanisms and role in living organisms.

Metabolic reprogramming is another hallmark of senescent cells and adaptive response to maintain their viability in a growth-arrested state [17]. Metabolic changes are highly susceptible to the type of stress stimuli, contributing to the

heterogeneity of the senescence phenotypes. On this basis, metabolomics has recently emerged in ageing research as a fundamental tool to depict the complexity of senescence, ageing, and the correlation with the accumulation of damages [37].

Our goal in the present study was to apply a combined analysis of senescence molecular biomarkers with global untargeted mass-spectrometry-based metabolomics to map the metabolic changes occurring in response to different senescence-inducing stimuli. We examined the metabolic differences across the different models of senescence including replicative senescence and SIPS. A general enrichment of intracellular metabolites was computed for the senescence model induced by replication, irradiation and hydroxyurea stress, while depletion of metabolites was observed upon etoposide treatment (**Figure 2. 5**). We found overlapping intracellular metabolic pathways (taurine, alanine, glutamate, aspartate and butanoate) across the four senescent models (**Figure 2. 6**). We then investigated intracellular metabolic pathways that were unique to specific senescence phenotypes (late passage: glutamine, arginine and histidine; irradiation: sucrose, amino and nucleotide sugars; hydroxyurea: glutathione; etoposide: glycerophospholipids) (**Figure 2. 6**).

Regarding the extracellular metabolome, we detected a general trend towards the enrichment of metabolites in all the senescence-induced models (**Figure 2. 9**). The analysis of the class of metabolites that were mainly affected by metabolic changes upon induction of senescence, revealed that amino acids were the most susceptible to these changes both in the intracellular and extracellular metabolome of all the senescence-induced cells (**Figure 2. 10**).

Below, we will discuss the level of the most relevant metabolic changes affecting amino acids and some of the derived metabolic pathways (**Figure 2. 8**), and the role they might play in the context of senescence associated pathogenesis.

Regarding histidine metabolism we found this to be representative of the replicative senescence phenotype. From the analysis of intracellular

metabolites in cells at late passage (P20) we observed a significant increase of the histidine-derived catabolic product, 1-methylhistidine, indicative of enhanced proteolysis of histidine which is a marker of frailty [38]. Depletion of ergothioneine, another histidine-derived metabolite, was observed in late passaged cells and cells treated with 12 Gy irradiation and 10 μ M etoposide. Ergothioneine is a powerful scavenger of hydroxyl radicals, thus it plays an important role against oxidative damage [39]. Low levels of ergothioneine have been found in patients with Parkinson's disease [40] and the elderly [41].

Accumulation of the alanine derivate phenylalanine was observed in the replicative senescence model in line with the study of James EL., et al 2015 [42]. However, in the cells exposed to IR and chemical-treated cells phenylalanine was depleted, which might be attributed to its higher consumption or secretion. Elevated serum phenylalanine has been linked to telomere loss in men [43], inflammatory diseases [44], and type 2 diabetes [45]. Of notice, phenylalanine is a precursor for the synthesis of catecholamines including tyramine, dopamine, epinephrine and norepinephrine. High levels of phenylalanine were observed specifically in the media of hydroxyurea cells. Catecholamines are hormones involved in the immune response [46] with roles in cellular proliferation and apoptosis [47]. Catecholamines act as anti-inflammatory molecules decreasing the levels of $\text{TNF}\alpha$, CCL2, IL-6 and $\text{IFN}\alpha$ [48]. Considering that, based on our findings, alanine metabolism is relevant for late passaged and hydroxyurea treated cells, this is suggesting that for these phenotypes, alanine metabolism might play a role in the pro-inflammatory mechanisms associated with senescence.

In agreement with previous studies we observed increased arginine biosynthesis through the urea cycle across all senescence conditions, except for etoposide-treated cells [42]. Changes in arginine biosynthesis were found to be relevant specifically for the replicative senescence model where metabolites responsible for the synthesis of arginine through the urea cycle were observed to be enriched. They include aspartate, arginine-succinate and citrulline. Relatively recently, prolonged exposure of endothelial cells to

arginine has been observed to induce senescence and the increased production of pro-inflammatory prostaglandins [49]. This might provide a possible explanation to the high levels of prostaglandin E1 detected in the late passaged cells, however further investigation and verification are required to validate our findings.

Increased glutaminolysis due to overexpression of GLS1 in senescent cells has been observed in previous studies [50]. High levels of glutamine were observed at later passages, together with decreased levels of glutamate, high levels of α -KG, malate and aspartate which are intermediate of the TCA cycle. This suggests a role of glutamine in sustaining the TCA cycle activity in replicative senescent cells.

Previous work has found that ATP is generally depleted in senescent cells [42]. In line with these findings, we found that the ratio ATP/ADP was decreased in cells at late passage and after irradiation, while it was increased upon chemical treatment with hydroxyurea and etoposide. With regard to energy metabolism, it is well known that in senescent cells aerobic glycolysis is the preferential route for glucose catabolism leading to the production of lactic acid [51]. In this study, high levels of lactic acid were observed for late passaged and hydroxyurea treated cells, but not upon irradiation and treatment with etoposide. Based on the enrichment pathway analysis of this study, in irradiated cells it was relevant the redirection of glucose metabolism towards the pentose phosphate pathway (PPP) for the synthesis of nucleotides. While in the etoposide-treated cells relevant changes were detected in the synthesis of glycerophospholipids whose levels were generally depleted. The PPP is an important route in cells supporting the regeneration of NADPH, regulation of redox homeostasis and biosynthesis [52]. Despite the PPP pathway has been poorly investigated relative to senescence, here we show that it might have a role in defining specific senescence phenotypes. In general, further analyses are needed to investigate the mechanisms of energy metabolism in senescence-induced HFF-1 cells also in comparison with other cell lines.

Elevated levels of serine were observed in all the senescent phenotypes induced in the present work paralleled by the depletion of serine-derived cystathionine and taurine which is a product of cysteine metabolism [53]. Several studies associated reduced levels of taurine to senescence [54] and age-related diseases [55, 56] where taurine plays as an antioxidant and inhibitor of pro-inflammatory molecules [57]. Methionine, a product of cystathionine catabolism, have been seen to accumulate in cells at late passage and treated with irradiation and hydroxyurea. Numerous studies on methionine restriction (MetR) in diet have revealed that methionine regulates the ageing process partially through the induction of oxidative stress via regulation of glutathione synthesis and production of hydrogen sulphide (H₂S) [58]. This seems to be the case of hydroxyurea treated cells showing increased levels of oxidised glutathione (GSSG) accompanied by relevant changes in glutathione metabolism as revealed by the pathway analysis.

A targeted metabolomics analysis of these senescence-induced phenotypes is required to validate our findings. This could allow the further validation and development of metabolic markers of senescence, informing future studies into the mechanism underpinning senescence induction in response to different stimuli. In medicine, the identification of new and specific biomarkers of senescence will be beneficial in the measurement of senescence burden within an individual to prevent age-related dysfunction and diseases, and predict response to treatment/surgery. Encouraging studies and clinical trials are showing the therapeutic effects of the pharmacological elimination of senescent cells through compounds called senolytics (inducers of senescent cell death) and senomorphics (SASP inhibitors) [59]. Hence, biomarkers of senescence will also help to assess the dosing of senolytic/senomorphics drugs in the clinical assessment of senescence burden specific for each individual. Moreover, a limitation of the present work was analysis of senescence induction in a single cell type. Future studies require the assessment of cellular response to senescence induction in a panel of cell lines for a more comprehensive analysis of various senescence phenotypes and their manifestation in cell lines originating from different tissue types. Understanding

the mechanisms of senescence induction in different tissue types will Aid in cataloguing the specific intra- and extracellular features associated with cellular senescence.

2.7. Conclusion

Our results have shown intra- and extracellular metabolomics profiles of different models of senescence including replicative and stress-induced senescence through DNA damage and ROS induction. We presented metabolomics as a powerful strategy for the identification of human cellular senescence biomarkers which characterise a wide variety of human pathologies including ageing, frailty, inflammation, cardiovascular, neurodegenerative diseases, and cancer. Moreover, these findings may provide potential therapeutic targets for preventing the development of age-related diseases, or as adjuvant therapies to improve patients' response to treatments.

2.8. References

1. WHO. *Ageing and health*. 2021; Available from: <https://www.who.int/news-room/fact-sheets/detail/ageing-and-health>.
2. Magalhaes JP., et al., *The business of anti-aging science*. Cell, 2017. **35**(11): p. 1062-1073.
3. Kirkwood, T., et al., *Understanding the odd science of aging*. Cell, 2005. **120**(4): p. 437-447.
4. Amadou, A., et al., *Prevalent diabetes and risk of total, colorectal, prostate and breast cancers in an ageing population: meta-analysis of individual participant data from cohorts of the CHANCES consortium*. Nature, 2021. **124**: p. 1882-1890.
5. Pavelka, L., et al., *Age at onset as stratifier in idiopathic Parkinson's disease – effect of ageing and polygenic risk score on clinical phenotypes*. Nature, 2022. **8**(102).
6. Ferrucci, L., et al., *Inflammageing: chronic inflammation in ageing, cardiovascular disease, and frailty*. Nature, 2018. **15**: p. 505-522.
7. Di Micco, R., et al., *Cellular senescence in ageing: from mechanisms to therapeutic opportunities*. Nature, 2020. **22**(75-95).
8. Dimri GP., et al., *A biomarker that identifies senescent human cells in culture and in aging skin in vivo*. Proceedings of the National Academy of Sciences of the United States of America, 1995. **92**(20): p. 9363-9367.
9. Lòpez-Otin, C., et al., *The Hallmarks of Aging*. Cell, 2013. **153**(6): p. 1194-1217.
10. Van Deursen, J., *The role of senescent cells in ageing*. Nature, 2014. **509**(7501): p. 439-446.
11. Kumari, R., et al., *Mechanisms of Cellular Senescence: Cell Cycle Arrest and Senescence Associated Secretory Phenotype*. Frontiers in Cell and Developmental Biology 2021. **9**(645593).
12. Childs, B., et al., *Senescent cells: an emerging target for diseases of ageing*. Nature, 2017. **16**: p. 718-735.
13. Harley CB., et al., *Telomeres shorten during ageing of human fibroblasts*. Nature, 1990. **345**: p. 458-460.
14. Allsopp, R., *Models of initiation of replicative senescence by loss of telomeric DNA*. Experimental Gerontology., 1996. **31**(1-2): p. 235-243.
15. Toussaint, O., et al., *Cellular and molecular mechanisms of stress-induced premature senescence (SIPS) of human diploid fibroblasts and melanocytes*. Experimental Gerontology, 2000. **35**(8): p. 927-945.
16. Toussaint, O., et al., *Stress-induced premature senescence and tissue ageing*. Biochemical Pharmacology , 2002. **64**(5-6): p. 1007-1009.
17. Hernandez-Segura, A., et al., *Hallmarks of cellular senescence*. Trends in Cell Biology, 2018. **28**(6): p. 436-453.
18. Petrova, N., et al., *Small molecule compounds that induce cellular senescence*. Aging Cell, 2016. **15**(6): p. 999-1017.
19. Azzam, E., et al., *Ionizing radiation-induced metabolic oxidative stress and prolonged cell injury*. Cancer Letter, 2012. **327**(0): p. 48-60.
20. Reisz, J., et al., *Effects of Ionizing Radiation on Biological Molecules—Mechanisms of Damage and Emerging Methods of Detection*. Antioxidants & Redox Signaling, 2014. **21**(2): p. 260-292.
21. Krakoff, I., *Clinical and pharmacologic effects of hydroxyurea*, in *Antineoplastic and Immunosuppressive Agents. Handbuch der experimentellen Pharmakologie / Handbook of Experimental Pharmacology*. 1975.
22. Singh, A., et al., *The Cell Killing Mechanisms of Hydroxyurea*. Genes (Basel), 2016. **7**(11): p. 99.
23. Yang, J., et al., *Etoposide pathway*. Pharmacogenet Genomics, 2009. **19**(7): p. 552-553.
24. Sharpless, N., et al., *Forging a signature of in vivo senescence*. Nature, 2015. **15**: p. 397-408.
25. Gilson Costa dos Santos, J., et al., *The remodel of the “central dogma”: a metabolomics interaction perspective*. Metabolomics, 2021. **15**(5): p. 48.
26. Ramell, A., et al., *Evaluation and comparison of bioinformatic tools for the enrichment analysis of metabolomics data*. BMC Bioinformatics, 2018. **19**(1).

27. d'Adda di Fagagna, F., et al., *A DNA damage checkpoint response in telomere-initiated senescence*. *Nature*, 2003. **426**(6963): p. 194-198.
28. Mah, L., et al., *gammaH2AX: a sensitive molecular marker of DNA damage and repair*. *Leukemia*, 2010. **24**(4): p. 679-686.
29. Sun, X., et al., *Ki-67: more than a proliferation marker*. *Chromosoma*, 2018. **127**(2): p. 175-186.
30. Kudlova, N., et al., *Cellular Senescence: Molecular Targets, Biomarkers, and Senolytic Drugs*. *International Journal of Molecular Sciences*, 2022. **23**(4168).
31. Yamamori, T., et al., *Ionizing radiation induces mitochondrial reactive oxygen species production accompanied by upregulation of mitochondrial electron transport chain function and mitochondrial content under control of the cell cycle checkpoint*. *Free Radical Biology and Medicine*, 2012. **53**(2): p. 260-270.
32. Yeo, E., et al., *Senescence-like changes induced by hydroxyurea in human diploid fibroblasts*. *Experimental Gerontology*, 2000. **35**(5): p. 553-571.
33. Nagano, T., et al., *Identification of cellular senescence-specific genes by comparative transcriptomics*. *Scientific Reports*, 2016. **6**(31758).
34. González-Gualda, E., et al., *A guide to assessing cellular senescence in vitro and in vivo*. *The FEBS Journal*, 2020. **288**(1): p. 56-80.
35. Saraste, A., et al., *Morphologic and biochemical hallmarks of apoptosis*. *Cardiovascular Research*, 2000. **45**(3): p. 528-537.
36. Tuttle, C., et al., *Cellular senescence and chronological age in various human tissues: A systematic review and meta-analysis*. *Aging Cell*, 2019. **19**(2): p. e13083.
37. Wiley, C., et al., *The metabolic roots of senescence: mechanisms and opportunities for intervention*. *Nature*, 2021. **3**: p. 1290-1301.
38. Calvani, R., et al., *Identification of a Circulating Amino Acid Signature in Frail Older Persons with Type 2 Diabetes Mellitus: Results from the Metabofrail Study*. *Nutrients*, 2020. **12**(1): p. 199.
39. Cheah, I., et al., *Ergothioneine; antioxidant potential, physiological function and role in disease*. *Biochimica et Biophysica Acta*, 2012. **1822**(5): p. 784-793.
40. Hatano, T., et al., *Identification of novel biomarkers for Parkinson's disease by metabolomic technologies*. *Journal of Neurology, Neurosurgery and Psychiatry*, 2016. **87**(3): p. 295-301.
41. Sotgia, S., et al., *Clinical and Biochemical Correlates of Serum L-Ergothioneine Concentrations in Community-Dwelling Middle-Aged and Older Adults*. *PlosOne*, 2014. **9**(1): p. e84918.
42. Emma L.J., et al., *Senescent Human Fibroblasts Show Increased Glycolysis and Redox Homeostasis with Extracellular Metabolomes That Overlap with Those of Irreparable DNA Damage, Aging, and Disease*. *Journal of Proteome Research*, 2015. **14**(4): p. 1854-1871.
43. Eriksson, J., et al., *Higher serum phenylalanine concentration is associated with more rapid telomere shortening in men*. *The american journal of clinical nutrition*, 2016. **105**(1): p. 144-150.
44. Neurauter, G., et al., *Chronic Immune Stimulation Correlates with Reduced Phenylalanine Turnover*. *Current Drug Metabolism*, 2008. **9**(7): p. 622-627.
45. Guash-Ferrè, M., et al., *Metabolomics in Prediabetes and Diabetes: A Systematic Review and Meta-analysis*. *Diabetes Care*, 2016. **39**(5): p. 833-846.
46. Brown, S., et al., *Catecholamines in a macrophage cell line*. *Journal of Neuroimmunology*, 2003. **135**(1-2): p. 47-55.
47. Offen, D., et al., *Dopamine-induced programmed cell death in mouse thymocytes*. *Biochimica et Biophysica Acta*, 1995. **1268**(2): p. 171-177.
48. Torress-Rosas, R., et al., *Dopamine mediates vagal modulation of the immune system by electroacupuncture*. *Nature Medicine*, 2014. **20**(3): p. 291-295.
49. Scalera F., et al., *Paradoxical effect of L-arginine: Acceleration of endothelial cell senescence*. *Biochemical and Biophysical Research Communications*, 2009. **386**(4): p. 650-655.
50. Johmura, Y., et al., *Senolysis by glutaminolysis inhibition ameliorates various age-associated disorders*. *Science*, 2021. **371**(6526): p. 265-270.
51. Wiley, C., et al., *From Ancient Pathways to Aging Cells— Connecting Metabolism and Cellular Senescence*. *Cell Metabolism*, 2016. **23**(6): p. 1013-1021.

52. Chen L., et al., *NADPH production by the oxidative pentose-phosphate pathway supports folate metabolism*. *Nature metabolism*, 2019. **1**: p. 404-415.
53. Brand, A., et al., *Metabolism of Cysteine in Astroglial Cells: Synthesis of Hypotaurine and Taurine*. *Journal of Neurochemistry*, 2002. **71**(2): p. 827-832.
54. Ito, T., et al., *Tissue Depletion of Taurine Accelerates Skeletal Muscle Senescence and Leads to Early Death in Mice*. *PLoS One*, 2014. **9**(9): p. e107409.
55. Shen, D., et al., *ADO/hypotaurine: a novel metabolic pathway contributing to glioblastoma development*. *Nature*, 2021. **7**(21).
56. Idrissi, A., et al., *Functional implication of taurine in aging*. *Advances in Experimental Medicine and Biology*, 2009. **643**(7): p. 199-206.
57. Schuller-Levis, G., et al., *Taurine: new implications for an old amino acid*. *FEMS Microbiology Letters*, 2003. **226**(2): p. 195-202.
58. Wang, S., et al., *Methionine restriction delays senescence and suppresses the senescence-associated secretory phenotype in the kidney through endogenous hydrogen sulfide*. *Cell Cycle*, 2019. **18**(14): p. 1573-1587.
59. Chaib, S., et al., *Cellular senescence and senolytics: the path to the clinic*. *Nature*, 2022. **28**: p. 1556-1568.

CHAPTER 3

Characterization of metabolites and proteins in the brain tissues of aged mice

Domenica Berardi¹, Gillian Farrell¹, Abdullah Alsultan¹, Ying Chen², Vasilis Vasiliou², Caroline H Johnson², Zahra Rattray^{1*}, and Nicholas Rattray^{1*}

¹Strathclyde Institute of Pharmacy and Biomedical Science, University of Strathclyde, Glasgow, G4 0RE.

²Laboratory of Epidemiology and Public Health, School of Public Health, Yale University, New Haven, Connecticut, USA.

*Corresponding authors: nicholas.rattray@strath.ac.uk and zahra.rattray@strath.ac.uk

3.1. Abstract

Metabolic reprogramming is a primary hallmark of ageing. Due to its high complexity, the metabolic changes that occur in the mammalian brain, as a consequence of the ageing process, are poorly understood. We conducted untargeted metabolomics and shot-gun proteomics analysis on brain tissues from adult (5 months) and old (10 months) wild-type mice using liquid chromatography-mass spectrometry. We found differences in the metabolic and protein fingerprints of aged brain tissues and distinguished several metabolites and proteins of the amino acid, TCA cycle, glucose, fatty acid and immune metabolism that were altered, delineating a putative metabolic map of the aged murine brain. Additionally, we performed spatial analysis of metabolite distribution in the brain of wild-type and Glcm (-/-) mice using matrix-assisted laser desorption/ionization mass spectrometric imaging (MALDI-MSI), revealing regional distribution of metabolites in specific brain regions. The integrated metabolic and protein age-associated changes hold potential to reveal novel therapeutic targets for the treatment of ageing and age-related diseases. Moreover, the advancement of mass spectrometry-based high spatial resolution technologies will launch a new era of analytical chemistry and biomedical research where we can begin to stratify out new ageing phenotypes relative to different tissues/organ types.

KEYWORDS: Ageing, brain, biomarker, metabolic reprogramming, mass spectrometry

3.2. Introduction

Ageing is associated with temporally acquired biomolecular dysregulation underpinning the declining function in many organs that ultimately leads to chronic disability and morbidity. For example frailty, the decline of cognitive function, cardiovascular disease, diabetes, kidney failure, sarcopenia and osteoporosis are common age-related ailments in human [1]. Although these are well-known clinical conditions, the complex biochemistry, and molecular and cellular networks contributing to their age-related degeneration are only beginning to be emerge [2]. Emerging evidence suggests that metabolic reprogramming plays a central role in age-related disease, and is affected by proteins implicated in the regulation of metabolic reactions [3-5].

In order to understand the fundamental mechanisms underpinning age-related disease, several studies have developed preclinical murine models to investigate aspects of ageing research [6] due to their relatively short lifespan, and minimal environmental confounders [7]. Aged mice are considered reliable models of ageing as they represent the closest phenotype to the physiological ageing process caused by the time-dependent accumulation of cellular damage [8, 9]. However, to further optimise the time cost of ageing research from model organisms, genetically modified murine models have significantly contributed to understanding the pathogenesis of age-related disabilities. For example, glutamate-cysteine ligase modifier (Gclm $-/-$) mice knockouts represent a model of stress-induced ageing because of their induced decreased levels of glutathione (GSH) [10]. Since these mice are more susceptible to oxidative stress [11, 12], they are prone to develop an early ageing phenotype through ROS accrued damage [13].

The brain and, particularly the hippocampus and cerebral cortex, are sensitive to the effects of ageing. In humans aged 30-90 years, a volume loss of 14%

and 35% has been reported for these regions of the brain, respectively [14]. Structural changes in these brain regions are accompanied by genetic alterations [15] and downstream protein expression [16] during the course of ageing, which has served to map a genetic and protein profile of the adult mouse brain [17-19]. Recently, a metabolic portrait of different brain regions has been defined by Fiehn et al (2021) [20]. They developed a metabolome atlas of the ageing mouse brain dissected as a function of its anatomic regions (cerebral cortex, olfactory bulb, hippocampus, hypothalamus, basal ganglia, thalamus, midbrain, pons, medulla, and cerebellum), and subsequently analysed the metabolome using gas and liquid chromatography–mass spectrometry (GC and LC-MS) therefore identifying over 1,547 metabolites in the mouse brain.

Considering the strong correlation between genes, proteins and metabolites [21], examining the variation of each alone cannot provide a complete picture of the molecular mechanisms driving the ageing phenotype. Moreover, new technologies exemplified by Matrix-Assisted Laser Desorption Ionization – Mass Spectrometry Imaging (MALDI-MSI) are emerging in ageing research as powerful technologies allowing a comprehensive spatial-specific characterization of molecular species (proteins, metabolites and lipid) without the need for tissue disintegration [22, 23]. Additionally, MALDI-MSI enables the identification of multiple molecular markers directly from a single tissue sample, which is a valuable advantage to accurately distinguish biological samples based on their molecular differences [24]. In this regard, MALDI-MSI can help develop more accurate understanding of how the ageing process affects various tissues, therefore providing more insights into the different ageing phenotypes.

In this study, we provide a network study between proteomics (acting as a proxy for functional genomics) and metabolomics on murine brain tissue using LC-MS and the application of MALDI-MSI to the brain tissues of aged mice. Accordingly, the aims of this study are to elucidate the underlying metabolic mechanisms of brain ageing and to determine the spatial distribution of

metabolites in aged murine brain tissue sections. Moreover, this work demonstrates the potential of mass spectrometry technologies that can enable the rapid and accurate identification and classification of pathological samples.

3.3. Materials

3.3.1. Animals

All experiments involving mice were conducted at Yale University (US) in accordance with the National Institutes of Health standards for care and use of experimental animals as stated in Principles of Laboratory Animal Care (NIH Publication No. 85-23, revised 1985). Gclm (-/-) mice and WT controls were bred from a line previously generated and backcrossed into a >99.8% C57BL/6J background. Mice were kept in a controlled environment (ambient temperature of 20-25°C, 12-hour light/dark cycle). A regular chow diet was provided (proteins, minerals, vitamins, and fat providing 16.12 kJ/g) and water were supplied *ad libitum*. Mice were euthanized by isoflurane asphyxiation at 5-month-old (young mice) and 10-month-old (old mice). All animal procedures were approved by and conducted in compliance with the Institutional Animal Care and Use Committee (IACUC) of Yale University.

3.3.2. Reagents

Reagents for LC-MS analysis – including methanol, acetonitrile and water – were purchased from Thermo Fisher Scientific. Conductive indium tin oxide (ITO)-coated microscope glass slides were purchased from Sigma Aldrich. MALDI matrix 1,5-diaminonaphthalene was purchased from Sigma-Aldrich.

3.4. Methods

3.4.1. Tissue collection

Upon isoflurane sacrifice, murine tissue samples were washed in 0.9% saline solution and frozen using the liquid nitrogen vapor flash freezing technique. This involved floating a weighing boat above the surface of the N₂(l) and placing the tissue in a weighing boat for 60 s. This process rapidly freezes the tissue but minimizes the chance of tissue fracture caused by direct flash freezing in liquid nitrogen. Samples were then stored at -80°C until further analysis.

3.4.2. Sample preparation for liquid chromatography – mass spectrometry (LC-MS)

Murine tissue was dissected on a metal block placed on dry ice, obtaining sections of 50mg +/- 1mg in weight taken from the forebrain. Subsequently, for metabolite extraction each brain section was homogenised with 500 µl of methanol:water (50:50, v/v). Following homogenization, metabolites were extracted by sonication for 10 min on ice. The brain tissue homogenates were centrifuged at 12,000 x g for 10 min at 4°C. Supernatants were collected and dried with a Speed vac centrifuge for 10 h (Savant-SPD121P). Dried metabolites were reconstituted in 100 µl of acetonitrile:water (50:50, v/v). Solvent blank samples were inserted in the analytical batch after every five samples (**Figure S2. 1**). Considering the low number of samples, QCs have not been inserted in the sequence run. Consequently, normalization was assumed based on the similar weighted tissue sections.

After tissue dissection, Label-Free sample preparation for proteomics was carried out according to the EasyPep™ MS Sample Prep Kits (Thermo Fisher Scientific). Briefly, tissue samples were lysed in 100 µl of lysis solution, homogenized and centrifuged at 16,000 x g for 10 min (see pages 26-27 for sample preparation workflow for proteomics). Following protein quantification, 100 µg of protein sample was reduced, alkylated, and digested with trypsin/Lys-C protease mix. Subsequently, peptides were cleaned through spin

columns and clean-up solutions provided by the vendor to remove hydrophilic and hydrophobic contaminants. The clean peptide solution was then dried with a Speed vac centrifuge for 10 h. Dried protein extracts were reconstituted in 100 µl of 0.1% formic acid in water for LC-MS analysis.

3.4.3. Liquid Chromatography tandem mass spectrometry (LC-MS/MS)

Metabolite and protein separation was performed on a binary Thermo Vanquish ultra-high performance liquid chromatography system. 5 µl of metabolic extract and 10 µl of protein extract were respectively injected on to a Thermo Accucore HILIC column (100 mm x 2.1 mm, particle size 2.6 µm) for metabolomics and Acclaim PepMap™ 100 (1.0 mm x 15cm, particle size 3 µm) for proteomics. The temperature of the column oven was maintained at 50°C for metabolomics and 40°C for proteomics analysis, respectively, while the autosampler temperature was set at 5°C. For chromatographic separation of metabolic extracts, a consistent flow rate of 300 µl/min was used where the mobile phase in positive/negative heated electrospray ionisation mode (HESI +/-) was composed of buffer A (acetonitrile with 0.1% formic acid) and buffer B (20 mM Ammonium formate in water with 0.1% formic acid). For chromatographic separation of protein extracts, a consistent flow rate of 50 µl/min was used where the mobile phase in positive heated electrospray ionisation mode (HESI+) was composed of buffer A (Water with 0.1% formic acid) and buffer B (acetonitrile with 0.1% formic acid). The elution gradient used for the chromatographic separation of metabolites and proteins is included in supplementary information (**Error! Reference source not found.**).

A high-resolution Exploris 240-Orbitrap mass spectrometer (ThermoFisher Scientific) was used to perform full scan and fragmentation analyses. Global operating parameters for metabolomics analysis were set as follows: spray voltages of 3900 V in HESI+ mode, and 2500 V in HESI- mode. The temperature of the transfer tube was set at 250°C with a vaporiser temperature of 250°C. Sheath, aux gas and sweep gas flow rates were set at 40, 10, 1 Arb, respectively. Data dependent acquisitions (DDA) were performed using the

following parameters: survey scan range was 50-750 *m/z* with a MS1 resolution of 120,000. Subsequent MS/MS scans were processed with a resolution of 15,000.

Global operating parameters for proteomics analysis were set as follows: spray voltages of 3400V in HESI+ mode and 3000 in HESI- mode. The temperature of the transfer tube was set as 320°C with a vaporiser temperature of 75°C. Sheath, aux gas and sweep gas flow rates were set at 25, 5 and 0 Arb, respectively. DDA were performed using the following parameters: full scan range was 275 – 1500 *m/z* with a MS1 resolution of 120,000. Subsequent MS/MS scans were processed with a resolution of 15,000. Further details are included in supplementary information (**Error! Reference source not found.**).

3.4.4. Mass spectrometry data processing for metabolomics and proteomics

Raw data files obtained from Thermo Scientific Xcalibur™ 4.2 software were imported into Compound Discoverer™ 3.2 for metabolomics analysis and Proteome Discoverer™ 3.0 for proteomics study. Untargeted metabolomics analysis and label-free top-down proteomics was applied. Details of both metabolomics and proteomics studies are included in supplementary information (**Error! Reference source not found., Error! Reference source not found.**).

3.4.5. Pathway Analysis with MetaboAnalyst

Prior to analysis of metabolic pathways with MetaboAnalyst 5.0 (<https://www.metaboanalyst.ca/>), the HMDB identifier and gene symbol was assigned to each selected metabolite and identified protein, respectively. For the individual metabolomics data, an enrichment analysis was performed with the MS12 ID list of metabolites classified based on their chemical structure. Subsequently, joint pathway analysis was performed by integrating the genes relative to identified proteins with the list of ID compounds and their associated Log2 Fold change values. The integration method combined both genes and metabolites into a single query, then used to perform enrichment analysis

through a hypergeometric test. The hypergeometric test allows to define the significance of the association between two sets of data (genes and metabolites) [25]. Finally, important nodes (compounds) were scored based on their betweenness centrality, and pathway analysis results were generated.

3.4.6. Statistical Analysis

For metabolomics and proteomics analysis, Principal Component Analysis (PCA) was performed to reduce data dimensionality and determine the clustering of each sample group. Differential analysis was used to compare differences between control and treatment groups and plotted as a Volcano plot (log₂-fold change vs. -log₁₀ p-value). Peak areas were log₁₀ transformed and p values calculated for the sample group by two-tailed t-test assuming that all data were normally distributed. A p-value <0.05 and a fold-change of 1.5 was deemed to be statistically significant.

3.4.7. Tissue preparation for MALDI Mass Spectrometry Imaging

Tissue sections were prepared by mounting individually frozen brain samples on a small aliquot of optimal cutting medium and sectioned to 12 µm using a Leica CM1950 Cryostat. Sagittal sections were taken. Each tissue section was then thaw mounted onto a pre-chilled (-15°C) and pre-weighed ITO microscope glass slide. ITO-coated slides were used as target mounts as they are suitable for high voltage applications and afford a more regulated and higher level of energy transfer.

3.4.8. MALDI Matrix Application

Recrystallized 1,5-diaminonaphthalene (DAN) was sublimated to previously prepared tissue sections on ITO slides (288 µg/cm² for brain samples and 218 µg/cm² for kidney). Bespoke sublimation apparatus was purchased from Chemglass Life Sciences and was designed to fit standard 70x25 mm ITO slide geometry [26]. The apparatus was coupled to an Edwards EM18

roughing pump alongside a digital thermocouple vacuum gauge controller to monitor the vacuum generated within the system (25 mTor being the target value). The base of the sublimation equipment was subsequently placed on a sand bath heated to 120°C for 6.5 min. Samples were immediately put forward for analysis.

3.4.9. MALDI Mass Spectrometry Imaging

Imaging mass spectrometry analysis was performed using a matrix assisted laser desorption ionization (MALDI)-Synapt-G2Si quadrupole time of flight (QtoF) mass spectrometer (Waters Corporation, Milford Massachusetts). The orthogonal QtoF mass analyzer was calibrated using red phosphorous clusters and operated in sensitivity mode. The equipped 1KHz solid state Nd:YAG laser was operated at a wavelength of 355 nm, with a 200Hz firing rate. Spectra were acquired in negative ionization modes with the QtoF analyzer operating in V-reflectron mode. An over-sampling raster technique was used to ablate the sample and matrix and obtain a highly resolved image using a scan duration of 1s. Spectra were digitally smoothed and baseline-corrected using MassLynx 4.2 software and sent to the HDI v1.4 software for processing, image analysis and generation of ion intensity maps.

3.5. Results

3.5.1. Altered metabolic pathways in aged murine brain tissue

To investigate the metabolic differences between old and young mice, we profiled their metabolome using an in-house untargeted liquid chromatography-mass spectrometry-based metabolomics pipeline (**Figure S2. 2**). After data acquisition, data processing and analysis were performed in Compound Discoverer 3.3. First, we used principal component analysis (PCA score and loading plots) to visualise and interpret the clustering of quantified metabolic data to examine global differences between old and young mice (**Figure 3. 1**).

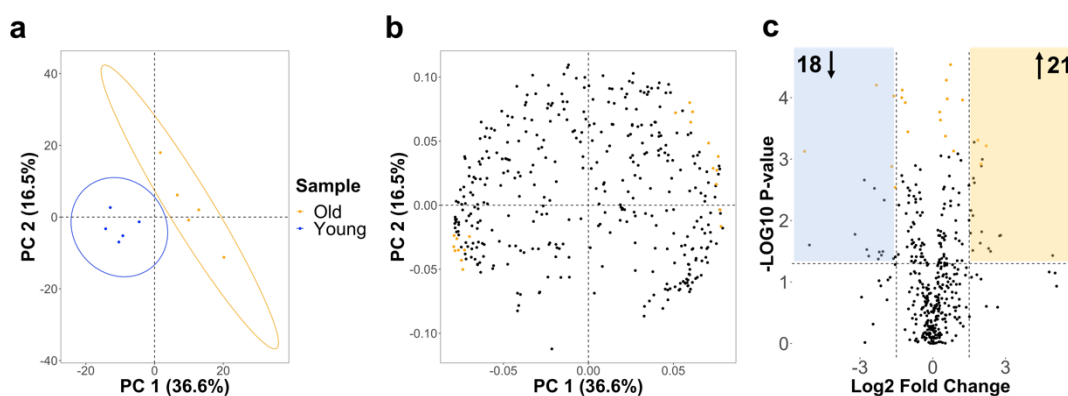


Figure 3. 1 Statistical analysis of the metabolic content of aged murine brain tissues. Graphical representation of the PCA statistical analysis and differentially expressed metabolites in aged murine brain tissue relative to control. For each sample group, five biological replicates were used. a) Data points in the two-dimensional PCA score plot and b) loading plot were central scaled. Ellipses are indicators of the clustered samples. C) Volcano plots display enriched (blue) and depleted (yellow) metabolic features by representing the log₂ fold change in altered features and the -log₁₀ adjusted p-values (two-tailed t-test) with cut off values selected at >1.5 and <0.05, respectively. *The first 20 features mostly contributing to the separation between young and old samples correspond to the PLS-DA components (Figure S2. 3), and have been highlighted as orange data points.*

From the results, a clear separation was observed between the metabolic profile of aged (10-month-old) murine brain tissue in comparison to the young control (5-month-old) (**Figure 3. 1a**). The loading plot show the features mainly contributing to this separation (**Figure 3. 1b**), and the volcano plot represents the differential number of metabolic features that are significantly altered in

aged mice relative to control (**Figure 3. 1c**). Together, these findings show a differential age-dependent metabolic phenotype in aged and younger murine brain tissue.

3.5.2. Amino acid metabolism is significantly altered in aged murine brain tissue

Next, we investigated which metabolite classes were altered in aged murine brain tissue relative to young mice, and ranked the most significantly altered metabolites (**Figure 3. 2**).

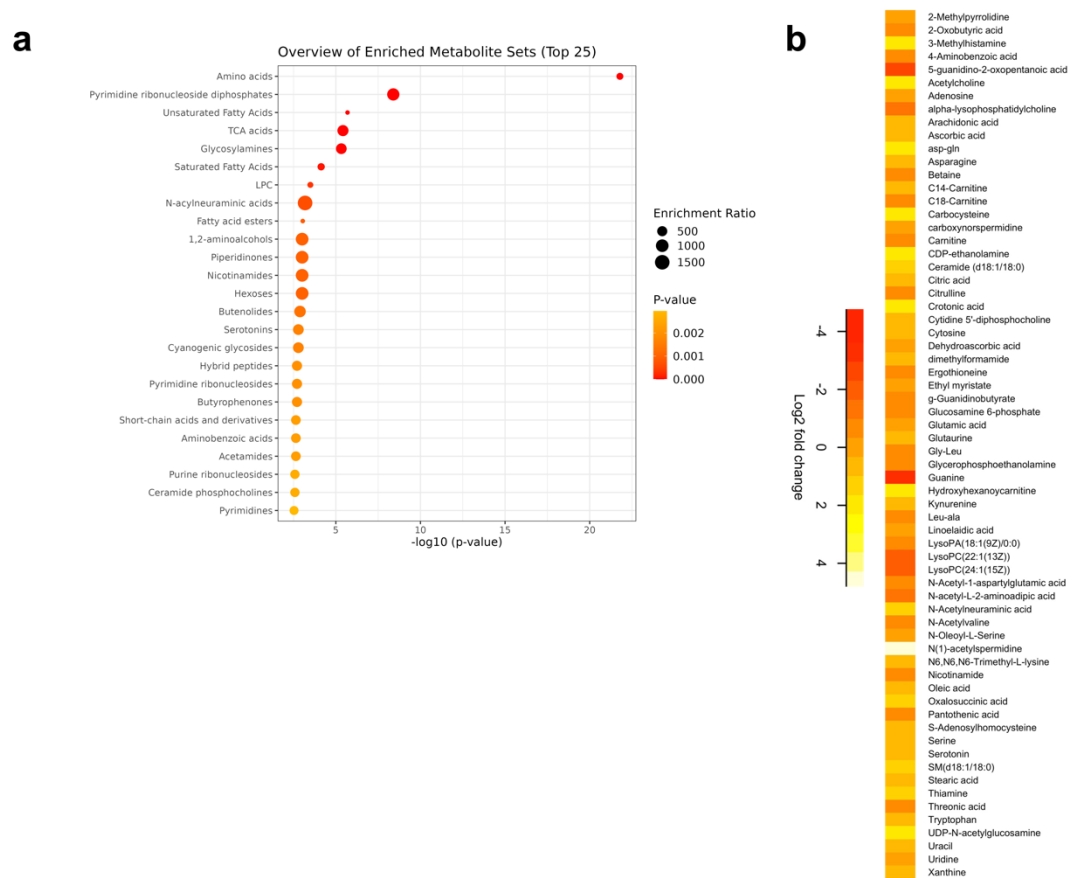


Figure 3. 2 Pathway enrichment analysis of metabolites occurring in aged murine brain tissue.

A) Metabolite enrichment analysis of aged murine brain tissue. Enrichment analysis was based on a hypergeometric test. Topological analysis was based on betweenness centrality. B) The list of significant metabolites ($p \leq 0.05$) altered in murine brain tissue with ageing. Variance of metabolite expression levels between old and young murine tissue is expressed as a Log₂ fold change.

From the enrichment study we observed that among the putatively identified metabolites, amino acids were the most significantly enriched followed by pyrimidine ribonucleoside diphosphates, unsaturated fatty acids, TCA acids, glycosylamines and lysophosphatidylcholines (LPC) (**Figure 3. 2a;**). Looking at the individual metabolites within the class of amino acids (**Figure 3. 2b;** **Table S2. 6**), we observed upregulation of glutamic acid and asparagine both involved in the TCA cycle and derived from glutamine metabolism. Among the pyrimidines high levels of UDP-N-acetyl glucosamine and Cytidine diphosphate were observed together with the downregulation of Glucosamine-6-phosphate and Uridine. Together, these observations suggest a rewiring of glutamine metabolism, in aged brain tissues, towards a higher synthesis of nucleotides together with its anaplerotic role in TCA cycle.

Furthermore, in aged brain tissues we measured an accumulation of unsaturated and saturated fatty acids (arachidonic acid, oleic acid, linoelaidic acid, stearic acid, margaric acid), decreased levels of phospholipids (LysoPC(22:1), LysoPC(24:1)), and enrichment of C18-sphingomyelin. Low levels of free carnitine and C14-carnitine was also detected, while enrichment of C18-carnitine was detected in the old brain tissues.

Mummichog software was also employed for the enrichment analysis (**Table S2. 6**). Both software tools showed similar results. However, considering that our data have a MSI2 level of metabolites annotation, while Mummichog is better suited for MSI level 3 putative IDs, we decided to continue the analysis using MetaboAnalyst.

3.5.3. Altered protein content in murine brain tissue

To analyse the global protein content variation in old murine brains compared to young mice brains, we profiled their proteome using a Bottom-up liquid chromatography–mass spectrometry–based proteomics pipeline (**Figure S2. 4**). After data acquisition, data processing and analysis were performed in Proteome Discoverer 3.0. We used PCA and differential analysis to visualise

and interpret the clustering of quantified protein data and ranked the most significant putatively identified proteins (**Figure 3. 3**).

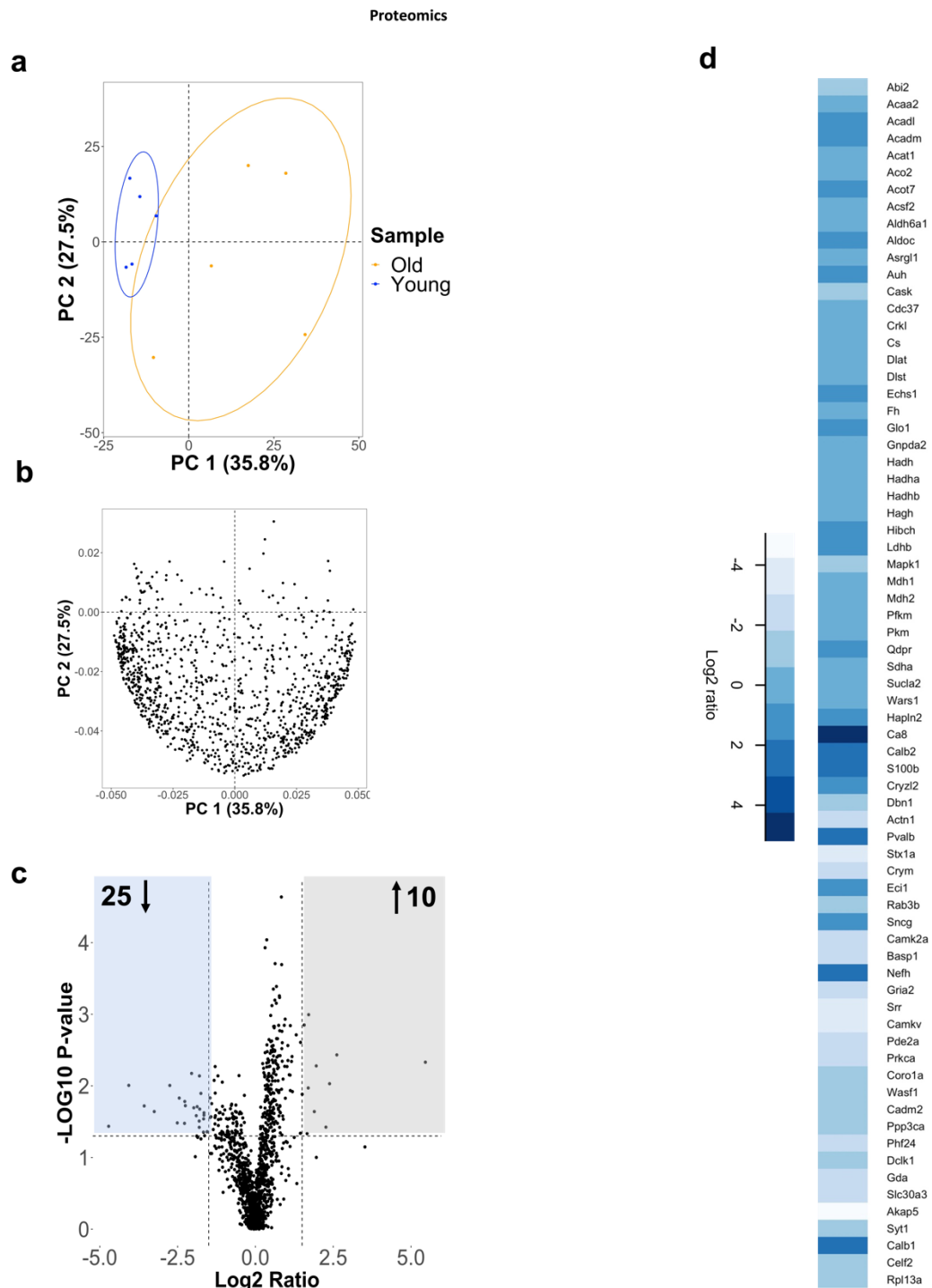


Figure 3. 3 Proteins altered in murine brain tissue as a function of age. A) PCA statistical analysis score plot and b) loading plot. Data points in the two-dimensional PCA plots were central scaled. c) volcano plot-based differential study of proteins in old vs young mice. Data display enriched (blue) and depleted (yellow) protein features by representing the log₂ fold change in altered features and the -

log₁₀ adjusted p-values (two-tailed t-test) with cut off values selected at >1.5 and <0.05, respectively. For each sample group, five biological replicates were used. d) Significantly altered protein genes in old mice relative to the young controls. Variance of the expression levels of proteins is represented with the Log₂Fold change.

We observed clustering of protein-related features in old and young mice (**Figure 3. 3a,b**). Differential analysis using the volcano plot showed the number of enriched and depleted features in old mice relative to the young controls (**Figure 3. 3c**). Similar to the metabolomics study, proteomics analysis also showed age-dependent protein content alteration in murine brain tissues. For the analysis of the proteins significantly altered in the brain tissues of aged mice, we first converted protein annotation codes into gene symbols through UniProt (<https://www.uniprot.org>) by selecting the mus musculus taxonomy database (**Figure 3. 3d**).

Based on the results, we observed a significant upregulation of proteins involved in the TCA cycle (Dlst, Sucla2, Fh, Mdh2, Dlat, Cs, Aco2, Sdha), gluconeogenesis (Mdh1, Aldoc), branched chain amino acids (Aldh6a1, Bcat1, Auh, Hibch), glycolysis (Pkm, Gnpda2, Pfkf), pyruvate metabolism (Hagh, Ldhd, Glo1), phenylalanine metabolism (Asrgl1, Qdpr), fatty acid β -oxidation (Acat1, Acaa2, Hadhb, Hadh, Acsf2, Hadha, Acadm, Acot7, Echs1, Acadl), and IL-2 signalling (Crkl). Downregulated proteins included the ones involved in nucleotide metabolism (Pde2a), IL-9 and IL-3 signalling pathways (Mapk1, Prkca), dopamine metabolism (Stx1a, Syt1, Cask), and proteins contributing to cell adhesion and communication (Actn1, Wasf1, Cadm2, Abi2, Cdc37). The role and location of the aforementioned proteins and enzymes have been described in **Table S2. 8**.

3.5.4. Combined metabolomics/proteomics network analysis of old murine brain tissues

Next, we performed a pathway level integrative analysis of proteomics and metabolomics data. A list of significant proteins and the complete peak list of metabolites, putatively identified in the brain tissues of aged and young mice, were integrated through MetaboAnalyst 5.0 (**Figure 3. 4**).

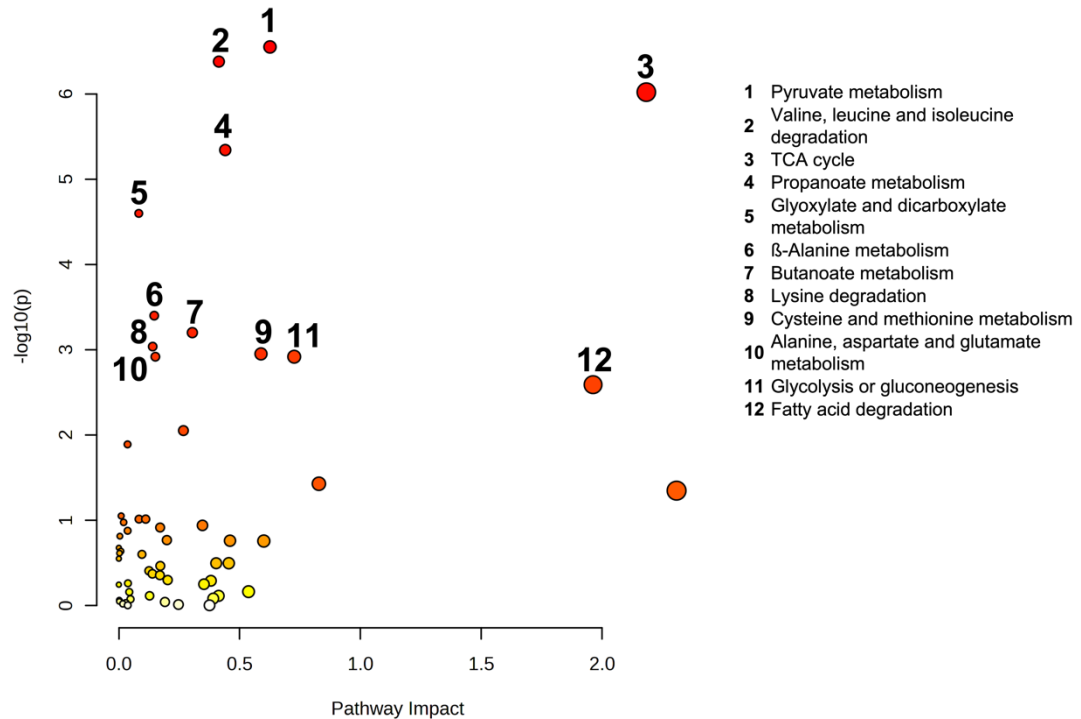


Figure 3. 4 Enriched metabolic pathways altered in aged murine brain tissue. Enrichment analysis resulted from the integration of identified putative protein genes and metabolites.

Among the top ten significant (FDR <0.05) and relevant (Impact factor >0.1) enriched pathways we found pyruvate metabolism, valine, leucine and isoleucine metabolism, TCA cycle, propanoate, glyoxylate and dicarboxylate metabolism, β -alanine, butanoate, lysine, cysteine and methionine, alanine, aspartate and glutamate metabolism, glycolysis and fatty acid degradation (**Figure 3. 4;Table S2. 9**).

Altered metabolic and protein features were mapped (**Figure 3. 5**) using the Encyclopaedia of Genes and Genomes (KEGG) database to map enriched pathways.

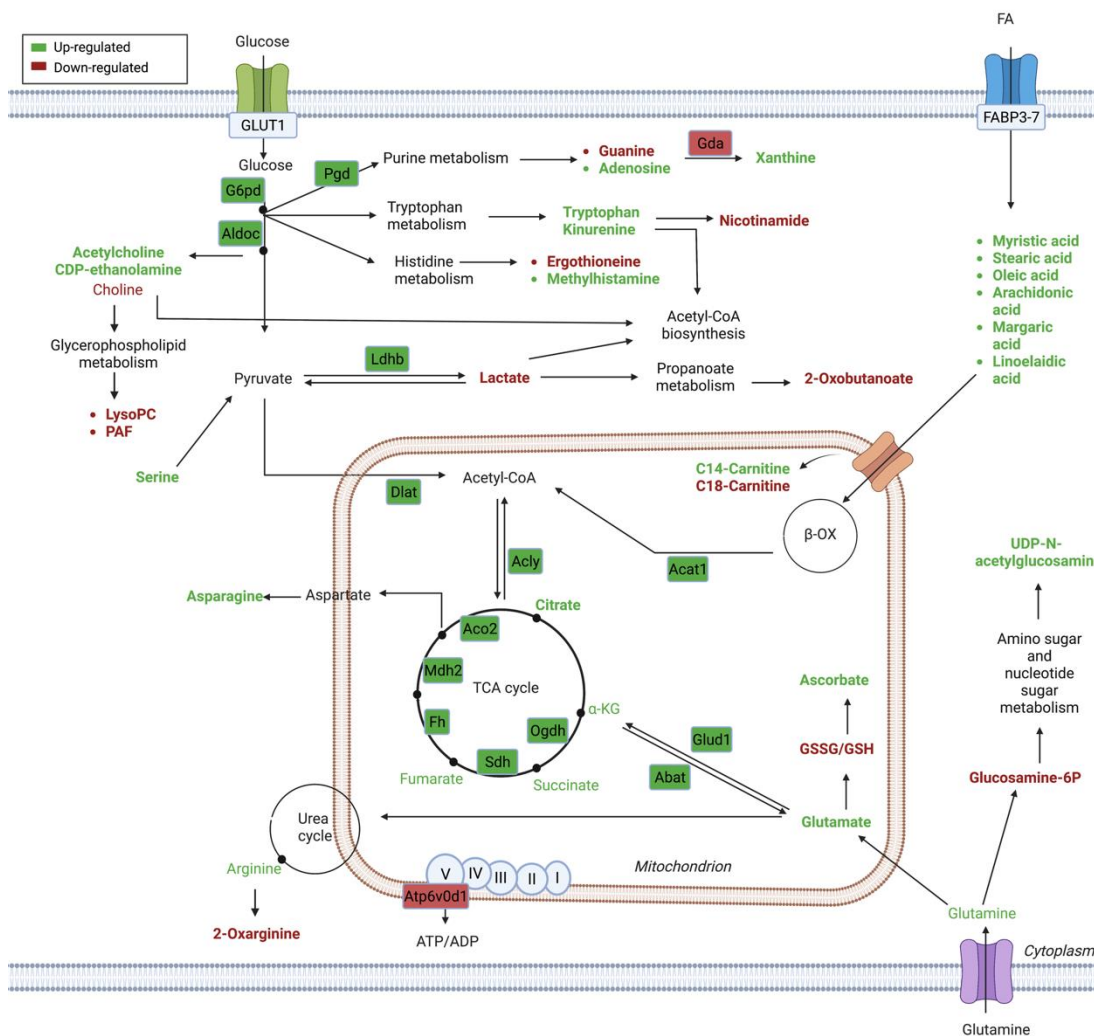


Figure 3.5 Graphical summary representation of the putatively identified metabolic pathways in the brain tissues of old mice. Enriched and depleted metabolic/protein features are in green and red, respectively. In bold are represented significant metabolites.

3.5.5. MALDI MSI reveals spatial localisation of putative lipids in the aged murine brain tissue

Considering the high lipid content in the brain, we investigated their spatial distribution in aged and young mice through the application of MALDI MSI in negative acquisition mode. A similar analysis was applied to glutamate-cysteine ligase modifier subunit gene (*Gclm* ^{-/-}) knockout murine models (**Figure 3.6**). This genetic modification is responsible for a 70-80% decrease

in GSH levels across various tissues including the brain, liver, kidney and lung [12].

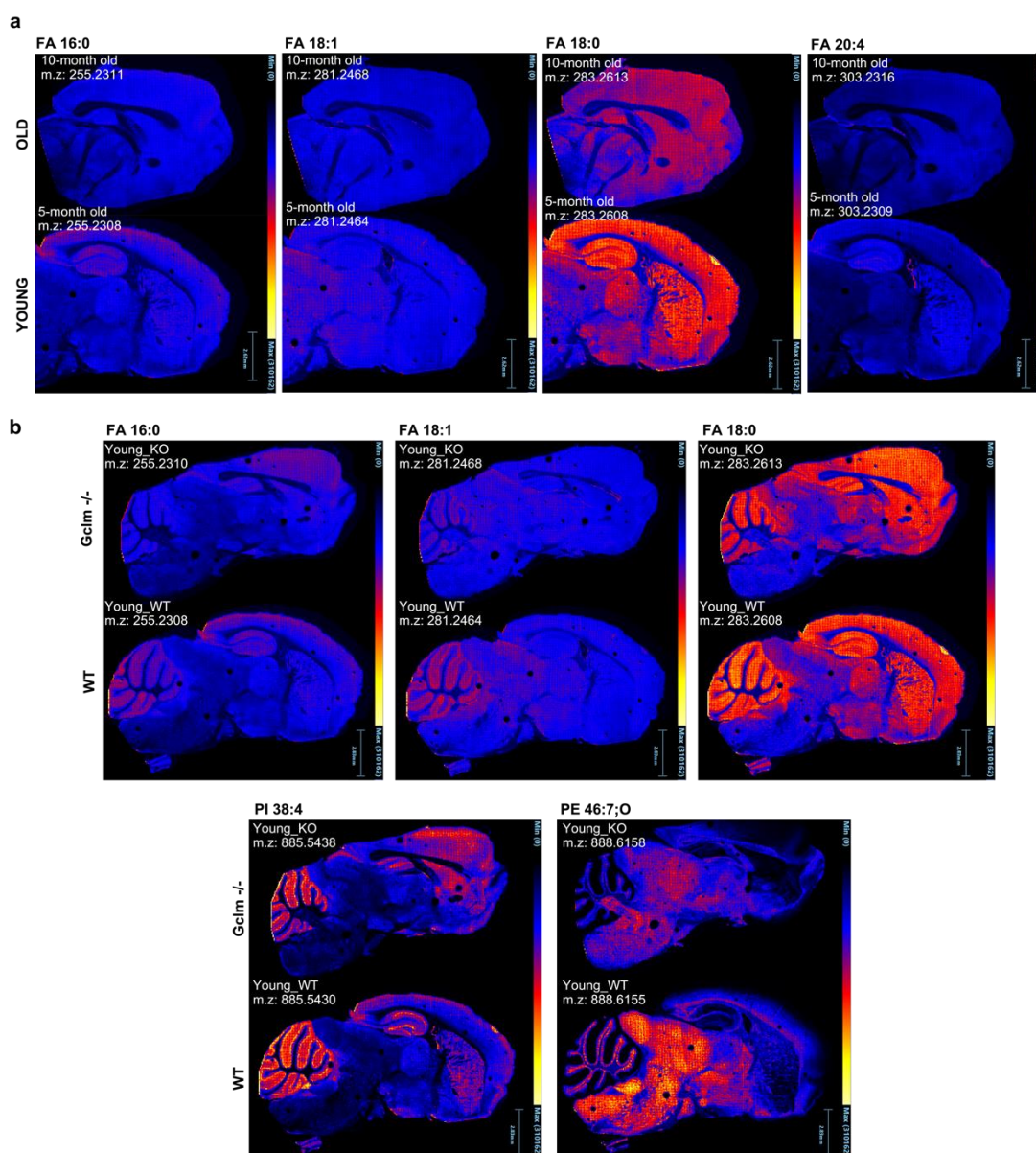


Figure 3. 6 MALDI-MSI analysis of the left-brain hemisphere of aged (10-months) and young (5-months) mice. a) Frontal and temporal lobe of wild type (WT) old and young mice. Fatty acid (FA) 16:0 (m/z 255.231), FA 18:1 (m/z 281.246), FA 18:0 (m/z 283.261), and FA 20:4 (m/z 303.231). b) Frontal, temporal and parietal lobe of young (5-months) mice wild-type (WT) and deficient in glutathione (GSH) synthesis (*Gclm* $-/-$). FA 16:0 (m/z 255.231), FA 18:1 (m/z 281.246), FA 18:0 (m/z 283.261), phosphatidylinositol (PI) 38:4 (m/z 885.543), and phosphatidylethanolamine (PE) 46:7:0 (m/z 888.616).

From the analysis of MSI images, we observed spatial localization of metabolites in the brains of both young (5 months) and old mice (10 months) (Figure 3. 6a). For example, FA 16:0 is mainly localised in the cerebral cortex

and hippocampus, FA 18:1 is present in the thalamus and hypothalamus, FA 18:0 is expressed over the entire area of the left-brain hemisphere. While no expression of FA 20:4 was detected in the cerebral cortex of neither old nor young mice.

Similarly, in the pairwise analysis of young and aged *Gclm* ^{-/-} mice, we detected FA 16:0 predominantly in the cerebral cortex, FA 18:1 in the thalamus and hypothalamus, and FA 18:0 is widely expressed in the whole brain. Additionally, WT and *Gclm* ^{-/-} mice expressed PI 38:4 particularly in the cerebellum, and PE 46:7;O especially in the midbrain, hypothalamus and thalamus (**Figure 3. 6b**).

The whole brain sections of these samples allowed us to observe that FA 16:0, FA 18:1, FA 18:0, PI 38:4 and PE 46:7;O are expressed in the cerebellum of both *Gclm* ^{-/-} and the WT phenotype.

Details on other identified peaks are reported in supplementary materials (**Table S2. 10**).

3.6. Discussion

Tissue metabolomics and proteomics offer the opportunity to study aberrant changes in metabolites and proteins occurring at the site of disease pathogenesis [27-30]. The implementation of mass spectrometry technologies in ageing research has shown the potential to provide a more holistic understanding of the mechanisms underpinning ageing-related pathophysiology. Moreover, the ongoing implementation of mass spectrometry-based technologies with a high spatial resolution of molecular classes is starting to be an attractive tool in histological studies of ageing with promising advantages for clinical applications [31-33].

In this work, we applied mass spectrometry-based metabolomics and proteomics techniques to study brain tissue derived from old and young mice. The goal of this study was to perform a comprehensive analysis of the global metabolic changes occurring in murine brain tissue during ageing, and the relative spatial localization of their differential expression. First, we examined the individual metabolic and protein content of old and young murine brain tissue through tandem LC-MS analysis (**Figure 3. 2, Figure 3. 3**). Then we integrated these findings into a network analysis to design a comprehensive map of the age-based metabolic pathways constituted by metabolites and proteins involved in metabolic reactions (**Figure 3. 4**).

In line with other studies [34], from our results, we observed a high content of organic molecules like amino acids, carboxylic acids, TCA acids and peptides. In particular, we detected elevated levels of glutamate, aspartic acid and homocysteine in the brain tissue of old mice when compared to younger subjects. These were accompanied by high levels of enzymes such as glutamate dehydrogenase 1 (Glud1), aspartate aminotransferase (Got1/2), and adenosylhomocysteine hydrolase-like protein 1 (Ahcyl1) for glutamate metabolism, aspartate and homocysteine synthesis, suggesting that these metabolic pathways were upregulated. These metabolites are central in the regulation of neuronal membrane potential, and their alterations may affect the regular function of neurological signalling [35]. Guanine nucleotide-binding

proteins (G proteins) play a key role in neurotransmission signalling [36] and it is interesting to observe that in old murine brain tissue the majority of G protein classes were found to be downregulated. This is suggesting that altered glutamate, aspartate and homocysteine metabolism may be a key target in the regulation of excitation/inhibition of neuronal imbalance as observed in Alzheimer's patients [37].

Similar to previous work [34], aged murine brain tissue is characterised by a metabolic shift towards the synthesis and accumulation of nucleotides. Accordingly, an enrichment of purine and pyrimidine levels was observed in this study. Nucleotides can be produced through the redirection of glucose metabolism towards the pentose phosphate pathway (PPP), or by directing the TCA acids towards biosynthetic pathways rather than being utilised for energy production [38]. Based on our results, PPP-derived histidine metabolites were upregulated together with molecules constituting the TCA cycle (α -KG, citrate, fumarate, malate, and succinate). Depleted energy status in the old (10 month) brains reflected the absence of peaks for adenosine triphosphate (ATP) and the accumulation of adenosine monophosphate (AMP) suggesting an increased AMP/ATP ratio in our samples. This hypothesis was further confirmed by proteomics data showing significantly depleted levels of Atp6v0d1, which is a subunit of the H⁺-ATPase enzyme responsible for ATP production through proton exchange [39].

Lipids are an alternative source of energy. Upon their β -oxidation NADH and FADH₂ cofactors are used by the electron transport chain to produce ATP. However, in the brain, where lipids constitute almost 50% of the dry weight, they predominantly serve as structural components of cell membranes and neuro-signalling molecules [40]. Moreover, compared to other tissue, the brain contains the largest diversity of lipids [41]. Based on our results different classes of fatty acids were detected including glycerolipids, glycerophospholipids, and sphingolipids. Among the glycerolipids, triacylglycerols (TAGs) represent only 0.2% of the total lipid content in normal conditions, however their level increase in pathological conditions [42]. In the

aged murine brain tissue, we detected increased levels of TGAs including stearic acid, oleic acid, and linoelaidic acid. Glycerophospholipids (phosphocholines and phosphoethanolamines) represent 50-60% of the total membrane mass [43]. They are precursors of arachidonic acid, docohexaenoic acid, and ceramide which represent second messengers in pro-inflammatory signalling pathways [44]. In this study, elevated arachidonic acid and ceramide levels were detected in aged murine brain tissues together with upregulation of other sphingolipids. Sphingolipids play an essential role in the induction of senescence [45], as well as the pathogenesis of Alzheimer's disease [46]. Together, with elevated levels of different lipid classes in aged murine brain tissue, we also observed an enrichment of lipid oxidative products, ketone bodies, and enzymes involved in lipid β -oxidation. These are responsible for the generation of oxidative stress in age-related neurodegenerative diseases [47].

In addition to the high abundance and heterogeneity of lipids in the brain, their spatial and regional composition in the brain determine their role in neuronal functionality under homeostatic conditions. Differences in lipid classes have been determined for the different cell types of the central nervous system [48]. More recently, the regional lipid composition in the brain was mapped using LC-MS analysis [20], which involves tissue lysis and extraction approaches for downstream analysis. Here we investigated the spatial distribution of lipids in murine brains while preserving their structure. This approach is similar to the tissue preservation seen in immunohistochemistry, with the ability to simultaneously detect hundreds of molecules and their relative abundance at the same time. This method was applied to naturally aged mice and early ageing mice through the depletion of glutathione and induction of oxidative stress. A qualitative analysis has only been considered in this study therefore determining the spatial expression of lipids (**Figure 3. 6**). For each analyte, peak intensities have been reported (**Table S2. 10**), however they have not been used for a quantification analysis as utilization of internal standards and a calibration curve is needed [49], which will be considered in future applications of the technique. In line with previous studies [20], we observed

that FA 16:0 (palmitic acid) is predominantly concentrated in the hippocampus, cerebral cortex and cerebellum. FA 18:0 (stearic acid) is distributed throughout the brain, while FA 18:1 (Oleic acid) is present only in the cerebellum and middle brain. Phosphatidylinositol (PI) 38:4 expression was detected predominantly in the olfactory bulb and cerebellum. Phosphoethanolamine (PE) 46:7;O levels were elevated in the medulla, midbrain and hypothalamus.

Applying MSI to the investigation of murine aged tissue provides a comprehensive map metabolome and proteome profile, which can in the long term be implemented for understanding the population-based heterogeneity of biomolecules and translatability of pre-clinical findings to humans. A targeted approach in the investigation of the age-dependent metabolic changes of mice tissues will allow a better understanding of the direction of these alterations. Of notice, we did not account for protein post-translational modifications (PTMs), the downstream response of which defines the phenotype of an organism and requires detailed analysis using a targeted approach. Finally, optimization of MALDI-MSI for the spatial identification and quantification of biomolecules is necessary for a more accurate determination of their tissue localization.

3.7. Conclusion

Our data show the existence of a different metabolome and proteome profile in aged murine brain tissue. Data derived from both metabolomics and proteomics analysis can be combined through a network analysis, providing a more detailed, albeit putative picture of the molecular and chemical changes occurring during ageing. In our study, metabolites of the energy metabolism (TCA acids and lipids) were mainly altered in the aged brain tissues. These results will drive future targeted analysis for an in-depth characterization of the energy metabolic alterations during ageing. Moreover, we presented mass spectrometry imaging systems as a powerful tool allowing the high-resolution spatial mapping of multiple molecules in one single experiment thus overcoming the limitations of the traditional histochemical analysis.

This is a preliminary example of multi-omics analysis integrated with a spatial investigation of the composition of tissues. Although method application needs to be improved, here we show the great potential of mass spectrometry–based technology in the design of advanced diagnostic studies that can be ultimately applied to clinical medicine.

3.8. References

1. Murabito, M., et al., *The Search for Longevity and Healthy Aging Genes: Insights From Epidemiological Studies and Samples of Long-Lived Individuals*. Journal of Gerontology A, 2012. **67A**(5): p. 470-479.
2. Houtkooper, R., et al., *Metabolic networks of longevity*. Cell, 2010. **142**(1): p. 9-14.
3. Gudenschwager, C., et al., *Directly Reprogrammed Human Neurons to Understand Age-Related Energy Metabolism Impairment and Mitochondrial Dysfunction in Healthy Aging and Neurodegeneration*. Oxidative Medicine and Cellular Longevity, 2021. **5586052**: p. 1-14.
4. Morris, O., et al., *Warburg-like Metabolic Reprogramming in Aging Intestinal Stem Cells Contributes to Tissue Hyperplasia*. Cell Reports, 2020. **33**(8): p. 108423.
5. Feng, Z., et al., *Reprogramming of energy metabolism as a driver of aging*. Oncotarget, 2016. **7**: p. 15410-15420.
6. Yuan, R., et al., *Mice as a mammalian model for research on the genetics of aging*. The official journal of the Institute for Laboratory Animal Research, 2011. **52**(1): p. 4-15.
7. Vanhooren, V., et al., *The mouse as a model organism in aging research: Usefulness, pitfalls and possibilities*. Ageing Research Reviews, 2013. **12**(1): p. 8-21.
8. Köks, S., et al., *Mouse models of ageing and their relevance to disease*. Mechanisms of ageing and development, 2016. **160**: p. 41-53.
9. Yousefzadeh, M., et al., *DNA damage—how and why we age?* eLife, 2021. **10**(e62852).
10. Kendig, E., et al., *Lipid metabolism and body composition in Gclm(-/-) mice*. Toxicology and Applied Pharmacology, 2011. **257**(3): p. 338-348.
11. Yang, Y., et al., *Initial characterization of the glutamate-cysteine ligase modifier subunit Gclm(-/-) knockout mouse. Novel model system for a severely compromised oxidative stress response*. Journal of Biological Chemistry, 2002. **277**(51): p. 49446-52.
12. McConnachie, L., et al., *Glutamate cysteine ligase modifier subunit deficiency and gender as determinants of acetaminophen-induced hepatotoxicity in mice*. Toxicological Sciences, 2007. **99**(2): p. 628-636.
13. Mock, J., et al., *Gait Analyses in Mice: Effects of Age and Glutathione Deficiency*. Aging Dis., 2018. **9**(4): p. 634-646.
14. Jernigan, T., et al., *Effects of age on tissues and regions of the cerebrum and cerebellum*. Neurobiology of Aging, 2001. **22**(4): p. 581-594.
15. Lee, C., et al., *Gene-expression profile of the ageing brain in mice*. Nature genetics, 2000. **25**: p. 294-297.
16. Tsugita A, e.a., *Proteome analysis of mouse brain: Two-dimensional electrophoresis profiles of tissue proteins during the course of aging*. Wiley Analytical Science, 2000. **21**(9): p. 1853-1871.
17. Lein, E., et al., *Genome-wide atlas of gene expression in the adult mouse brain*. Nature, 2007. **445**(7124): p. 168-176.
18. Hawrylycz, M., et al., *An anatomically comprehensive atlas of the adult human brain transcriptome*. Nature, 2012. **489**(7416): p. 391-399.
19. Sharma, K., et al., *Cell type- and brain region-resolved mouse brain proteome*. Nature Neuroscience, 2015. **18**(12): p. 1819-1831.
20. Ding, J., et al., *A metabolome atlas of the aging mouse brain*. Nature, 2021. **12**(6021).
21. Gilson Costa dos Santos, J., et al., *The remodel of the “central dogma”: a metabolomics interaction perspective*. Metabolomics, 2021. **15**(5): p. 48.
22. Peffers, M., et al., *Matrix assisted laser desorption ionization mass spectrometry imaging identifies markers of ageing and osteoarthritic cartilage*. Arthritis Research & Therapy, 2014. **16**(3): p. R110.
23. Aichler, M., et al., *MALDI Imaging mass spectrometry: current frontiers and perspectives in pathology research and practice*. Nature, 2015. **95**: p. 422-431.
24. Lazova, R., et al., *Imaging mass spectrometry--a new and promising method to differentiate Spitz nevi from Spitzoid malignant melanomas*. Journal of the American Academy of Dermatology, 2012. **34**(1): p. 82-90.

25. Ramell, A., et al., *Evaluation and comparison of bioinformatic tools for the enrichment analysis of metabolomics data*. BMC Bioinformatics, 2018. **19**(1).
26. Hankin, J., et al., *Sublimation as a method of matrix application for mass spectrometric imaging*. Journal of the American Society for Mass Spectrometry, 2007. **18**(9): p. 1646-1652.
27. Bai, B., et al., *Deep Multilayer Brain Proteomics Identifies Molecular Networks in Alzheimer's Disease Progression*. Neuron, 2020. **105**(6): p. 975-991.
28. Sathe, G., et al., *Quantitative proteomic analysis of the frontal cortex in Alzheimer's disease*. Journal of Neurochemistry, 2021. **156**(6): p. 988-1002.
29. Goldstein, D., et al., *Cerebrospinal fluid biomarkers of central catecholamine deficiency in Parkinson's disease and other synucleinopathies*. Brain, 2012. **135**(6): p. 1900-1913.
30. Stoessel, D., et al., *Promising Metabolite Profiles in the Plasma and CSF of Early Clinical Parkinson's Disease*. Frontiers in Aging Neuroscience, 2018. **10**(51).
31. Schwartz, S., et al., *Proteomic-Based Prognosis of Brain Tumor Patients Using Direct-Tissue Matrix-Assisted Laser Desorption Ionization Mass Spectrometry*. Cell and tumor biology, 2005. **65**(17): p. 7674-7681.
32. Ait-Belkacem, R., et al., *Monitoring therapeutic monoclonal antibodies in brain tumor*. mAbs, 2014. **6**(6): p. 1385-1393.
33. Hanrieder, J., et al., *MALDI imaging of post-mortem human spinal cord in amyotrophic lateral sclerosis*. Journal of Neurochemistry, 2012. **124**(5): p. 695-707.
34. Ivanisevic, J., et al., *Metabolic drift in the aging brain*. Aging (Albany NY), 2016. **8**(5): p. 1000-1013.
35. Hösli, L., et al., *Depolarization of cultured astrocytes by glutamate and aspartate*. Neuroscience, 1979. **4**(11): p. 1593-1598.
36. Tse, M., et al., *Neuronal functions of activators of G protein signaling*. Neurosignals, 2013. **21**(3-4): p. 259-271.
37. Maestù, F., et al., *Neuronal excitation/inhibition imbalance: core element of a translational perspective on Alzheimer pathophysiology*. Ageing Research Reviews, 2021. **69**(101372).
38. Tozzi, M., et al., *Pentose phosphates in nucleoside interconversion and catabolism*. The FEBS Journal, 2006. **273**(6): p. 1089-1101.
39. Smith, A., et al., *Vacuolar H⁺-ATPase α 2 Subunit: Molecular Characterization, Developmental Regulation, and Localization to Specialized Proton Pumps in Kidney and Bone*. Journal of the American Society of Nephrology, 2005. **16**(5): p. 1245-1256.
40. Bozek, K., et al., *Organization and Evolution of Brain Lipidome Revealed by Large-Scale Analysis of Human, Chimpanzee, Macaque, and Mouse Tissues*. Neuron, 2015. **85**(4): p. 695-702.
41. Martorell, N., et al., *Selective brain regional changes in lipid profile with human aging*. GeroScience, 2022. **44**: p. 763-783.
42. Cook, H., *Metabolism of triacylglycerol in developing rat brain*. Neurochemical Research, 1981. **6**: p. 1217-1229.
43. Farooqui, A., et al., *Glycerophospholipids in brain: their metabolism, incorporation into membranes, functions, and involvement in neurological disorders*. Chemistry and Physics of lipids, 2000. **106**(1): p. 1-29.
44. Adibhatla, R., et al., *Role Of Lipids In Brain Injury And Diseases*. Future lipidology, 2017. **2**(4): p. 403-422.
45. Venable, M., et al., *Role of ceramide in cellular senescence*. Journal of Biological Chemistry, 1995. **270**(51): p. 30701-30708.
46. Lee, J., et al., *Amyloid-beta peptide induces oligodendrocyte death by activating the neutral sphingomyelinase-ceramide pathway*. Journal of Cell Biology, 2004. **164**(1): p. 123-131.
47. Montine, T., et al., *Fatty Acid Oxidation in the Pathogenesis of Alzheimer's Disease*. The American Journal of Pathology, 2005. **166**(5): p. 1283-1289.
48. Fitzner, D., et al., *Cell-Type- and Brain-Region-Resolved Mouse Brain Lipidome*. Cell Reports, 2020. **32**(108132).
49. Tobias, F., et al., *Considerations for MALDI-Based Quantitative Mass Spectrometry Imaging Studies*. Journal of Proteome Research, 2020. **19**(9): p. 3620-3630.

CHAPTER 4

Received: 4 July 2022 / Revised: 21 July 2022 / Accepted: 26 July 2022 / Published: 27 July 2022. *Cancers* **2022**, *14*(15), 3661; <https://doi.org/10.3390/cancers14153661>

Research article

The Differential Metabolic Signature of Breast Cancer Cellular Response to Olaparib Treatment

Domenica Berardi¹, Yasmin Hunter^{1†}, Lisa van den Driest¹, Gillian Farrell¹, Nicholas J. W. Rattray^{1*} and Zahra Rattray^{1*}

Received 4th July 2022, revised ...

¹Strathclyde Institute of Pharmacy and Biomedical Sciences, University of Strathclyde, Glasgow G4 0RE, UK

[†]Current address: School of Life Sciences, University of Glasgow, Glasgow G12 8QQ, UK

*Corresponding authors: nicholas.rattray@strath.ac.uk and zahra.rattray@strath.ac.uk

4.1. Abstract

Metabolic reprogramming and genomic instability are key hallmarks of cancer, the combined analysis of which has gained recent popularity. Given the emerging evidence indicating the role of oncometabolites in DNA damage repair and its routine use in breast cancer treatment, it is timely to fingerprint the impact of olaparib treatment in cellular metabolism. Here, we report the biomolecular response of breast cancer cell lines with DNA damage repair defects to olaparib exposure.

Following evaluation of olaparib sensitivity in breast cancer cell lines, we immunoprobed DNA double strand break foci and evaluated changes in cellular metabolism at various olaparib treatment doses using untargeted mass spectrometry-based metabolomics analysis. Following identification of altered features, we performed pathway enrichment analysis to measure key metabolic changes occurring in response to olaparib treatment.

We show a cell-line dependent response to olaparib exposure, and an increased susceptibility to DNA damage foci accumulation in triple-negative breast cancer cell lines. Metabolic changes in response to olaparib treatment were cell-line and dose- dependent, where we predominantly observed metabolic reprogramming of glutamine-derived amino acids and lipids metabolism.

Our work demonstrates the effectiveness of combining molecular biology and metabolomics studies for the comprehensive characterisation of cell lines with different genetic profiles. Follow-on studies are needed to map the baseline metabolism of breast cancer cells and their unique response to drug treatment. Fused with genomic and transcriptomics data, such readout can be used to identify key oncometabolites and inform the rationale for the design of novel drugs or chemotherapy combinations.

KEYWORDS: Breast cancer, triple-negative, oncometabolites, DNA damage, precision medicine, metabolic reprogramming

4.2. Introduction

In a bid to develop new therapies against various cancer types, genomic instability, its underpinning mechanisms and contribution to tumorigenesis have been extensively investigated over the past few decades. Genomic instability, a well-known contributor to cancer, presents a therapeutic vulnerability that can be targeted in the development of novel chemotherapy agents [1].

To maintain their genomic integrity, cells are equipped with a range of DNA damage repair (DDR) pathways and responses to counteract DNA lesions formed in response to endogenous and exogenous insults [2]. Hereditary mutations in these pathways have been correlated with increased cancer susceptibility, such that defects in homologous recombination contribute to approximately 10% of all breast cancers.

These defects in DDR machinery result in the loss of function for genes implicated in DNA repair (i.e. breast cancer susceptibility gene 1/2- BRCA1/BRCA2) or dysregulation of cell cycle phases [3-5]. While these genetic alterations increase the susceptibility to oncogenesis- they serve as therapeutic vulnerabilities- such that in the presence of a defective DNA repair pathway the inhibition of an alternate DDR mechanism will lead to cell death. This concept is referred to as synthetic lethality, which has formed the rationale for existing DDR inhibitors [6, 7]. One such class of drugs, poly(ADP-ribose) polymerase (PARP) inhibitors, targets vulnerabilities in the homologous recombination DDR pathway [8].

PARP inhibitors as a class of DDR inhibitors block the activity of PARP enzymes involved in DNA damage repair; therefore, leading to accumulation of DNA double-strand breaks that gives rise to genomic instability and subsequent apoptosis [9]. Several PARP inhibitors are currently approved as monotherapies for the treatment of locally advanced or metastatic breast cancer for patients with breast cancer harboring germline BRCA1/2 mutations or HER2-negative receptor status [8]. In 2022, olaparib was approved by the FDA as an adjuvant treatment for patients with human epidermal growth factor receptor 2 (HER2)-negative and germline BRCA-mutated breast cancers following readout from the OlympiA trial [10].

While PARP inhibitors present a therapeutic opportunity for targeting DDR defects in breast and ovarian cancers, emerging evidence has shown a role for oncometabolites- small molecule intermediates of cellular metabolism- in determining the response to these chemotherapies. The biology of oncometabolites and their role in modulating DDR has been increasingly studied over the past few years, guiding new combination therapies and novel biological targets for drug discovery [1].

Metabolic reprogramming- a key feature of all cancers [11]- gives rise to chemoresistance in both treatment-naïve and treatment-resistant breast cancers [12]. As with genomic instability, drivers of metabolic reprogramming can be broadly classified as intrinsic and extrinsic in origin [13]. Intrinsic stimuli such as oncogenes and tumour suppressor genes, modulate cellular metabolism in breast cancer with several regulators including BRCA1/2, MYC, phosphatidylinositol-4,5-bisphosphate 3-kinase (PI3K) and p53 as examples. The functional interplay between these regulators of cellular metabolism, mediates DNA damage repair pathways and subsequent response to DDR chemotherapies. Recent evidence has shown that the upregulation of glucose utilization and glutamine metabolism are required to sustain increased tumour bioenergetic and biosynthetic demand, which vary according to the cellular genetic makeup [14]. Intermediates from glucose and glutamine metabolism have been identified as key oncometabolites regulating the response to chemotherapy drugs, presenting novel biomarkers and potential actionable targets for novel drug discovery [13].

DDR mechanisms induce cellular metabolic changes through interference with purine and pyrimidine biosynthetic pathways, amino acid metabolism, protein biosynthesis and energy metabolism, impacting several metabolic routes [15]. Mediators of DDR pathways, including PARP regulate several pathways exemplified by the pentose-phosphatase pathway, the TCA cycle and glycolysis. In breast cancer, PARP inhibition reduces glucose consumption and alters amino acid and nucleotide metabolism depending on the different cellular subtypes [16]. Moreover, BRCA-1 deficient breast tumors appear to rely on glucose consumption through enhanced glycolysis [17]. Differences in the metabolic signature between cell lines harboring different DNA repair

mutations and measuring their response to PARP inhibitors can inform the rationale for selecting PARP inhibitors in certain breast cancer types and explore potential additional vulnerabilities as druggable targets [18].

DNA repair and regulation of metabolism are critical for maintaining homeostasis in normal human cells. However, the extensive dysregulation and aberrant function of both these pathways promotes tumorigenesis. Until recent, DNA repair and metabolic pathways have routinely been researched as distinct fields within their own right, but emerging research evidence an intrinsic inter-dependency between these pathways. Here, we report the differential cellular response of breast cancer cell line models with different mutational signatures (see **Table S3. 2** Cell lines used in this study and their corresponding clinicopathologic profiles (ER: estrogen receptor, PR: progesterone receptor, and HER2: Human epidermal growth factor 2 receptor)

Cell Line	Histology	Subtype	Immunoprofile	Genetic alterations
MCF-7	Metastatic Adenocarcinoma	Luminal A	ER+, PR+, HER2-	PIK3CA, CDKN2A, GATA3, PIK3CA, TP53
MDA-MB-231	Metastatic Adenocarcinoma	Basal	ER-, PR-, HER2-	BRAF, CDKN2A, KRAS, NF2, TP53
HCC1937	Primary Ductalcarcinoma	Basal-like	ER-, PR-, HER2-	BRCA1, TP53

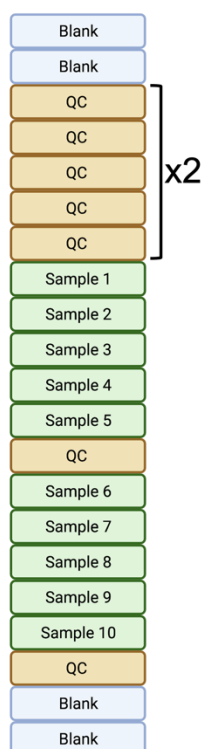


Figure S3. 2 Sample batch order. 2 blanks were injected at the beginning and at the end of the run. 10 QCs were injected before injections of the samples. Then QCs were injected after every 5 samples. QCs have been prepared by pooling together all the sample after drying and reconstitution with water:acetonitrile (50:50, v/v).

Elution Gradient used for LC-MS

Buffer A composition: 10 mM ammonium acetate in 95% acetonitrile, 5% water with 0.1% acetic acid

Buffer B composition: 10 mM ammonium acetate in 50% acetonitrile, 50% water with 0.1% acetic acid

Table S3. 3 Corresponding elution gradient used for the chromatographic separation of metabolite extracts

Retention (min)	Flow (ml/min)	%A	%B	Curve
0.000	0.500	99.0	1.0	5
1.000	0.500	99.0	1.0	5
3.000	0.500	85.0	15.0	5
6.000	0.500	50.0	50.0	5
9.000	0.500	5.0	95.0	5
10.000	0.500	5.0	95.0	5
10.500	0.500	99.0	1.0	5
14.000	0.500	99.0	1.0	5

Table S3. 4 Normality test for cell viability and immunofluorescence quantification data. The Shapiro-Wilk test has been performed with R software. p-values of >0.05 were considered as normally distributed. P-value (p).

Cell viability		Immunofluorescence		

Cell line	p	Cell line	p p53	p γ H2AX
MCF7	0.5	MCF7	0.7	0.1
MDA-MB-231	0.3	MDA-MB-231	0.3	0.9
HCC1937	0.3	HCC1937	0.7	0.1

Table S3. 5 Setting for LC-MS data analysis and processing

Method settings	
Application mode	Small molecule
Method duration	14 min
Global parameter	
Ion source type	H-ESI
Spray voltage	Static
Positive Ion (V)	3900
Negative Ion (V)	2700
Gas Mode	Static
Sheath Gas (Arb)	40
Aux Gas (Arb)	10
Sweep Gas (Arb)	1
Ion Transfer Tube Temp (°C)	320
Vaporizer Temp (°C)	300
APPI Lamp	Not in use
MS Global Settings	
Infusion Mode	Liquid Chromatography
Expected LC Peak Width (s)	6
Advanced Peak Determination	False
Mild Trapping	True
Default Charge State	1
Internal Mass Calibration	EASY-IC™
Mode	Run Start
	<p>Experiment</p> <pre> graph TD A[Full Scan] --> B[Apex Detection] B --> C[Intensity] C --> D[ddMS²] E[5 Scans] --- C </pre>
Start time	0 min
End time	14 min
Full Scan	
Orbitrap resolution	60,000
Scan range (m/z)	70-1050
RF Lens (%)	50
AGC Target	Standard
Maximum Injection Time Mode	Custom
Microscans	1
Data Type	Profile

Polarity	+/-
Source Fragmentation	Disabled
Use EASY-CM™	On
Apex Detection	
Desired Apex Window (%)	50
Intensity	
Intensity threshold	5.0e4
Data Dependent Mode	Number of scans
Number of Dependent Scans	5
ddMS² Scan	
Multiplex Ions	False
Isolation Window (m/z)	2
Isolation Offset	Off
Collision Energy Type	Normalised
HCD Collision Energies (%)	15,30,45
Orbitrap Resolution	15,000
Scan Range Mode	Auto
AGC Target	Standard
Maximum Injection Time Mode	Auto
Microscans	1
Data Type	Profile
Use EASY-IC™	On
Data processing	
<pre> graph TD A[Input files] --> B[Select spectra] B --> C[Align retention times] C --> D[Detect compounds] D --> E[Assign compound annotation] D --> F[Search Chem Spider] D --> G[Group compounds] F --> H[Apply mzLogic] G --> I[Search mzCloud] G --> J[Predict composition] G --> K[Fill gaps] K --> L[Apply QC corrections] L --> M[Mark background compounds] </pre>	
Input Files	.raw data
Select Spectra	
Lower RT Limit	0
Upper RT Limit	0
First Scan	0
Last Scan	0
Lowest charge state	0
Highest charge state	0
Min. precursor mass	0 Da
Max precursor Mass	5000 Da
Total intensity threshold	0
Minimum peak count	1
Scan event filters	

Mass analyzer	Not specified
MS Order	Any
Activation type	Not specified
Min collision energy	0
Max collision energy	1000
Scan type	Any
Polarity mode is	+/-
Peak Filters	
S/N threshold (FT-only)	1.5
General settings	
Precursor selection	Use MS(n-1) precursor
Use isotope pattern in precursor reevaluation	True
Provide profile spectra	Automatic
Store chromatograms	False
Align retention times	
Alignment model	Adaptive curve
Alignment fallback	None
Maximum shift	0.3 min
Shift reference file	True
Mass tolerance	3 ppm
Remove outlier	True
Detect compounds	
Mass tolerance	3 ppm
Intensity tolerance (%)	30
S/N threshold	3
Min. peak intensity	500,000
Base ions	[M+H] ⁺ +1; [M-H] ⁻ -1
Peak detection	
Filter peaks	True
Max peak width	0.5 min
Remove singlets	True
Min #scans per peak	5
Min #isotopes	1
Isotope grouping	
Min spectral distance score	0
Remove potentially false positive isotopes	True
Group compounds	
Mass tolerance	5 ppm
RT tolerance	0.2 min
Preferred ions	[M+H] ⁺ +1; [M-H] ⁻ -1 + 2 nd analysis: [M+H] ⁺ +1; [M-H] ⁻ -1; [M+ACN+H] ⁺ +1; [M+FA-H] ⁻ -1; [M+ACN+Na] ⁺ +1; [M+H+Na] ⁺ +2; [M+H+NH ₄] ⁺ +2; [M+Na] ⁺ +1; [M+NH ₄] ⁺ +1
Fill gaps	
Mass tolerance	5 ppm
S/N threshold	1.5
Use real peak detection	True (re-detected low-intensity peaks)
Apply QC correction	
Regression model	Linear
Min QC coverage [%]	30
Max QC area RSD [%]	30
Max corrected QC area RSD [%]	25
Max #files between QC files	15
Max background compounds	

Max sample/blank	5
Max blank/sample	0
Hide background	True
Search ChemSpider	
Database(s)	CheBI, Human Metabolome Database
Search mode	By formula mass
Mass tolerance	5 ppm
Max # of results per compound	100
Max # of predicted composition per compound	3
Apply mzLogic	
FT Fragment mass tolerance	10 ppm
IT Fragment mass tolerance	0.4 Da
Max # compounds	0
Max # mzCloud similarity results to consider per compound	10
Match factor threshold	30 + 2 nd analysis at 70
Predict compositions	
Mass tolerance	5 ppm
Pattern matching	
Intensity tolerance (%)	30
Intensity threshold (%)	0.1
S/N threshold	3
Min spectral fit (%)	30
Min pattern Cov (%)	90
Use dynamic recalibration	True
Use fragments matching	True
Mass tolerance	5 ppm
S/N threshold	3
Assign compound annotations	
Mass tolerance	5 pmm
Data source 1	mzCloud search
Data source 2	Predicted compositions
Data source 3	massList search
Data source 4	ChemSpider search
Data source 5	Metabolika search
Search mzCloud	
Compound classes	All
Precursor mass tolerance	10 ppm
FT fragment mass tolerance	10 ppm
IT fragment mass tolerance	0.4 Da
Library	Autoprocessed; reference
Post processing	Recalibrated
Max # results	10
Annotate matching fragments	True
DDA Search	
Identity search	Cosine
Match activation type	True
Match activation energy	Match with tolerance
Activation energy tolerance	20
Apply intensity threshold	True
Similarity search	None
Match factor threshold	60
Differential analysis	
Log10 transform values	True

Figure S3. 3 The formation of p53BP1 foci in response to treatment with either growth medium or medium containing olaparib. Representative images of immunolabelled P53BP1 foci (red), DAPI (blue) nuclear counterstain and composite (p53BP1 (red) and DAPI (blue)) in MCF-7, MDA-MB-231, and HCC1937 cells treated with olaparib for seven days (a-c).

Figure S3. 4 The formation of γ H2AX foci formation in response to treatment with either growth medium or medium containing olaparib. Representative images of immunolabelled γ H2AX foci (green), DAPI (blue) nuclear counterstain and composite (γ H2AX and DAPI) in MCF-7, MDA-MB-231, and HCC1937 cells treated with for seven days (a-c).

Table S3. 6 ANOVA analysis of olaparib dose-dependent DNA DSB immunofoci formation

Cell line	Foci	p-value
MCF-7	53BP1	0.011
	γ H2AX	4.876×10^{-10}
MDA-MB-231	53BP1	0.0009
	γ H2AX	4.096×10^{-10}
HCC1937	53BP1	1.204×10^{-6}
	γ H2AX	1.441×10^{-5}

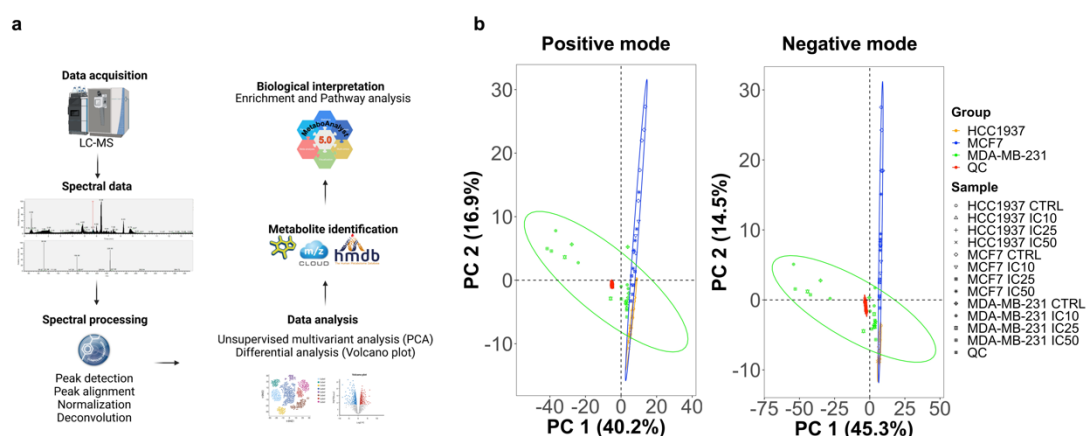


Figure S3. 5 Global metabolic features identified in MCF7, MDA-MB-231 and HCC1937 upon exposure to IC_{10} , IC_{25} and IC_{50} olaparib doses for seven days acquired in positive and negative ionization mode. a) Workflow used in this study to perform pathway analysis from metabolomics analyses. b) Global PCA score plots of the analysed breast cancer cell lines for data acquired in positive and negative ionization mode. For each treatment group, five replicates were used. Data points in the two-dimensional PCA score plot were central scaled. Ellipses represent 95% confidence interval.

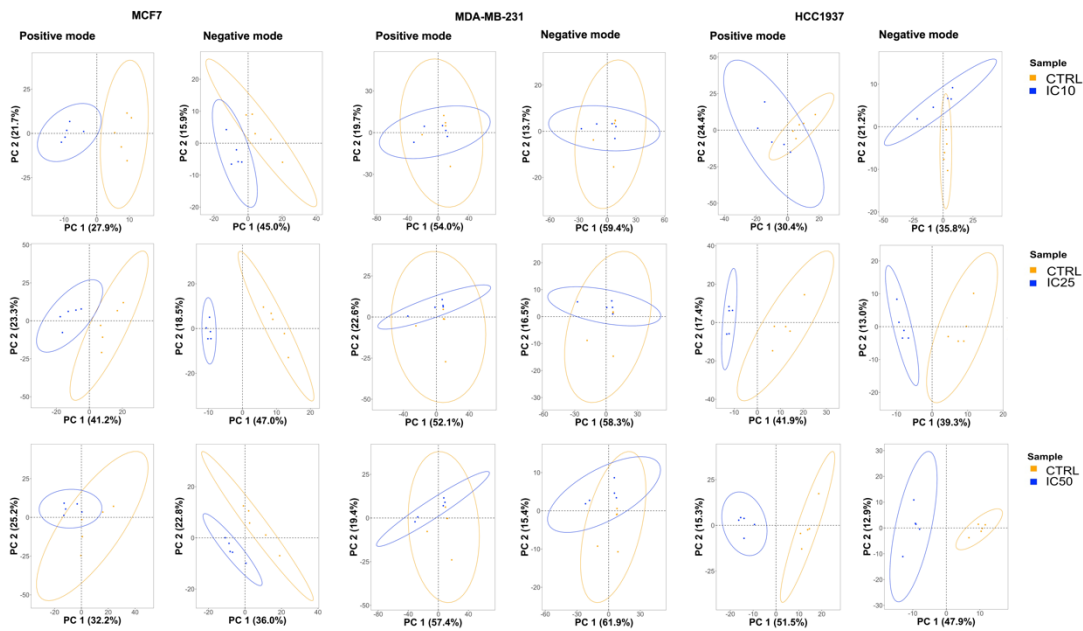


Figure S3. 6 PCA pairwise analysis of untargeted metabolomics data collected, in both positive and negative mode, from MCF7, MDA-MB-231, and HCC1937 cells treated with IC₁₀, IC₂₅ and IC₅₀ olaparib treatment doses. Data points in the two-dimensional PCA score plot were central scaled. The plot was designed on R through the ggplot2 graphical package (n=5). Ellipses represent 95% confidence interval.

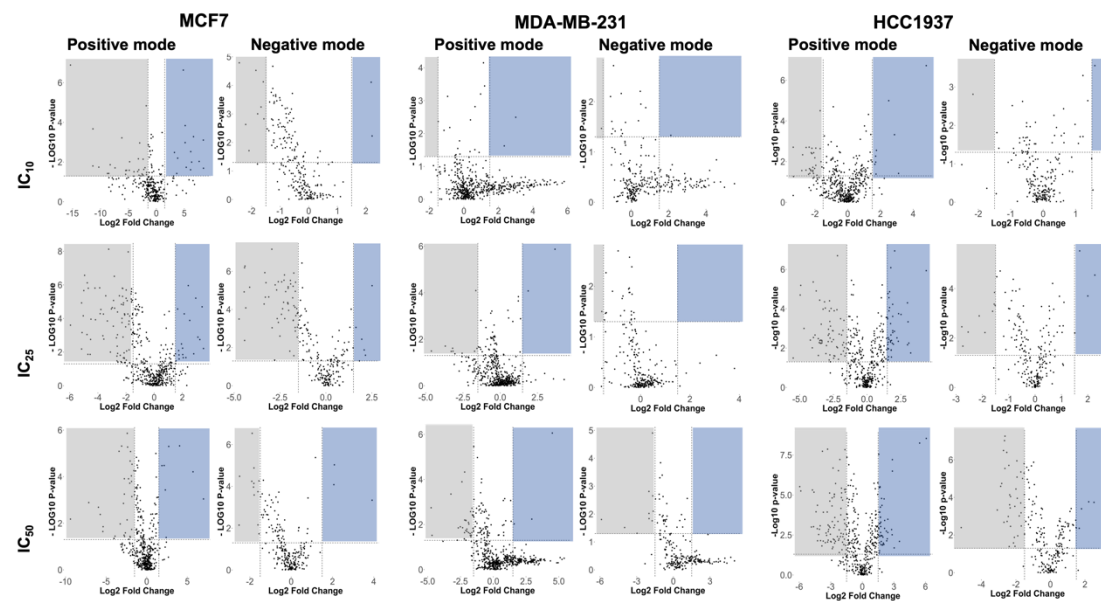


Figure S3. 7 Volcano plots showing the log₂ fold change and the -log₁₀ adjusted p-values in metabolite levels induced by treatment with different doses of Olaparib (IC₁₀, IC₂₅, and IC₅₀) in MCF7, MDA-MB-231 and HCC1937 cells. Data were selected at the cut off values adjusted p<0.05 and fold change >1.5. Blue and grey boxes indicate metabolites significantly enriched and depleted in the different samples, respectively.

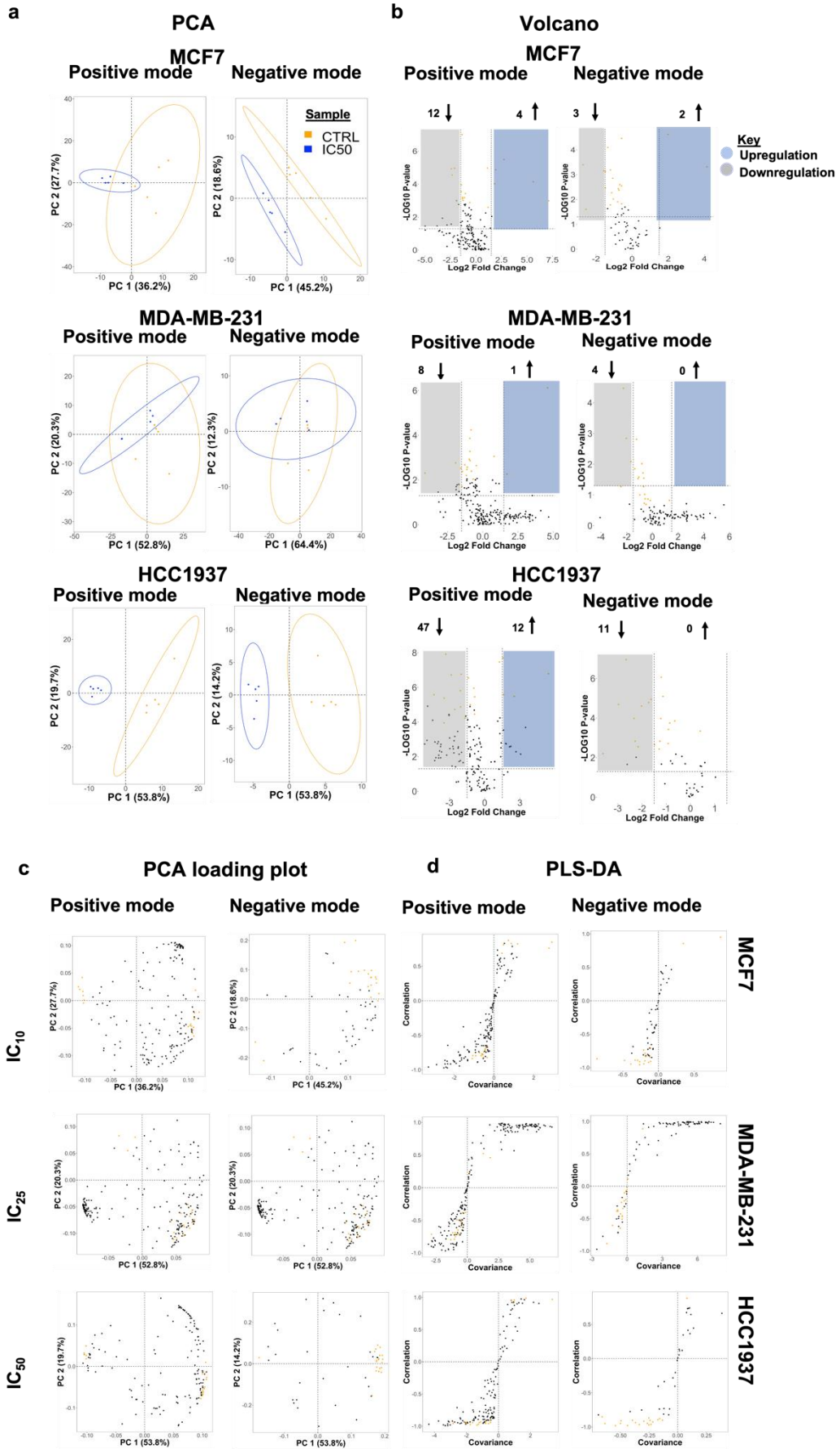


Figure S3. 8 Statistical analysis with new data processing method using 70% of annotation threshold and more ion adducts ([M+H]⁺+1; [M-H]⁻-1; [M+ACN+H]⁺+1; [M+FA-H]⁻-1; [M+ACN+Na]⁺+1; [M+H+Na]⁺+2; [M+H+NH₄]⁺+2; [M+Na]⁺+1; [M+NH₄]⁺+1). A) PCA pairwise analysis of untargeted metabolomics data collected, in both positive and negative mode, from MCF7, MDA-MB-231, and HCC1937 cells treated with IC₁₀, IC₂₅ and IC₅₀ olaparib treatment doses. Data points in the two-dimensional PCA score plot were central scaled. The plot was designed on R through the ggplot2 graphical package (n=5). Ellipses represent 95% confidence interval. B) Volcano plots showing the log₂ fold change and the -log₁₀ adjusted p-values in metabolite levels induced by treatment with different doses of Olaparib (IC₁₀, IC₂₅, and IC₅₀) in MCF7, MDA-MB-231 and HCC1937 cells. Data were selected at the cut off values adjusted p<0.05 and fold change >1.5. Blue and grey boxes indicate metabolites significantly enriched and depleted in the different samples, respectively. The first 20 features mostly contributing to the separation between young and old samples are indicated as orange data points and correspond to the PLS-DA components highlighted in the c) loading plot and d) PLS-DA analysis.

Table S3. 7 Global differential number of altered metabolites for samples treated with IC₁₀, IC₂₅ and IC₅₀ of Olaparib and their relative control (non-treated) samples. Metabolites identified in both positive and negative mode with p-value = <0.05 and Log₂ Fold Change = >1.5.

Sample	HESI +	HESI -
MCF7 IC10/Ctrl	41	10
MCF7 IC25/Ctrl	111	62
MCF7 IC50/Ctrl	41	15
MDA231 IC10/Ctrl	2	1
MDA231 IC25/Ctrl	12	1
MDA231 IC50/Ctrl	34	9
HCC1937 IC10/Ctrl	36	2
HCC1937 IC25/Ctrl	107	13
HCC1937 IC50/Ctrl	134	43

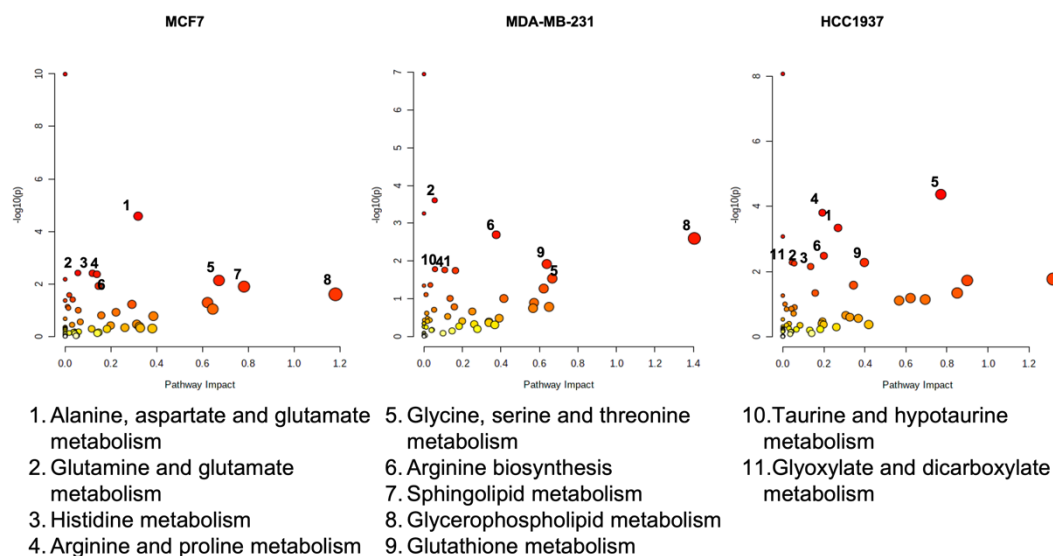


Figure S3. 9 Enrichment analysis of non-treated MCF7, MDA-MB-231 and HCC1937 cells.

Table S3. 8 Metabolic pathways in different breast cancer cells (MCF7, MDA-MB-231, and HCC1937) before and after treatment with IC₅₀ dose of Olaparib. FDR = False Discovery Rate.

	- Olaparib				+ Olaparib			
	Pathways	P-value	FDR	Impact	Pathways	P-value	FDR	Impact
MCF7	Aminoacyl-tRNA biosynthesis	1.02E-10	8.57E-09	0	Aminoacyl-tRNA biosynthesis	8.19E-10	6.88E-08	0
	Alanine, aspartate and glutamate metabolism	2.63E-05	0.001104	0.31879	Arginine biosynthesis	4.37E-06	0.000184	0.54769
	Glutamine and glutamate metabolism	3.83E-03	0.072247	0.055556	Alanine, aspartate and glutamate metabolism	1.31E-05	0.000366	0.25749
	Histidine metabolism	3.94E-03	0.072247	0.11935	Arginine and proline metabolism	0.000141	0.002965	0.20848
	Arginine and proline metabolism	4.30E-03	0.072247	0.13859	Glutamine and glutamate metabolism	0.000363	0.006102	0.055556
	Valine, leucine and isoleucine biosynthesis	0.006688	0.088594	0	Valine, leucine and isoleucine biosynthesis	0.000807	0.011293	0
	Glycine, serine and threonine metabolism	0.007382	0.088594	0.67221	Taurine and hypotaurine metabolism	0.002633	0.0316	0.085714
	Arginine biosynthesis	0.012025	0.11847	0.14615	Glycine, serine and threonine metabolism	0.003952	0.040556	0.67221
	Sphingolipid metabolism	0.012694	0.11847	0.78164	Butanoate metabolism	0.004345	0.040556	0.12169
	Glycerophospholipid metabolism	0.025021	0.20274	1.1815	Vitamin B6 metabolism	0.00747	0.062741	0.96579
MDA-MB-231	Aminoacyl-tRNA biosynthesis	1.11E-07	9.31E-06	0	Aminoacyl-tRNA biosynthesis	4.87E-08	4.09E-06	0
	Glutamine and glutamate metabolism	0.000246	0.010315	0.055556	Arginine biosynthesis	4.44E-05	0.001297	0.54769
	Valine, leucine and isoleucine biosynthesis	0.000549	0.015362	0	Valine, leucine and isoleucine biosynthesis	4.63E-05	0.001297	0
	Arginine biosynthesis	0.00201	0.042201	0.37538	Glutamine and glutamate metabolism	0.000348	0.007318	0.055556
	Glycerophospholipid metabolism	0.002519	0.042319	1.4051	Arginine and proline metabolism	0.002382	0.040027	0.19139
	Glutathione metabolism	0.012023	0.16708	0.63816	Glycine, serine and threonine metabolism	0.003697	0.05176	0.35674
	Taurine and hypotaurine metabolism	0.016455	0.16708	0.057143	Alanine, aspartate and glutamate metabolism	0.007553	0.087816	0.25155
	Arginine and proline metabolism	0.017286	0.16708	0.10783	Pantothenate and CoA biosynthesis	0.008364	0.087816	0.025568
	Alanine, aspartate and glutamate metabolism	0.017902	0.16708	0.16342	Cysteine and methionine metabolism	0.016897	0.1577	0.74161
	Glycine, serine and threonine metabolism	0.029087	0.24434	0.66667	Taurine and hypotaurine metabolism	0.020936	0.17277	0.057143
HCC1937	Aminoacyl-tRNA biosynthesis	8.36E-09	7.03E-07	0	Aminoacyl-tRNA biosynthesis	6.05E-09	5.08E-07	0
	Glycine, serine and threonine metabolism	4.24E-05	0.001781	0.77013	Arginine biosynthesis	4.03E-06	0.000169	0.54769
	Arginine and proline metabolism	0.000156	0.004357	0.19275	Alanine, aspartate and glutamate metabolism	7.18E-05	0.002011	0.25692
	Alanine, aspartate and glutamate metabolism	0.000455	0.009555	0.26907	Glutamine and glutamate metabolism	0.000348	0.007318	0.055556
	Valine, leucine and isoleucine biosynthesis	0.00084	0.014109	0	Arginine and proline metabolism	0.000585	0.009829	0.19275
	Arginine biosynthesis	0.003289	0.046045	0.2	Valine, leucine and isoleucine biosynthesis	0.000774	0.010591	0
	Glyoxylate and dicarboxylate metabolism	0.005277	0.052485	0.043771	Glycine, serine and threonine metabolism	0.000883	0.010591	0.37754
	Glutathione metabolism	0.005277	0.052485	0.39739	Taurine and hypotaurine metabolism	0.002532	0.02658	0.085714
	Glutamine and glutamate metabolism	0.005623	0.052485	0.055556	Cysteine and methionine metabolism	0.004844	0.045211	0.67619
	Histidine metabolism	0.007034	0.05908	0.13548	Butanoate metabolism	0.022626	0.19004	0.12169

Figure S3. 10 Venn diagram representing the metabolic pathways in MCF7, MDA-MB-231 and HCC1937 cells .a) Baseline metabolic pathways and b) following a seven day treatment with olaparib at IC₅₀ doses.

Table S3. 9 Comparison analysis between MetaboAnalyst and Mummichog software. FDR = False discovery rate. Gamma = Gamma p-value. FET = Fisher's Exact test.

	MetaboAnalyst				Mummichog			
	Pathways	P-value	FDR	Impact	Pathways	Gamma	FET	Empirical
MCF7	Aminoacyl-tRNA biosynthesis	1.02E-10	8.57E-09	0	Biopterin metabolism	0.00589	0.073132	0.04
	Alanine, aspartate and glutamate metabolism	2.63E-05	0.001104	0.31879	Aspartate and asparagine metabolism	0.006205	0.22605	0.05
	Glutamine and glutamate metabolism	3.83E-03	0.072247	0.055556	Glycosphingolipid metabolism	0.007238	0.10342	0.02
	Histidine metabolism	3.94E-03	0.072247	0.11935	Arginine and Proline Metabolism	0.035136	0.50139	0.23
	Arginine and proline metabolism	4.30E-03	0.072247	0.13859	Hyaluronan Metabolism	1	0.18265	0.1
	Valine, leucine and isoleucine biosynthesis	0.006688	0.088594	0	N-Glycan biosynthesis	1	0.18265	0.1
	Glycine, serine and threonine metabolism	0.007382	0.088594	0.67221	Glycosphingolipid biosynthesis - ganglioseries	1	0.095694	0.08
	Arginine biosynthesis	0.012025	0.11847	0.14615	Sialic acid metabolism	1	0.18265	0.1
	Sphingolipid metabolism	0.012694	0.11847	0.78164	Linoleate metabolism	1	0.33331	0.15
	Glycerophospholipid metabolism	0.025021	0.20274	1.1815	Keratan sulfate degradation	1	0.18265	0.15
MDA-MB-231	Aminoacyl-tRNA biosynthesis	1.11E-07	9.31E-06	0	N-Glycan biosynthesis	0.041385	0.030525	0
	Glutamine and glutamate metabolism	0.000246	0.010315	0.055556	Glycosphingolipid metabolism	0.048443	0.10242	0.04
	Valine, leucine and isoleucine biosynthesis	0.000549	0.015362	0	Androgen and estrogen biosynthesis and metabolism	0.063099	0.31089	0.16
	Arginine biosynthesis	0.00201	0.042201	0.37538	Tryptophan metabolism	0.067861	0.39214	0
	Glycerophospholipid metabolism	0.002519	0.042319	1.4051	Aspartate and asparagine metabolism	0.071958	0.50513	0
	Glutathione metabolism	0.012023	0.16708	0.63816	Glycosphingolipid biosynthesis - ganglioseries	0.072898	0.17698	0.12
	Taurine and hypotaurine metabolism	0.016455	0.16708	0.057143	Keratan sulfate degradation	0.072898	0.17698	0
	Arginine and proline metabolism	0.017286	0.16708	0.10783	Glycosphingolipid biosynthesis - globoseries	0.072898	0.17698	0.12
	Alanine, aspartate and glutamate metabolism	0.017902	0.16708	0.16342	Glycosphingolipid biosynthesis - lactoseries	0.072898	0.17698	0.12
	Glycine, serine and threonine metabolism	0.029087	0.24434	0.66667	Keratan sulfate biosynthesis	0.072898	0.17698	0.12
HCC1937	Aminoacyl-tRNA biosynthesis	8.36E-09	7.03E-07	0	Beta-Alanine metabolism	0.01192	0.12328	0.04
	Glycine, serine and threonine metabolism	4.24E-05	0.001781	0.77013	Histidine metabolism	0.014179	0.16175	0.04
	Arginine and proline metabolism	0.000156	0.004357	0.19275	Tryptophan metabolism	0.016674	0.20218	0.08
	Alanine, aspartate and glutamate metabolism	0.000455	0.009555	0.26907	Aspartate and asparagine metabolism	0.047357	0.64926	0.32
	Valine, leucine and isoleucine biosynthesis	0.00084	0.014109	0	Tyrosine metabolism	0.072263	0.7102	0.1
	Arginine biosynthesis	0.003289	0.046045	0.2	Sialic acid metabolism	1	0.20095	0.06
	Glyoxylate and dicarboxylate metabolism	0.005277	0.052485	0.043771	Linoleate metabolism	1	0.28641	0.15
	Glutathione metabolism	0.005277	0.052485	0.39739	Keratan sulfate degradation	1	0.20095	0.07
	Glutamine and glutamate metabolism	0.005623	0.052485	0.055556	Biopterin metabolism	1	0.36314	0.13
	Histidine metabolism	0.007034	0.05908	0.13548	Glycine, serine, alanine and threonine metabolism	1	0.87947	0.81

Table S3. 10 Classification of the metabolites identified in MCF7, MDA-MB-231 and HCC1937 at all Olaparib doses (IC₁₀, IC₂₅ and IC₅₀) after seven days treatment. Class, name, Log₂ fold change, and the p-value (p) is represented for each compound. PC: phosphocholine; PE: phosphoethanolamine; PUFA: poly unsaturated fatty acid; SM: Sfingomyelin.

Class	Name	MCF7						MDA-MB-231						HCC1937					
		FC IC10	p	FC IC25	p	FC IC50	p	FC IC10	p	FC IC25	p	FC IC50	p	FC IC10	p	FC IC25	p	FC IC50	p
Amide	Nicotinamide	-0.5	0.1	-0.5	0.3	-0.1	0.3	-0.1	0.5	-0.2	0.1	-0.5	0	0.4	0.1	0.3	0	-0.1	0.3
Amine	N-Oleylethanolamine	-1.5	0.1	-0.8	0.6	-0.1	0.6	-0.5	0.3	-3.2	0	-0.6	0.3	-1.6	0.2	-2.5	0	-1.2	0
Amine	Triethanolamine	1	0.6	-0.6	0	0.1	0.2	2.9	0.4	0.6	0.8	3.1	0.4	-0.5	0.5	0.4	0.1	0.4	0.5
Amino acid	3-Sulfinoalanine	-1.1	0.5	-1.8	0	-1.1	0.2	-	-	-0.7	0.3	-	-	0.3	0.7	-0.4	0.6	-0.7	0
Amino acid	4-Guanidinobutanoic acid	-1.3	0	-2	0	-1.1	0	-0.2	0.5	-0.3	0.6	-0.5	0.2	-1	0.1	-1.8	0	-1.8	0
Amino acid	4-Hydroxyproline	-1	0	-2.1	0	-1.1	0	-0.4	0.2	-	-	-0.4	0.1	-0.3	0.4	-0.3	0.3	-0.9	0
Amino acid	4-Oxoproline	-0.7	0.3	0.9	0	0.2	0.2	0.4	0.6	-0.3	0	0.8	0.1	0.6	0	1	0	1.5	0
Amino acid	Betaine	-	-	-0.8	0	0	0.7	0	0.3	-0.2	0.1	-0.4	0	-0.1	0.7	0	0.5	-0.4	0
Amino acid	Choline	-3.7	0.1	-2.1	0	-2.1	0.1	0.1	0.5	-1.3	0	-1.5	0	-2.1	0	-2.9	0	-3.7	0
Amino acid	Citrulline	-0.3	0.6	1.8	0	-0.4	0	-0.3	0.2	-0.3	0.1	-0.3	0	-0.1	0.5	0.3	0.5	0.1	0.9
Amino acid	Creatine	-0.3	0.6	-1.7	0	-0.5	0.1	-0.8	0	-0.4	0.2	-1.1	0	0.1	0.3	-0.4	0	-0.7	0
Amino acid	Creatinine	-	-	-0.1	0.2	0.1	0.7	-0.5	0	-0.4	0.1	-0.4	0.2	-0.1	0.4	0.3	0.4	-0.2	0.3
Amino acid	Gamma-Aminobutyric acid	-0.9	0	-1.8	0	-0.7	0	-0.2	0.1	-0.1	0.2	-0.2	0.1	-0.2	0.7	0	0.9	-0.5	0
Amino acid	Glycine	-1.3	0	-2.1	0	-1	0	-	-	-	-	-	-	-	-	-	-	-	-
Amino acid	Hypotaurine	0.3	0.3	-0.4	0.1	-0.6	0	0.3	0.6	-0.2	0.1	-0.5	0	-0.7	0	-0.6	0	-1.3	0
Amino acid	L-Alanine	-0.8	0	-1.7	0	-0.9	0	-	-	-	-	-	-	-	-	-	-	-	-
Amino acid	L-Arginine	6.7	0	-0.5	0	-0.1	0.6	-0.1	0.6	-0.1	0.7	0.3	0.4	0	0.5	0.3	0.1	-0.2	0.1
Amino acid	L-Asparagine	0.3	0.3	-0.4	0.2	1	0	-	-	-	-	-	-	0.9	0.2	1.1	0.1	1.3	0.1
Amino acid	L-Aspartic acid	-0.6	0	-2.2	0	-1.4	0	0.3	0.1	0.3	0.3	0.8	0	-0.1	0.9	-0.5	0	-1.6	0
Amino acid	L-Cystathionine	5.2	0	-2.1	0	-0.3	0.1	-0.1	0.9	1.2	0.4	0.8	0.6	-1.7	0	-2.2	0	-3.8	0
Amino acid	L-Glutamic acid	-1.3	0	-2.1	0	-1.3	0	-0.4	0.5	-0.7	0	-1.1	0	-0.4	0.1	-0.5	0	-2.1	0
Amino acid	L-Glutamine	-11.4	0	-1	0	-0.4	0.1	-0.1	0.2	0.2	0.4	-0.1	0.7	-0.2	0	-0.3	0	-0.5	0
Amino acid	L-Isoleucine	-	-	-1.5	0.3	-0.6	1	-1.4	1	1.5	0.3	-0.3	0.7	0.1	0.2	-0.6	0.7	0.1	1
Amino acid	L-Leucine	-	-	-1.4	0	-0.4	0.1	0.2	0.4	-	-	-0.5	0.1	-	-	-0.6	0	-1.3	0
Amino acid	L-Lysine	-1.1	0	-1	0	-0.4	0.3	-0.3	0.1	-0.4	0.1	0.1	0.5	0.2	0.3	0.3	0	-0.4	0
Amino acid	L-Methionine	-0.9	0	-2.3	0	-1	0	-0.1	0.2	-0.3	0	-0.4	0.1	0.1	1	-0.1	0.2	-0.9	0
Amino acid	L-Ornithine	-	-	-	-	-	-	-	-	-	-	-	-	0.2	0.6	0.3	0.1	-0.1	0.7

Amino acid	L-Phenylalanine	-1.3	0.7	-	-	-	-	-0.1	0.4	-0.4	0	-0.3	0.1	-0.2	0.9	-0.3	0.2	-0.7	0
Amino acid	L-Proline	-1.3	0	2	0.1	-0.3	0.5	0.1	0.6	-0.3	0.4	-0.4	0.1	-	-	-	-	-	-
Amino acid	L-Serine	2.2	0	2.5	0	2.1	0	0.3	0.2	0.3	0.5	0.9	0	-0.1	0.7	-0.3	0	-1	0
Amino acid	L-Tryptophan	-1.6	0	-2.4	0	-1.3	0	-0.3	0.1	-0.8	0	-0.9	0	-0.3	0.5	-0.8	0	-0.8	0
Amino acid	L-Tyrosine	0.1	0.7	-2.3	0	-1.3	0	-0.4	0	-0.5	0	-0.6	0	0.1	0	-0.4	0.1	-1	0
Amino acid	L-Valine	-1.2	0	-1.4	0	-0.6	0	0.1	0.6	0.1	0.9	0.4	1	0.1	0.8	0.2	1	0.6	0.4
Amino acid	N-a-Acetyl-L-arginine	-	-	-1.6	0	-0.6	0	0.5	0.5	-0.2	0.4	-0.6	0.1	-0.3	0.2	0	0.5	-0.4	0
Amino acid	N-Acetylaspartylglutamic acid	-0.5	0.1	-1.5	0	-0.7	0.1	0.2	0.7	-0.3	0.4	-0.1	0.2	-1.3	0	-0.8	0	-2.9	0
Amino acid	N-Acetylisoleucine	-0.1	0	0.3	0.1	-0.1	0.5	2.4	0.4	0.4	0.8	1.4	0.5	0	0.6	0.1	0	0.1	0.2
Amino acid	N-Acetylleucine	-	-	0.9	0.7	0.4	0.7	-	-	0.4	0.6	-	-	-	-	-	-	0.7	0.5
Amino acid	N-Acetyltaurine	-0.4	0.1	-0.8	0	-0.7	0	0.1	0.9	-0.2	0.2	-5.9	0	-0.7	0.1	-0.7	0	-1.1	0
Amino acid	Ornithine	4.8	0	-0.4	0.3	-0.2	0.2	-0.5	0.1	-0.6	0	-0.3	0.2	0.2	0.6	0.3	0.1	-0.1	0.7
Amino acid	Pyroglutamic acid	-10.3	0	-0.7	0	-0.2	0.5	-0.1	0.2	0.2	0.4	-0.3	0.6	-0.3	0	-0.3	0	-0.6	0
Amino acid	Taurine	-0.4	0.1	-0.8	0	-0.7	0	0.1	0.9	-0.2	0.2	-5.9	0	-0.7	0.1	-0.7	0	-1.1	0
Amino acid	Thiamine	5.4	0.4	-1.2	0	-0.9	0	-1.2	0	-0.4	0.1	-0.3	0.3	-0.3	0.5	-0.2	0.4	-1.1	0
Amino acid	Threonine	0.1	0.4	1.4	0.5	0.6	0.9	-1.9	0.6	-0.5	0.1	0.6	0.5	-0.2	0.7	-0.3	0.1	0.7	0.3
Benzenoid	Benzoic acid	0.6	0.9	0.3	0.4	0.1	0.4	0.4	0	0.1	0.6	0.3	0.4	-0.2	0.3	-0.2	0	0.8	0
Carbohydrate	D-Glucose	-0.2	0.9	1	0	0.2	0.2	-0.2	0.4	-0.4	0	0.1	0.2	1.1	0	0.9	0	0.8	0
Carbohydrate	Glyceraldehyde3-phosphate	-1.5	0	-2.3	0	-1.4	0	0.2	0.3	-0.2	0.2	-1.3	0	0.2	0.9	-0.3	0.3	-1.7	0
Carbohydrate	Mannose6-phosphate	-0.3	0.2	-0.7	0.1	-0.2	0.3	0.8	0	0	0.9	0.2	0.3	0.3	0	0.7	0	0.5	0
Carbohydrate	N-Acetyl-glucosamine 1-phosphate	-1.3	0	-2.4	0	-1.6	0	-0.1	0.1	-0.6	0	-1.2	0	-	-	-	-	-	-
Carbohydrate	Threonic acid	-0.7	0	-0.9	0	-0.3	0.7	-0.5	0	-0.3	0.1	-0.8	0	-0.5	0	-0.6	0	-1.6	0
Carboxylic acid	5-L-Glutamyl-taurine	2.2	0	1.2	0	2.1	0	-	-	-	-	-	-	-	-	-	-	-	-
Carboxylic acid	Citric acid	-0.4	0.1	-1.3	0	-0.3	0.2	0.1	0.8	-0.2	0.9	-	-	-	-	-	-	-0.9	0
Carboxylic acid	Dodecanedioic acid	0.4	0.7	0.7	0.1	0.5	0.1	1.8	0.4	0.1	0.7	-1.1	0.6	0.3	0.3	0.3	0.2	0.4	0.1
Carboxylic acid	Fumaric acid	-	-	-	-	-	-	-	-	-	-	-	-	0.3	0.2	0.1	0.1	-2.3	0
Carboxylic acid	L-Lactic acid	-0.6	0	-0.5	0.1	0.4	0.3	0.1	0.7	-0.4	0	-0.5	0.1	-0.1	0.8	0.1	0.3	-0.9	0

Carboxylic acid	Phthalic acid	-	-	-1.6	0	-0.7	0.5	-0.5	0.7	0.7	0.3	-	-	-	-	-	-	-	
Carboxylic acid	Pyruvic acid	-0.7	0	-1	0	-0.6	0	1.7	0.5	-0.3	1	0	0.1	-0.5	0	-0.6	0	-1.2	0
Carboxylic acid	Succinic acid	-0.9	0.1	-1.2	0.1	-0.6	0.3	-	-	-	-	-	-	-	-	-	-	-	-
Carboxylic acid	Tetradecanedioic acid	-0.4	0.1	-0.2	0.3	-0.6	0	-	-	-	-	-	-	0.2	0.4	0.1	0.5	0.2	0.1
Carnitine	2-Methylbutyroyl	-0.7	0	-2	0	-1.2	0	0.1	1	-0.4	0	-0.9	0	-0.3	0.1	-1.2	0	-3.3	0
Carnitine	Butenylcarnitine	-	-	1.1	0.3	-0.2	0.6	1.2	0	1.9	0	2.9	0	1.1	0.3	1.5	0	1.2	0
Carnitine	Decanoylcarnitine	0.4	0.8	-0.1	1	0.2	1	0	0.9	-1.4	0.3	1	0.9	-1.5	0.6	-0.9	0.6	-0.7	1
Carnitine	Dodecanedioyl carnitine	-1.3	0.4	0.6	0.1	0	1	2.9	0.5	0.9	0.6	-	-	1.2	0	1.1	0	1.8	0
Carnitine	Heptadecanoyl carnitine	-	-	-1.8	0.4	1.3	0	0.2	0.7	-1	0.1	-0.4	0.3	0.7	0.7	0.2	0.8	1.2	0
Carnitine	L-Carnitine	-0.2	0.8	0	0.5	-0.4	0.1	-0.4	0.4	0.4	0.8	1.7	0.6	1.1	0.1	0.5	0.1	1	0
Carnitine	L-Hexanoylcarnitine	0.6	0.6	1.4	0.3	0	1	-0.4	0.1	-1.3	0	-1.6	0	-0.9	0	1.8	0	1.7	0
Carnitine	L-Palmitoylcarnitine	-8.5	0.2	0.3	0.5	0.5	0.5	0.1	0.9	-0.9	0.1	-0.9	0.1	0.1	0.7	1.2	0.1	1.6	0
Carnitine	Pentadecanoyl carnitine	-1.6	0.2	-0.5	0.1	0	0.9	0.7	0.2	-	-	-1.2	0.8	-1.1	0.1	-2.7	0	-1.4	0
Carnitine	Propionylcarnitine	-15.4	0	-1.4	0.2	-0.7	0.6	0.1	0.9	0.2	0.9	-0.9	0	0.1	0.6	-0.9	0	-2.8	0
Carnitine	Stearoylcarnitine	-1.2	0.9	2	0	2.4	0.1	-0.4	0.9	-1	0.2	-0.7	0.2	1.1	0.2	1.6	0	2.1	0
Carnitine	Tiglylcarnitine	-0.4	0.1	-0.3	0	0.2	0.4	0	0.9	-0.2	0.1	-0.5	0	0.1	0.3	0.1	0.3	-1.9	0
Carnitine	trans-2-Dodecenoylcarnitine	-1	0.6	0.8	0.8	-0.5	0.2	-0.6	0.8	-0.4	0.1	0.3	0.3	-0.9	0	-0.5	0.1	-0.8	0
Carnitine	trans-Hexadec-2-enoyl carnitine	-	-	-0.7	0.1	0.4	0.9	0.2	0.8	-0.9	0.2	-0.5	0.3	-0.8	0.1	-1.2	0	-1.2	0
Ceramide	Cer(d18:1/16:0)	-0.6	0.2	-2.4	0	-0.7	0.1	0.4	0.9	-1.7	0.1	-1.3	0.2	-1.5	0	-	-	-2.7	0
Ceramide	Cer(d18:1/24:1(15Z))	-2.3	0.1	-2.7	0	-3	0.1	-	-	-	-	-	-	-1.5	0.1	-3.6	0	-3.7	0
Cholesterol ester	Cholesteryl acetate	-1.4	0.6	-0.9	0	-0.8	0.2	-0.1	0.2	-0.4	0.1	-1.3	0	-	-	-	-	-	-
Fatty acid	Glycerol 3-phosphate	-1	0	-1.6	0	-0.7	0	-0.6	0.1	-0.8	0.1	-2	0	-0.1	0.6	0	0.9	-0.8	0
Fatty acid	Linoleamide	-2.8	0.1	-1.5	0.6	-0.1	1	-0.1	0.6	-3	0	0	0.7	-1.2	0.4	-0.8	0.4	-1.2	0.3
Fatty acid	Stearic acid	-0.4	0.5	0.4	0.4	-0.3	0.6	0.2	0.8	0.7	0.8	0.7	0.7	0.3	0.5	0.3	0.1	0.7	0
Fatty acid	Stearoylethanolamide	-	-	-	-	-	-	-	-	-1.2	0	-1.3	0	-0.8	0.6	-1.3	0.2	-1.4	0.1
Fatty acid	Tetraglyme	-	-	0.7	0.1	-2	0	0.8	0.4	0.7	0.8	2.4	0.2	0.7	0.1	0.4	0	0.9	0
Fatty amide	Oleamide	-2.8	0.1	-1.5	0.6	-0.1	1	-0.1	0.6	-3	0	0	0.7	-1.2	0.4	-0.8	0.4	-1.2	0.3
Furanone	Ascorbic acid	0	1	-0.8	0	-0.2	0.2	1.3	0.5	-	-	1.4	0.3	-2.2	0	-1.6	0	-0.3	0.1

Inorganic compound	Pyrophosphate	0	0.3	0.9	0	0.5	0.2	0.6	0.3	0.6	0.2	0.9	0	0.9	0.1	1.5	0	1.7	0
Keto acid	Acetoacetic acid	7.7	0	-0.5	0	0	0.2	-0.1	0.4	-0.2	0.1	-0.7	0	-0.2	0.3	-0.4	0	-1.5	0
Keto acid	alpha-Ketoglutaric acid	-0.4	0	-1.4	0	0.4	0	0.5	0	0.1	0.2	-0.3	0.1	-0.6	0	-0.4	0	-0.6	0
Keto acid	Levulinic acid	-	-	-	-	-	-	-	-	-1.1	0	-0.6	0	-1.1	0.1	-0.8	0	-2.4	0
Nucleobase	Adenine	-1.2	0	-1.9	0	-0.8	0	-	-	-	-	-	-	-0.3	0.2	-1.6	0	-5.2	0
Nucleoside	2'-Deoxycytidine	-	-	-	-	-	-	-	-	-	-	-	-	-0.4	0.5	-0.1	0.7	-0.9	0
Nucleoside	5'-Methylthioadenosine	-1	0.2	-1.4	0	-0.8	0	-1.5	0.2	-0.4	0.6	-0.8	0.8	-0.6	0.1	-0.7	0	-0.9	0
Nucleoside	Adenosine	-1	0.2	0.9	0	1.1	0.1	-1.5	0.2	-0.4	0.6	-0.8	0.8	-0.6	0.1	-0.7	0	-0.9	0
Nucleoside	Thymidine	-	-	-	-	-	-	-	-	-	-	-	-	-0.3	0.2	0.2	0.9	-2.1	0
Nucleotide	3'-AMP	-	-	0.9	0	1.1	0.1	-	-	-	-	-	-	-	-	-	-	0.4	0.9
Nucleotide	CDP-ethanolamine	-	-	-	-	-	-	-	-	-	-	-	-	2.5	0	-	-	2.9	0
Nucleotide	Cytidine 5'-diphosphocholine	-	-	-	-	-	-	-	-	-	-	-	-	1.4	0	1.7	0	1.3	0
Nucleotide	NAD	4.7	0.3	-1.5	0	-0.6	0	0.5	0.2	0	0.2	-0.5	0	-0.3	0.2	-0.6	0	-1	0
Nucleotide	NADH	-0.5	0	-1.2	0	-0.5	0.1	-	-	-	-	-4.7	0	-	-	-	-	-	-
Nucleotide	Uridine	-0.8	0	-1.9	0	-1	0	0.4	0.4	-1.1	0.4	-2	0	-0.6	0.1	-0.7	0	-1	0
Nucleotide	Uridine 5'-diphosphogalactose	-	-	-	-	-	-	-0.1	0.2	-0.2	0.1	-0.8	0	-	-	-	-	-	-
Nucleotide	Uridine 5'- diphosphoglucuronic acid	-0.6	0	-1.4	0	-1	0	0.1	0.8	-	-	-	-	-0.5	0	-0.9	0	-1.9	0
Nucleotide	Uridine diphosphate-N-acetylglucosamine	-0.5	0	-2	0	-1.4	0	-0.9	0	-0.7	0	-1.7	0	-0.5	0	-1	0	-2	0
Nucleotide	Uridine diphosphategalactose	-0.9	0	-1.4	0	-0.6	0	-	-	-	-	-	-	-0.7	0	-1.1	0	-2.7	0
PC	1,2-Dipalmitoleoyl-sn-glycero-3-phosphocholine	-	-	-3.1	0	-2.8	0	0.5	0.3	-1.8	0.1	-1.3	0.1	-	-	-	-	-	-
PC	LysoPC(14:1(9Z)/0:0)	-1.7	0.6	-3.7	0	-2.4	0	-	-	-	-	-	-	-	-	-	-	-	-
PC	LysoPC(24:1(15Z))	-2.4	0.5	-2.1	0	-1.8	0.2	0.8	0.3	-1.4	0.2	-2.1	0.1	-2.6	0	-4.2	0	-4	0
PC	LysoPC(P-16:0/0:0)	-1.9	0.3	-1	0.1	-1.3	0.2	-	-	-	-	-	-	-1.9	0.1	-3.3	0	-3.3	0
PC	PC(16:0/18:1(9Z))	-	-	-0.8	0.2	-0.7	0.8	0.4	0.3	-1.5	0.3	-1.2	0.1	-0.6	0.1	-2.8	0	-2.9	0
PC	PC(16:0/18:3(9Z,12Z,15Z))	-4.2	0.3	-0.5	0.1	-1.2	0.1	0.5	0.2	-	-	-	-	-0.5	0.3	-1.3	0	-1.5	0
PC	PC(18:1(9Z)e/2:0)	-	-	-0.5	0.1	-1.5	0.1	0.5	0.5	-1.4	0.1	-1.9	0	-2.8	0	-4	0	-3.3	0
PE	1-oleoyl-2-linoleyl-sn-glycero-3-phosphoethanolamine	-0.8	0.1	-2.5	0	-1.8	0	-	-	-	-	-	-	-0.6	0.3	-1.6	0	-3.2	0
PE	1-Palmitoyl-2-linoleoyl PE	-0.8	0.1	-2.7	0	-1.6	0	0	0.9	-0.9	0.3	-0.3	0.5	-	-	-	-	-	-
PE	LysoPE(18:0/0:0)	-	-	-1.9	0.3	-1	0.4	-	-	-	-	-1.2	0.2	-2.1	0	-2.8	0	-1.4	0.1
PE	LysoPE(18:1(9Z)/0:0)	-1.2	0	-2.1	0	-1.1	0	0.8	0.1	-	-	-	-	-	-	-	-	-	-
PE	PE(16:0/22:6(4Z,7Z,10Z,13Z,16Z,19Z))	-0.1	0.7	-0.7	0	-0.1	0.3	-	-	-1.3	0.6	-	-	-	-	-	-	-	-

PE	PE(18:0/20:4(5Z,8Z,11Z,14Z))	-	-	-0.1	0.1	0.2	0.1	1.4	0.3	-0.5	0.4	0.2	0.6	2.1	0.4	1.7	0.7	1.6	0.4
PE	PE(P-16:0/20:4(5Z,8Z,11Z,14Z))	0.5	0.7	0	0.5	0.6	0.5	-	-	-0.3	0.2	-	-	-	-	-	-	-	-
Peptide	Carnosine	5.2	0	-0.2	0.4	0	0.8	-0.2	0.3	-0.4	0	-0.4	0	-0.9	0	-1.2	0	-1.5	0
Peptide	L-Glutathione(reduced)	-1	0	-3.3	0	-1.4	0	0	0.4	-0.3	0.1	-1.7	0	-0.6	0	-1.2	0	-1.7	0
Peptide	L-Glutathione(oxidized)	-	-	1.5	0	-	-	1.2	0.1	-	-	-	-	-0.2	0.6	-	-	-	-
Peptide	Ophthalmic acid	5.9	0.1	-2.2	0	0.2	0.4	0.4	0	0.5	0	0.8	0	1.6	0	1.6	0	1.5	0
Peptide	Pro-leu	8.4	0	-1	0	0.1	1	1	0	1.2	0	1.3	0	-0.2	0.7	-0.1	0.7	-0.5	0
Phenylketone	Kynurenine	-1.7	0.3	-	-	-	-	-	-	-0.3	0.4	1.2	0.1	-	-	-	-	-	-
Polyamine	N-Acetylputrescine	-1.3	0	-2.8	0	-2.4	0	-	-	-	-	-	-	-	-	-	-	-	-
Polyamine	N1,N12-Diacetyl spermine	1.8	0.4	3.1	0	5.7	0	3	0	3.7	0	4.5	0	4.8	0	4.4	0	5.4	0
Polyamine	N1,N8-Diacetyl spermidine	1	0	0.5	0	2.2	0	1.1	0	1.4	0	0.7	0	1.3	0	0.5	0	0.5	0
Polyamine	N8-Acetyl spermidine	8.4	0	0.7	0	2.7	0	1	0.3	1.2	0	0.8	0	1	0	0.6	0	0	0.8
PUFA	Alpha-Linolenic acid	-	-	0.6	0.9	2	0.4	-0.3	0.6	-1	0.8	0.3	0.6	-1.3	0.5	-1.3	0.6	-1.5	0.5
PUFA	Linolenelaidic acid	-	-	2.3	1	-1.9	0	0.1	0.5	-1.7	0.2	1	0.3	-1.4	0.6	-2.7	0.2	0	0.5
Pyridine	Pyridoxal	-	-	0.8	0.1	0.2	0.9	1.3	0.5	1	0.7	1	0.6	0.2	0.6	0.2	0.4	0.2	0.8
Pyridine	Pyridoxamine	-1.4	0.2	-2	0	-0.3	0.8	1.8	0.4	0	0.8	0.5	0.7	-0.1	0.4	0.1	0.7	-0.5	0.2
Pyridine	Pyridoxine	-0.7	0	-1.5	0	7	0	-	-	-	-	-1.1	0.7	0.6	0.9	1.4	0	-	-
Pyrrolidine	1-Methyl pyrrolidine	-	-	2.1	0	0.9	0.1	-0.3	0.2	0.9	0.6	0.2	0.9	0.9	0	1	0	1.5	0
Pyrrolidine	Pyrrolidine	-0.6	0.3	-0.9	0.6	-0.8	0.3	-1	0.7	-2.6	0.1	1.9	0.5	-2.1	0	-0.1	0.6	-0.3	0.2
SM	SM(d18:0/14:0)	-3.1	0.1	-2.3	0	-3.1	0.1	-	-	-	-	-	-	-2.3	0	-3.9	0	-4.1	0
SM	SM(d18:1/16:0)	-4	0.1	-5.2	0	-3.9	0	1.1	0.3	-1.3	0.3	-1.2	0.1	-2.3	0	-3.4	0	-4.3	0

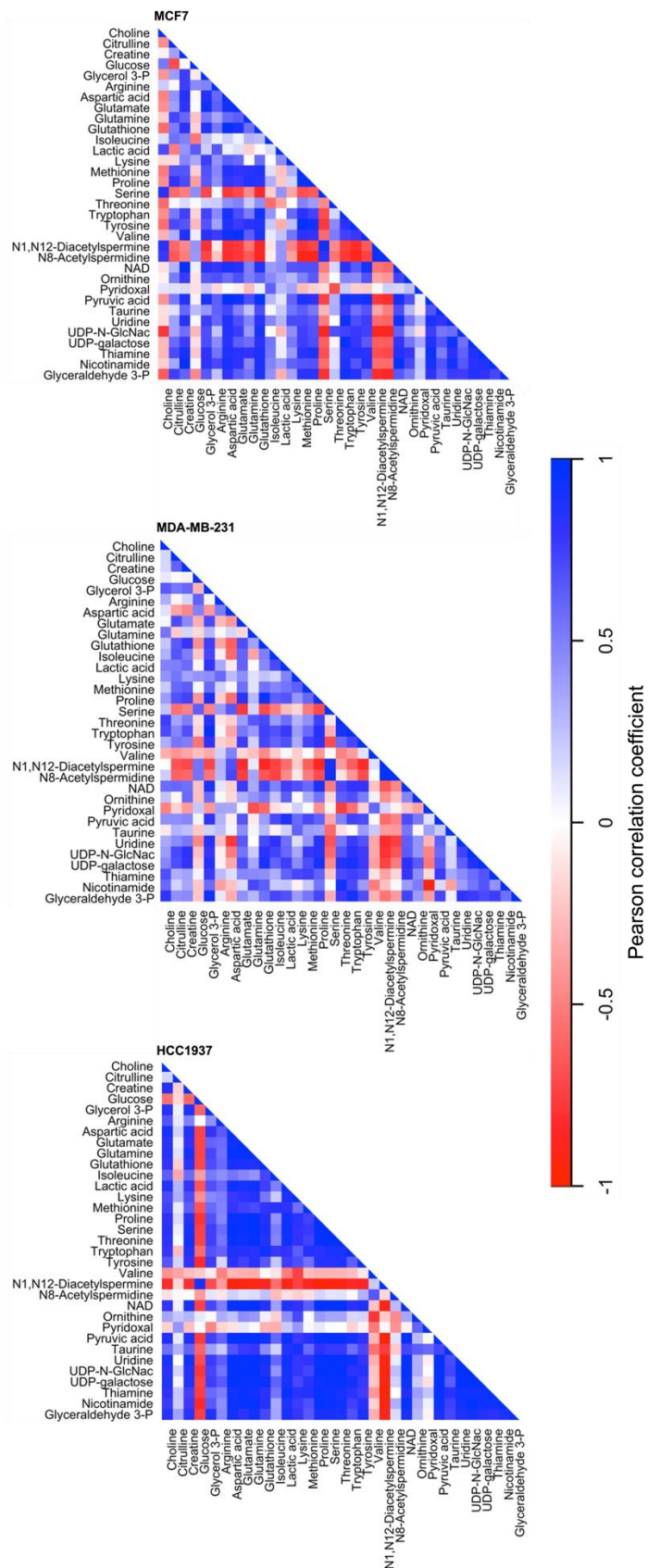


Figure S3. 11 Pearson's correlation analysis between the relevant metabolites identified within each different breast cancer cell line. Pearson's coefficient is set in a range of 1 to -1, indicative of a positive and negative correlation, respectively.

Table S3. 11 Effect scores of enriched metabolic genes in MCF-7, MDA-MB-231 and HCC1937 cells evaluated through the Dependency Map Portal (DepMap) database. Fitness effect score is based on the Chronos algorithm. Fitness Effect Score (FES).

PATHWAYS			MCF 7	MDA -MB- 231	HCC193 7
	FULL NAME	GENE	FES	FES	FES
Arginine biosynthesis					
	Glutamine synthetase	GLUL	-0.13	-0.05	-0.02
	Glutaminase 2	GLS2	-0.05	-0.11	-0.05
	Glutamic-oxaloacetic transaminase 1	GOT1	0.03	-0.06	-0.07
	Glutamic-Pyruvic Transaminase	GPT	0.04	0.11	-0.22
	Ornithine transcarbamylase	OTC	0.15	0.1	0.14
	Arginase 1	ARG1	0.23	0.09	0.02
	Nitric Oxide Synthase 1	NOS1	-0.02	-0.14	0
	Argininosuccinate Synthase 1	ASS1	-0.18	-0.4	-0.56
	Argininosuccinate Lyase	ASL	-0.11	-0.12	-0.05
Alanine, aspartate and glutamate metabolism					
	Succinate-semialdehyde dehydrogenase	SSDH	-0.15	-0.09	-0.24
	Aminobutyrate aminotransferase	ABAT	-0.05	-0.08	0.01
	Glutamate Decarboxylase 1	GAD1	-0.04	0	-0.1
	Glutamate Dehydrogenase 1	GLUD1	-0.02	-0.07	0.08
	Asparagine Synthetase	ASNS	-0.37	-0.56	-0.4
	Glycine Amidinotransferase	GATM	-0.05	-0.12	-0.18
Arginine and proline metabolism					
	Ornithine Decarboxylase 1	ODC1	-0.05	0.05	0.11
	Spermidine/Spermine N1-Acetyltransferase	SAT2	-0.19	0	-0.18
Taurine and hypotaurine					
	Glutamate Decarboxylase 1	GAD1	-0.04	0	-0.1
	Glutamate Decarboxylase Like 1	GADL1	0.08	-0.12	0.05
	Gamma-Glutamyltransferase 6	GGT6	-0.05	-0.09	-0.01
Glycine, serine and threonine metabolism					
	Serine Dehydratase	SDS	0.21	0.01	0.02
	Serine Hydroxymethyltransferase	SHMT	0.09	-0.11	-0.17

	Alanine-Glyoxylate Aminotransferase	AGXT	0	0.06	-0.09
	Guanidinoacetate Methyltransferase	GAMT	-0.07	0.02	0.04
	Antiquitin 1	ATQ1	-0.15	-0.08	0.02
	Arginine:glycine amidinotransferase	AGAT	-0.05	-0.12	-0.18
Vitamin B6 metabolism					
	Pyridoxine 5-prime-phosphate oxidase	PNPO	0	-0.06	0.04
Cysteine and methionine metabolism					
	Betaine-homocysteine methyltransferase	BHMT	-0.1	-0.08	0.04
	Glutathione Synthetase	GSS	-0.09	-0.01	0.17
	ChaC Glutathione Specific Gamma-Glutamylcyclotransferase 1	CHAC	0.1	-0.12	-0.19

) and DDR defects to olaparib exposure through combined analysis of DNA damage and metabolomics profiling. Combined evaluation of the DNA damage response and metabolic reprogramming offers new opportunities in the development of novel chemotherapies against cancer.

4.3. Materials

4.3.1. Cell lines and chemicals

All cell lines used in this study were purchased from the vendor and maintained in accordance with manufacturer instructions. All cell culture reagents were obtained from Gibco (Thermo Fisher Scientific). MCF7 (RRID:CVCL_0031, Sigma, EACC collection) and MDA-MB-231 cells (RRID:CVCL_0062, ATCC) were purchased and maintained in Dulbecco's Modified Eagle Medium (DMEM, high glucose) supplemented with 10% v/v FBS (high glucose, Invitrogen), 1% v/v non-essential amino acids (NEAA) and 1% v/v penicillin-streptomycin (Invitrogen). Corresponding cell line origins, hormone receptor status and mutational profiles are included in **Table S3. 2**. HCC1937 cells obtained from ATCC (RRID:CVCL_0290) were maintained in RPMI supplemented with 10% v/v FBS and 1% v/v penicillin-streptomycin. All

cell lines were maintained at 37°C in a pre-humidified atmosphere containing 5% v/v CO₂ and used within ten passages for the purposes of this work (passage 2-10). Olaparib (SantaCruz Biotechnology Inc.) was prepared as a 100 mM stock solution in DMSO, aliquoted and stored at -20°C until use. γH2AX, p53BP1 primary antibodies (Cell Signalling Technologies) were used for foci immunostaining alongside the Alexa Fluor® 488-conjugated secondary antibody (Fisher Scientific).

4.4. Methods

4.4.1. Cell Viability Assays

MCF-7, MDA-MB-231 and HCC1937 cells undergoing exponential growth were seeded at a density of 4,000 cells/well in 96 well plates and incubated overnight to facilitate cell attachment. On the following day, cells were exposed to either blank growth medium (control) or growth medium containing different concentrations of olaparib (treatment medium) ranging from 0.01-500 μM for seven days at 37°C and 5% v/v CO₂. Treatment media were replaced every three days with treatment medium. Following a seven-day incubation, cell viability was measured using CellTiter 96® Aqueous Non-Radioactive Cell Proliferation Assay (Promega) (3-(4,5-dimethylthiazol-2-yl)-5-(3-carboxymethoxyphenyl)-2-(4-sulfophenyl)-2H-tetrazolium (MTS) reagent. The resultant absorbance at 490 nm was measured using a GM3500 Glomax® Explorer Multimode Microplate Reader (Promega).

Growth curves represent percentage cell growth following treatment with different concentrations of olaparib and are plotted as a semi-log dose-response curve. The half maximal inhibitory concentration (IC₅₀) was determined using a linear regression model. Statistical analysis was performed using GraphPad Prism (RRID:SCR_002798, v.9.0.1). Three

independent biological replicates (five wells per treatment concentration) were performed for each cell line.

4.4.2. Immunostaining for γ H2AX and p53BP1

Foci immunodetection for γ H2AX and p53BP1 was performed in both control (growth medium) and for cells treated with olaparib (IC₁₀, IC₂₅ and IC₅₀ doses) for seven days. Briefly, cell monolayers were fixed in chilled 4% w/v formaldehyde containing 2% w/v sucrose in PBS, followed by fixation in ice-cold methanol (100% v/v). Subsequently, cells were permeabilized in 0.25% v/v Triton X-100 in PBS, blocked with 5% v/v goat serum/5% w/v BSA, immunoprobed with either a primary rabbit anti- γ H2AX antibody (RRID:AB_420030) (1:1000) or primary rabbit anti-P53BP1 (1:200) antibody (RRID:AB_11211252, CST #2675 for p53BP1) overnight at 4°C. Cell monolayers were treated with goat, anti-rabbit Alexa Fluor® 488 conjugated secondary antibody and counterstained with DAPI. Image acquisition was carried out using an Invitrogen EVOS Auto Imaging System (AMAFD1000-Thermo Fisher Scientific) with a minimum of 100 cells imaged per treatment condition. Resultant foci images were analysed in Cell Profiler (v.4.2.1.) using a modified version of the speckle counting pipeline.

4.4.3. Sample preparation and metabolite extraction

MCF-7, MDA-MB-231 and HCC1937 cells were seeded at a density of 2×10^6 cells per well in 6-well plates, and exposed to growth medium containing olaparib at IC₁₀, IC₂₅ and IC₅₀ doses, as determined from the MTS assay (n=5 per treatment concentration). Following exposure to olaparib, the growth medium was aspirated from each well, centrifuged to remove cell debris, and stored at -80°C. Next, treated cells were washed with pre-chilled PBS, with the metabolites quenched and

extracted in a final volume of 1.5 ml pre-chilled (-80°C) mixed solvent (methanol:acetonitrile:water=50:30:20, v/v). Resultant cell pellets were collected, and submerged in liquid nitrogen, vortexed and sonicated for 3 min in an ice-water bath. This procedure was performed in triplicate. Resultant extracts were centrifuged at 13,000x g for 10 min at 4°C and the pellets were retained for protein quantification using the Bradford assay. The resultant supernatant was collected, and dried with a Speed vac centrifuge (Savant-SPD121P). Dried metabolite pellets were reconstituted in acetonitrile:water (50:50, v/v) at volumes normalized to the relative protein content. Quality control (QC) samples were prepared by pooling samples across all control and treatment groups. Solvent blank and QC samples were inserted in analytical batch after every five samples to assess the stability of detecting system (**Figure S3. 2**).

4.4.4. Liquid Chromatography Tandem Mass Spectrometry (LC-MS/MS)

Metabolite separation was performed on a binary Thermo Vanquish ultra-high-performance liquid chromatography system where 5 µl of reconstituted cellular extract was injected on to a Thermo Accucore HILIC column (100 mm x 2.1 mm, particle size 2.6 µm). The temperature of the column oven was maintained at 35°C while the autosampler temperature was set at 5°C. For chromatographic separation, a consistent flow rate of 500 µl/min was used where the mobile phase in positive heated electrospray ionisation mode (HESI+) was composed of buffer A (10 mM ammonium formate in 95% acetonitrile, 5% water with 0.1% formic acid) and buffer B (10 mM ammonium formate in 50% acetonitrile, 50% water in 0.1% formic acid). Likewise, in negative ionisation mode (HESI-) buffer A (10 mM ammonium acetate in 95% acetonitrile, 5% water with 0.1% acetic acid) and buffer B (10 mM ammonium acetate in 50% acetonitrile, 50% water with 0.1% acetic

acid). The elution gradient used for the chromatographic separation of metabolites is included in supplementary information (**Table S3. 3**).

A high-resolution Exploris 240-Orbitrap mass spectrometer (ThermoFisher Scientific) was used to perform full scan and fragmentation analyses. Global operating parameters were set as follows: spray voltages of 3900 V in HESI+ mode, and 2700 V in HESI-mode. The temperature of the transfer tube was set as 320°C with a vaporiser temperature of 300°C. Sheath, aux gas and sheath gas flow rates were set at 40, 10 and 1 Arb, respectively. Top-5 Data dependent acquisitions (DDA) were performed using the following parameters: full scan range was 70 – 1050 *m/z* with a MS1 resolution of 60,000. Subsequent MS/MS scans were processed with a resolution of 15,000. High-purity nitrogen was used as nebulising and as the collision gas for higher energy collisional dissociation. Further details are included in supplementary information (**Table S3. 5**).

4.4.5. Mass Spectrometry Data Processing

Raw data files obtained from Thermo Scientific Xcalibur™ software 4.2 were imported into Compound Discoverer™ 3.2 software where the “Untargeted Metabolomics with Statistics Detect Unknowns with ID Using Online Databases and mzLogic” feature was selected (**Table S3. 5****Error! Reference source not found.**). The workflow analysis performs retention time alignment, unknown compound detection, predicts elemental compositions for all compounds, and hides chemical background (using Blank samples). For the detection of compounds, mass and retention time (RT) tolerance were set to 3 ppm and 0.3 min, respectively. The library search was conducted against the mzCloud, Human Metabolome Database (HMDB) and Chemical Entities of Biological Interest (ChEBI) database. A compound table was generated

with a list of MSI2 level putative metabolites (known and unknown). Among them, we selected all the known compounds fully matching at least two of the annotation sources. The selected metabolites were then used to perform pathway and statistical analysis.

4.4.6. Pathway Analysis with MetaboAnalyst

Prior to analysis of the metabolic pathways with MetaboAnalyst 5.0 (<https://www.metaboanalyst.ca/>), a HMDB identification code was assigned to each selected metabolite. A joint pathway analysis was performed by integrating the genes relative to each cell line (**Table S3. 2**) with the list of ID compounds and their associated Log2 Fold change values. The integration method combined both genes and metabolites into a single query, then used to perform the enrichment analysis. This latter was based on a hypergeometric test. Finally, important nodes (compounds) were scored based on their betweenness centrality, and pathway analysis results were generated.

4.4.7. Statistical Analysis

All data are presented as mean \pm standard deviation ($n \geq 5$). For cell viability and immunofluorescence quantification data, the Shapiro normality test was performed (**Table S3. 4**). For metabolomics analysis, Principal Component Analysis (PCA) was performed to test analytical reproducibility of QC injections, reduce the dimensionality of our data and determine the metabolic profiles of the different sample groups. Differential analysis was used to compare differences between control and treatment groups and plotted as a Volcano plot (log-fold change vs. $-\log_{10}$ p-value). Peak areas were \log_{10} transformed and p values calculated for the sample group by two-tailed t-test test assuming that all

data were normally distributed. A p value < 0.05 and fold-change of 1.5 was deemed to be statistically significant.

4.5. Results

4.5.1. Olaparib sensitivity analysis

To determine the olaparib dose range for subsequent foci and metabolomics experiments, we measured the sensitivity of MCF7, MDA-MB-231 and HCC1937 cell lines to olaparib exposure over a seven day treatment duration. The rationale behind exploring sensitivity to olaparib in these cell lines, was to perform a comparison between two triple-negative (MDA-MB-231 and HCC1937) and a non-triple-negative (MCF-7) cell line.

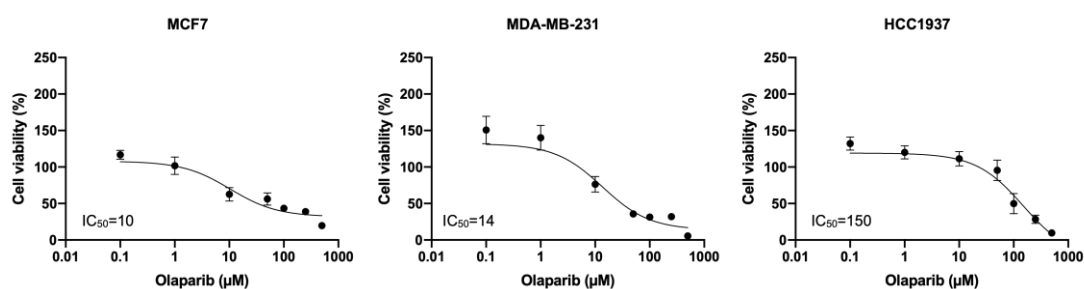


Figure 4. 1 Corresponding MTS dose-response curves for MCF7, HCC1937 and MDA-MB-231 cells treated with ascending doses of olaparib (0.1-500 μM) for seven days. The corresponding R^2 values for fitted dose-response curves in MCF7 ($IC_{50}= 10 \mu M$), MDA-MB-231 ($IC_{50}= 14 \mu M$), and HCC1937 ($IC_{50}= 150 \mu M$) cells were 0.89, 0.91 and 0.85, respectively. The equation for the non-linear regression curve is $Y= Bottom - (Top - Bottom)/(1+(X/IC_{50}))$. IC_{50} is the concentration of drug that gives a response halfway between Bottom and Top. This is not the same as the response at $Y=50$.

Our results show that exposure to olaparib caused a reduction in cell viability in all cell lines in a dose-dependent manner (**Figure 4. 1**). We observed superior efficacy of olaparib in reducing cell viability in both MCF7 and MDA-MB-231 cells, with a calculated half maximal inhibitory concentration (IC_{50}) of 10 μM and 14 μM, respectively. However, in the

case of HCC1937 cells, a higher concentration of olaparib was required to achieve the same reduction in cell viability (150 μ M), indicating a lower efficacy of response to olaparib in this cell line.

4.5.2. Exposure to olaparib induces dose-dependent formation of γ H2AX and 53BP1 foci in breast cancer cells

PARP inhibition induced by olaparib exposure results in the accumulation of DNA damage in cells by compromising their DDR mechanisms. Therefore, we next investigated the extent to which olaparib exposure at various doses (IC_{10} , IC_{25} and IC_{50} - determined from MTS assays) promotes the accumulation of DNA double strand breaks (DSBs) in MCF-7, MDA-MB-231 and HCC1937 cell lines. Key markers for DNA DSB formation include phosphorylated histone H2 variant H2AX (γ H2AX) [19] and the damage sensor p53-binding protein 1 (p53BP1), which are rapidly recruited to sites of DNA damage and their accumulation is directly proportional to the number of DSB lesions [20]. To measure the extent of DNA DSB formation, we performed immunofluorescence of p53BP1 and γ H2AX foci.

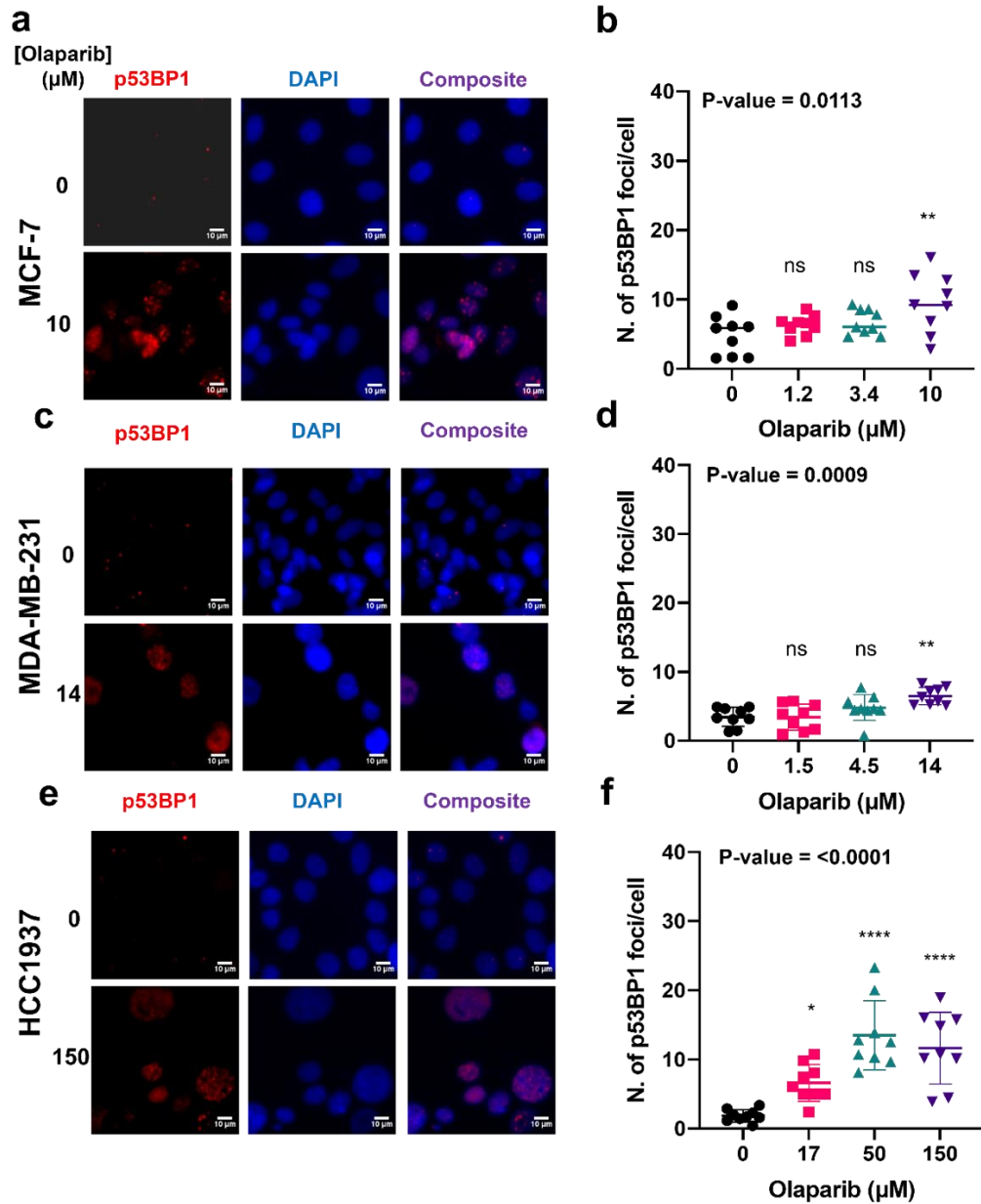


Figure 4. 2 The formation of p53BP1 foci in response to treatment with either growth medium or medium containing olaparib. Representative images of immunolabelled P53BP1 foci (red), DAPI (blue) nuclear counterstain and composite (p53BP1 (red) and DAPI (blue)) in MCF-7, MDA-MB-231, and HCC1937 cells treated with olaparib for seven days (a, c, e). Corresponding p53BP1 foci counts determined using Cell Profiler (b, d, f). 9 repeats with on average >100 cells per each sample. p-values have been determined through ANOVA test. Dunnett's multiple comparison test was used as a follow up to ANOVA test and the p-values were represented as: non-significant=ns, 0.05=*, 0.005=**, 0.0005=***, >0.00005=****.

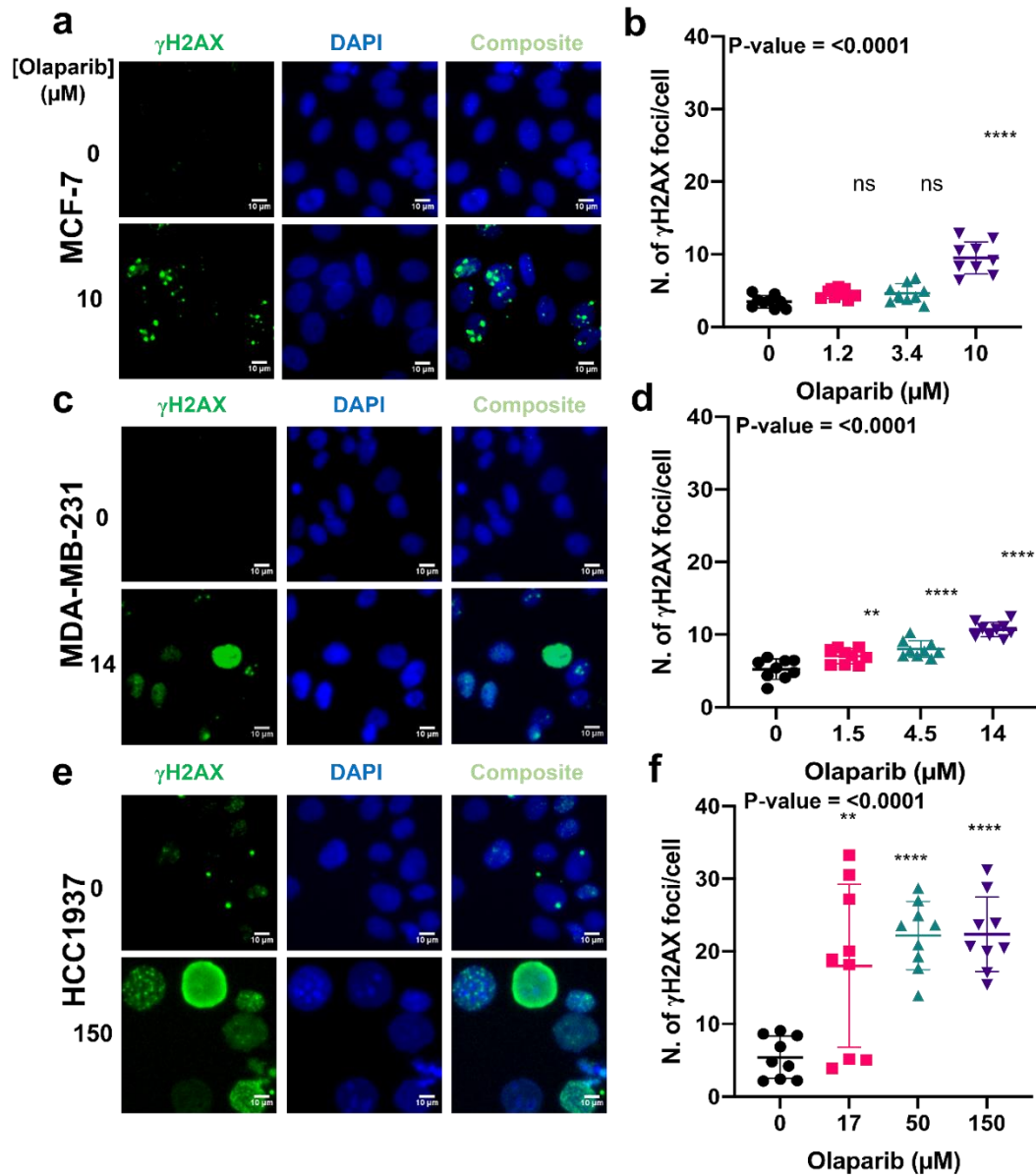


Figure 4.3 The formation of γ H2AX foci formation in response to treatment with either growth medium or medium containing olaparib. Representative images of immunolabelled γ H2AX foci (green), DAPI (blue) nuclear counterstain and composite (γ H2AX and DAPI) in MCF-7, MDA-MB-231, and HCC1937 cells treated with for seven days (a, c, e). Corresponding γ H2AX foci counts determined using Cell Profiler (b, d, f). (>100 cells per sample). Dunnett's multiple comparison test was used as a follow up to ANOVA and corresponding p-values were represented as: non-significant=ns, 0.05=*, 0.005=**, 0.0005=***, >0.00005=****.

Based on our results, p53BP1 and γ H2AX foci levels increased in a dose-dependent manner in both MCF7 and MDA-MB-231 cells in

response to ascending doses of olaparib (**Figure 4. 2a,b,d,e**; **Figure 4. 3a,b,d,e**). However, in HCC1937 cells, a significant increase in foci numbers was not observed in comparison to increased foci numbers with ascending olaparib doses for MCF-7 and MDA-MB-231 cells (**Figure S3. 3c**; **Figure S3. 4c**). Generally, a higher number of both p53BP1 (mean >10 foci per cell) and γ H2AX (mean > 20 foci per cell) foci were observed in the HCC1937 cell line, compared to the MCF7 and MDA-MB-231 cells, where a mean of <10 foci per cell were measured for both markers. These results are consistent with the dose-dependent sensitivity of MCF7 and MDA-MB-231 cells in response to olaparib exposure, further confirming cell-line dependent response to olaparib exposure.

4.5.3. Biomolecular pathways altered in response to olaparib exposure vary across different cell lines

To comprehensively measure the extent of variation induced by olaparib exposure in MCF-7, MDA-MB-231 and HCC1937 cell lines, we profiled their metabolome using an in-house untargeted liquid chromatography-mass spectrometry-based metabolomics pipeline (**Figure S3. 5a**). After data acquisition, data processing and analysis were performed in Compound Discoverer 3.2. First, we used principal component analysis (PCA) to visualise and interpret the clustering of quantified metabolite data to examine global differences between treatment groups and cell lines examined, which was followed by pairwise PCA between control and treated groups across positive and negative analysis modes (**Figure 4. 4**).

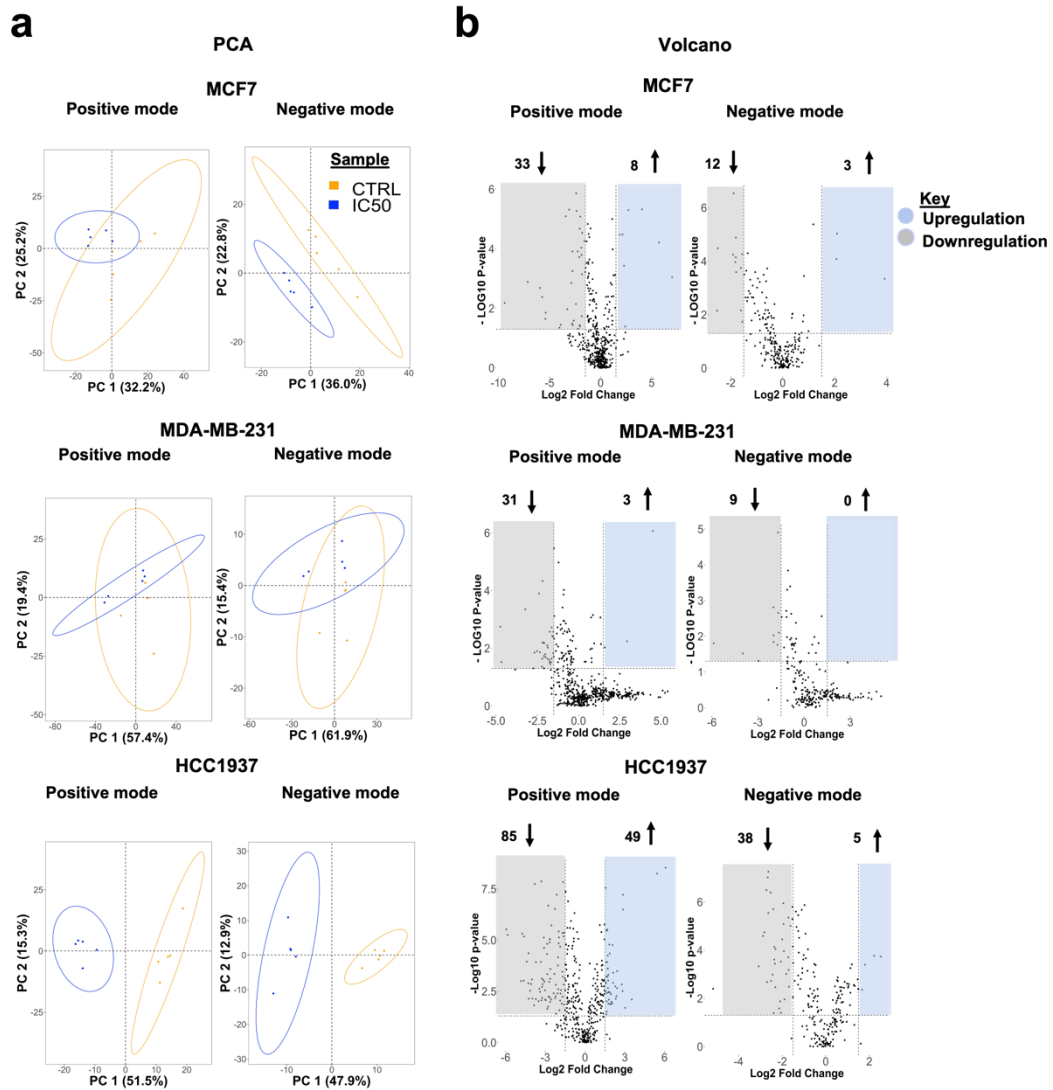


Figure 4. 4 Statistical analyses of global metabolic features identified in MCF7, MDA-MB-231 and HCC1937 upon exposure to IC₁₀, IC₂₅ and IC₅₀ olaparib doses for seven days. Data acquired in positive and negative ionization mode. For each treatment group, five replicates were used. Data points in the two-dimensional PCA score plot were central scaled. a) PCA pairwise analysis and differential analysis of metabolites altered in IC₅₀-treated cells, ellipses represent the 95% confidence interval. b) Volcano plots displaying enriched (blue) and depleted (grey) metabolic features by representing the log₂ fold change in altered features and the -log₁₀ adjusted p-values with cut off values selected at >1.5 and <0.05, respectively.

Pooled quality control (QC) data confirm the stability of the data acquisition system across all the measurements performed in positive and negative ionization acquisition modes (**Figure S3. 5b**). Distinct

clustering patterns were observed, with better separation for the IC₅₀ olaparib treatment dose across all cell lines (**Figure 4. 4a, Figure S3. 6**). Volcano plots indicate the differential number of metabolic features that are significantly altered following exposure to olaparib, relative to control (**Figure 4. 4b, Figure S3. 7**). From a metabolic perspective, we observed that HCC1937 (BRCA1-mutated) cells were the most susceptible to exposure at the IC₅₀ olaparib treatment dose, while the MCF7 cells showed a higher number of significantly altered metabolic features at the IC₂₅ olaparib treatment concentration. Together, these findings show a differential dose- and cell line- dependent metabolic response to olaparib exposure. Similar results were obtained by processing the data with 70% annotation threshold and increasing the number of adduct ions (**Figure S3. 8**).

4.5.4. Amino acid and lipid metabolism are significantly altered in response to olaparib exposure

To analyse specific biomolecular pathways altered by olaparib exposure, we used MetaboAnalyst to identify key metabolic pathways significantly perturbed by olaparib treatment, and performed enrichment analysis for both control and treated samples (**Figure 4. 5, Figure S3. 9**). Among the pathways ranked in the top ten, we selected altered pathways with a corresponding pathway impact >0.1, and a p-value <0.05.

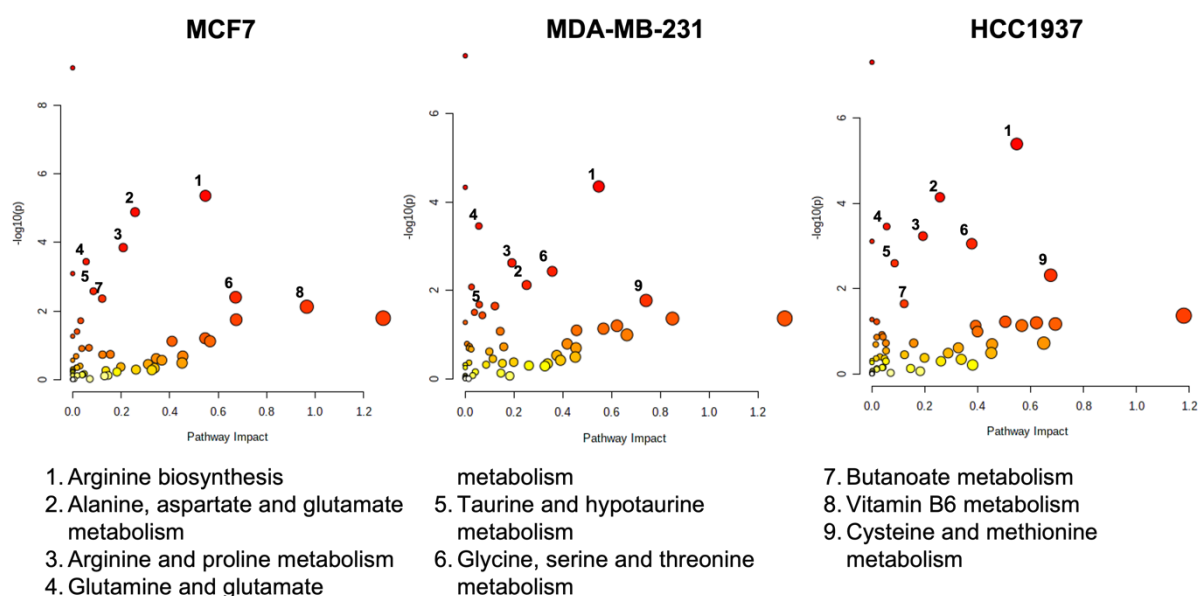


Figure 4. 5 Pathway enrichment analysis of MCF7 (10 μ M), MDA-MB-231 (14 μ M) and HCC1937 (150 μ M) cells following a seven-day exposure to olaparib. Enrichment analysis was based on the hypergeometric test. Topological analysis was based on betweenness centrality. The tight integration method was used by combining genes and metabolites into a single query. A $p < 0.05$, and pathway impact > 0.1 were deemed significant.

Across all cell lines examined, the top ten putative pathways significantly altered in Metaboanalyst (see Figure 4. 5) were based on amino acid (arginine biosynthesis, glutamine, glycine, serine and threonine metabolism) and lipid metabolism (butanoate metabolism). Following the identification of metabolic pathways altered by olaparib exposure, we constructed a Venn diagram (Figure S3. 10) to outline common overlapping and cell line-specific altered metabolic features.

Overlapping pathways are mostly represented by amino acid metabolism (glutamine, glutamate, aspartate, alanine, arginine and proline), suggesting a strong reliance of breast cancer cell metabolism on amino acids under baseline conditions (control samples). Upon olaparib exposure, the same pathways (amino acid metabolism) were among the most significantly-altered across all cell lines, while fatty acid (butanoate metabolism) and vitamin B6 metabolism were only significantly perturbed in MCF-7 cells.

Mummichog software was also employed to putatively design metabolic pathways. Based on our results, only a few pathways matched the ones revealed from MetaboAnalyst (**Table S3. 9**). Considering that our data have a MSI2 level of metabolites annotation, while Mummichog is better suited for MSI level 3 putative IDs, we decided to continue the analysis using MetaboAnalyst.

Next, we explored individual metabolites that were associated with significantly altered metabolic pathways in response to olaparib exposure and evaluated relative changes in their levels between control and treatment samples. These results are presented through a heatmap clustering analysis (**Figure 4. 6**). A correlation analysis between each metabolite is shown in **Figure S3. 11**, and a wider list of compounds specific for each cell type is provided in **Table S3. 10**.

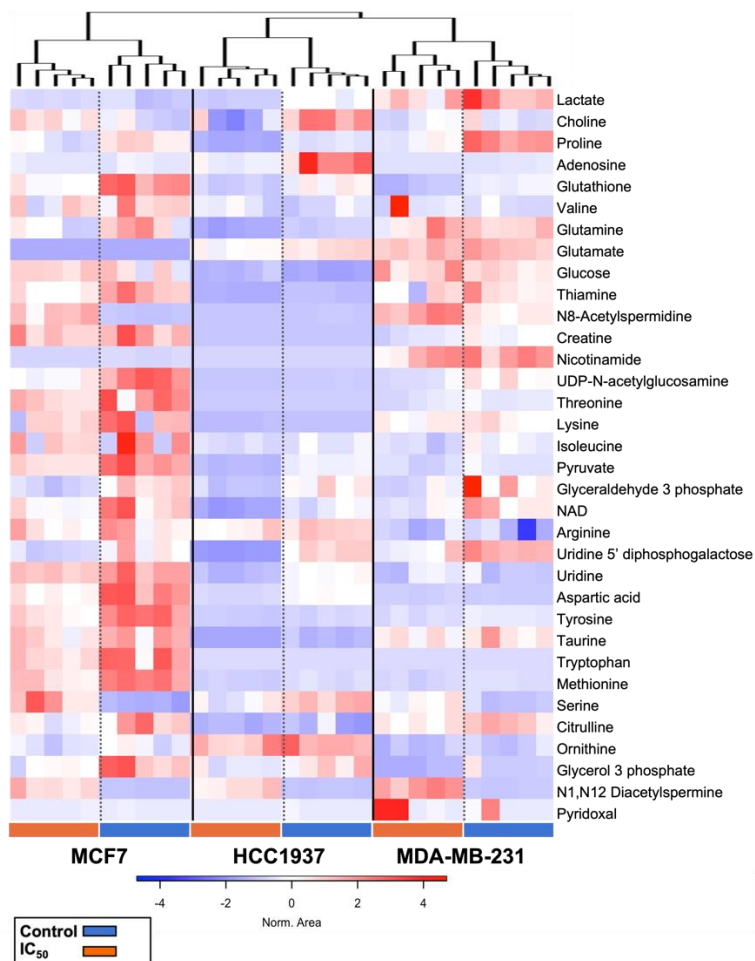


Figure 4. 6 Heatmap cluster analysis of relevant metabolites associated with the pathways altered upon exposure to olaparib in MCF7 (10 μ M), MDA-MB-231 (14 μ M) and HCC1937 (150 μ M) cells for seven days. Clustering and distance function are Ward and Canberra, respectively. Normalised areas indicate chromatographic peaks areas that have been normalised based on the QC samples to compensate for batch effects.

Multiple amino acids (glutamine, glutamate, arginine, proline, methionine, glycine, threonine, taurine, and hypotaurine) were found to be depleted following olaparib exposure (relative to control) in all cell lines examined. Arginine and proline metabolism were significantly depleted by olaparib exposure, with depletion of their derived polyamines detected in all cell lines examined. Conversely, catabolic products of arginine and proline metabolism (N8-Acetylspermidine, N1-N8-Diacetylspermidine, and N1-N12-Diacetylspermine) were enriched.

Elevated levels of serine were observed in MCF7 and MDA-MB-231 cells, while depletion of serine levels was seen in HCC1937 cells.

Alpha-ketoglutarate (α -KG- glutamine-derived intermediate of the TCA cycle) was enriched in MCF7 and depleted in MDA-MB-231 and HCC1937 cells. A negative correlation was observed between α -KG and glutamine levels, and a positive correlation between α -KG, and citric and fumaric acid (TCA cycle intermediates). Aspartate (a TCA cycle product), accumulated in the KRAS-mutant MDA-MB-231 cells, while aspartate depletion was observed in MCF7 and HCC1937 cells. Glucose levels were significantly elevated relative to control samples in HCC1937 cells. Asparagine (a byproduct of aspartate) was absent in MDA-MB-231 cells, while its enrichment was detected in MCF7 and HCC1937 cells. In parallel, accumulation of AMP was observed in both MCF7 and HCC1937 cell lines, while it was absent in MDA-MB-231 cells and enrichment of PPI was detected in all cell lines examined following olaparib exposure.

In the case of lipid metabolism, we observed a global depletion of phosphocholines (PC) and phosphoethanolamines (PE) in all cell lines following olaparib treatment. Acylcarnitine levels varied across the cell lines, with an overall enrichment of long (C14 – C21) and very-long chain acylcarnitines (>C22) in all cell lines treated with olaparib. Moreover, we observed enriched alpha-linoleic acid (a polyunsaturated fatty acid-PUFA) levels in MCF7 and MDA-MB-231 cells, which was absent in HCC1937 cells.

Compared to non-treated cells, elevated levels of glucose were detected in all cell lines studied following olaparib treatment, while downregulation of most nucleobases was observed. Finally, NAD⁺ downregulation was detected in all cell lines treated with olaparib.

An overview of the metabolic features altered in response to olaparib exposure is given in **Figure 4. 7**, where we mapped cell line differences in metabolite levels through the Kyoto Encyclopaedia of Genes and Genomes (KEGG) database. Moreover, in the figure we represented the fitness effect score of metabolic enzymes relative to each Olaparib-treated cell, which have been obtained through a cross comparison with the Dependency Map Portal (DepMap; **Table S3. 11**). The fitness effect score measures the effect of knocking out a gene on cell proliferation. A negative score indicates that the knocked-out gene causes a slower cell proliferation, while a positive score is indicative of a consequent enhanced proliferation [21].

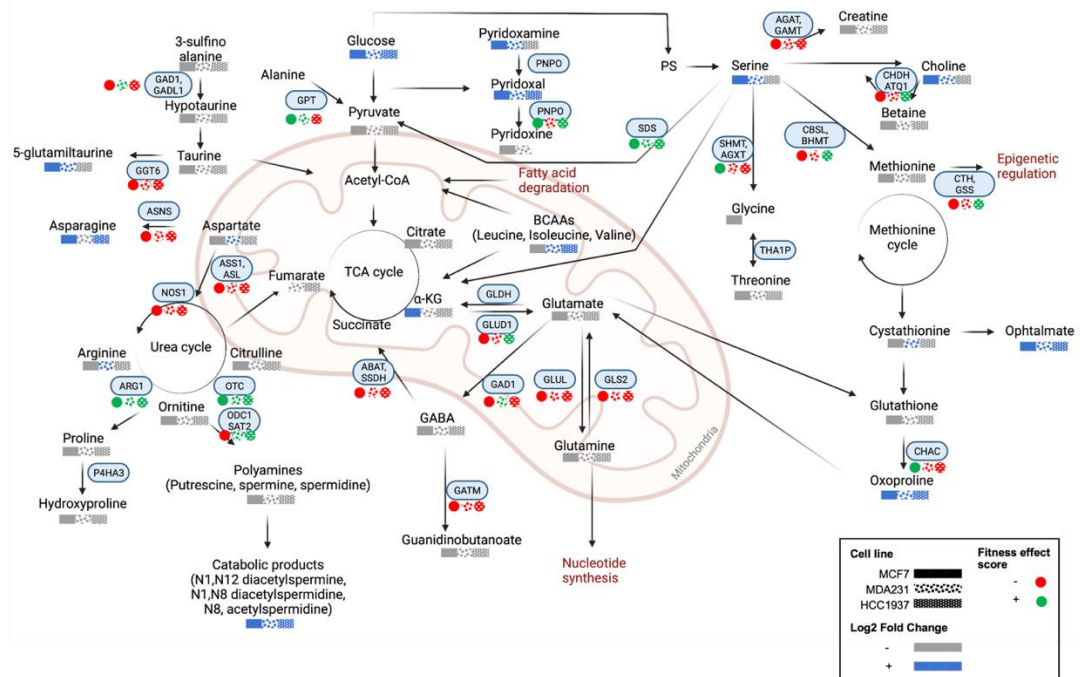


Figure 4. 7 A summary of putatively identified metabolic pathways altered in response to olaparib exposure. Significantly altered features with a Log₂ fold change of >1.5 (blue-enriched and grey-depleted). Fitness effect score of metabolic enzymes (light-blue boxes) in relation to PARP expression in each cell line. Positive and negative scores are in green and red, respectively. MCF-7 (█), MDA-MB-231 (▒), and HCC1937 (▓). Fitness effect score is based on the Chronos algorithm.

4.6. Discussion

PARP inhibitors have shown promising results in the treatment of metastatic breast cancers harbouring germline BRCA1/2 mutations [22, 23]. Recent clinical studies have shown evidence of PARP inhibitor efficacy in the management of breast cancer, irrespective of tumour BRCAness [24]. Prior work has shown that BRCA1-mutated cells carrying a TP53 mutation are resistant to treatment with PARP inhibitors [25]. Therefore, additional factors beyond BRCAness may govern sensitivity to PARP inhibition.

In this study we analyzed the sensitivity of two triple-negative (MDA-MB-231 and HCC1937) and MCF-7 (ER+, PR-, HER2-) cell lines to olaparib PARP inhibition (PARP1/2). The rationale for selecting these cell lines was to explore how their different genetic profiles (see **Table S3. 2**) define the observed differential biomolecular perturbations in response to olaparib treatment. Initially, we examined the responsiveness of MCF-7, MDA-MB-231 and HCC1937 cell lines to olaparib exposure using the MTS cell viability assay (**Figure 4. 1**). Our results show differential sensitivity to olaparib exposure across the cell lines examined, with MCF-7 and MDA-MB-231 showing sensitivity to olaparib treatment at lower micromolar concentrations, and the BRCA1-mutant HCC1937 cell line showing less sensitivity (IC_{50} - 150 μ M). These findings are in agreement with previous reports of HCC1937 resistance to PARP inhibition, where the identification of predictive biomarkers of response to PARP inhibitor treatments was recommended beyond BRCA1/2 status [25].

Our analysis of γ H2AX and p53BP1 DNA DSB immunolabelled foci (**Figure 4. 2**, **Figure 4. 3**) showed a higher occurrence of DNA damage

foci in HCC1937 cells in comparison with MCF-7 and MDA-MB-231 cells with wild-type BRCA status. These observations suggest that BRCA status does not necessarily translate to olaparib sensitivity, and additional DDR components may define responsiveness. At present, routine clinical decision making surrounding the selection of treatment interventions are based on BRCA status, anatomical location, hormone receptor status and tumour stage, with very limited attention given to other mediators of DDR- namely homologous recombination- known to confer a BRCAness phenotype similar to BRCA 1 or 2 loss. Several recent studies have used whole-genome sequencing or the integration of homologous recombination panel scoring systems to provide an additional framework for predicting responders to PARP inhibitor treatment [26, 27].

Genetic biomarkers are routinely used in the clinical stratification of breast cancers and predicting treatment-emergent resistance [28]. While genome-wide studies have improved patient stratification efforts, they lack the potential to account for functional phenotypic effects resulting from protein expression levels, or gain- or loss of function effects. Metabolomics has emerged in the past decade as an additional research toolbox for studying potential biomarkers of breast cancer with a range of applications ranging from early detection to the discovery of new metabolites and prognostic classification of patients with breast cancer [29].

Our goal in the present study was to apply combined analysis of DNA damage foci formation with global untargeted mass-spectrometry based metabolomics to map the metabolic changes occurring following exposure to olaparib. We examined the baseline differences in cellular metabolism across the cell line panel and extended this evaluation to examine cell line dependent response to olaparib treatment. From the

pathway enrichment analysis of baseline cells non-treated with Olaparib we found overlapping metabolic pathways (alanine, aspartate, glutamine, arginine, proline, glycine, serine, and threonine metabolism) enriched across all three breast cancer cell lines studies, and metabolic pathways that were unique to specific cell lines (MCF7: sphingolipid and glycerophospholipid metabolism; MDA-MB-231: taurine and hypotaurine metabolism; HCC1937: glyoxylate and dicarboxylate metabolism) (**Figure S3. 1, Table S3. 1**).

Our analysis of metabolites significantly altered in response to olaparib treatment correlate with reports from Bhute *et al*, where metabolic markers of PARP inhibition were reported as changes in amino acid metabolism (glutamine and alanine), downregulation of osmolyte levels (taurine, and GPC), phosphocreatine, lactate and pyruvate in MCF7 cells [30]. We reported downregulation of those metabolites also in the MDA-MB-231 and HCC1937 cells, while low levels of fumarate were observed only in the HCC1937 cells (**Figure 4. 6**). Bhute *et al*. also reported increased NAD⁺ levels for cells treated with veliparib. In our results NAD⁺ levels increased in the MCF7 cells treated with olaparib at the IC₁₀ treatment concentration, accompanied by a decrease in NAD⁺ levels at ascending concentrations of olaparib. Reduced levels of NAD⁺ were also detected in the MDA-MB-231 and HCC1937 cells at all treatment concentrations. Recent studies have shown that in Triple Negative Breast Cancer (TNBC) cells, olaparib enhances the signalling pathways of other NAD⁺-dependent deacetylase (i.e., sirtuins) [30, 31]. These findings are in agreement with our observation of depleted acetyl-amino acid levels and enrichment of methyl-pyridines, -pyrrolidines, and -nucleosides. Further studies are needed to confirm the divergence of NAD⁺ flow towards alternative pathways and its association with specific breast cancer subphenotypes.

Glutamine- a precursor for protein, nucleotide, and lipid biosynthesis- is a fundamental amino acid in breast cancer cell metabolism, playing a pivotal role in providing anaplerotic intermediates for the tricarboxylic acid (TCA) cycle [32]. Previous reports have indicated a reduction of glutamine levels only for the TNBC cells after treatment with veliparib, and in the MCF7 cells only in combination with other DDR inhibitors [16]. Our results show reduced glutamine levels in all cell lines treated with olaparib, suggesting increased glutamine utilisation. Once internalised by cells, glutamine can be converted to glutamate and alpha-ketoglutarate (α -KG). α -KG- a by-product of isocitrate- is oxidised in the TCA cycle through a reaction catalysed by isocitrate dehydrogenase (IDH), which is frequently mutated in cancer. Several studies have studied α -KG as an oncometabolite, where elevated levels induce the reversal of enhanced glycolysis through downregulation of the Hypoxia-inducible factor (HIF1), which following PARP inhibition leads to cell death [33, 34]. Recent findings have shown that mutant IDH - and the consequent synthesis of aberrant α -KG forms - confers a BRCAness phenotype [35], downregulating the expression of the DNA repair enzyme Ataxia-telangiectasia mutated (ATM) kinase [36], altering the methylation status of loci surrounding DNA breaks [37]. Together, these alterations lead to homology-dependent repair (HDR) impairment and increase susceptibility to PARP inhibition. On this basis, the reduced α -KG levels observed in olaparib-treated MDA-MB-231 and HCC1937 cells shows the basis for potential resistance to the anti-proliferative effects of olaparib. The increased utilisation of α -KG by HCC1937 cells, is paralleled by an increased consumption of serine at ascending doses of Olaparib. These observations are consistent with reports that in BRCA1-mutated TNBC cell lines, approximately 50% of α -KG results from the flux of serine metabolism [38].

Glutamine is also a source of nitrogen groups for the synthesis of nucleobases and nucleotides, either directly or through a process involving the transamination of glutamate and the TCA cycle-derived oxaloacetate that generates aspartate [39-41]. Our results show low levels of glutamine are associated with overall reduction in nucleobase and nucleotide levels. MCF7 and HCC1937 cells showed accumulation of adenosine monophosphate (AMP), which represents a depleted energy and nutrient status of the cells known to activate the metabolic sensor AMP-activated protein kinase (AMPK) leading to cell growth inhibition [42]. Different studies have considered activation of AMPK a metabolic cancer suppressor and an attractive therapeutic target for TNBC [43], however, its signalling network in response to PARP inhibition in different breast cancer cells needs to be established. Opposite to what observed by Bhute *et al*, Aspartate, a byproduct of the TCA cycle, accumulated in the MDA-MB-231 cells after PARP inhibition compared to its reduction in the MCF7 and HC1937 cells. Lowered plasma aspartate levels have been diagnosed in breast cancer patients suggesting an increased tumour utilisation of this metabolite [44]. Moreover, we observed that aspartate metabolism is relevant both in the baseline model and in response to olaparib, which suggests a role of this metabolite in regulating the different metabolic phenotypes of breast cancer cells. However, its role has been poorly investigated and little is known about its association with PARP inhibition.

Among the pathways of aspartate utilisation, asparagine is converted through the enzyme asparagine synthetase (ASNS). The reaction requires glutamine as a substrate and consumption of adenosine triphosphate (ATP) to produce adenosine monophosphate (AMP) and pyrophosphate (PPi). Physiological levels of asparagine occur at levels of <0.05 mM in human plasma [45]. Cancer cells harbouring mutant KRAS (e.g. MDA-MB-231), possess lower ASNS expression levels, leading to lower baseline aspartate levels explaining the rationale for the

lack of aspartate detection in MDA-MB-231 lines [46]. In breast cancer cells the increased bioavailability of asparagine promotes metastatic progression [47], due to its role in protein synthesis and regulation of amino acid homeostasis [48]. We found elevated asparagine levels in olaparib-treated MCF7 and HCC1937 cells, suggesting a role for asparagine in the observed responses to exposure to PARP inhibitor.

Beyond asparagine synthesis, aspartate amidation through ASNS presents a source of amino building blocks for the synthesis of arginine in the urea cycle, which is in turn responsible for the synthesis of polyamines catalysed by ornithine decarboxylase (ODC). Polyamine accumulation previously has been correlated with the increased proliferation of both hormone-dependent and independent breast cancer cells [49], and recently found to contribute to BRCA1-mediated DNA repair [50]. Moreover, metabolic profiling of plasma samples from patients with TNBC revealed an increase of diacetyl spermines associated with elevated expression of MYC, a well-known oncogene driving TNBC development and proliferation. Here, we found elevated diacetyl spermine levels following olaparib treatment in both TNBC and non-TNBC cells, suggesting an upregulation of polyamine catabolism, irrespective of cell line BRCA- and hormone receptor- status. Parallel to their relevance in cellular metabolism, amino acids serve also as biological buffers through regulation of cellular pH. Low extracellular pH is associated with positively charged amino acids and a known hallmark of cancer arising from enhanced glycolysis, production and altered lactate metabolism, resulting in altered mTOR pathway activation, ultimately regulating cancer cell metabolism [51, 52].

Glutathione (GSH), is involved in the protection against ROS and regulation of intracellular redox homeostasis. Elevated GSH levels have previously been reported in TNBC compared to luminal breast cancers,

suggesting the relevance of GSH to our observations of lower sensitivity to olaparib in TNBC cell lines [17, 53].

Lipids mediate various cellular biological functions, including energy storage, cell membrane structural composition and signal transduction, the increased biosynthesis of which is a marker of metabolic rewiring observed in malignant breast cancers [54, 55]. Our findings show downregulation of fatty acid biosynthesis following olaparib treatment, with a reduction in phospholipid levels including lysophosphatidylcholines and glycerolphosphocholines in all cell lines. Poly-unsaturated fatty acids (PUFAs), have previously been implicated in MCF7 and MDA-MB-231 cell apoptosis through the induction of lipid peroxidation and altered cellular redox state [56]. Moreover, elevated PUFA levels have been associated with the proteolytic cleavage of PARP and its inhibition, leading to cell death [57]. On this basis, the reduced PUFA levels observed in HCC1937 cells may indicate their resistance to olaparib treatment. Only a limited number of studies have reported a correlation between PUFAs and breast cancer subphenotypes, requiring further validation by additional studies.

Future targeted metabolomics studies using additional TNBC cell lines and clinical tumour clinical specimens are required to validate our observations. Validation of our findings could define prognostic biomarkers that will aid diagnose and enable the implementation of precision medicine in the management of breast cancer.

4.7. Conclusion

Our data show differential sensitivity of breast cancer cell lines to olaparib treatment that was dose-dependent and demonstrated the increased sensitivity of TNBC cells to DNA damage foci accumulation.

The application of metabolomics to the study of breast cancer remains in its infancy, with only a handful of studies reporting combined metabolomics and phenotypic analyses. Data acquired from metabolomics analysis can be validated against routine molecular biology and phenotypic assays, providing a powerful platform for biomarker detection or the discovery of novel actionable pathways for drug development.

Our results show that fingerprinting the metabolic profile of cells can be a powerful tool for uncovering potential oncometabolites or mechanisms giving rise to chemoresistance. Findings from such studies may provide potential additional actionable targets for modulating response to drug treatment or the design of new drug combinations that will overall enhance DNA damage efficacy, ultimately improving patient response to radiotherapy and adjuvant chemotherapy.

4.8. References

1. Gueble, S., et al. *Oncometabolites as Regulators of DNA Damage Response and Repair*. *Seminars in Radiation Oncology* 2022. **32**(1): p. 82-94.
2. Huang, R., et al., *DNA damage repair: historical perspectives, mechanistic pathways and clinical translation for targeted cancer therapy*. *Signal Transduction and Targeted Therapy*, 2021. **6**(254).
3. He, C., et al., *DNA damage repair functions and targeted treatment in breast cancer*. *Breast Cancer* 2020. **27**(3): p. 355-362.
4. Rizzolo, P., et al., *Inherited and acquired alterations in development of breast cancer*. *The application of clinical genetics*, 2011. **4**: p. 145-158.
5. Godet, I., et al., *BRCA1 and BRCA2 mutations and treatment strategies for breast cancer*. *Integr Cancer Sci Ther*, 2017. **4**(1).
6. O'Neil, N., et al., *Synthetic lethality and cancer*. *Nature Reviews Genetics*, 2017. **18**(10): p. 613-623.
7. Li, S., et al., *Development of synthetic lethality in cancer: molecular and cellular classification*. *Signal Transduction and Targeted Therapy* volume, 2020. **5**(241).
8. Lord, C., et al., *Synthetic lethality and cancer therapy: lessons learned from the development of PARP inhibitors*. *Annual Review of Medicine*, 2015. **66**: p. 455-470.
9. Cortesi, L., et al., *An Overview of PARP Inhibitors for the Treatment of Breast Cancer*. *Targeted Oncology*, 2021. **16**(3): p. 255-282.
10. FDA. *FDA approves olaparib for adjuvant treatment of high-risk early breast cancer*. 2022; Available from: <https://www.fda.gov/drugs/resources-information-approved-drugs/fda-approves-olaparib-adjuvant-treatment-high-risk-early-breast-cancer>.
11. Pavlova, N., et al., *The Emerging Hallmarks of Cancer Metabolism*. *Cell Metabolism*, 2016. **27-47**.
12. Maria, R., et al., *Impact of chemotherapy on metabolic reprogramming: Characterization of the metabolic profile of breast cancer MDA-MB-231 cells using 1H HR-MAS NMR spectroscopy*. *Journal of Pharmaceutical and Biomedical Analysis*, 2017. **146**: p. 324-328.
13. Gandhi, et al., *Metabolic Reprogramming in Breast Cancer and Its Therapeutic Implications*. *Cell*, 2019. **8**(2): p. 89.
14. Palaskas, et al., *18F-fluorodeoxy-glucose positron emission tomography marks MYC-overexpressing human basal-like breast cancers*. *Cancer Research*, 2011. **71**(15): p. 5164-74.
15. Turgeon, M., et al., *DNA Damage, Repair, and Cancer Metabolism*. *Frontiers in Oncology*, 2018. **8**: p. 1-8.
16. Bhute, V., et al., *The Poly (ADP-Ribose) Polymerase Inhibitor Veliparib and Radiation Cause Significant Cell Line Dependent Metabolic Changes in Breast Cancer Cells*. *Scientific Reports*, 2016. **6**(36061).
17. Tang, X, et al., *A joint analysis of metabolomics and genetics of breast cancer*. *Breast Cancer Research*, 2014. **16**(415).
18. Huang A., et al., *Synthetic lethality as an engine for cancer drug target discovery*. *Nature Reviews Drug Discovery*, 2019. **19**(1): p. 23-38.
19. Mah, L., et al., *gammaH2AX: a sensitive molecular marker of DNA damage and repair*. *Leukemia*, 2010. **24**(4): p. 679-686.
20. Schultz, L., et al., *p53 binding protein 1 (53BP1) is an early participant in the cellular response to DNA double-strand breaks*. *Journal of Cell Biology*, 2000. **151**(7): p. 1381-1390.
21. Dempster, J., et al., *Chronos: a cell population dynamics model of CRISPR experiments that improves inference of gene fitness effects*. *Genome Biology*, 2021. **22**(343).
22. Robson, M., et al., *Olaparib for Metastatic Breast Cancer in Patients with a Germline BRCA Mutation*. *New England Journal of Medicine*, 2017. **377**(6): p. 523-533.
23. AstraZeneca. *Lynparza approved in the US as adjuvant treatment for patients with germline BRCA-mutated HER2-negative high-risk early breast cancer*. 2022 04/2022]; Available from: <https://www.astrazeneca.com/media-centre/press-releases/2022/lynparza-approved-in-the-us-as-adjuvant-treatment-for-patients-with-germline-brca-mutated-her2-negative-high-risk-early-breast-cancer.html>.

24. Xu, L., et al., *Efficacy and safety of PARP inhibitors in advanced or metastatic triple-negative breast cancer: a systematic review and meta-analysis*. *Frontiers in Oncology*, 2021. **11**(742139).
25. Keung, M., et al., *Response of Breast Cancer Cells to PARP Inhibitors Is Independent of BRCA Status*. *Journal of Clinical Medicine*, 2020. **9**(4): p. 940.
26. Davies, H., et al., *HRDetect is a predictor of BRCA1 and BRCA2 deficiency based on mutational signatures*. *Nature Medicine*, 2017. **23**(4): p. 517-525.
27. McGrail, D., et al., *Improved prediction of PARP inhibitor response and identification of synergizing agents through use of a novel gene expression signature generation algorithm*. *npj Systems Biology and Applications*, 2017. **3**(8).
28. Harbeck, N., et al., *Breast cancer*. *Nature*, 2019. **5**: p. 66.
29. Hart, C., et al., *Metabolomics in Breast Cancer: current status and perspectives*. *Advances in Experimental Medicine and Biology*, 2016. **882**: p. 217-234.
30. Bhute, V., et al., *Metabolic responses induced by DNA damage and poly (ADP-ribose) polymerase (PARP) inhibition in MCF-7 cells*. *Metabolomics*, 2015. **6**: p. 1779-1791.
31. Gajan, A., et al., *Analysis of Adaptive Olaparib Resistance Effects on Cisplatin Sensitivity in Triple Negative Breast Cancer Cells*. *Frontiers in Oncology*, 2021. **11**: p. 1-14.
32. Najumudeen, A., et al. , *The amino acid transporter SLC7A5 is required for efficient growth of KRAS-mutant colorectal cancer*. *Nature Genetics*, 2021. **53**: p. 16-26.
33. Tennant, D., et al., *Reactivating HIF prolyl hydroxylases under hypoxia results in metabolic catastrophe and cell death*. *Oncogene*, 2009. **28**(45): p. 4009-21.
34. Scalia, M., et al., *PARP-1 Inhibitors DPQ and PJ-34 Negatively Modulate Proinflammatory Commitment of Human Glioblastoma Cells*. *Neurochemical Research*, 2013. **38**: p. 50-58.
35. Sulkowski, P., et al. , *2-Hydroxyglutarate produced by neomorphic IDH mutations suppresses homologous recombination and induces PARP inhibitor sensitivity*. *Science Translational Medicine*, 2017. **9**(375).
36. Inoue, S., et al., *Mutant IDH1 Downregulates ATM and Alters DNA Repair and Sensitivity to DNA Damage Independent of TET2*. *Cancer Cell*, 2016. **30**(2): p. 337-348.
37. Sulkowski, P., et al., *Oncometabolites suppress DNA repair by disrupting local chromatin signalling*. *Nature*, 2020. **582**: p. 586-591.
38. Possemato, R., et al. , *Functional genomics reveal that the serine synthesis pathway is essential in breast cancer*. *Nature*, 2011. **476**: p. 346-350.
39. DeBerardinis, R., et al., *Q's next: the diverse functions of glutamine in metabolism, cell biology and cancer*. *Oncogene*, 2010. **29**: p. 313-324.
40. Okazaki, A., et al. , *Glutaminase and poly(ADP-ribose) polymerase inhibitors suppress pyrimidine synthesis and VHL-deficient renal cancers*. *Journal of Clinical Investigation*, 2017. **127**(5): p. 1631-1645.
41. Son, J., et al. , *Glutamine supports pancreatic cancer growth through a KRAS-regulated metabolic pathway*. *Nature*, 2013. **496**: p. 101-105.
42. Høyer-Hansen, M., et al., *AMP-activated protein kinase: a universal regulator of autophagy?* *Autophagy*, 2007. **3**(4): p. 381-383.
43. Cao, W., et al., *AMP-activated protein kinase: a potential therapeutic target for triple-negative breast cancer*. *Breast Cancer Research*, 2019. **21**.
44. Xie, G., et al. , *Lowered circulating aspartate is a metabolic feature of human breast cancer*. *Oncotarget*, 2015. **6**(32): p. 33369-81.
45. Stegink, L., et al., *Plasma amino acid concentrations and amino acid ratios in normal adults and adults heterozygous for phenylketonuria ingesting a hamburger and milk shake meal*. *The American Journal of Clinical Nutrition*, 1991. **53**(3): p. 670-5.
46. Gwinn, D., et al. , *Oncogenic KRAS regulates amino acid homeostasis and asparagine biosynthesis via ATF4 and alters sensitivity to L-asparaginase*. *Cancer Cell*, 2018. **33**(1): p. 91-107.
47. Knott, S., et al. , *Asparagine bioavailability governs metastasis in a model of breast cancer*. *Nature* 2018. **554**: p. 378-381.
48. Krall, A., et al. , *Asparagine promotes cancer cell proliferation through use as an amino acid exchange factor*. *Nature Communications*, 2016. **7**(11457).

49. Kim, I., et al., *Polyamine involvement in the secretion and action of TGF-alpha in hormone sensitive human breast cancer cells in culture*. Breast Cancer Research and Treatment. 1991. **18**(2): p. 83-91.
50. Lee, C., et al., *Promotion of homology-directed DNA repair by polyamines*. Nature Communication, 2019. **10**(65).
51. Zhang, X., et al., *Tumor pH and its measurement*. The Journal of Nuclear Medicine, 2010. **51**(8): p. 1167-1170.
52. Balgi, A., et al., *Regulation of mTORC1 signaling by pH*. PlosOne, 2011. **6**(6): p. e21549.
53. Lien, E., et al., *Glutathione biosynthesis is a metabolic vulnerability in PI3K/Akt-driven breast cancer*. Nature Cell Biology, 2016. **18**(5): p. 572-578.
54. Beckonert, O., et al., *Visualizing metabolic changes in breast-cancer tissue using 1H-NMR spectroscopy and self-organizing maps*. NMR in Biomedicine, 2003. **16**: p. 1-11.
55. Cao, M., et al., *Glycerophosphodiester phosphodiesterase domain containing 5 (GDPD5) expression correlates with malignant choline phospholipid metabolite profiles in human breast cancer*. NMR in Biomedicine, 2012. **25**(9): p. 1033-1042.
56. Deshpande, R., et al., *Alpha-linolenic acid regulates the growth of breast and cervical cancer cell lines through regulation of NO release and induction of lipidperoxidation*. Journal of Molecular Biochemistry, 2013. **2**: p. 6-17.
57. Kim, J., et al., *Growth-Inhibitory and Proapoptotic Effects of Alpha-Linolenic Acid on Estrogen-Positive Breast Cancer Cells*. Annals of the New York Academy of Sciences., 2009. **1171**: p. 190-195.

CHAPTER 5

5.1. General discussion and conclusion

The implementation and advancement of instrumentation, software, and databases in the field of mass spectrometry have played a leading role in the field of metabolomics thanks to advancements in detection sensitivity and high-speed data acquisition. Consequently, the refinement of untargeted and targeted metabolomics approaches has seen the expansion of their applications to a broader range of research areas.

In this thesis, untargeted mass-spectrometry-based metabolomics has been applied to the fields of ageing and cancer research to characterise the phenotypic heterogeneity between and within biological samples at different scales, including cells and tissues. For each chapter of the thesis, the primary findings, conclusions and future perspectives are discussed below:

In **chapter 2** the heterogeneous nature of different models and mechanisms of cellular senescence (replicative senescence and DNA-damage induced senescence) were investigated. For this scope, we first induced senescence by multiple passages cell culture passages (P= 3-20) and varied the doses of irradiation (0-12 Gy), hydroxyurea (0-1000 μ M) and etoposide (0-50 μ M). Subsequently, we analysed the changes in cellular morphology and expression of senescence molecular markers (β -galactosidase, γ H2AX, and Ki-67) coupled to the application of liquid chromatography-mass spectrometry (LC-MS) for intra- and extra-cellular extraction of cellular metabolites.

Findings from the work performed in this chapter led to the following conclusions:

1. Human foreskin fibroblasts present phenotypic and molecular markers of senescence in response to 20 passages in culture (replicative senescence), and exposure to 12 Gy irradiation, 800 μ M hydroxyurea and 10 μ M etoposide. Cellular enlargement and flattening was observed, which was accompanied with elevated expression of β -

galactosidase, enhanced expression of γ H2AX DNA damage foci, and reduced levels of the Ki-67 proliferation marker.

2. All the senescence-like phenotypes were characterised by intracellular metabolic rewiring of amino acid (histidine, alanine, aspartate, glutamate and arginine) metabolism. Individual phenotypes such as irradiation, late passaged and etoposide treated cells showed altered glutamine and glutamate metabolism. Cells treated with hydroxyurea and late passaged cells presented relevant changes in the arginine and proline metabolism. while cells treated with etoposide showed changes in glycine, serine and threonine metabolism.
3. The data relative to the extracellular content of the senescence-like phenotypes revealed the enrichment of inflammatory molecules such as prostaglandins (replicative senescence), nitrotyramine (hydroxyurea), and norepinephrine (etoposide). Depletion of methyl dopamine was observed only for irradiated cells.
4. Overall, this study has provided evidence that global mass spectrometry-based metabolomics analysis – combined with morphological and molecular studies – is an effective approach for the identification of putative metabolic pathways that evolve upon the development of different senescence sub-phenotypes.

Since the heterogeneity of senescence relates not only to its method of induction but also to the cell type and tissue of origin, a limitation of this study is the employment of a single cell line (Human Foreskin Fibroblasts). Future work should consider using a panel of cell lines and types originating from different tissues including neurons, cardiomyocytes, endothelial cells, immune cells, etc. Moreover, other methods of senescence induction such as alteration of mitochondrial functionality, proteasome disruption, and epigenetic alteration should be considered for follow-up studies.

Combining intra- and extracellular metabolomics using mass spectrometry has provided a wider understanding of the metabolic changes occurring upon the induction of different senescence phenotypes. However, the data presented here has developed a pipeline and generated hypotheses on how the different

senescence cell types may be profiled. Validation of this study using a targeted metabolomics approach is essential. For example, by isotope tracing of ¹³C-labelled glucose and ¹⁴N-labelled glutamine to follow their incorporation through downstream biochemical reactions and provide more accurate insights into determined metabolic perturbations.

Moving from the analysis of cellular senescence at the cellular to tissue scale, studies of ageing using metabolomics and proteomics approaches are currently in their infancy; however, they represent the powerful technologies needed to discover and map key biological processes associated with physiological ageing and age-related disease. The research presented in chapter 3 supports evidence for the potential of mass spectrometry-based metabolomics approaches when applied to tissue ageing.

In this work, the metabolome of brain tissues from old mice (aged 10-months) was inspected and compared to brain tissue dissected from young mice (aged 5-months). Integrating metabolomics and proteomics data generated a preliminary multi-omics profile of the biology of ageing in murine brain tissue alongside the opportunity to determine the spatial localization of metabolites using mass spectrometry imaging (MSI).

Key conclusions from **chapter 3** are summarised as follows:

1. Alignment of metabolomics and proteomics data revealed that in the aged murine brain tissue, enrichment of glutamate, aspartate and cysteine-derived metabolic pathways is evident, which regulate neurotransmission signalling and thus can be potential targets in the treatment of neurodegenerative disease.
2. A focus on the lipid components of the metabolome/proteome of aged brain tissue showed that fatty acids and enzymes involved in pro-inflammatory pathways are upregulated, therefore confirming previous literature findings and our observations in cell lines on the presence of an inflammatory secretory phenotype associated with the ageing process (inflammaging).

3. The employment of matrix-assisted laser desorption/ionization mass spectrometry (MALDI-MSI) allowed the visualization and spatial characterization of different classes of lipids across the surface of murine brains, therefore presenting MALDI-MSI as a powerful diagnostic tool applicable in clinical settings.
4. In summary, this research has shown that the employment of global mass spectrometry-based metabolomics, integrated with global proteomics and high-resolution spatial localization of metabolites as a powerful approach that can be deployed for in-depth chemical analysis of ageing.

As noted in chapter 2, an untargeted approach was used for both metabolomics and proteomics analysis here, with the caveat of generating putative data that serve as hypothesis-driven information. Thus, targeted metabolomics/proteomics will be necessary to verify the findings presented in this research in models of murine brain tissue.

A consideration in proteomics analysis is the prospect of integrating information about the post-translational modifications of identified proteins, as they are essential in the regulation of the metabolism, structure, activity, and localization of proteins providing a more extensive understanding of the biology of ageing.

A key aspect of using the MSI method is visualising the spatial distribution of molecules throughout the tissues and can represent the bases to start designing reliable quantitative analyses of metabolite distribution in tissue. The data presented in this study are not suitable for quantitation as they lack internal standards and appropriate normalization to correct for sample variation and variability in signal intensity between different samples. Moreover, the thickness of tissue sections varied between samples contributing to their heterogeneity. In future applications of MSI, we will optimise sample preparation protocols and data quantitation to render this technique more consistent, reliable and reproducible.

An area of significant growth in the field of metabolomics is the application of metabolomics for uncovering potential oncometabolites or mechanisms responsible for resistance to chemotherapy. Acquired resistance is dependent on the cell line, type of drug, and genetic mutations inherent to the cancer cell type or accumulated during tumour development. In this research we focused on different breast cancer cells holding different genetic profiles: from the less aggressive MCF7 cells to the most aggressive triple-negative breast cancer cells MDA-MB-231 and the BRCA-1 mutated HCC1937 cells. We first analysed their sensitivity to DNA damage repair (DDR) inhibition using a PARP inhibitor (olaparib), then investigated the extent of DNA damage following treatment, and finally studied the metabolic changes in response to DDR inhibition with olaparib.

From the results presented in **chapter 4** we conclude:

1. Breast cancer cell lines harbouring different mutational profiles have different sensitivity to drug treatment: BRCA1/2-proficient MCF7 and MDA-MB-231 were more sensitive to olaparib treatment, while BRCA1-mutant HCC1937 cells showed some resistance to Olaparib treatment.
2. Despite developing some resistance, following DDR inhibition the BRCA1-mutated HCC1937 cells presented a higher occurrence of DNA damage foci compared to the other cell lines, therefore suggesting that Olaparib resistance extends beyond BRCA status in breast cancer cells.
3. Breast cancer cells rely on common metabolic pathways mainly based on amino acid metabolism (alanine, aspartate, glutamine, arginine, proline, glycine, serine and threonine). Unique metabolic features for the individual cell lines included sphingolipid and glycerophospholipid metabolism (MCF7), taurine and hypotaurine metabolism (MDA-MB-231) and glyoxylate and dicarboxylate metabolism (HCC1937). Changes in these metabolic pathways among treatment with Olaparib might be at the basis of their differential response to the drug.

4. Overall, the research presented in **chapter 4** showed the potential for combining metabolomics and molecular analysis in the study of breast cancer to provide an in-depth characterisation of their different sub-phenotypes and better profile their differential response to drug treatment.

In future work we will apply this analytical approach to other breast cancer cell lines with a different variation in their BRCA1/2 status. Currently we are also expanding the range of DDR drugs investigated to include other standard of care treatments. Together, the implementation of these approaches might be useful for designing a panel of different breast cancer cell lines and treatments associated with specific phenotypic and metabolic profiles for each individual condition.

Similar to the findings for the ageing chapter, validation of our results through a targeted approach will be required. Moreover, information on the extracellular metabolic content and integration with proteomics data would represent further improvements to the study that will be considered for future works.

Conclusions

Overall, the work presented in this thesis show the potential of mass spectrometry-based metabolomics for biomarker discovery and the stratification of different biological phenotypes and responses to treatments that cannot be distinguished using traditional biological techniques.

Findings from these studies have suggested potential explanations for the metabolic rewiring occurring within different senescence cells, murine-aged brain tissue, and different breast cancer cell lines in response to DNA damage. Our results have revealed specific metabolic pathways for each ageing and breast tumour phenotype that might be targeted in the treatment of age-related diseases and cancer. Ultimately, this will be helpful in improving patient response to therapies against age-related diseases including cancer.

APPENDICES

6.1. Appendix 1

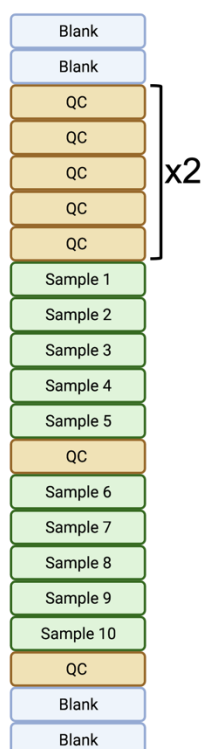


Figure S1. 1 Sample batch order. 2 blanks were injected at the beginning and at the end of the run. 10 QCs were injected before injections of the samples. Then QCs were injected after every 5 samples. QCs have been prepared by pooling together all the sample after drying and reconstitution with water:acetonitrile (50:50, v/v).

Table S1. 1 Elution gradient used for the chromatographic separation of metabolite extracts

Time	Flow (ml/min)	%B	Curve
0.000	0.300	20	5
11.000	0.300	60	5
15.000	0.300	20	5
20.000	0.300	20	5

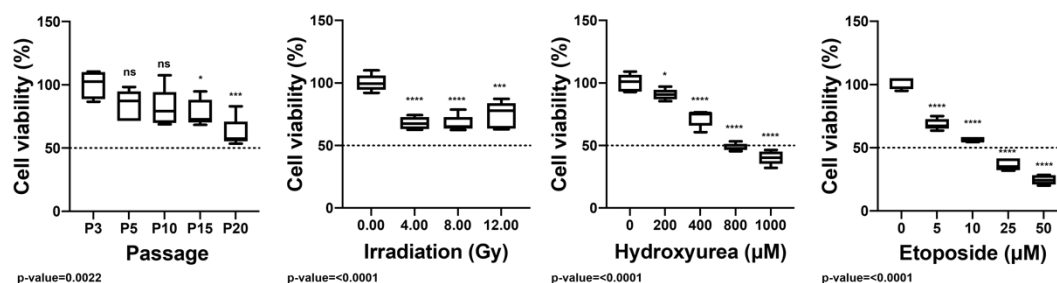


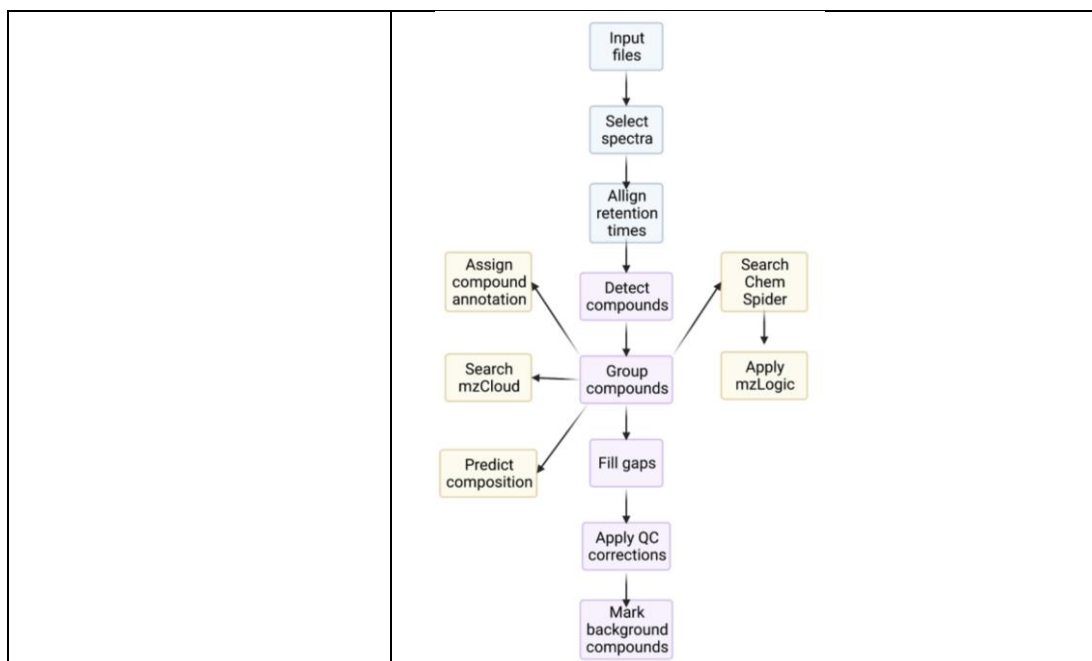
Figure S1. 2 Viability response of HFF-1 cells at different passages, different doses of X-Ray, hydroxyurea and etoposide. Passaged, irradiated and etoposide-treated cells were kept in culture for 1 week, while hydroxyurea cells were treated for 2 weeks. After the incubation time, cells were stained with crystal violet, subsequently solubilised in ethanol, and absorbance was read at 600 nm.

p-values have been determined through ANOVA test. Dunnett's multiple comparison test was used as a follow up to ANOVA test and the p-values were represented as: non-significant=ns, 0.05=, 0.005=**, 0.0005=***, 0.00005=****.*

Table S1. 2 Setting for LC-MS data analysis and processing

Method settings	
Application mode	Small molecule
Method duration	20 min
Global parameter	
Ion source type	H-ESI
Spray voltage	Static
Positive Ion (V)	3900
Negative Ion (V)	2500
Gas Mode	Static
Sheath Gas (Arb)	40
Aux Gas (Arb)	10
Sweep Gas (Arb)	1
Ion Transfer Tube Temp (°C)	320
Vaporizer Temp (°C)	300
APPI Lamp	Not in use
MS Global Settings	
Infusion Mode	Liquid Chromatography
Expected LC Peak Width (s)	6
Advanced Peak Determination	False
Mild Trapping	True
Default Charge State	1
Internal Mass Calibration	EASY-IC™
Mode	Run Start
	<p>Experiment</p> <pre> graph TD A[Full Scan] --> B[MIPS] B --> C[Intensity] C --> D[Precursor fit] D --> E[Charge state] E --> F[Dynamic exclusion] F --> G[Isotope exclusion] G --> H[Apex Detection] H --> I[ddMS²] E --- J[5 Scans] </pre>
Start time	0 min
End time	20 min
Full Scan	
Orbitrap resolution	60,000
Scan range (m/z)	50-750
RF Lens (%)	70
AGC Target	Custom
Maximum Injection Time Mode	Auto

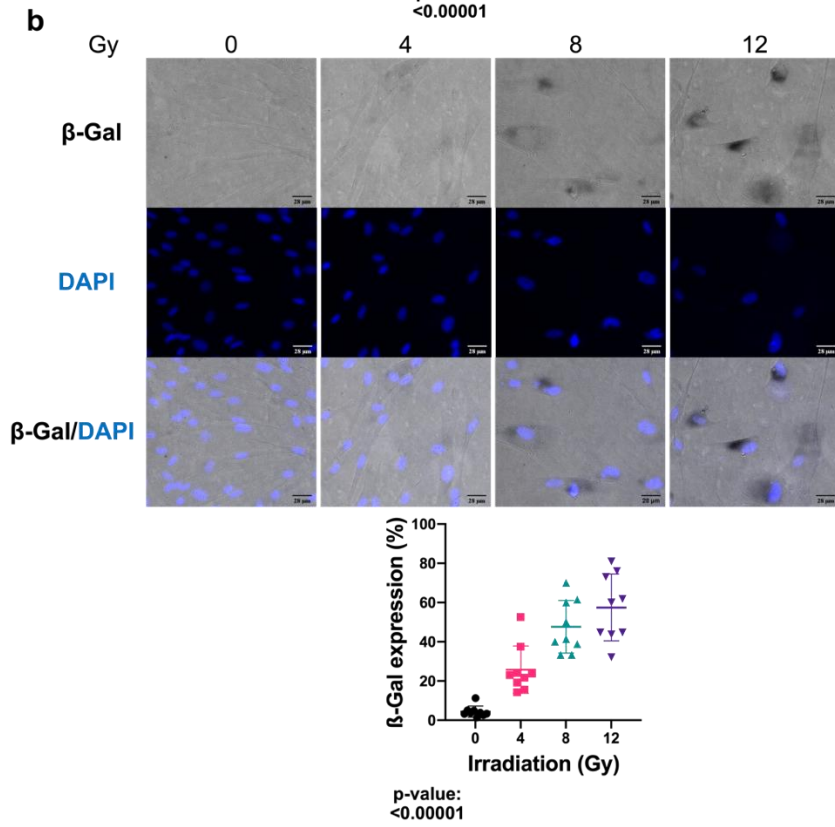
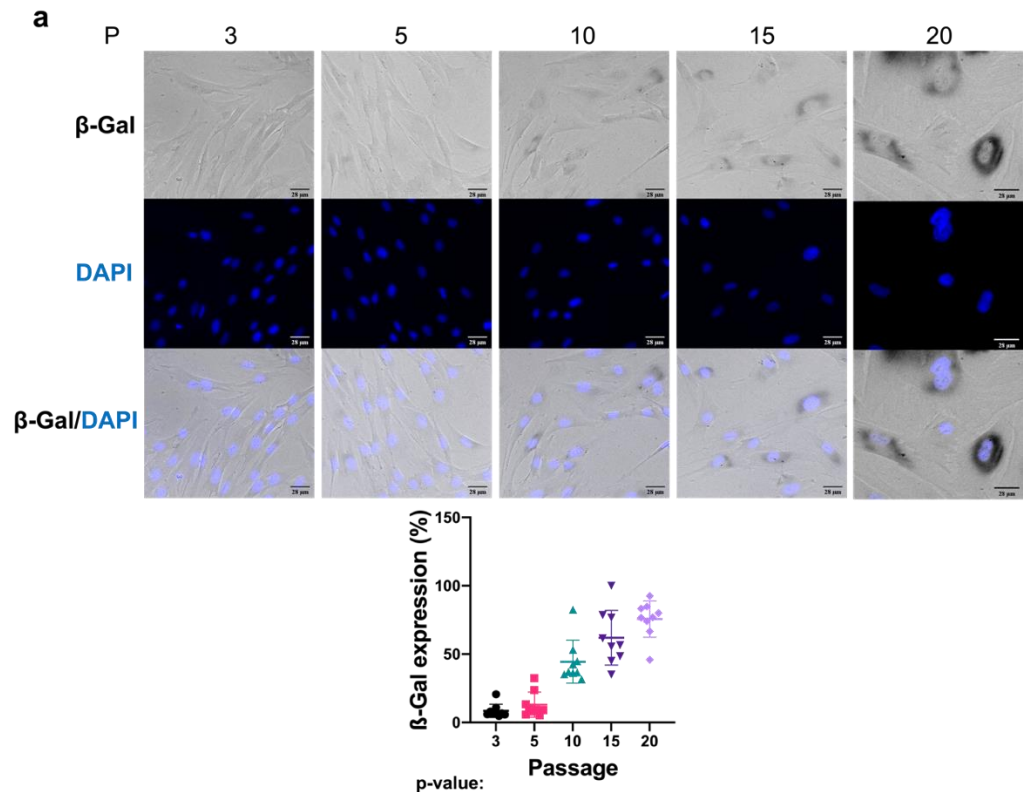
Microscans	1
Data Type	Profile
Polarity	Both (+/-)
Source Fragmentation	Disabled
Use EASY-CM™	On
Monoisotopic peak determination (MIPS)	
Intensity Threshold	1-0e4
Data Dependent Mode	Number of Scans
Number of Dependent Scans	5
Precursor fit	
Fit threshold (%)	70
Fit window (<i>m/z</i>)	0.7
Charge state	1-2
Dynamic exclusion	
Dynamic exclusion mode	Custom
Exclude after n time	1
Exclusion duration (s)	60
Mass tolerance	Ppm
Low	3
High	3
Exclude isotopes	Enabled
Perform dependent scan on single scan precursor only	Enabled
Isotope exclusion	Assigned
Apex Detection	
Desired Apex Window (%)	50
ddMS² Scan	
Multiplex Ions	False
Isolation Window (<i>m/z</i>)	0.7
Isolation Offset	Off
Collision Energy Type	Normalised
HCD Collision Energies (%)	10,20,30,40,100
Orbitrap Resolution	15,000
Scan Range Mode	Auto
AGC Target	Standard
Maximum Injection Time Mode	Auto
Microscans	1
Data Type	Profile
Use EASY-IC™	On
	Data processing



Input Files	.raw data
Select Spectra	
Lower RT Limit	0
Upper RT Limit	0
First Scan	0
Last Scan	0
Lowest charge state	0
Highest charge state	0
Min. precursor mass	0 Da
Max precursor Mass	5000 Da
Total intensity threshold	0
Minimum peak count	1
Scan event filters	
Mass analyzer	Not specified
MS Order	Any
Activation type	Not specified
Min collision energy	0
Max collision energy	1000
Scan type	Any
Polarity mode is	+/-
Peak Filters	
S/N threshold (FT-only)	1.5
General settings	
Precursor selection	Use MS(n-1) precursor
Use isotope pattern in precursor reevaluation	True
Provide profile spectra	Automatic
Store chromatograms	False
Align retention times	
Alignment model	Adaptive curve
Alignment fallback	None
Maximum shift	0.3 min
Shift reference file	True
Mass tolerance	3 ppm
Remove outlier	True
Detect compounds	

Mass tolerance	3 ppm
Intensity tolerance (%)	30
S/N threshold	3
Min. peak intensity	500,000
Base ions	[M+H] ⁺ +1; [M-H] ⁻ -1
Peak detection	
Filter peaks	True
Max peak width	0.5 min
Remove singlets	True
Min #scans per peak	5
Min #isotopes	1
Isotope grouping	
Min spectral distance score	0
Remove potentially false positive isotopes	True
Group compounds	
Mass tolerance	5 ppm
RT tolerance	0.2 min
Preferred ions	[M+H] ⁺ +1; [M-H] ⁻ -1; [M+ACN+H] ⁺ +1; [M+FA-H] ⁻ -1; [M+ACN+Na] ⁺ +1; [M+H+Na] ⁺ +2; [M+H+NH ₄] ⁺ +2; [M+Na] ⁺ +1; [M+NH ₄] ⁺ +1
Fill gaps	
Mass tolerance	5 ppm
S/N threshold	1.5
Use real peak detection	True (re-detected low-intensity peaks)
Apply QC correction	
Regression model	Linear
Min QC coverage [%]	30
Max QC area RSD [%]	30
Max corrected QC area RSD [%]	25
Max #files between QC files	15
Max background compounds	
Max sample/blank	5
Max blank/sample	0
Hide background	True
Search ChemSpider	
Database(s)	CheBI, Human Metabolome Database
Search mode	By formula mass
Mass tolerance	5 ppm
Max # of results per compound	100
Max # of predicted composition per compound	3
Apply mzLogic	
FT Fragment mass tolerance	10 ppm
IT Fragment mass tolerance	0.4 Da
Max # compounds	0
Max # mzCloud similarity results to consider per compound	10
Match factor threshold	70

Predict compositions	
Mass tolerance	5 ppm
Pattern matching	
Intensity tolerance (%)	30
Intensity threshold (%)	0.1
S/N threshold	3
Min spectral fit (%)	30
Min pattern Cov (%)	90
Use dynamic recalibration	True
Use fragments matching	True
Mass tolerance	5 ppm
S/N threshold	3
Assign compound annotations	
Mass tolerance	5 pmm
Data source 1	mzCloud search
Data source 2	Predicted compositions
Data source 3	massList search
Data source 4	ChemSpider search
Data source 5	Metabolika search
Search mzCloud	
Compound classes	All
Precursor mass tolerance	10 ppm
FT fragment mass tolerance	10 ppm
IT fragment mass tolerance	0.4 Da
Library	Autoprocessed; reference
Post processing	Recalibrated
Max # results	10
Annotate matching fragments	True
DDA Search	
Identity search	Cosine
Match activation type	True
Match activation energy	Match with tolerance
Activation energy tolerance	20
Apply intensity threshold	True
Similarity search	None
Match factor threshold	20
Differential analysis	
Log10 transform values	True



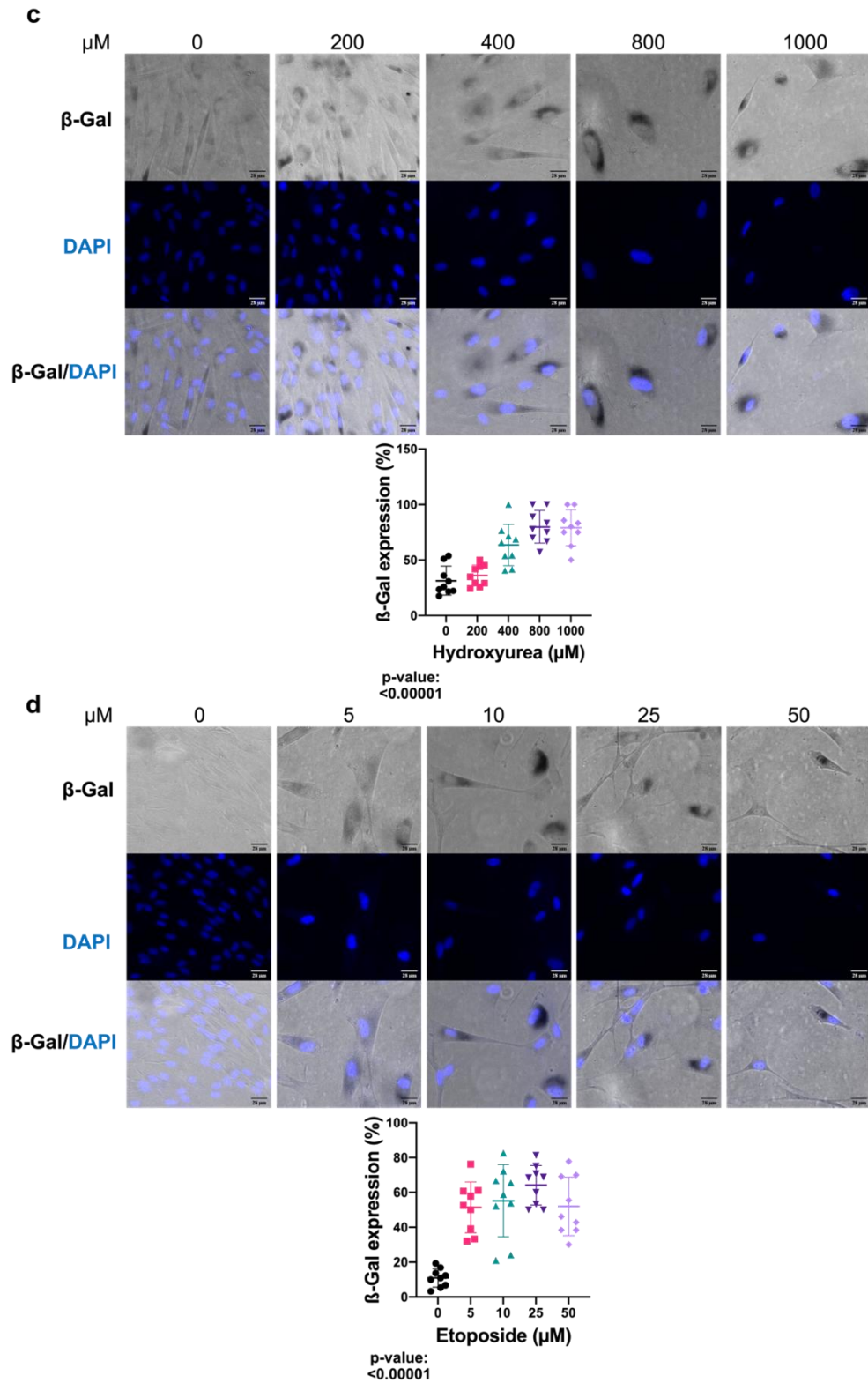


Figure S1. 3 The expression of $\beta\text{-Gal}$ in senescence-induced HFF-1 cells. Representative phase contrast images of $\beta\text{-Gal}$ staining (grey), DAPI immunolabelled nuclei (blue) and composite ($\beta\text{-Gal}$ (grey) and DAPI (blue)) in cells at different passages (a), increasing irradiation doses for 1 week (b), treatment with increasing concentrations of hydroxyurea for 2 weeks (c) and etoposide for 1 week (d). For each condition, corresponding $\beta\text{-Gal}$ expression levels expressed have been reported as a percentage of manually counted stained cells relative to the number of counted nuclei

using ImageJ. 9 repeats with on average >50 cells per each sample. p-values have been determined ANOVA test.

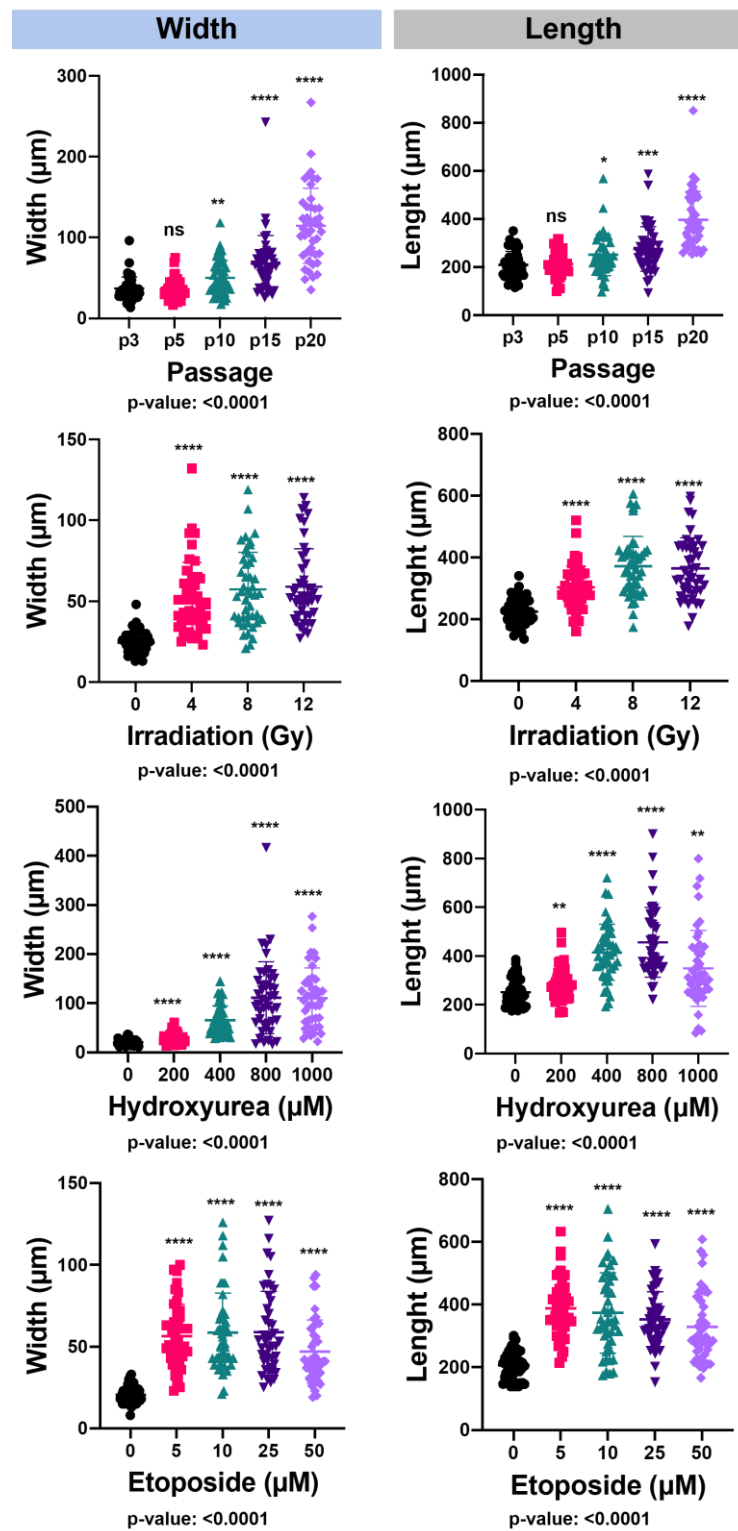
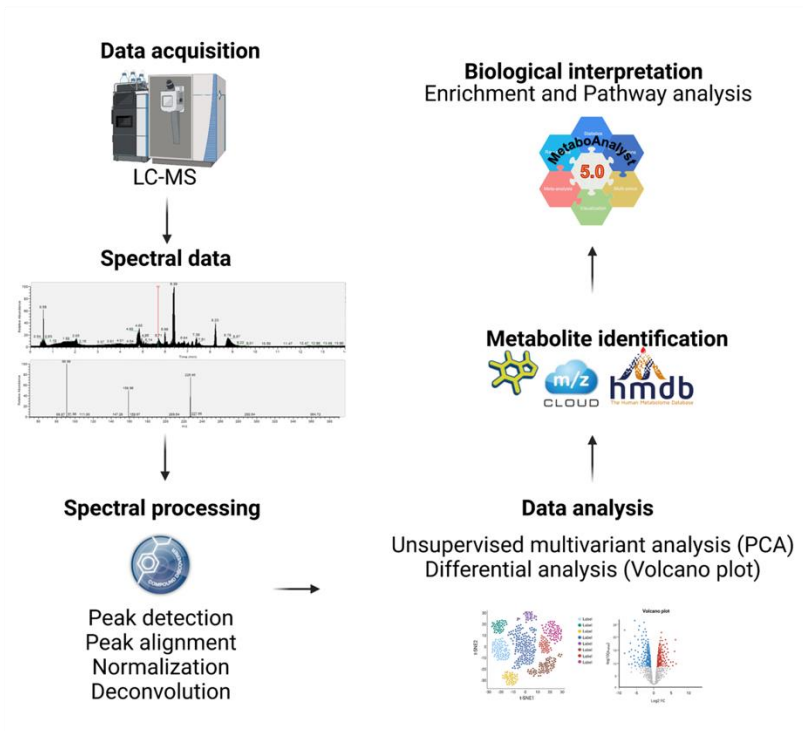


Figure S1.4 Measurements of width and length of HFF-1 cells. Cells at late passage (P20), 12 Gy irradiation, for 1 week, 800 μM hydroxyurea for 2 weeks, and 10 μM etoposide for 1 week. Cells stained for $\beta\text{-Gal}$ expression have been analysed to measure width and length of individual cells. A total number of 45 cells have been analysed per each passage and dosage. Width and length have been measured through the line tool in ImageJ and expressed as μm . Dunnett's multiple comparison

test was used as a follow up to ANOVA and corresponding *p*-values were represented as: non-significant=ns, 0.05=*, 0.005=**, 0.0005=***, 0.00005=****.

a



b

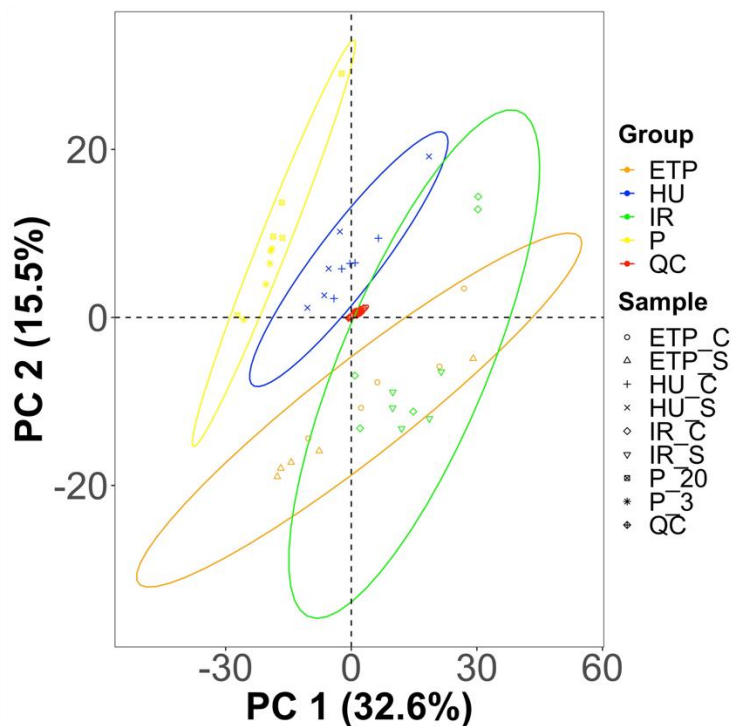


Figure S1. 5 Statistical analysis of global metabolomics features identified in different induced senescence models. These include replicative senescence at passage 20, 12 Gy irradiation for 1 week, 800 μ M hydroxyurea for 2 weeks, and 10 μ M etoposide for 1 week. A) Workflow used in this study to perform pathway analysis from metabolomics analyses. b) Global PCA score plots of the analysed senescent cells for data acquired in positive/negative switching mode. For each treatment

group, five replicates were used. Data points in the two-dimensional PCA score plot were central scaled.

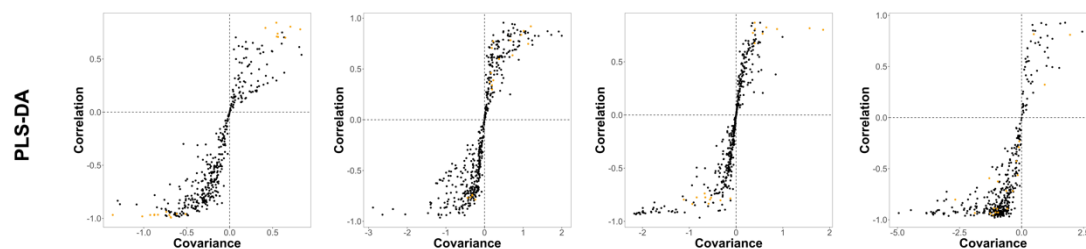


Figure S1. 6 Pairwise partial least square-discriminant analysis (PLS-DA) of different senescence-induced cells. The orange circles represent the first 20 discriminating compounds that allow to differentiate between non-treated and treated cells.

Table S1. 3 Table with a list of the first 20 PLS-DA compounds for all the conditions. *m/z* value, *Log2*Fold change and *p*-values have been reported.

Passaged cells

Name	<i>m/z</i>	<i>Log2</i> Fold Change: (P2) / (P3)	<i>P</i> -value: (P2) / (P3)
Glutamic acid	146.04583	-1.62	0.00434357
Hypoxanthin	137.04573	2.49	2.4426E-05
Oleic acid	281.24857	1.71	0.0004958
Palmitoylcarnitine	400.34193	1.61	0.00088284
Taurine	126.02192	-2.04	0.00012555
Cystathionine	223.07467	-2.53	0.00028365
Mannitol	181.07173	1.85	0.00109008
Mannitol 1-phosphate	263.05263	1.79	0.00027652
Margaric acid	269.24849	1.72	0.00018146
Glutaurine	255.0645	-1.79	0.00065101
C18-Carnitine	428.3738	2.05	0.00034163
4-tert-Octylphenol monoethoxylate	249.18586	3.47	2.2719E-05
N-(4-Amino-1-carboxybutyl)glutamic acid	263.12367	-1.72	0.00073906
N-methylethanolamine phosphate	156.04198	-1.77	0.00139772
Tauropine	198.043	-1.61	0.00013689
N-[2-[(2-Amino-2-carboxyethyl)amino]-2-carboxyethyl]aspartic acid	308.10803	-1.31	0.00016296
11(E)-Eicosenoic Acid	309.27988	1.26	0.00076382
Istamylin AO	338.19231	2	0.00087487
5-Chrysenecarboxylate	273.09088	1.34	0.00151022
N-Carboxy-L-methionine	192.03353	1.28	0.00266446

Irradiation

Name	<i>m/z</i>	<i>Log2</i> Fold Change: (IR_S) / (IR_C)	<i>P</i> -value: (IR_S) / (IR_C)
Mannitol	181.07177	1.33	0.00208751
Taurine	126.02193	-0.99	1.1063E-05
Hypotaurine	110.02703	-0.67	0.01110353
Hex-2-ulose	215.03276	-0.64	0.01713014
D-Serine	106.04986	0.82	0.01273863
O-Acetylserine	146.04583	-0.8	0.00453899
N1-(4-fluorophenyl)-2-[(4-methylphenyl)thio]acetamide	262.08969	2.15	0.00364413
3-(dimethylamino)-1-[4-(phenylsulfonyl)phenyl]prop-2-en-1-one	316.1002	2.83	8.2363E-05
Gluconic acid	195.05103	-0.97	0.00227185
2-Amino-9-(2-deoxy-pentofuranosyl)-3,9-dihydro-6H-purin-6-one	309.12942	1.44	0.01265897
N-(4-Amino-1-carboxybutyl)glutamic acid	263.12368	-0.54	0.01165327
Acetylcholine	146.11748	-0.61	0.00912991
Hypoxanthine	137.0457	1.14	0.00799589
L-coprine	203.10257	1.02	0.00774634
Fructose 6-phosphate	283.01887	0.66	0.02152925
Propylhexedrine	156.17465	0.43	0.00900832
1-O-Phosphonopentitol	233.04199	0.41	0.01172122
Carbaryl	219.11264	-0.41	0.01130008
primidone	219.11249	-0.41	0.01130008
D-Erythritol 4-phosphate	203.03146	0.67	0.00402284

Hydroxyurea

Name	<i>m/z</i>	<i>Log2</i> Fold Change: (HU_S) / (HU_C)	<i>P</i> -value: (HU_S) / (HU_C)
1-linoleoyl-sn-glycero-3-phosphoethanolamine	500.27672	0.91	8.2899E-05
1-O-Phosphonopentitol	233.04199	1.33	6.939E-05
2-[2-[5-(Ethoxycarbonyl)-2-morpholinoanilino]-2-oxoethoxy]acetic acid	367.1501	-1.4	0.00073902
2-Acetamidoglucal	204.08658	1.55	0.00105595
9-Oxohexadecanoic acid	251.20162	-1.93	2.973E-05
AS3325000	104.07057	-1.86	0.00015055
ATEE	284.14922	-2.16	6.0124E-07
Eicosapentanoic acid	301.21713	0.87	0.00014036
gamma-thiomethyl glutamate	194.04815	3.76	1.2257E-06
glu-ser	298.10122	1.11	0.00136137
Glutathione oxidized	613.15879	1.17	0.00040934
Glycerylphosphoryl ethanolamine	216.06301	-1.35	0.00038785
JMV 390-1	450.26099	-1.44	7.0594E-05
MFCDD00672375	162.04072	1.53	9.0473E-05
Oleic acid	281.24852	-0.27	0.00247994
Ornaline	263.12372	-2.3	6.7425E-05
Phosphocreatine	212.04303	0.66	0.00049777
Stearamide	284.29475	-1.64	0.00194058
Taurine	126.02195	-0.89	0.00040309
γ-Aminobutyric acid (GABA)	104.07057	-1.86	0.00015055

Etoposide

Name	<i>m/z</i>	<i>Log2</i> Fold Change: (ET_S) / (ET_C)	<i>P</i> -value: (ET_S) / (ET_C)
(2S,3R,4R,5S,6S,7R)-2,3,4,5,6,7,8-Heptahydroxooctanal	239.07721	-1.51	0.00745754
11(Z),14(Z)-Eicosadienoic Acid	307.26432	-0.4	0.01832904
2,2,6,6-Tetramethyl-4-piperidinol	158.15387	1	0.0087173
3-Hydroxy-L-proline	132.06583	0.19	0.01613917
9-Oxononanoic acid	173.11701	-3.14	0.01048479
Eicosapentanoic acid	301.21716	0.76	0.01884245
ELAIDYLPHOSPHOCHOLINE	434.33913	-1.12	0.00231899
Gluconic acid	195.05101	-2.34	0.00574793
Glutaurine	255.06456	-1.58	0.00609376
Glycerophosphoglycerol	247.05784	-0.36	0.00588946
Hex-2-ulose	179.05609	-1.53	0.01055774
Hypotaurine	110.02701	-1.7	0.00842153
Lauryldimethylamine oxide	230.24757	-1.89	0.00691505
LysopC(P-18:0)	508.3747	-0.47	0.00480342
N-[2-[(2-Amino-2-carboxyethyl)amino]-2-carboxyethyl]aspartic acid	308.10806	-0.94	0.00945972
O-Acetylserine	146.04585	-1.34	0.00556472
Stearamide	284.29466	-1.44	0.00446605
Taurine	126.02193	-1.7	0.00301198
Triethylamine	102.12774	-2.05	0.00577499
Triethylene glycol	173.0782	-1.05	0.00386296

Table S1. 4 Output tables of pathway enriched analysis performed with MetaboAnalyst and Mummichog software in different cell treatment conditions (multiple passages, irradiation, hydroxyurea, and etoposide). P values (p) are FDR = False Discovery Rate.

Multiple passages

MetaboAnalyst

	Tot	Exp	Hits	p	Imp
Alanine, aspartate and glutamate metabolism	28	0.6	6	0.00	0.45
D-Glutamine and D-glutamate metabolism	6	0.13	3	0.01	0.5
Histidine metabolism	16	0.34	4	0.01	0.27
Taurine and hypotaurine metabolism	8	0.17	3	0.01	0.71
Biosynthesis of unsaturated fatty acids	36	0.77	5	0.01	0
Arginine biosynthesis	14	0.3	3	0.03	0.12
Aminoacyl-tRNA biosynthesis	48	1.02	5	0.03	0
Butanoate metabolism	15	0.32	3	0.04	0.03

Mummichog

	Tot	Exp	Hits	p	Emp
Methionine and cysteine metabolism	94	1.97	6	0.00	0.01
Vitamin A (retinol) metabolism	67	0.56	5	0.01	0
Selenoamino acid metabolism	35	0.84	2	0.03	0
Glycerophospholipid metabolism	15 6	2.11	4	0.12	0.1
De novo fatty acid biosynthesis	10 6	0.7	2	0.13	0.06

Irradiation

MetaboAnalyst

	Tot	Exp	Hits	p	Emp
Taurine and hypotaurine metabolism	8	0.05	2	0.09	0.71
Starch and sucrose metabolism	18	0.12	2	0.23	0.15
Amino sugar and nucleotide sugar metabolism	37	0.24	2	0.62	0.08

Mummichog

	Tot	Exp	Hits	p	Emp
Caffeine metabolism	11	0.1	2	0.09	0.03
Ubiquinone Biosynthesis	10	0.21	1	0.18	0.08
Bile acid biosynthesis	82	0.26	1	0.22	0.1
Aspartate and asparagine metabolism	11 4	1.65	1	0.48	0.39
Methionine and cysteine metabolism	94	0.77	1	0.54	0.34

Hydroxyurea

MetaboAnalyst

	Tot	Exp	Hits	p	Imp
Alanine, aspartate and glutamate metabolism	28	0.49	4	0.08	0.36
Butanoate metabolism	15	0.26	3	0.08	0.06
Pentose phosphate pathway	22	0.38	3	0.16	0.22
Glutathione metabolism	28	0.49	3	0.24	0.31
Arginine biosynthesis	14	0.24	2	0.39	0

Mummichog

	Tot	Exp	Hits	p	Imp
Methionine and cysteine metabolism	94	2.19	6	0.04	0.06
Nitrogen metabolism	6	0.51	2	0.07	0.08
Arachidonic acid metabolism	95	1.16	3	0.08	0
Glycerophospholipid metabolism	15 6	2.83	5	0.10	0.08
Glutamate metabolism	15	1.29	3	0.12	0.07

Etoposide**MetaboAnalyst**

	Tot	Exp	Hits	p	Emp
Glycerophospholipid metabolism	36	0.44	5	0.00	0.08
Taurine and hypotaurine metabolism	8	0.1	3	0.00	0.71
Aminoacyl-tRNA biosynthesis	48	0.59	3	0.53	0
Pentose phosphate pathway	22	0.27	2	0.62	0.22

Mummichog

	Tot	Exp	Hits	p	Emp
Methionine and cysteine metabolism	94	0.63	3	0.01	0.01
Bile acid biosynthesis	82	0.16	1	0.14	0.03
Glycerophospholipid metabolism	15 6	0.95	2	0.22	0.21
Linoleate metabolism	46	0.32	1	0.27	0.12
Lysine metabolism	52	0.55	1	0.43	0.18

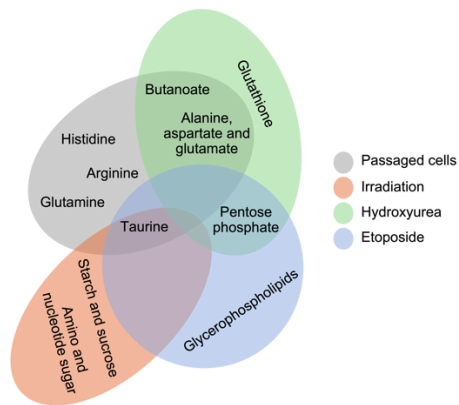


Figure S1. 7 Venn diagram. The diagram represents the metabolic pathways of normal human fibroblast at late passaged cells, and cells treated with irradiation, hydroxyurea, and etoposide.

Table S1. 5 List of metabolites identified in normal human fibroblasts. Cells at passage 20, after 12 Gy X-ray treatment for 1 week, 800 μ M hydroxyurea and 10 μ M etoposide treatment for 2 and 1 week, respectively. Class, name, Log₂ fold change, and p-value (*p*) is represented for each compound. In bold are the significant compounds.

Class	Name	Multiple passage		Irradiation		Hydroxyurea		Etoposide	
		P20/P3		12 Gy/Ctrl		800 μ M/Ctrl		10 μ M/Ctrl	
		Log ₂ Fold Change	<i>P</i>	Log ₂ Fold Change	<i>P</i>	Log ₂ Fold Change	<i>P</i>	Log ₂ Fold Change	<i>P</i>
Amino acids	1-Methylhistidine	1.52	0.01	-	-	0.29	0.97	-0.46	0.74
TCA acids	2- Oxoglutarate	0.67	0.02	-0.17	0.87	0.83	0.05	-0.38	0.65
Acyl carnitines	C18-Carnitine	2.05	0.00	0.37	0.12	0.59	0.01	-0.55	0.36
Cholines	Acetylcholine	1.38	0.01	-0.61	0.01	0.11	0.48	-0.88	0.03
Purine ribonucleosides	Adenosine	1.36	0.00	-0.57	0.12	-	-	0.56	0.33
Purine ribonucleoside diphosphates	ADP	-0.12	0.81	-0.01	0.73	-0.2	0.61	-0.57	0.14
Dicarboxylic acids	α -Aminoadipic acid	-1.3	0.01	-0.54	0.07	-0.25	0.28	-1.22	0.02
Pyrimidine ribonucleoside monophosphates	AMP	-	-	0.79	0.12	1.55	0.14	-0.78	0.21
Unsaturated Fatty Acids	Arachidonic acid	1.18	0.00	0.10	0.39	-0.21	0.21	0.48	0.13
Amino acids	Argininosuccinic acid	0.14	0.50	-0.31	0.56	-0.51	0.12	-0.80	0.09
Amino acids	Asparagine	1.68	0.01	-0.05	0.79	-0.21	0.78	-1.63	0.04
Amino acids	Aspartate	0.07	0.51	-0.28	0.42	-0.92	0.00	-0.69	0.09
Purine ribonucleoside triphosphates	ATP	0.96	0.04	0.56	0.27	-0.35	0.21	-0.89	0.38
Amino acids	Alanine	-0.5	0.06	0.87	0.49	-	-	-1.13	0.04
Hybrid peptides	Carnosine	0.12	0.51	0.02	0.68	0.13	0.48	-1.69	0.12
Pyrimidine ribonucleoside diphosphates	CDP	-	-	0.5	0.11	0.29	0.09	-	-
Pyrimidine ribonucleoside diphosphates	CDP-Ethanolamine	-0.62	0.05	-0.13	0.63	-0.15	0.66	-0.70	0.06
Cholines	Choline	-0.28	0.13	-0.15	0.06	-0.06	0.77	-0.64	0.03
TCA acids	Citrate	0.1	0.65	0.06	0.25	0.07	0.88	-1.7	0.38
Amino acids	Citrulline	0.78	0.09	-0.58	0.26	-0.01	0.99	-2.35	0.07
Pyrimidine ribonucleoside monophosphates	CMP	-0.07	0.42	0.51	0.12	-0.19	0.68	-0.08	0.94

Amino acids	Creatine	-0.24	0.07	0.45	0.64	0.01	0.83	-0.10	0.47
Amino acids	Creatinine	0.15	0.55	-0.13	0.42	0.09	0.21	-0.68	0.15
Amino acids	Cystathionine	-2.53	0.00	-0.57	0.08	-1.01	0.00	-1.29	0.01
Carbohydrates	Fructose	0.67	0.04	-	-	-	-	-	-
Monosaccharides	Glucose 1P	-	-	1.31	0.05	-	-	0.02	0.32
Aldotriose	Glyceraldehyde 3-phosphate	0.64	0.16	0.31	0.28	0.55	0.01	-0.59	0.28
Monosaccharides	Glucosamine 6P	-0.2	0.44	-0.18	0.32	-	-	-0.76	0.08
Amino acids	Serine	1.71	0.00	0.82	0.01	0.31	0.11	0.49	0.14
Amino acids	Tryptophan	0.28	0.22	-0.10	0.39	-0.26	0.27	-0.80	0.16
Alcohols	Diethanolamine	0.49	0.23	2.88	0.04	0.96	0.09	-2.21	0.25
Nucleobasis	Dihydrothymine	-0.76	0.01	-0.21	0.57	-0.19	0.23	-0.34	0.82
Vitamins	Folic acid	-	-	-0.05	0.35	-0.15	0.45	-0.82	0.16
Aldotriose	Glycerol 3P	-1.25	0.00	-0.05	0.46	0.08	0.32	-0.47	0.58
Amino acids	GABA	-0.62	0.03	-	-	-1.86	0.00	-	-
Sugar acids	Galactonic acid	-	-	-0.14	0.28	-	-	-	-
Nucleoside	GDP	-	-	-	-	0.35	0.04	-	-
Sugar acids	Gluconic acid	-0.31	0.77	-0.97	0.00	-0.84	0.01	-2.34	0.01
Carboxylic acids	Glutathione GSH	1.16	0.03	0	0.95	0.87	0.01	-0.62	0.21
Carboxylic acids	Glutathione GSSG	0.75	0.06	0.43	0.17	1.17	0.00	-0.78	0.07
Amino acids	Glycine	0.29	0.11	-	-	-0.05	0.89	-0.62	0.19
Nucleoside	GMP	0.32	0.55	0.41	0.08	-	-	-	-
Amino acids	Guanidinosuccinic acid	-0.25	0.01	0.28	0.40	-	-	0.35	0.07
Nucleobasis	Guanine	-	-	1.49	0.05	-	-	0.48	0.09
Acyl carnitines	C12-Carnitine	-1.18	0.04	-	-	-4.12	0.15	-1.17	0.53
Aralkylamines	Histamine	0.31	0.83	0.19	0.55	0.18	0.37	-0.21	0.40
Taurines	Hypotaurine	-0.77	0.03	-0.67	0.01	-0.20	0.89	-1.70	0.01
Taurines	Hypoxanthine	-	-	1.14	0.01	-0.10	0.84	-	-
Amino acids	Arginine	0.68	0.86	0.17	0.56	0.10	0.73	-0.85	0.22
Amino acids	Ergothioneine	-1.66	0.05	-1.68	0.02	0.11	0.15	-0.73	0.04
Amino acids	Glutamine	1.06	0.01	0.25	0.49	0.21	0.14	-0.37	0.47
Carboxylic acids	Glutamic acid	-1.62	0.00	-0.32	0.83	-0.61	0.05	-1.01	0.08
Amino acids	Histidine	-0.38	0.05	-0.02	0.99	-0.08	0.97	-1.37	0.12
Amino acids	1-methylhistidine	1.52	0.01	-	-	0.29	0.97	-0.46	0.74
Butyrophenones	Kynurenine	1.17	0.01	-	-	-0.73	0.02	-	-

Amino acids	Methionine	1.15	0.04	0.08	0.57	0.02	0.87	-0.51	0.23
Amino acids	Phenylalanine	0.44	0.28	-0.15	0.39	-0.34	0.27	-0.76	0.28
Amino acids	Threonine	0.54	0.07	0.28	0.35	-0.06	0.60	-0.31	0.34
Amino acids	Tyrosine	0.5	0.10	-0.06	0.62	-0.22	0.36	-0.86	0.19
Carboxylic acids	Lactate	0.5	0.08	-0.47	0.29	0.07	0.72	-0.73	0.03
Amino acids	Leucine	0.45	0.09	-0.01	0.62	-0.26	0.25	-0.79	0.16
Unsaturated Fatty Acids	Oleic acid	1.71	0.00	-0.09	0.49	-0.27	0.00	-	-
Amino acids	Lysine	0.37	0.15	0.20	0.65	0.09	0.70	-0.85	0.21
LPC	LysoPC(P-18:0)	-	-	-0.10	0.68	-	-	-0.47	0.00
TCA acids	Malate	0.03	0.57	0.16	0.49	-0.36	0.09	-0.76	0.07
Sugar alcohols	Mannitol	1.85	0.00	1.33	0.00	0.21	0.15	0.22	0.15
Nicotinamide dinucleotides	NAD	0.69	0.27	-	-	-	-	-	-
Nicotinamide dinucleotides	NADH	-	-	-	-	-0.03	0.54	-	-
Nicotinamide	Nicotinamide	0.25	0.13	-0.02	0.56	0.1	0.47	-0.62	0.18
Catechols	Norepinephrine	-	-	-	-	-0.07	0.73	-	-
Carboxylic acids	Ophthalmic acid	0.43	0.07	0.24	0.10	-0.14	0.59	-0.43	0.47
Amino acids	Ornithine	-	-	-0.07	0.26	-0.33	0.09	-1.23	0.07
Saturated Fatty Acids	Palmitic acid	0.56	0.02	-	-	-	-	-	-
Acyl carnitines	Palmitoylcarnitine	1.61	0.00	0.32	0.16	0.91	0.00	-0.57	0.51
Phosphoric acid	Phosphoric acid	0.46	0.03	-0.18	0.50	-	-	-	-
Benzoic acids	Phthalic acid	0.38	0.07	-	-	-0.68	0.03	-0.84	0.10
Amino acids	Phenylalanine	0.44	0.27	-0.15	0.38	-0.34	0.27	-0.76	0.28
Amino acids	Proline	-0.26	0.38	-0.16	0.30	-0.08	0.81	-1.01	0.05
Acyl carnitines	Propionylcarnitine	-1.05	0.03	-0.33	0.11	-0.13	0.78	-0.75	0.07
Carboxylic acids	Pyroglutamic acid	0.17	0.58	0.08	0.86	0.10	0.45	-	-
Short-chain acids and derivatives	Pyruvate	1.32	0.00	-0.51	0.31	0.56	0.07	-0.71	0.06
Glycosylamines	Adenosylhomocysteine	-0.37	0.19	-0.19	0.64	-0.86	0.02	-0.42	0.21
Saturated Fatty Acids	Stearic acid	0.71	0.01	0.02	0.39	0.29	0.28	0.01	0.39
Pyrimidine nucleotide sugars	Thiamine	0.57	0.20	0.23	0.22	-0.25	0.19	-0.86	0.14
Tertiary amines	Triethanolamine	0.8	0.08	-0.22	0.51	0.19	0.93	-	-
Pyrimidine ribonucleoside diphosphates	UDP	0.19	0.59	-0.57	0.19	0.14	0.31	-0.95	0.03
Pyrimidine ribonucleoside monophosphates	UMP	-	-	0.96	0.03	-	-	-0.06	0.45

Pyrimidine ribonucleoside diphosphates	UDP-N-acetylglucosamine	-0.1	0.9	-	-	0.58	0.01	-1.18	0.04
Amino acids	Valine	0.4	0.11	0.03	0.59	-0.21	0.21	-0.66	0.19
Amino acids	Taurine	-2.04	0.00	-0.99	0.00	-0.89	0.00	-1.70	0.00

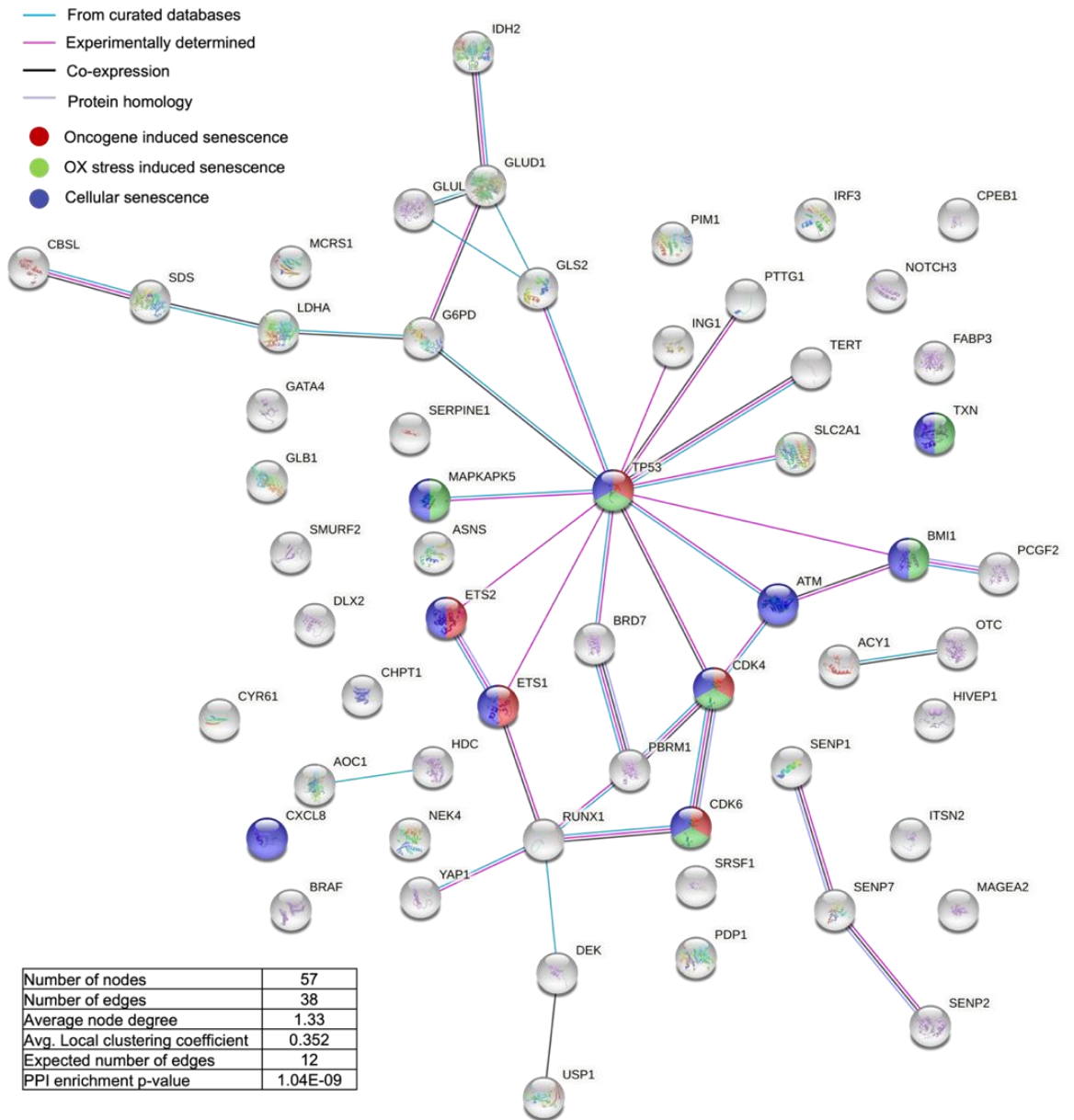


Figure S1. 8 Known and predicted protein-protein interactions. Analysis performed through STRING Data Sources. Input data are represented by the list of senescence genes (Table S 3) and the enzymatic genes in the metabolic pathway model of Figure 8.

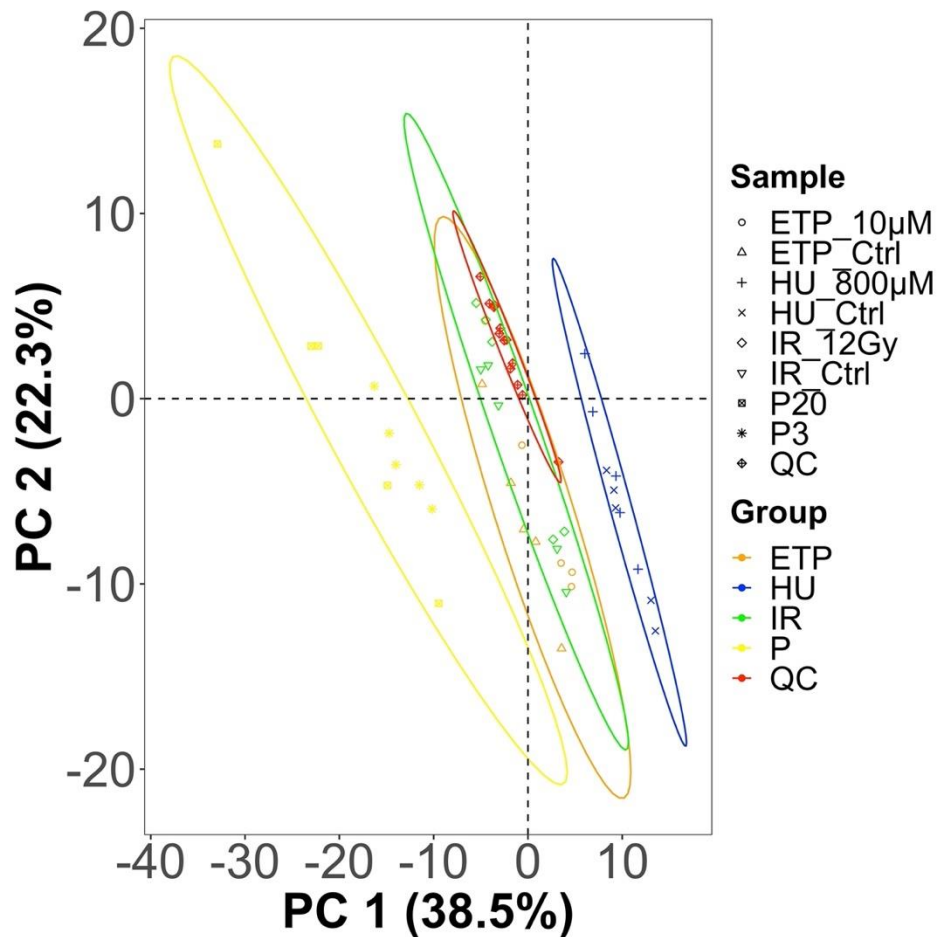


Figure S1. 9 PCA analysis of growth media samples collected from HFF-1 cells. Cells at passage 20, and after treatment with 12 Gy irradiation, 800 μM hydroxyurea and 10 μM etoposide. For each treatment group, five replicates were used. Data points in the two-dimensional PCA score plot were central scaled. Ellipses represent 95% confidence interval.

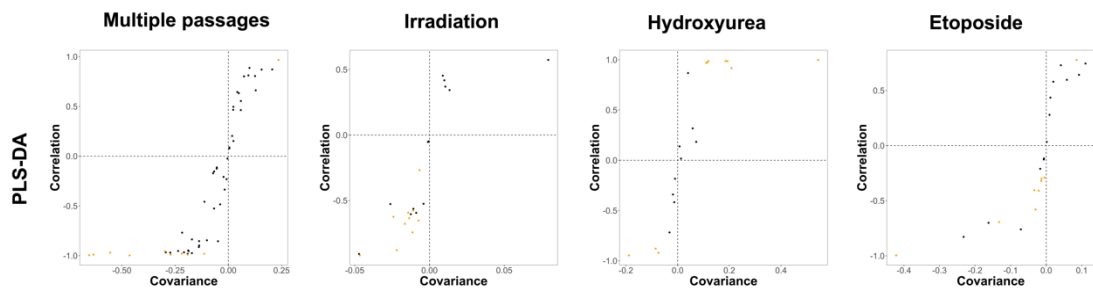


Figure S1. 10 Pairwise partial least square-discriminant analysis (PLS-DA) of the media collected from different senescence-induced cells. The orange circles represent the first 10 discriminating compounds that allow to differentiate between non-treated and treated cells.

Table S1. 6 Table with a list of the first 10 PLS-DA compounds for all the conditions. *m/z* value, *Log2*Fold change and *p*-values have been reported.

Multiple passages

Name	<i>m/z</i>	Log2 Fold Change: (P20) / (P3)	P-value: (P20) / (P3)
2-Acetamidoglucal	204.08648	3.25	2.9518E-05
2-Oxoglutaric acid	145.01419	1.71	0.0001334
4-Methylcarbostyryl	160.07561	1.42	2.061E-07
4-tert-Octylphenol monoethoxylate	249.18594	3.03	4.7197E-06
Penicillin G	335.22178	0.99	6.4655E-05
Ethanolamine	62.06006	-1.26	8.6738E-06
Glutamic acid	148.06039	0.56	0.0004203
Kynurenine	209.09198	0.91	5.9344E-06
trans-10-Heptadecenoic Acid	267.23281	3.06	5.96E-05
trans-Petroselinic acid	281.24849	2.22	1.4774E-06

Irradiation

Name	<i>m/z</i>	Log2 Fold Change: (IR_S) / (IR_C)	P-value: (IR_S) / (IR_C)
Glutamine	169.05833	-0.8	0.0040540
Methyl acetoacetate	115.04004	-0.28	0.0098361
4-hydroxyphenylglycine	168.06542	-0.37	0.0401772
Pyridoxal	168.06545	-0.18	0.0800630
6-Oxohexanoic acid	129.05568	-0.13	0.0822309
Trimethoprim impurity B	305.12444	-0.22	0.1111955
γ-Glutamyl-L-glutamic acid	277.10308	-0.39	0.1842875
N-(2-Pyridinylmethyl)-5,6,7,8-tetrahydro[1,2,4]triazolo[5,1-b]quinazolin-9-amine	281.14953	-0.28	0.1937640
Thiamine	265.11177	-0.59	0.2188043
N2-Methylguanosine	298.11454	-0.26	0.2406694

Hydroxyurea

Name	<i>m/z</i>	Log2 Fold Change: (HU_S) / (HU_C)	P-value: (HU_S) / (HU_C)
1-Methylnicotinamide	137.07089	-0.67	0.0007944
3-Hydroxy-5-(hydroxymethyl)-2-methylisonicotinaldehyde oxime	183.07634	4.17	5.8499E-07
4-Methylcarbostyryl	160.07554	1.49	9.3029E-08
Glutamine	169.05826	-1.72	6.8071E-05
epsilon-(gamma-Glutamyl)-lysine	276.15527	1.29	0.0042030
gamma-Glu-gln	276.11895	0.86	7.3181E-07
Glutarimide	114.0549	-0.59	0.0001444
γ-Glu-Ala	219.09746	0.8	0.0001052
N'2-cinnamoyl-3-(1H-pyrrol-1-yl)thiophene-2-carbohydrazide	320.0828	0.8	6.9906E-05
Salsolinol	180.10177	1.38	8.9868E-06

Etoposide

Name	<i>m/z</i>	Log2 Fold Change: (ET_S) / (ET_C)	P-value: (ET_S) / (ET_C)
1-Nitronaphthalene	175.08628	-2.11	0.010472
3-Indoleacetamide	175.08635	-2.11	0.0104565
4-hydroxyphenylglycine	168.06542	-0.32	0.0213889
6-Methylnicotinamide	137.07091	-0.36	0.0037892
7Z,10Z-Hexadecadienoic acid	251.20161	0.88	0.0301742
Glutamine	169.0583	-1.6	0.0002118
Lactic acid	89.0244	-0.1	0.0300426
Methyl acetoacetate	115.04004	-0.29	0.0423871
γ-Glu-Ala	219.09749	-0.19	0.0461277
Trimethoprim impurity B	305.12446	-0.44	0.0179563

Table S1. 7 List of metabolites identified in the media of normal human fibroblasts. Cells at passage 20, after 12 Gy X-ray treatment for 1 week, 800 μ M hydroxyurea and 10 μ M etoposide treatment for 2 and 1 week, respectively. Name, Log₂ fold change, and p-value (p) is represented for each compound. In bold are significant compounds.

Name	Multiple passage		Irradiation		Hydroxyurea		Etoposide	
	P20/P3		12 Gy/Ctrl		800 μ M/Ctrl		10 μ M/Ctrl	
	Log2 Fold Change	P	Log2 Fold Change	P	Log2 Fold Change	P	Log2 Fold Change	P
(1R,2S)-1-(7,8-Dihydro-6-pteridiny)-1,2-propanediol							-0.33	0.27
1-Methylguanine	-0.35	0.00						
1-Methylnicotinamide	0.28	0.16	-0.16	0.51	-0.67	0.00		
1-Nitrosonaphthalene	0.07	0.57					-2.11	0.01
1,2,3-cyclopropanetricarboxylic acid	-0.49	0.99						
1,4-Dihydroxyoctahydro-2,3-quinoxalinedione	0.66	0.00						
2-(6 α -μετηψλτηιο)ηεξνλμαλιχ αχιδ			-0.64	0.50				
2-{2-[5-(Ethoxycarbonyl)-2-morpholinoanilino]-2-oxoethoxy}acetic acid	-0.77	0.01						
2-{2-Oxo-2-[4-(1H-pyrrol-1-yl)piperidino]ethoxy}acetic acid	-0.24	0.04						
2-Acetamidoglucal	3.25	0.00						
2-amino-2,3,7-trideoxy-D-lyxo-hept-6-ulosonic acid	1.52	0.00						
2-Amino-3-methoxybenzoic acid	-0.16	0.19						
2-Aminooctanedioic acid	0.83	0.00						
2-Oxoglutaric acid	1.71	0.00						
2-Quinolinecarboxylic acid			-0.22	0.64	0.22	0.01		
3-[(3-Hydroxyundecanoyl)oxy]-4-(trimethylammonio)butanoate	-0.79	0.00						
3-[(methoxycarbonyl)amino]-2,2,3-trimethylbutanoic acid	0.54	0.01						

3-Hydroxy-3-methylbutanoic acid	-0.38	0.53						
3-Hydroxy-5-(hydroxymethyl)-2-methylisonicotinaldehyde oxime					4.17	0.00		
3-Indoleacetamide	0.07	0.57					-2.11	0.01
3-oxopalmitic acid	1.11	0.00						
4-Aminobenzoic acid	0.07	0.66						
4-hydroxyphenylglycine			-0.37	0.04	-0.21	0.03	-0.32	0.02
4-Methyl-5-thiazoleethanol			-0.58	0.24	0.08	0.42	-0.34	0.65
4-Methylcarbostyryl	1.42	0.00	0.15	0.64	1.49	0.00		
4-tert-Octylphenol monoethoxylate	3.03	0.00						
5-Amino-3-(4-methoxyphenyl)-5-oxopentanoic acid	0.47	0.13						
6-Methylnicotinamide							-0.36	0.00
6-Oxohexanoic acid	-0.04	0.60	-0.13	0.08	0.16	0.67	-0.08	0.89
7Z,10Z-Hexadecadienoic acid	1.11	0.00	0.34	0.27			0.88	0.03
abacavir carboxylate							0.63	0.30
C10-Carnitine	-0.58	0.00						
Choline					-0.05	0.69		
Cysteinylglycine disulfide							0.25	0.07
DL-2,6-Diaminopimelic acid	-0.11	0.74						
Ecgonine	1.05	0.00					-0.01	0.65
EDDA	1.18	0.00						
epsilon-(gamma-Glutamyl)-lysine	0.70	0.00			1.29	0.00	-0.09	0.26
Ethanolamine	-1.26	0.00						
gamma-Glu-gln	0.25	0.01	0.04	0.34	0.86	0.00	0.09	0.39
glu-thr	0.57	0.01						
Glutamic acid	0.56	0.00						
Glutamine	-1.06	0.00	-0.80	0.00	-1.72	0.00	-1.60	0.00
Glutarimide	-0.39	0.09	-0.15	0.29	-0.59	0.00	-0.13	0.28
Hex-2-ulose					1.88	0.95		
Kynurenine	0.91	0.00						
Lactic acid	0.02	0.73	-0.11	0.27			-0.10	0.03
Methyl acetoacetate	-0.09	0.57	-0.28	0.01	-0.12	0.21	-0.29	0.04

Mono(2-ethylhexyl) phthalate (MEHP)	0.83	0.00					0.94	0.11
N-((3S,4R)-6-Cyano-3-hydroxy-2,2-dimethylchroman-4-yl)-N-hydroxyacetamide	0.25	0.89						
N-(2-Pyridinylmethyl)-5,6,7,8-tetrahydro[1,2,4]triazolo[5,1-b]quinazolin-9-amine			-0.28	0.19				
N-[(2S)-2-Hydroxypropanoyl]methionine	1.32	0.01						
N-Acetyl cytosine	-0.49	0.01						
N-Acetyl-D-quinovosamine	-0.57	0.05						
N,N-dimethyl-N'-(3-phenyl[1,2,4]triazolo[4,3-b]pyridazin-6-yl)iminoformamide							-0.43	0.11
N'2-cinnamoyl-3-(1H-pyrrol-1-yl)thiophene-2-carbohydrazide					0.80	0.00		
N2-Dimethylguanosine	-0.33	0.11						
N2-Methylguanosine			-0.26	0.24			-0.81	0.13
Norleucine	0.31	0.69						
Oxaceprol	-0.57	0.05	-0.25	0.65			-0.30	0.23
phenacetin			0.00	0.24			0.06	0.62
Phenylalanine			1.11	0.77				
Pivagabine	0.60	0.18						
Prostaglandin E1	0.92	0.00						
Pyridoxal	-0.33	0.04	-0.18	0.08				
Salsolinol	0.78	0.00			1.38	0.00		
Thiamine			-0.59	0.22				
thr-phe					-0.27	0.29		
trans-10-Heptadecenoic Acid	3.06	0.00						
trans-Petroselinic acid	2.22	0.00						
Trimethoprim impurity B	-0.04	0.43	-0.22	0.11	-0.19	0.53	-0.44	0.02
γ-Glu-Ala	-0.13	0.10						
γ-Glu-Ala			0.01	0.53	0.80	0.00	-0.19	0.05

Y-Glutamyl-L-glutamic acid	0.99	0.00	-0.39	0.18				
----------------------------	------	------	-------	------	--	--	--	--

6.2. Appendix 2

Table S2. 1 Corresponding elution gradient used for the chromatographic separation of metabolites and protein extracts

Metabolomics				Proteomics			
Time	Flow [ml/min]	%B	Curve	Time	Flow [ml/min]	%B	Curve
0	0.3	20	5	0	0.05	3	5
11	0.3	60	5	65	0.05	20	5
15	0.3	20	5	70	0.05	40	5
20	0.3	20	5	74	0.05	95	5
				79	0.05	95	5
				84	0.05	3	5
				100	0.05	3	5

Table S2. 2 LC-MS/MS method summary for metabolomics and proteomics

	Metabolomics	Proteomics
Method setting		
Application mode	Small molecules	Peptide
Method duration (min)	20	100
Global parameters		
Ion source type	H-ESI	H-ESI
Spray voltage	Static	Static
Positive ion (V)	3900	3400
Negative ion (V)	2500	3000
Gas mode	Static	Static
Sheath gas (Arb)	40	25
Aux gas (Arb)	10	5
Sweep gas (Arb)	1	0
Ion transfer tube temp (°C)	250	320
Vaporizer temp (°C)	250	75
Infusion mode	Liquid chromatography	Liquid chromatography
Expected LC peak width (s)	20	10
Mild trapping	TRUE	TRUE
Default charge state	1	2
Internal mass calibration	EASY-IC	EASY-IC
Mode	Run start	Scan-to-scan
Experiment		
Start time (min)	0	0
End time (min)	20	100
Filters		

Full scan		
Orbitrap resolution	60,000	120,000
Scan range (<i>m/z</i>)	50-750	275-1500
RF Lens (%)	70	70
AGC Target	Custom	Custom
Maximum injection time mode	Auto	Custom
Maximum injection time (ms)	-	25
Microscans	1	1
Data type	Profile	Profile
Polarity	Positive/negative	Positive
Use EASY-C	On	On
MIPS		
Mono isotopic peak determination	Small molecule	Peptide
Relax restrictions when too few precursors are found	Checked	Checked
Intensity		
Intensity threshold	1.0e4	1.0e4
Precursor fit		
Fit threshold (%)	70	-
Fit window (<i>m/z</i>)	0.7	-
Charge state		
Include charge state (s)	1-2	1-2
Dynamic exclusion		
Dynamic exclusion mode	Custom	Custom
Exclude after n time	1	1
Exclude duration (s)	60	45
Mass tolerance	Ppm	ppm
Low	3	5
High	3	5
Exclude isotopes	Checked	Checked
Isotope exclusion	Assigned	-
Apex detection		
Designed apex window (%)	50	-
ddMS/MS		
Multiplex ions	FALSE	FALSE
Isolation window (<i>m/z</i>)	0.7	1.2
Isolation Offset	Off	Off

Collision energy type	Normalised	Normalised
HCD Collision energies (%)	10,20,30,40,100	30
Orbitrap resolution	15,000	15,000
Scan range mode	Auto	Auto
AGC Target	Standard	Custom
Normalised AGC target (%)	-	100
Maximum injection time mode	Auto	Auto
Microscans	1	1
Data type	Profile	Centroid
Use EASY-C	On	On

Table S2. 3 Data processing workflows for metabolomics analysis through Compound Discoverer 3.3

	Metabolomics
	<pre> graph TD A[Input files] --> B[Select spectra] B --> C[Allign retention times] C --> D[Detect compounds] D --> E[Group compounds] E --> F[Fill gaps] F --> G[Apply QC corrections] G --> H[Mark background compounds] D --> I[Assign compound annotation] D --> J[Search Chem Spider] E --> K[Search mzCloud] E --> L[Predict composition] J --> M[Apply mzLogic] </pre>
Input files	.raw data
Select spectra	
Lower RT limit	0
Upper RT limit	0
First Scan	0
Last Scan	0
Min precursor mass	0 Da
Max. precursor mass	5,000 Da
Tot intensity threshold	0
Min peak count	1
Min collision energy	0
Max collision energy	1,000
Polarity mode	is -;+
S/N threshold	1.5
Align retention time	

Alignment model	Adaptive curve
Max shift (min)	2
Mass tolerance	5 ppm
Remove outlier	TRUE
Detect compound	
Mass tolerance	5 ppm
Min. peak intensity	10,000
Min N scan per peak	5
Use most intense isotope only	TRUE
Chromatographic S/N threshold	1.5
Gap ratio threshold	0.35
Max peak width (min)	1
Min relative valley depth	0.1
Base ions	[M+H] ⁺ +1; [M-H] ⁻ -1
Group compounds	
Mass tolerance	5 ppm
RT tolerance (min)	0.2
Align peaks	FALSE
Preferred ions	[M+H] ⁺ +1; [M-H] ⁻ -1; [M+ACN+H] ⁺ +1; [M+FA-H] ⁻ -1; [M+ACN+Na] ⁺ +1; [M+H+Na] ⁺ +2; [M+H+NH ₄] ⁺ +2; [M+Na] ⁺ +1; [M+NH ₄] ⁺ +1
Area integration	Most common
Area contribution	3
CV contribution	10
Peak rating threshold	4.5
Number of files	2
Fill gaps	(re-detected low-intensity peaks)
Mass tolerance	5 ppm
S/N Threshold	1.5
Search mzCloud	
Compound classes	All
Library	Autoprocessed; Reference
Search MSn tree	TRUE
Identity search	Cosine
Match activation type	TRUE
Match activation energy	Match with tolerance
Activation energy	20
Apply intensity threshold	TRUE
Similarity search	Confidence forward

Match factor threshold	50
Predict composition	
Mass tolerance	5 ppm
Min element count	C H
Intensity tolerance	30
Intensity threshold	0.1
S/N threshold	3
Use dynamic recalibration	TRUE
Use fragments matching	TRUE
Mass tolerance	5 ppm
S/N threshold	3
Search ChemSpider	
Databases	BioCyc, CheBI, HMDB, KEGG
Search mode	by formula or mass
Mass tolerance	5 ppm
Max N of results per compound	100
Max N of predicted composition	3
Apply mzLogic	
Max N compounds	0
Max N mzCloud	10
Match factor threshold	70
Assign compound annotations	
Mass tolerance	5 ppm
Use mzLogic	TRUE
Use spectral distance	TRUE
Apply QC correction	
Min QC coverage	NA
Max QC area RSD	NA
Max corrected QC area	NA
Mark background compounds	
Max sample/blank	5
Max blank/sample	0
Hide background	TRUE
<u>DDA Search</u>	
Identity search	Cosine
Match activation type	True
Match activation energy	Match with tolerance
Activation energy tolerance	20
Apply intensity threshold	True
Similarity search	None

Match factor threshold	20
Differential analysis	
Log10 transform values	True

Table S2. 4 Data processing workflows (processing and consensus) for proteomics analysis through Proteome Discoverer 3.0

	Proteomics
Processing	<pre> graph TD A[Spectrum files RC] --> B[Minora feature detection] B --> C[Spectrum selector] C --> D[Sequest HT] D --> E[Percolator] </pre>
Spectrum files RC	
Protein database	Mus musculus (TaxID:10090)
Enzyme name	Trypsin
Precursor mass tolerance	20 ppm
Fragment mass tolerance	0.5 Da
Regression model	Non-linear regression
Parameter tuning	Coarse
Minora	
Min. trace length	5
S/N threshold	1
Max Δ RT (min)	0.2
PMS confidence at least	High
Spectrum selector	
Precursor selection	Use MS1 precursor
Min precursor mass	350 Da
Max precursor mass	6500 Da
Min peak count	1
Scan type	Is full
Polarity mode	Any
Sequest HT	
Max missed cleavage	2
Min peptide length	6
Max peptide length	144
Percolator	
Target/Decoy selection	Concatenated

Validation based on	q-Value
Target FDR (Strict)	0.01
Targetd FDR (Relaxed)	0.05
Consensus	<pre> graph TD MSF[MSF files] --> FM[Feature mapper] MSF --> PSM[PSM grouper] FM --> PIQ[Precursor ions quantifier] PIQ --> PM[Protein marker] PSM --> PV[Peptide validator] PV --> PPF[Peptide and protein filter] PPF --> PA[Protein annotation] PPF --> PS[Protein scorer] PS --> PFDV[Protein FDR validator] PFDV --> PG[Protein grouping] PG --> PIPA[Peptide in protein annotation] </pre>
MSF Files	
Merge mode	Globally by search engine type
Reported FASTA tale lines	Best match
Feature mapper	
Perform RT alignment	TRUE
Max RT shift (min)	10
Min S/N threshold	5
Precursor ions quantifier	
Peptide to use	Unique + Razor
Consider protein groups	TRUE
Precursor abundance based on	Insensity
Min replicate features (%)	60
Protein abundance calculation	Summed abundances
Protein ratio calculation	Protein abundance based
Max allowed fold change	100
Hypothesis test	ANOVA (Individual proteins)
PMS Grouper	
Site probability threshold	75
Peptide validator	
Validation mode	Automatic
Target FDR (strict)	0.01
Target FDR (relaxed)	0.05
Peptide and protein filter	
Peptide confidence at least	High
Min peptide length	6
Min N of peptide sequences	1

Protein marker	
Contaminant database	PD_Contaminants_2015_5fasta
Additional marker database	Mus musculus (TaxID:10090)
Protein annotation	
Aspect	Biological process, Cellular component, molecular function
Protein grouping	TRUE
Peptide in protein annotation	
Protein modifications reported	Only for master proteins
Modification sites reported	All and specific



Figure S2. 1 Sample batch order. 2 blanks were injected at the beginning and at the end of the run and after every 5 samples.

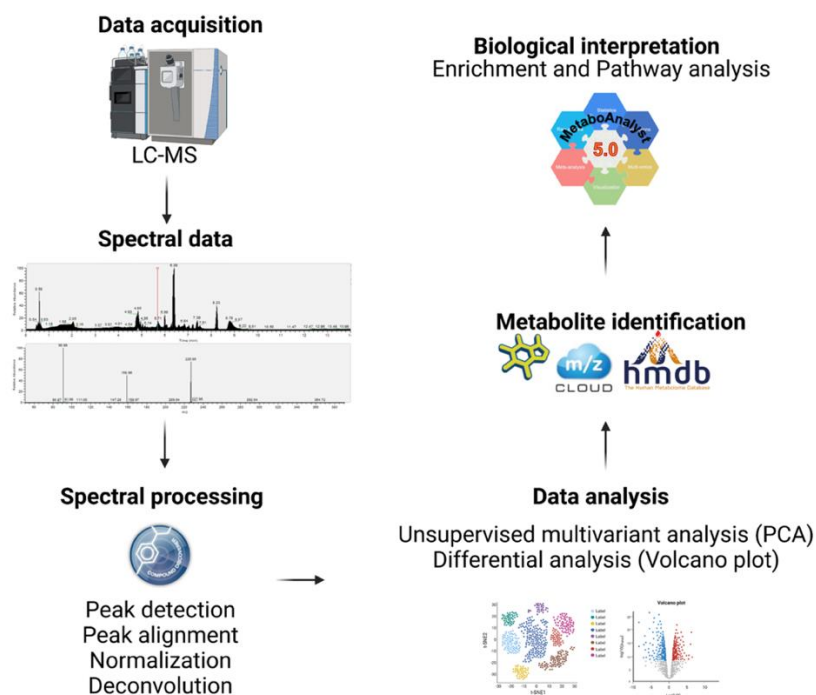


Figure S2. 2 Workflow used in this study to perform pathways analysis from metabolomics analyses

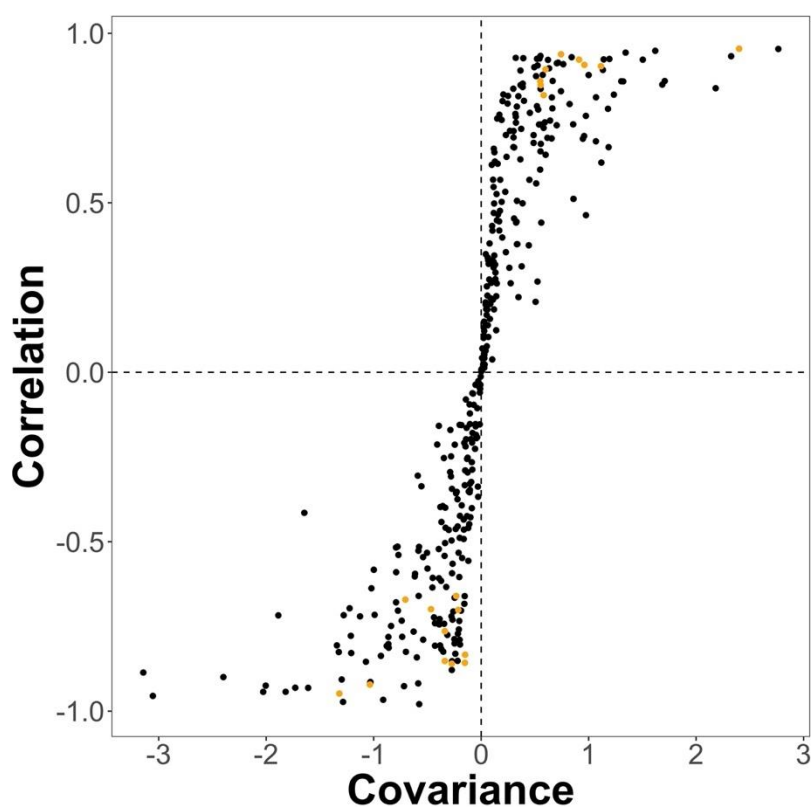


Figure S2. 3 Pairwise partial least square-discriminant analysis (PLS-DA) of old vs young brain tissues. The orange circles represent the first 20 discriminating compounds that allow to differentiate between young and old murine brain tissues.

Table S2. 5 Table with a list of the first 20 PLS-DA compounds for all the conditions. *m/z* value, Log₂Fold change and *p*-values have been reported.

Name	<i>m/z</i>	Log ₂ Fold Change: (Old) / (Young)	P-value: (Old) / (Young)
1-(4Z,7Z,10Z,13Z,16Z,19Z-docosahexaenoyl)-sn-glycero-3-phosphocholine	568.339	-1.6	9E-05
1-[(1Z)-octadec-1-enyl]-sn-glycero-3-phosphoethanolamine	464.315	-1.54	3E-03
1-Oleoyl-2-hydroxy-sn-glycero-3-PE	478.294	-1.03	4E-04
2,2'-({2-[(Carboxylatomethyl)amino]ethyl}ammonio)diacetate	233.077	1.23	1E-04
2-Iminobutanoic acid	102.055	0.32	2E-04
3-Methylhistamine	126.103	1.86	5E-04
3-O-beta-D-galactosyl-sn-glycerol	272.134	-1.13	1E-04
Arachidonic acid	303.233	0.86	7E-04
C14-Carnitine	372.310	0.56	5E-05
CDP-ethanolamine	447.067	2.2	6E-04
Crotonic acid	87.044	1.99	1E-03
Cytidine 5'-diphosphocholine	489.114	0.52	4E-04
Serine	106.050	0.73	3E-05
Glucuronamide	192.051	-5.28	7E-04
Homoanserine	255.145	-1.28	1E-04
Glutamic acid	148.060	0.29	2E-04
LysoPC(24:1(15Z))	606.448	-1.69	1E-03
N-acetyl-L-2-aminoadipic acid	202.072	-1.26	8E-05
PAF C-18:1	550.386	-2.32	6E-05
Uracil	111.020	0.6	1E-04

Table S2. 6 Classes of enriched metabolites in the brain tissues of old mice relative to the young mice. Analysis performed through MetaboAnalyst and Mummichog software.

MetaboAnalyst

	Tot	Hits	p
Amino acids	277	12	0
Pyrimidine ribonucleoside diphosphates	10	3	0
Unsaturated Fatty Acids	267	4	0

TCA acids	9	2	0
Glycosylamines	10	2	0
Saturated Fatty Acids	38	2	0.01
LPC	79	2	0.03

Mummichog

	Tot	Hits	p
Pyrimidine ribonucleoside diphosphates	20	4	0
Peptides	22	1	0.04
Glycosylamines	15	1	0.08
Aralkylamines	15	2	0.2
Amino acids	510	16	0.51
Dipeptides	438	2	0.82

Table S2. 7 Classification of putative metabolites identified in the brain tissues of old and young mice. Variation of metabolite expression in old/young mice is represented with the Log2 fold change, while P is the p-value associated with each metabolite. Significant metabolites are highlighted in Bold.

Class	Name	Log2 Fold Change	P
Long-chain fatty acids	11(Z)-Eicosenoic acid	-0.71	1E-03
HODEs	13S-hydroxyoctadecadienoic acid	1.82	8E-02
Amino acids	2-Aminoadipic acid	-0.23	2E-01
	2-aminopentanenitrile	0.80	2E-01
Carnitines	2-methylbutyrylcarnitine	-0.32	5E-01
Tricarboxylic acids	2-methylcitric acid	0.16	4E-01
Keto acid	2-Oxobutyric acid	-0.41	4E-02
TCA acids	2-Oxoglutaric acid	1.09	4E-01
Aniline	3-Aminobenzamide	2.04	1E-03
Hydroxy fatty acids	3-Hydroxy-3-methylglutaric acid	0.37	1E-01
Hydroxy acids	3-Hydroxybutyric acid	0.03	8E-01
Carnitines	3-hydroxypalmitoleoylcarnitine	-0.38	2E-01
Amines	3-Methylhistamine	1.86	5E-04
Benzene	4-Aminobenzoic acid	-0.79	2E-02
Amino acids	4-Guanidinobutyric acid	5.04	7E-02
Amino acids	4-Oxoproline	-0.81	2E-01
Short-chain keto acids	5-guanidino-2-oxopentanoic acid	-2.64	4E-02
Purine ribonucleosides	5'-S-Methy5'-thioadenosine	0.75	1E-01
lineolic acids	9-HpODE	1.60	8E-02
Benzene	Acetanilide	0.29	1E-01
Acetohydroxamic acids	Acetohydroxamic acid	-1.23	2E-03

Carnitines	Acetylcarnitine	-0.25	2E-01
Acyl cholines	Acetylcholine	2.00	1E-03
Purines	Adenine	-0.26	5E-01
Purine ribonucleosides	Adenosine	0.31	2E-02
Purine ribonucleoside monophosphates	Adenosine 5'-monophosphate	0.58	1E-01
Unsaturated Fatty Acids	Adrenic acid	0.22	2E-01
Amino acids	Alanine	-0.23	1E-01
Dipeptides	Alanyproline	1.35	8E-02
Glycerophosphocholines	alpha-lysophosphatidylcholine	-1.02	3E-03
Unsaturated Fatty Acids	Arachidonic acid	0.86	7E-04
Peptides	arg-ala	-0.19	2E-01
Amino acids	Arginine	0.35	3E-01
Vitamin	Ascorbic acid	0.49	5E-03
Dipeptides	asp-gln	1.65	8E-03
Amino acids	Asparagine	0.44	3E-03
Amino acids	Aspartic acid	0.35	6E-02
Carnitines	C12-Carnitine	0.04	3E-01
Carnitines	C14-Carnitine	0.56	5E-05
Carnitines	C18-Carnitine	-0.43	7E-03
Amino acids	Carbocysteine	1.65	3E-02
Amino acids	carboxynorspermidine	-0.32	4E-02
Carnitines	Carnitine	-0.50	4E-03
Peptides	Carnosine	0.82	5E-02
Pyrimidine ribonucleoside diphosphates	CDP-ethanolamine	2.20	6E-04
Ceramide	Ceramide (d18:1/18:0)	1.03	8E-04
Amino acids	Choline	-0.13	8E-01
TCA acids	Citric acid	0.52	2E-02
Amino acids	Citrulline	-0.98	4E-03
Amino acids	Creatine	-0.09	2E-01
Amino acids	Creatinine	0.20	5E-02
Dipeptides	CYS-ASP	-2.94	2E-01
Ribonucleoside diphosphates	Cytidine 5'-diphosphocholine	0.52	4E-04
Pyrimidones	Cytosine	0.73	6E-03
Amines	Deanol	0.56	7E-02
gamma butyrolactones	Dehydroascorbic acid	0.24	2E-02
1,2-aminoalcohols	Diethanolamine	-0.29	2E-01
Dialkylamines	Diethylamine	0.29	2E-01
Pyrimidones	Dihydrothymine	0.85	1E-01
Unsaturated Fatty Acids	Docosahexaenoic acid	-0.22	2E-01
Carboxylic acids	Ergothioneine	-0.55	4E-03
1,2-aminoalcohols	Ethanolamine	0.08	1E-01
Fatty acid esters	Ethyl myristate	0.29	2E-02
TCA acids	Fumaric acid	0.70	3E-01
Nitrofurans	Furazolidone	-0.27	8E-01
Monosaccharide phosphates	Glucosamine 6-phosphate	-0.51	5E-02
Carboxylic acids	Glutamic acid	0.29	2E-04
Amino acids	Glutamine	0.06	3E-01
Dicarboxylic acids	Glutaric acid	-0.15	2E-01
Carboxylic acids	Glutathione (reduced)	-0.25	5E-01
Amino acids	Glutaurine	0.84	3E-03
Peptide	Gly-Leu	-0.70	4E-03
Dipeptides	Gly-pro	0.53	4E-01
Dipeptides	Glycyleucine	-0.22	2E-01

Dipeptides	Glycylglutamine	-0.04	6E-01
purine nucleosides	Guanine	-3.21	2E-02
Carnitines	Hexanoylcarnitine	0.94	3E-01
Peptide	Homoanserine	-1.28	1E-04
Carnitines	Hydroxyhexanoylcarnitine	1.72	2E-03
Xanthines	Hypoxanthine	-0.23	2E-01
Purine nucleosides	Inosine	-0.27	2E-01
Monoalkylamines	Isoamylamine	1.14	5E-01
Pyrimidines	Isocytosine	0.88	3E-01
Amino acids	Kynurenine	0.58	5E-02
Carboxylic adicids	Lactic acid	-0.19	5E-01
Dipeptides	Leu-ala	-0.52	3E-02
Dipeptides	Leu-Val	-0.12	8E-01
Dipeptides	Leucylproline	0.33	6E-02
Unsaturated Fatty Acids	Linoelaidic acid	0.32	2E-02
Amino acids	Lysine	0.04	8E-01
LPC	LysoPC(22:1(13Z))	-2.00	5E-03
LPC	LysoPC(24:1(15Z))	-1.69	1E-03
Unsaturated Fatty Acids	Maleamic acid	0.10	4E-01
Carbohydrates	Mannitol	-0.20	5E-02
Long-chain fatty acids	Margaric acid	0.34	5E-02
Amino acids	methionine	-0.10	1E+00
Amino acids	Methionine sulfoxide	0.39	3E-01
Fatty acid methyl esters	Methyl stearate	0.14	9E-02
Imidazolyl carboxylic acids	Methylimidazoleacetic acid	0.49	5E-02
Carbohydrates	muramic acid	0.33	1E-01
Saturated Fatty Acids	Myristic acid	0.24	3E-01
Dipeptides	N-Acetyl-aspartylglutamic acid	-0.77	5E-02
Amino acids	N-acetyl-2-amino adipic acid	-1.26	8E-05
Amino acids	N-Acetylglutamic acid	-0.39	3E-01
n-acyl-alpha-amino acids	N-Acetylalanine	0.10	3E-01
Amino acids	N-Acetylaspartic acid	0.06	7E-01
Amino acids	N-Acetyl leucine	-0.96	1E-01
n-acylneuraminic acids	N-Acetylneuraminic acid	1.08	4E-03
n-acyl-alpha-amino acids	N-Acetylornithine	0.09	1E+00
Amino acids	N-Acetylvaline	-0.64	7E-03
Amino acids	N-Ethylglycine	0.34	9E-04
Amino acids	N-Formylmethionine	-0.26	7E-01
Acylamide	N-Oleoyl Taurine	-2.20	3E-02
Acylamide	N-Oleoyl Serine	0.26	5E-02
Amino acids	N-Tigloylglycine	0.90	6E-02
Amino acids	N6,N6,N6-Trimethyllysine	0.49	5E-02
Amino acids	nicotianamine	0.44	8E-02
Pyridines	Nicotinamide	-0.68	4E-02
Unsaturated Fatty Acids	Oleic acid	0.33	1E-02
Glycosylamines	Orotidine	0.58	5E-02
TCA acids	Oxalosuccinic acid	1.09	2E-02
Fatty acids	PAF C-18:1	-2.32	6E-05
Phosphosphingolipids	Palmitoyl sphingomyelin	0.06	3E-01
Carnitines	Palmitoylcarnitine	-0.08	5E-01
Alcohols	Pantothenic acid	-0.48	3E-02
Saturated Fatty Acids	Pentadecanoic Acid	0.55	3E-01
Amino acids	Phenylalanine	0.22	1E-01
Peptide	Pro-Leu	0.12	6E-01
Amino acids	Proline	0.14	2E-01

Carnitines	Propionylcarnitine	-0.05	9E-01
Pyridine carboxaldehydes	Pyridoxal	0.59	7E-01
Glycosylamines	S-Adenosylhomocysteine	0.67	9E-04
Amino acids	Saccharopine	-1.40	6E-03
Amino acids	Serine	0.73	3E-05
Tryptamines	Serotonin	0.44	2E-02
Amines	Sphingosine (d18:1)	0.16	8E-01
Saturated Fatty Acids	Stearic acid	0.39	2E-02
Carbohydrates	Streptozotocin	-0.46	3E-02
Carboxylic acids	Succinate	0.24	6E-01
TCA acids	Succinic acid	-0.33	5E-01
Sulfonic acids	Taurine	0.15	4E-01
Pyrimidines	Thiamine	1.50	1E-02
Dipeptides	Thr-Gln	-0.08	2E-01
Amino acids	Threonine	0.57	8E-02
Tertiary amines	Triethanolamine	0.80	9E-01
Tertiary amines	Trimethylamine	0.80	1E-01
Amino acids	Tryptophan	0.46	4E-02
Amino acids	Tyrosine	0.02	3E-01
Pyrimidine ribonucleoside diphosphates	UDP-N-acetylglucosamine	1.71	5E-04
Pyrimidones	Uracil	0.60	1E-04
Ureas	Urea	0.25	2E-01
Pyrimidine nucleosides	Uridine	-0.25	5E-02
Amino acids	Valine	0.21	1E-01
Xanthines	Xanthine	0.45	6E-03
Amino acids	β -Alanine	0.01	9E-01

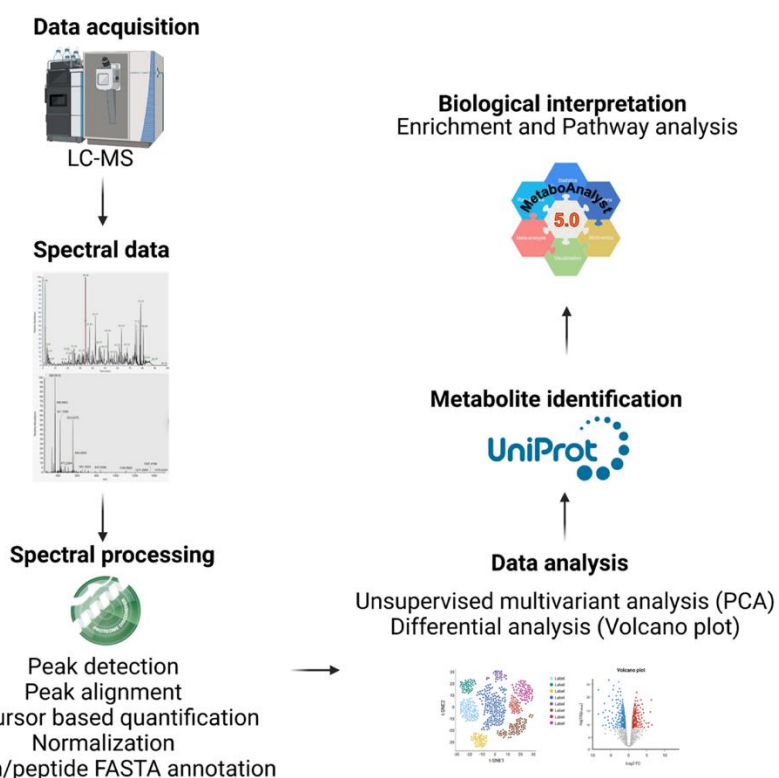


Figure S2. 4 Workflow used in this study to perform pathway analysis from proteomics analyses.

Table S2. 8 List of genes encoding proteins/enzymes involved in certain metabolic pathways. Name, pathways, role and location for each gene have been reported, which were acquired from UniProt.

NAME	PATHWAY	ROLE	LOCATION
Abi2	Adhesion and communication	Regulator of actin cytoskeleton dynamics underlying cell motility and adhesion. Functions as a component of the WAVE complex, which activates actin nucleating machinery Arp2/3 to drive lamellipodia formation	-
Acaa2	Fatty acid β -oxidation	Catalyzes the last step of the mitochondrial beta-oxidation pathway, an aerobic process breaking down fatty acids into acetyl-CoA.	Mitochondrial
Acadl	Fatty acid β -oxidation	Long-chain specific acyl-CoA dehydrogenase is one of the acyl-CoA dehydrogenases that catalyze the first step of mitochondrial fatty acid beta-oxidation, an aerobic process breaking down fatty acids into acetyl-CoA and allowing the production of energy from fats	Mitochondrial
Acadm	Fatty acid β -oxidation	Catalyze the first step of mitochondrial fatty acid beta-oxidation,	Mitochondrial
Acat1	Fatty acid β -oxidation	Catalyzes the last step of the mitochondrial beta-oxidation pathway, an aerobic process breaking down fatty acids into acetyl-CoA	Mitochondrial
Aco2	TCA cycle	Catalyzes the isomerization of citrate to isocitrate via cis-aconitate	Mitochondrial
Acot7	Fatty acid β -oxidation	Catalyzes the hydrolysis of acyl-CoAs into free fatty acids and coenzyme A (CoASH), regulating their respective intracellular levels	Mitochondrial
Acsf2	Fatty acid β -oxidation	Catalyze the initial reaction in fatty acid metabolism, by forming a thioester with CoA. Has some preference toward medium-chain substrates. Plays a role in adipocyte differentiation	Mitochondrial
Actn1	Adhesion and communication	F-actin cross-linking protein which is thought to anchor actin to a variety of intracellular structures. This is a bundling protein	-

Akap5	Cell biogenesis, transport and transduction	Multivalent scaffold protein that anchors the cAMP-dependent protein kinase/PKA to cytoskeletal and/or organelle-associated proteins, targeting the signal carried by cAMP to specific intracellular effectors.	Synapse
Aldh6a1	BCAAs	Plays a role in valine and pyrimidine metabolism. Binds fatty acyl-CoA	Mitochondrial
Aldoc	Gluconeogenesis	Catalyzes the conversion of beta-D-fructose 1,6-bisphosphate into glyceraldehyde 3-phosphate	cytoplasmic
Asrgl1	Phenylalanine metabolism	Involved in the production of L-aspartate, which can act as an excitatory neurotransmitter in some brain regions	cytosolic
Auh	BCAAs	Catalyzes the fifth step in the leucine degradation pathway, the reversible hydration of 3-methylglutaconyl-CoA (3-MG-CoA) to 3-hydroxy-3-methylglutaryl-CoA (HMG-CoA)	Mitochondrial
Basp1	Developmental processes	Nucleic acid binding activity	Membrane
Bcat1	BCAAs	Catalyzes the first reaction in the catabolism of the essential branched chain amino acids leucine, isoleucine, and valine	cytosolic
Ca8	One-carbon metabolism	Does not have a carbonic anhydrase catalytic activity	cytosolic
Cadm2	Adhesion and communication	Adhesion molecule that engages in homo- and heterophilic interactions with the other nectin-like family members, leading to cell aggregation	-
Calb1	Developmental processes	Buffers cytosolic calcium. May stimulate a membrane Ca ²⁺ -ATPase and a 3',5'-cyclic nucleotide phosphodiesterase.	cytoplasmic and synapse
Calb2	Other	Calretinin is a calcium-binding protein which is abundant in auditory neurons	cytosolic
Camk2a	Cell cycle and proliferation	Calcium/calmodulin-dependent protein kinase that functions autonomously after Ca ²⁺ /calmodulin-binding and autophosphorylation, and is involved in various processes, such as synaptic	cytoplasmic

		plasticity, neurotransmitter release and long-term potentiation	
Camkv	Protein metabolism	Does not appear to have detectable kinase activity.	Cell membrane
Cask	Dopamine metabolism	Multidomain scaffolding Mg ²⁺ -independent protein kinase that catalyzes the phosphotransfer from ATP to proteins such as NRXN1, and plays a role in synaptic transmembrane protein anchoring and ion channel trafficking	-
Cdc37	Adhesion and communication	Co-chaperone that binds to numerous kinases and promotes their interaction with the Hsp90 complex, resulting in stabilization and promotion of their activity.	-
Celf2	RNA metabolism and transcription	RNA-binding protein implicated in the regulation of several post-transcriptional events	Nucleus and cytoplasm
Cltb	Adhesion and communication	Clathrin is the major protein of the polyhedral coat of coated pits and vesicles.	-
Coro1a	Cell adhesion and transport	May be a crucial component of the cytoskeleton of highly motile cells, functioning both in the invagination of large pieces of plasma membrane, as well as in forming protrusions of the plasma membrane involved in cell locomotion	Cytoplasm and cytoskeleton
Crkl	IL-2 signaling	Mediates the transduction of intracellular signals.	cytosolic
Crym	Transport and other biological processes	Specifically catalyzes the reduction of imine bonds in brain substrates that may include cystathionine ketimine (CysK) and lanthionine ketimine (LK). Binds thyroid hormone which is a strong reversible inhibitor.	cytosolic
Cryz12	Redox metabolism	Oxidoreductase activity, acting on CH-OH group of donors, NAD or NADP as acceptors	Lysosome
Cs	TCA cycle	Conversion of acetyl-CoA into Citrate with release of CoA	Mitochondrial
Dbn1	Cell signalling and cell communication	Required for actin polymerization at immunological synapses (IS) and for the recruitment of the	cytosolic

		chemokine receptor CXCR4 to IS	
Dclk1	Cell biogenesis and protein metabolism	Involved in a calcium-signaling pathway controlling neuronal migration in the developing brain	Axon, Synapse
Dlat	TCA cycle	Catalyzes the conversion of pyruvate to acetyl-CoA and CO ₂	Mitochondrial
Dlst	TCA cycle	Catalyzes the overall conversion of 2-oxoglutarate to succinyl-CoA and CO ₂	Mitochondrial
Echs1	Fatty acid β -oxidation	Converts unsaturated trans-2-enoyl-CoA species ((2E)-enoyl-CoA) to the corresponding (3S)-3-hydroxyacyl-CoA species through addition of a water molecule to the double bond	Mitochondrial
Eci1	Other	Able to isomerize both 3-cis and 3-trans double bonds into the 2-trans form in a range of enoyl-CoA species	Mitochondrial
Fh	TCA cycle	Catalyzes the reversible stereospecific interconversion of fumarate to L-malate	Mitochondrial
Gda	Other	Catalyzes the hydrolytic deamination of guanine, producing xanthine and ammonia	cytoplasmic
Glo1	Pyruvate metabolism	Catalyzes the conversion of hemimercaptal, formed from methylglyoxal and glutathione, to S-lactoylglutathione. Involved in the regulation of TNF-induced transcriptional activity of NF-kappa-B	cytosolic
Gnpda2	Glycolysis	Catalyzes the reversible conversion of alpha-D-glucosamine 6-phosphate (GlcN-6P) into beta-D-fructose 6-phosphate (Fru-6P) and ammonium ion, a regulatory reaction step in de novo uridine diphosphate-N-acetyl-alpha-D-glucosamine (UDP-GlcNAc) biosynthesis via hexosamine pathway.	cytosolic
Gria2	Cell signalling and cell communication	Receptor for glutamate that functions as ligand-gated ion channel in the central nervous system and plays an important role in excitatory synaptic transmission	Cell membrane
Hadha	Fatty acid β -oxidation	Acylates monolysocardiolipin into cardiolipin, a major mitochondrial membrane	Mitochondrial

		phospholipid which plays a key role in apoptosis and supports mitochondrial respiratory chain complexes in the generation of ATP.	
Hadhb	Fatty acid β -oxidation	Catalyzes the last three of the four reactions of the mitochondrial beta-oxidation pathway.	Mitochondrial
Hagh	Pyruvate metabolism	Catalyzes the hydrolysis of S-D-lactoyl-glutathione to form glutathione and D-lactic acid	Mitochondrial
Hapln2	Adhesion and communication	Mediates a firm binding of versican V2 to hyaluronic acid. May play a pivotal role in the formation of the hyaluronan-associated matrix in the central nervous system (CNS) which facilitates neuronal conduction and general structural stabilization	Extracellular
Hibch	BCAAs	isobutyryl-CoA dehydrogenase that functions in valine catabolism	Mitochondrial
Ldhb	Pyruvate metabolism	Interconverts simultaneously and stereospecifically pyruvate and lactate with concomitant interconversion of NADH and NAD ⁺	cytosolic
Mapk1	IL-9, IL-3 signaling	Depending on the cellular context, the MAPK/ERK cascade mediates diverse biological functions such as cell growth, adhesion, survival and differentiation through the regulation of transcription, translation, cytoskeletal rearrangements	cytosolic
Mdh1	Gluconeogenesis	Catalyzes the reduction of aromatic alpha-keto acids in the presence of NADH	cytoplasmic
Mdh2	TCA cycle	Catalyzes the conversion of malate into oxaloacetate with release of NADH	Mitochondrial
Nefh	Cell biogenesis and stress response	Important function in mature axons. May additionally cooperate with the neuronal intermediate filament proteins to form neuronal filamentous networks	cytoplasmic
Pde2a	Signal transduction and cellular development	cGMP-activated cyclic nucleotide phosphodiesterase with a dual-specificity for the second messengers cAMP and cGMP, which are key	Cell membrane and cytoplasm

		regulators of many important physiological processes	
Pfkm	Glycolysis	Catalyzes the phosphorylation of D-fructose 6-phosphate to fructose 1,6-bisphosphate by ATP, the first committing step of glycolysis	cytoplasmic
Phf24	Cell signalling	Showing features for region, zinc finger	Other
Pkm	Glycolysis	Catalyzes the final rate-limiting step of glycolysis by mediating the transfer of a phosphoryl group from phosphoenolpyruvate (PEP) to ADP, generating ATP	cytosolic
Ppp3ca	Other	Acts as cofactor for myogenic bHLH transcription factors such as MYOD1	Cytoplasm and cytoskeleton
PrKca	IL-9, IL-3 signaling	Calcium-activated, phospholipid- and diacylglycerol (DAG)-dependent serine/threonine-protein kinase that is involved in positive and negative regulation of cell proliferation, apoptosis, differentiation, migration and adhesion, cardiac hypertrophy, angiogenesis, platelet function and inflammation	-
Pvalb	Cell signalling	In muscle, parvalbumin is thought to be involved in relaxation after contraction. It binds two calcium ions.	cytosolic
Qdpr	Phenylalanine metabolism	Catalyzes the conversion of quinonoid dihydrobiopterin into tetrahydrobiopterin	cytosolic
Rab3b	Biogenesis and protein metabolism	Protein transport. Probably involved in vesicular traffic	Cell membrane and Golgi
Rpl13a	Protein metabolism	Associated with ribosomes but is not required for canonical ribosome function and has extra-ribosomal functions	cytoplasmic
S100b	Other	Weakly binds calcium but binds zinc very tightly-distinct binding sites with different affinities exist for both ions on each monomer	cytosolic and nucleus
Sdha	TCA cycle	Responsible for transferring electrons from succinate to ubiquinone (coenzyme Q)	Mitochondrial
Slc30a3	Stress response and transport	Proton-coupled zinc ion antiporter mediating the import of zinc from cytoplasm into synaptic vesicles and	Cytoplasm, synapse

		participating to cellular zinc ion homeostasis in the brain	
Sncg	Cell signalling and cell communication	Plays a role in neurofilament network integrity	cytoplasmic
Srr	Other	Catalyzes the synthesis of D-serine from L-serine	cytoplasmic
Stx1a	Dopamine metabolism	Plays an essential role in hormone and neurotransmitter calcium-dependent exocytosis and endocytosis	-
Sucla2	TCA cycle	Couples the hydrolysis of succinyl-CoA to the synthesis of ATP and thus represents the only step of substrate-level phosphorylation in the TCA	Mitochondrial
Syt1	Dopamine metabolism	Calcium sensor that participates in triggering neurotransmitter release at the synapse	-
Wasf1	Adhesion and communication	Downstream effector molecule involved in the transmission of signals from tyrosine kinase receptors and small GTPases to the actin cytoskeleton. Promotes formation of actin filaments	-

Table S2. 9 Metabolic pathways enriched in the brain tissues of aged mice after integrative analysis with metabolomics and proteomics data. FDR = False discovery rate.

	Total	Hits	FDR	Impact
Pyruvate metabolism	45	13	0.00	0.63
Valine, leucine and isoleucine degradation	88	18	0.00	0.41
Citrate cycle (TCA cycle)	42	12	0.00	2.18
Propanoate metabolism	48	12	0.00	0.44
Glyoxylate and dicarboxylate metabolism	56	12	0.00	0.08
beta-Alanine metabolism	44	9	0.01	0.15
Butanoate metabolism	29	7	0.01	0.30
Lysine degradation	49	9	0.01	0.14
Cysteine and methionine metabolism	71	11	0.01	0.59

Alanine, aspartate and glutamate metabolism	61	10	0.01	0.15
Glycolysis or Gluconeogenesis	61	10	0.01	0.73
Fatty acid degradation	102	13	0.02	1.96

Table S2. 10 List of lipids identified from MALDI-MSI analysis. For each *m/z* value peak intensity is reported in Young-wild type (Young-WT), Old-WT, and Young-knocked out (Young-KO) samples.

NAME	<i>m/z</i>	Ion	Young-WT	Old-WT	Young-KO
CerPE36:2;O6	749.5066	[M-H]-	11187	7543	
CerPE36:3;O6	747.4948	[M-H]-	139627	65555	104551
CerPE38:2;O4	745.5485	[M-H]-	62633	29195	37379
CerPE40:5;O4	767.5344	[M-H]-	54173	31832	37456
DGCC32:4	718.532	[M-H]-	94280	25170	45030
DGCC34:5	744.5476	[M-H]-	180137	79410	100573
DGCC36:10	762.4992	[M-H]-	53194	22021	39284
DGCC38:8	794.5598	[M-H]-	29996	19556	19040
DGCC38:9	792.5391	[M-H]-	20664	11098	17165
DGDG 30:0	863.577	[M-H]-	5124		
DGDG30:0	863.577	[M-H]-			5124
DGTA 34:5	728.5466	[M-H]-	32055		
DGTA 34:6	726.5378	[M-H]-	35453		
DGTA 38:9	776.5441	[M-H]-	25864		
DGTA34:5	728.5466	[M-H]-			32055
DGTA34:6	726.5378	[M-H]-			35453
DGTA36:8	750.5318	[M-H]-	35997	26970	28591
DGTA38:10	774.5362	[M-H]-	143131	77571	127406
DGTA38:9	776.5441	[M-H]-			25864
FA16:0	255.2311	[M-H]-	406278	157167	271516
FA16:3;O4	313.143	[M-H]-	301333	229492	327901
FA16:4;O3	295.1076	[M-H]-		25262	
FA16:4;O4	311.1256	[M-H]-	96404	67021	95585
FA18:0	283.2613	[M-H]-	527615	313714	436081
FA18:1	281.2468	[M-H]-	447602	218221	320325
FA20:4	303.2316	[M-H]-	310162	149052	217446
FA22:4	331.2625	[M-H]-	84582	50588	25652
FA22:6	327.231	[M-H]-	234821	87186	163779
Hex2Cer30:2;O4	834.522	[M-H]-	41581	24872	30834
Hex2Cer32:4;O4	858.5248	[M-H]-	15693	14998	11558

Hex2Cer32:5;O4	856.503	[M-H]-	38601	24168	44752
Hex2Cer34:5;O4	884.5382	[M-H]-	8674	5624	12048
HexCer 32:1;O4	702.5124	[M-H]-	23886		
HexCer32:1;O4	702.5124	[M-H]-			23886
HexCer32:2;O4	700.5041	[M-H]-	44020	9735	30020
HexCer36:2;O5	772.5548	[M-H]-	13118	14587	8975
HexCer36:6;O4	748.5022	[M-H]-	57190	21020	22908
IPC40:5;O4	886.5501	[M-H]-	128009	134249	140514
LPA10:0	325.1161	[M-H]-		13846	
LPA18:0	437.266	[M-H]-	29922	19805	24796
LPAO-10:0;O	327.123	[M-H]-		27987	
LPAO-16:2	391.2231	[M-H]-	37288	15799	34180
LPAO-18:2	419.255	[M-H]-	104117	95526	
LPAO-18:3	417.2386	[M-H]-	32772	16567	128120
LPC28:2;O	674.4788	[M-H]-	45233	16558	24091
LPE18:0	480.3061	[M-H]-	41966	36113	47130
LPEO-18:1	464.3105	[M-H]-	31742	20058	36524
LPEO-18:2	462.2957	[M-H]-	24027	17671	17044
LPG14:2;O	467.1899	[M-H]-	26736	19316	32470
LPI 32:0	795.5327	[M-H]-	7742		
LPI32:0	795.5327	[M-H]-			7742
LPS12:2	436.1611	[M-H]-		9478	
NAE14:3;O3	312.1324	[M-H]-	161777	116300	160655
NAT10:0;O2	310.1083	[M-H]-	47819	22352	22123
NAT10:0;O3	326.1196	[M-H]-		7337	
NAT14:3	328.118	[M-H]-		24394	45700
PA 52:10	907.6221	[M-H]-	18447		
PA20:5	469.199	[M-H]-		24722	28036
PA34:1	673.4758	[M-H]-	137470	50147	64938
PA36:1	701.5071	[M-H]-	52816	39716	47571
PA36:2	699.4908	[M-H]-	73048	26172	43069
PA42:6	775.5382	[M-H]-	33572	17567	28308
PA42:6;O	791.534	[M-H]-	151038	62068	121370
PA50:10	879.5852	[M-H]-	8275	7985	7847
PA52:10	907.6221	[M-H]-			18447
PA52:11	905.6073	[M-H]-		17696	12824
PA52:11	905.6102	[M-H]-			25480
PAO-38:1	715.5675	[M-H]-	53006	17325	30890
PAO-52:11	891.6213	[M-H]-	38715	27869	43942
PE 40:6;O	806.5334	[M-H]-	11494		

PE 44:11	836.525	[M-H]-	14414		
PE 44:6;O	862.5937	[M-H]-	8241		
PE 44:7;O	860.571	[M-H]-	160		
PE34:1	716.5392	[M-H]-	15152	19020	11450
PE38:4	766.5317	[M-H]-	146001	89349	99033
PE40:6	790.5319	[M-H]-	307053	155271	165867
PE40:6;O	806.5334	[M-H]-			11494
PE44:11	836.525	[M-H]-			14414
PE44:6;O	862.5937	[M-H]-			8241
PE44:7;O	860.571	[M-H]-			160
PE46:6;O	890.6215	[M-H]-	112030	171825	128219
PE46:7;O	888.6135	[M-H]-	377239	452991	277102
PEO-38:7	746.5218	[M-H]-	21802	10543	34720
PEO-40:8;O	788.5273	[M-H]-	28283	18070	31654
PI 38:0	893.6081	[M-H]-	9877		
PI 40:6	909.553	[M-H]-	10037		
PI34:1	835.5239	[M-H]-	42697	25746	34416
PI36:4	857.5189	[M-H]-	76358	17450	29908
PI38:0	893.6081	[M-H]-			9877
PI38:3	887.5562	[M-H]-	66260	21156	38167
PI38:4	885.5428	[M-H]-	484494	281109	609455
PI38:5	883.5356	[M-H]-	38689	23434	52417
PI40:6	909.553	[M-H]-			10037
PS44:5	892.613	[M-H]-		17559	27886
SHexCer 36:1;O3	822.5295	[M-H]-	13115		
SHexCer 40:2;O3	876.5865	[M-H]-	11776		
SHexCer36:1;O3	822.5295	[M-H]-			13115
SHexCer40:1;O3	878.5922	[M-H]-	32496	38856	34127
SHexCer40:2;O3	876.5865	[M-H]-			11776
SHexCer42:1;O3	906.6198	[M-H]-		31266	41135
SHexCer42:1;O3	906.6222	[M-H]-			47783
SHexCer42:2;O3	904.6078	[M-H]-		43730	13591
SHexCer42:2;O3	904.6097	[M-H]-			54849
SPB18:0;O	284.2645	[M-H]-	84403	40620	54816
SPB18:1;O	282.2501	[M-H]-	83329	41596	47060
ST 24:2;O5;GlcA	581.3007	[M-H]-	16790		
ST18:0;O7;T	464.164	[M-H]-		8279	15937
ST18:5;O4	299.134	[M-H]-		34105	48685
ST18:5;O5	315.1512	[M-H]-	123018	79014	121613

ST20:0;O7;S	465.1702	[M-H]-	25493	11079	21461
ST20:1;O7;S	463.1571	[M-H]-		8968	
ST20:3;O5;T	454.1987	[M-H]-	44703	31345	48532
ST20:3;O6;T	470.1964	[M-H]-		15732	16582
ST20:4;O5;T	452.182	[M-H]-	28822	20889	33091
ST20:4;O6;T	468.1924	[M-H]-	22913	27377	31187
ST20:5;O5;T	450.1656	[M-H]-	20852	12613	23885
ST20:5;O6;T	466.1754	[M-H]-	28575	8572	23404
ST22:3;O4;S	439.186	[M-H]-		8354	11199
ST22:4;O4;S	437.1697	[M-H]-		16239	25478
ST22:4;O5;S	453.1905	[M-H]-	39570	29146	49771
ST22:5;O5;S	451.1727	[M-H]-	36307	11928	22200
ST24:1;O6;GlcA	599.313	[M-H]-	20260	12858	23282
ST24:2;O5;GlcA	581.3007	[M-H]-			16790
ST24:4;O7;GlcA	609.2524	[M-H]-		6716	7921
ST24:5;O8;GlcA	623.256	[M-H]-		4944	
ST26:7;O7	455.1997	[M-H]-	16440	11381	19990
ST28:5;O8;T	610.2606	[M-H]-		6616	11820
ST28:6;O8;T	608.2464	[M-H]-		7486	15263
ST28:7;O2	403.259	[M-H]-	31474	22392	32326
TG 46:10;O	773.5461	[M-H]-	12861		
TG46:10;O	773.5461	[M-H]-			12861
TG52:10;O3	889.6169	[M-H]-	166475	211158	117197

6.3. Appendix 3

Table S3. 2 Cell lines used in this study and their corresponding clinicopathologic profiles (ER: estrogen receptor, PR: progesterone receptor, and HER2: Human epidermal growth factor 2 receptor)

Cell Line	Histology	Subtype	Immunoprofile	Genetic alterations
MCF-7	Metastatic Adenocarcinoma	Luminal A	ER+, PR+, HER2-	PIK3CA, CDKN2A, GATA3, PIK3CA, TP53
MDA-MB-231	Metastatic Adenocarcinoma	Basal	ER-, PR-, HER2-	BRAF, CDKN2A, KRAS, NF2, TP53
HCC1937	Primary Ductalcarcinoma	Basal-like	ER-, PR-, HER2-	BRCA1, TP53

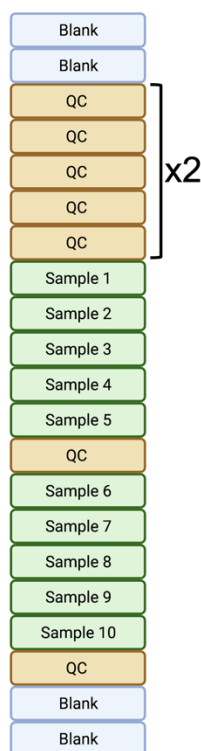


Figure S3. 2 Sample batch order. 2 blanks were injected at the beginning and at the end of the run. 10 QCs were injected before injections of the samples. Then QCs were injected after every 5 samples. QCs have been prepared by pooling together all the sample after drying and reconstitution with water:acetonitrile (50:50, v/v).

Elution Gradient used for LC-MS

Buffer A composition: 10 mM ammonium acetate in 95% acetonitrile, 5% water with 0.1% acetic acid

Buffer B composition: 10 mM ammonium acetate in 50% acetonitrile, 50% water with 0.1% acetic acid

Table S3. 3 Corresponding elution gradient used for the chromatographic separation of metabolite extracts

Retention (min)	Flow (ml/min)	%A	%B	Curve
0.000	0.500	99.0	1.0	5
1.000	0.500	99.0	1.0	5
3.000	0.500	85.0	15.0	5
6.000	0.500	50.0	50.0	5
9.000	0.500	5.0	95.0	5
10.000	0.500	5.0	95.0	5
10.500	0.500	99.0	1.0	5
14.000	0.500	99.0	1.0	5

Table S3. 4 Normality test for cell viability and immunofluorescence quantification data. The Shapiro-Wilk test has been performed with R software. *p*-values of >0.05 were considered as normally distributed. *P*-value (*p*).

Cell viability		Immunofluorescence		
Cell line	<i>p</i>	Cell line	<i>p</i> p53	<i>p</i> γH2AX
MCF7	0.5	MCF7	0.7	0.1
MDA-MB-231	0.3	MDA-MB-231	0.3	0.9
HCC1937	0.3	HCC1937	0.7	0.1

Table S3. 5 Setting for LC-MS data analysis and processing

Method settings	
Application mode	Small molecule
Method duration	14 min
Global parameter	
Ion source type	H-ESI
Spray voltage	Static
Positive Ion (V)	3900
Negative Ion (V)	2700
Gas Mode	Static
Sheath Gas (Arb)	40
Aux Gas (Arb)	10
Sweep Gas (Arb)	1
Ion Transfer Tube Temp (°C)	320
Vaporizer Temp (°C)	300
APPI Lamp	Not in use
MS Global Settings	
Infusion Mode	Liquid Chromatography
Expected LC Peak Width (s)	6
Advanced Peak Determination	False
Mild Trapping	True
Default Charge State	1
Internal Mass Calibration	EASY-IC™
Mode	Run Start
	Experiment

	<pre> graph TD A[Full Scan] --> B[Apex Detection] B --> C[Intensity] C --> D[ddMS²] D --- E[5 Scans] </pre>
Start time	0 min
End time	14 min
Full Scan	
Orbitrap resolution	60,000
Scan range (<i>m/z</i>)	70-1050
RF Lens (%)	50
AGC Target	Standard
Maximum Injection Time Mode	Custom
Microscans	1
Data Type	Profile
Polarity	+/-
Source Fragmentation	Disabled
Use EASY-CM™	On
Apex Detection	
Desired Apex Window (%)	50
Intensity	
Intensity threshold	5.0e4
Data Dependent Mode	Number of scans
Number of Dependent Scans	5
ddMS² Scan	
Multiplex Ions	False
Isolation Window (<i>m/z</i>)	2
Isolation Offset	Off
Collision Energy Type	Normalised
HCD Collision Energies (%)	15,30,45
Orbitrap Resolution	15,000
Scan Range Mode	Auto
AGC Target	Standard
Maximum Injection Time Mode	Auto
Microscans	1
Data Type	Profile
Use EASY-IC™	On
	Data processing

	<pre> graph TD A[Input files] --> B[Select spectra] B --> C[Align retention times] C --> D[Detect compounds] D --> E[Group compounds] E --> F[Fill gaps] F --> G[Apply QC corrections] G --> H[Mark background compounds] D --> I[Search Chem Spider] I --> J[Apply mzLogic] E --> K[Assign compound annotation] E --> L[Search mzCloud] F --> M[Predict composition] </pre>
Input Files	.raw data
Select Spectra	
Lower RT Limit	0
Upper RT Limit	0
First Scan	0
Last Scan	0
Lowest charge state	0
Highest charge state	0
Min. precursor mass	0 Da
Max precursor Mass	5000 Da
Total intensity threshold	0
Minimum peak count	1
Scan event filters	
Mass analyzer	Not specified
MS Order	Any
Activation type	Not specified
Min collision energy	0
Max collision energy	1000
Scan type	Any
Polarity mode is	+/-
Peak Filters	
S/N threshold (FT-only)	1.5
General settings	
Precursor selection	Use MS(n-1) precursor
Use isotope pattern in precursor reevaluation	True
Provide profile spectra	Automatic
Store chromatograms	False
Align retention times	
Alignment model	Adaptive curve
Alignment fallback	None
Maximum shift	0.3 min
Shift reference file	True
Mass tolerance	3 ppm
Remove outlier	True
Detect compounds	
Mass tolerance	3 ppm

Intensity tolerance (%)	30
S/N threshold	3
Min. peak intensity	500,000
Base ions	[M+H] ⁺ +1; [M-H] ⁻ -1
Peak detection	
Filter peaks	True
Max peak width	0.5 min
Remove singlets	True
Min #scans per peak	5
Min #isotopes	1
Isotope grouping	
Min spectral distance score	0
Remove potentially false positive isotopes	True
Group compounds	
Mass tolerance	5 ppm
RT tolerance	0.2 min
Preferred ions	[M+H] ⁺ +1; [M-H] ⁻ -1 + 2 nd analysis: [M+H] ⁺ +1; [M-H] ⁻ -1; [M+ACN+H] ⁺ +1; [M+FA-H] ⁻ -1; [M+ACN+Na] ⁺ +1; [M+H+Na] ⁺ +2; [M+H+NH ₄] ⁺ +2; [M+Na] ⁺ +1; [M+NH ₄] ⁺ +1
Fill gaps	
Mass tolerance	5 ppm
S/N threshold	1.5
Use real peak detection	True (re-detected low-intensity peaks)
Apply QC correction	
Regression model	Linear
Min QC coverage [%]	30
Max QC area RSD [%]	30
Max corrected QC area RSD [%]	25
Max #files between QC files	15
Max background compounds	
Max sample/blank	5
Max blank/sample	0
Hide background	True
Search ChemSpider	
Database(s)	CheBI, Human Metabolome Database
Search mode	By formula mass
Mass tolerance	5 ppm
Max # of results per compound	100
Max # of predicted composition per compound	3
Apply mzLogic	
FT Fragment mass tolerance	10 ppm
IT Fragment mass tolerance	0.4 Da
Max # compounds	0
Max # mzCloud similarity results to consider per compound	10
Match factor threshold	30 + 2 nd analysis at 70
Predict compositions	
Mass tolerance	5 ppm
Pattern matching	
Intensity tolerance (%)	30
Intensity threshold (%)	0.1
S/N threshold	3

Min spectral fit (%)	30
Min pattern Cov (%)	90
Use dynamic recalibration	True
Use fragments matching	True
Mass tolerance	5 ppm
S/N threshold	3
Assign compound annotations	
Mass tolerance	5 pmm
Data source 1	mzCloud search
Data source 2	Predicted compositions
Data source 3	massList search
Data source 4	ChemSpider search
Data source 5	Metabolika search
Search mzCloud	
Compound classes	All
Precursor mass tolerance	10 ppm
FT fragment mass tolerance	10 ppm
IT fragment mass tolerance	0.4 Da
Library	Autoprocessed; reference
Post processing	Recalibrated
Max # results	10
Annotate matching fragments	True
DDA Search	
Identity search	Cosine
Match activation type	True
Match activation energy	Match with tolerance
Activation energy tolerance	20
Apply intensity threshold	True
Similarity search	None
Match factor threshold	60
Differential analysis	
Log10 transform values	True

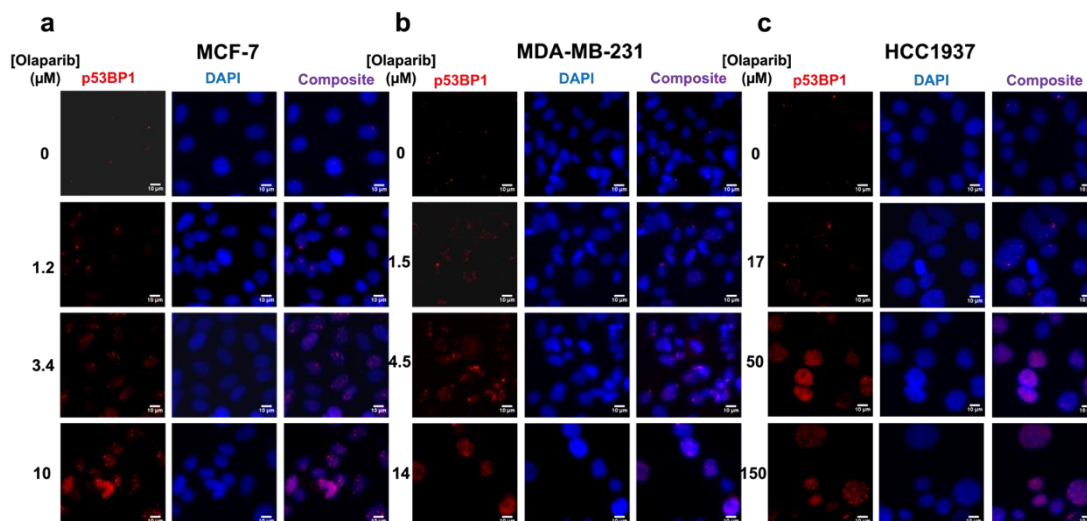


Figure S3. 3 The formation of p53BP1 foci in response to treatment with either growth medium or medium containing olaparib. Representative images of immunolabelled P53BP1 foci (red), DAPI (blue) nuclear counterstain and composite (p53BP1 (red) and DAPI (blue)) in MCF-7, MDA-MB-231, and HCC1937 cells treated with olaparib for seven days (a-c).

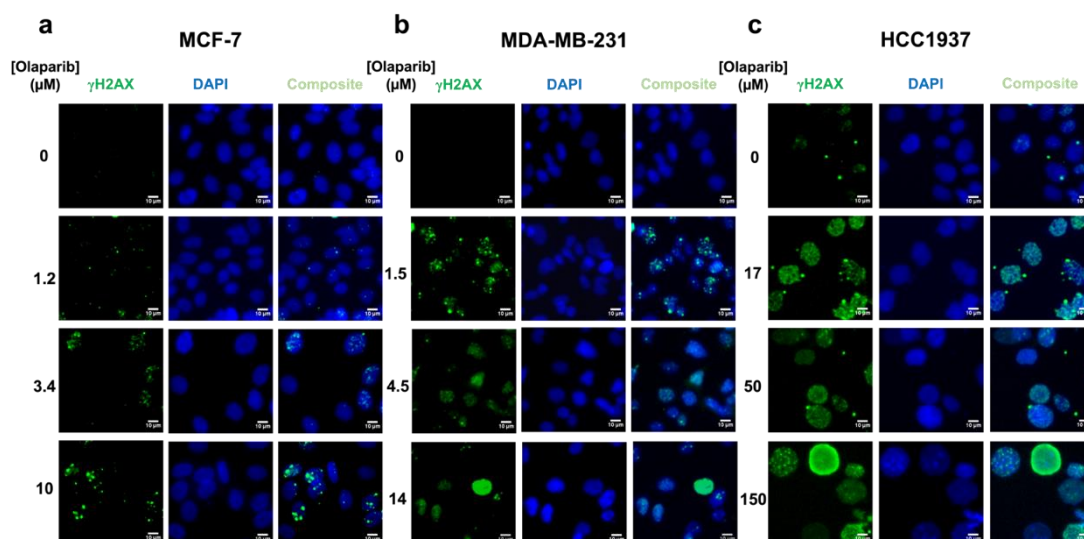


Figure S3. 4 The formation of γ H2AX foci formation in response to treatment with either growth medium or medium containing olaparib. Representative images of immunolabelled γ H2AX foci (green), DAPI (blue) nuclear counterstain and composite (γ H2AX and DAPI) in MCF-7, MDA-MB-231, and HCC1937 cells treated with for seven days (a-c).

Table S3. 6 ANOVA analysis of olaparib dose-dependent DNA DSB immunofoci formation

Cell line	Foci	p-value
MCF-7	53BP1	0.011
	γ H2AX	4.876×10^{-10}
MDA-MB-231	53BP1	0.0009
	γ H2AX	4.096×10^{-10}
HCC1937	53BP1	1.204×10^{-6}
	γ H2AX	1.441×10^{-5}

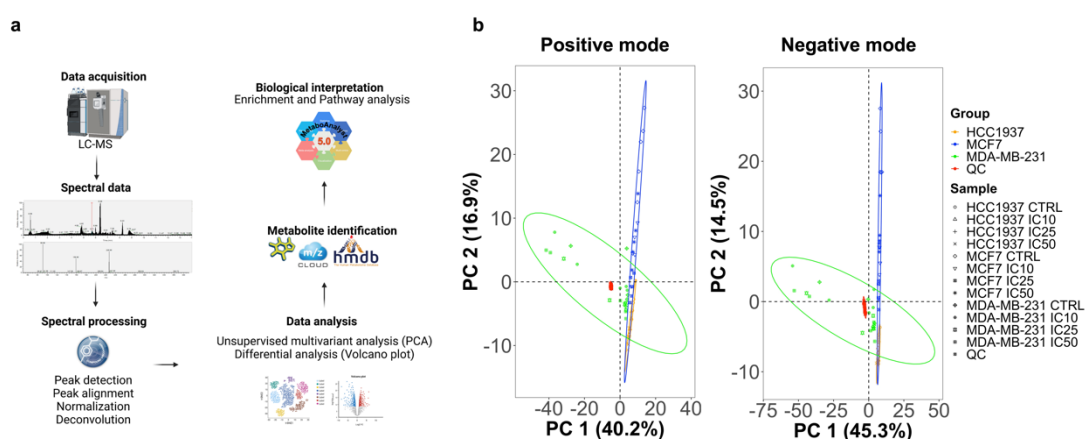


Figure S3. 5 Global metabolic features identified in MCF7, MDA-MB-231 and HCC1937 upon exposure to IC₁₀, IC₂₅ and IC₅₀ olaparib doses for seven days acquired in positive and negative ionization mode. a) Workflow used in this study to perform pathway analysis from metabolomics analyses. b) Global PCA score plots of the analysed breast cancer cell lines for data acquired in positive and negative

ionization mode. For each treatment group, five replicates were used. Data points in the two-dimensional PCA score plot were central scaled. Ellipses represent 95% confidence interval.

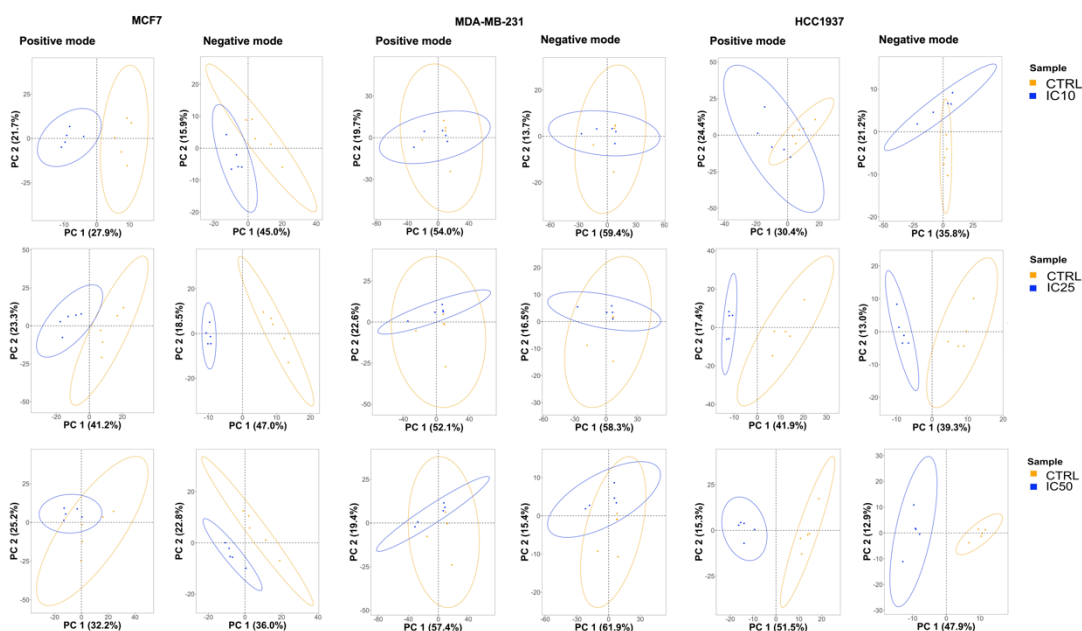


Figure S3. 6 PCA pairwise analysis of untargeted metabolomics data collected, in both positive and negative mode, from MCF7, MDA-MB-231, and HCC1937 cells treated with IC₁₀, IC₂₅ and IC₅₀ olaparib treatment doses. Data points in the two-dimensional PCA score plot were central scaled. The plot was designed on R through the ggplot2 graphical package (n=5). Ellipses represent 95% confidence interval.

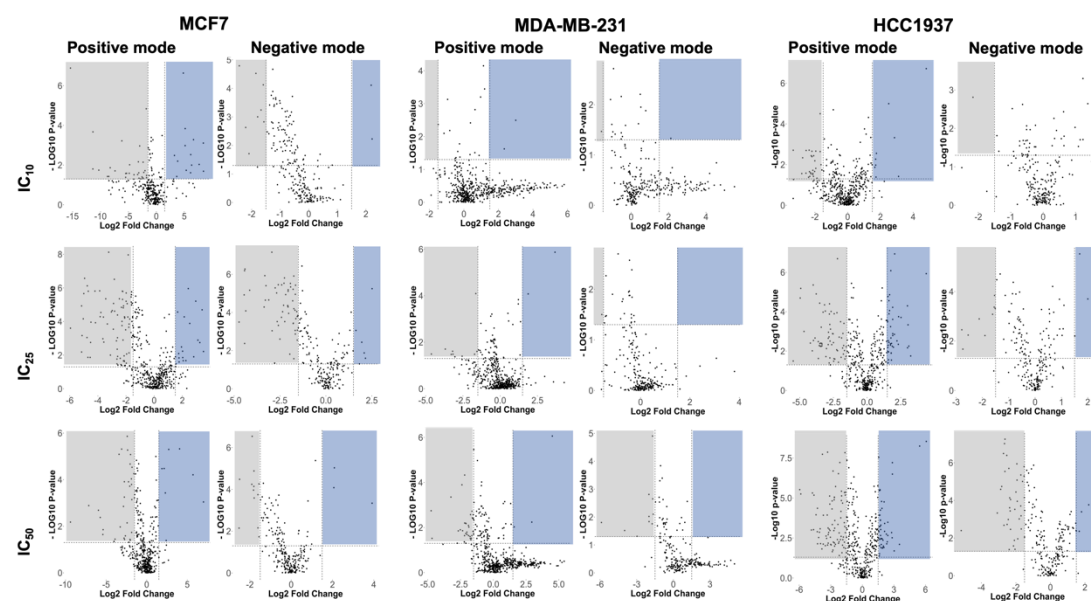


Figure S3. 7 Volcano plots showing the log₂ fold change and the -log₁₀ adjusted p-values in metabolite levels induced by treatment with different doses of Olaparib (IC₁₀, IC₂₅, and IC₅₀) in MCF7, MDA-MB-231 and HCC1937 cells. Data were selected at the cut off values adjusted p<0.05 and fold change >1.5. Blue and grey boxes indicate metabolites significantly enriched and depleted in the different samples, respectively.

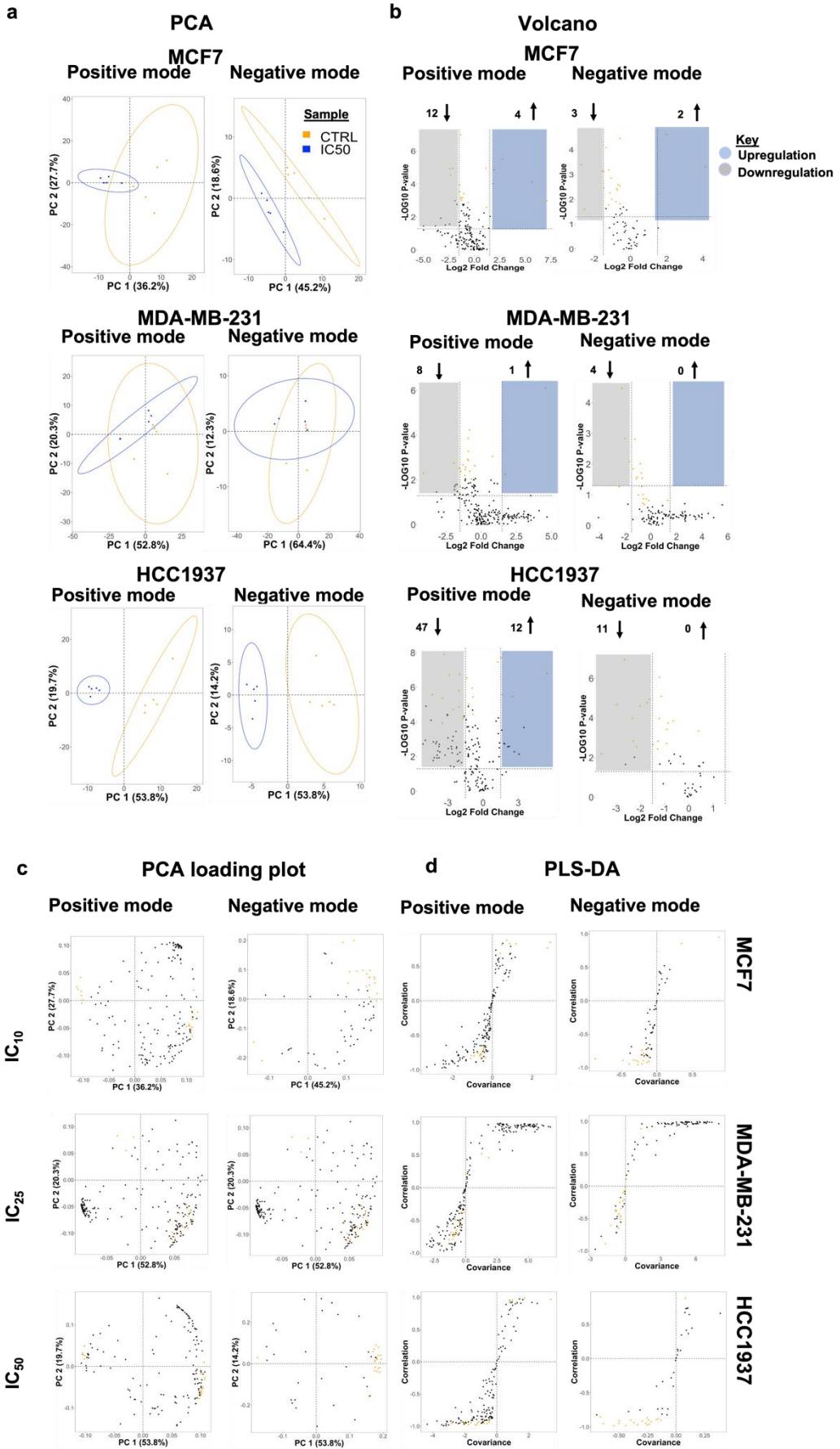


Figure S3. 8 Statistical analysis with new data processing method using 70% of annotation threshold and more ion adducts ([M+H]⁺+1; [M-H]⁻-1; [M+ACN+H]⁺+1; [M+FA-H]⁻-1; [M+ACN+Na]⁺+1; [M+H+Na]⁺+2; [M+H+NH₄]⁺+2; [M+Na]⁺+1; [M+NH₄]⁺+1). A) PCA pairwise analysis of untargeted metabolomics data collected, in both positive and negative mode, from MCF7, MDA-MB-231, and HCC1937 cells treated with IC₁₀, IC₂₅ and IC₅₀ olaparib treatment doses. Data points in the two-dimensional PCA score plot were central scaled. The plot was designed on R through the ggplot2 graphical package (n=5). Ellipses represent 95% confidence interval. B) Volcano plots showing the log₂ fold change and the -log₁₀ adjusted p-values in metabolite levels induced by treatment with different doses of Olaparib (IC₁₀, IC₂₅, and IC₅₀) in MCF7, MDA-MB-231 and HCC1937 cells. Data were selected at the cut off values adjusted p<0.05 and fold change >1.5. Blue and grey boxes indicate metabolites significantly enriched and depleted in the different samples, respectively. The first 20 features mostly contributing to the separation between young and old samples are indicated as orange data points and correspond to the PLS-DA components highlighted in the c) loading plot and d) PLS-DA analysis.

Table S3. 7 Global differential number of altered metabolites for samples treated with IC₁₀, IC₂₅ and IC₅₀ of Olaparib and their relative control (non-treated) samples. Metabolites identified in both positive and negative mode with p-value = <0.05 and Log₂ Fold Change = >1.5.

Sample	HESI +	HESI -
MCF7 IC10/Ctrl	41	10
MCF7 IC25/Ctrl	111	62
MCF7 IC50/Ctrl	41	15
MDA231 IC10/Ctrl	2	1
MDA231 IC25/Ctrl	12	1
MDA231 IC50/Ctrl	34	9
HCC1937 IC10/Ctrl	36	2
HCC1937 IC25/Ctrl	107	13
HCC1937 IC50/Ctrl	134	43

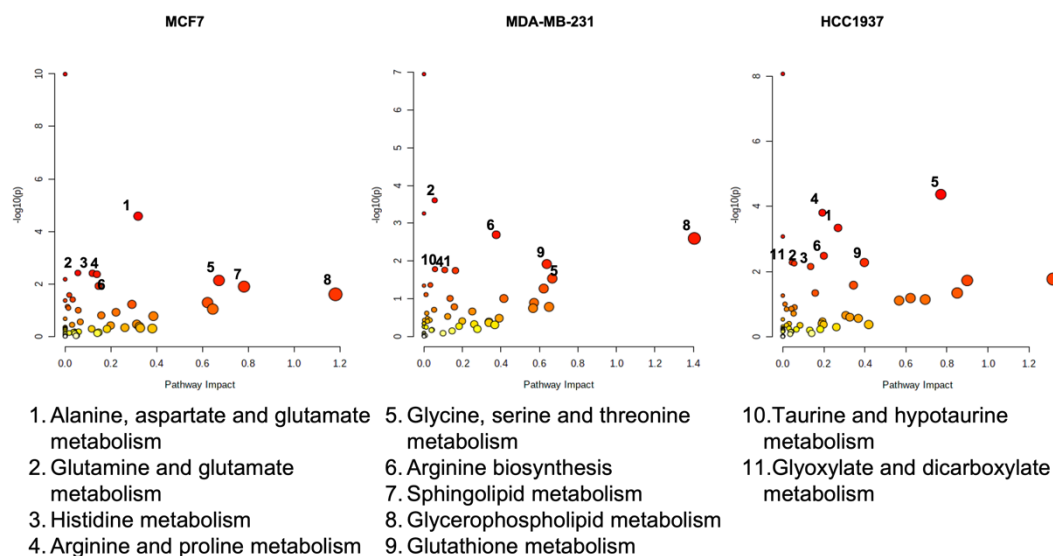


Figure S3. 9 Enrichment analysis of non-treated MCF7, MDA-MB-231 and HCC1937 cells.

Table S3. 8 Metabolic pathways in different breast cancer cells (MCF7, MDA-MB-231, and HCC1937) before and after treatment with IC₅₀ dose of Olaparib. FDR = False Discovery Rate.

	- Olaparib				+ Olaparib			
	Pathways	P-value	FDR	Impact	Pathways	P-value	FDR	Impact
MCF7	Aminoacyl-tRNA biosynthesis	1.02E-10	8.57E-09	0	Aminoacyl-tRNA biosynthesis	8.19E-10	6.88E-08	0
	Alanine, aspartate and glutamate metabolism	2.63E-05	0.001104	0.31879	Arginine biosynthesis	4.37E-06	0.000184	0.54769
	Glutamine and glutamate metabolism	3.83E-03	0.072247	0.055556	Alanine, aspartate and glutamate metabolism	1.31E-05	0.000366	0.25749
	Histidine metabolism	3.94E-03	0.072247	0.11935	Arginine and proline metabolism	0.000141	0.002965	0.20848
	Arginine and proline metabolism	4.30E-03	0.072247	0.13859	Glutamine and glutamate metabolism	0.000363	0.006102	0.055556
	Valine, leucine and isoleucine biosynthesis	0.006688	0.088594	0	Valine, leucine and isoleucine biosynthesis	0.000807	0.011293	0
	Glycine, serine and threonine metabolism	0.007382	0.088594	0.67221	Taurine and hypotaurine metabolism	0.002633	0.0316	0.085714
	Arginine biosynthesis	0.012025	0.11847	0.14615	Glycine, serine and threonine metabolism	0.003952	0.040556	0.67221
	Sphingolipid metabolism	0.012694	0.11847	0.78164	Butanoate metabolism	0.004345	0.040556	0.12169
	Glycerophospholipid metabolism	0.025021	0.20274	1.1815	Vitamin B6 metabolism	0.00747	0.062741	0.96579
	MDA-MB-231	Aminoacyl-tRNA biosynthesis	1.11E-07	9.31E-06	0	Aminoacyl-tRNA biosynthesis	4.87E-08	4.09E-06
Glutamine and glutamate metabolism		0.000246	0.010315	0.055556	Arginine biosynthesis	4.44E-05	0.001297	0.54769
Valine, leucine and isoleucine biosynthesis		0.000549	0.015362	0	Valine, leucine and isoleucine biosynthesis	4.63E-05	0.001297	0
Arginine biosynthesis		0.00201	0.042201	0.37538	Glutamine and glutamate metabolism	0.000348	0.007318	0.055556
Glycerophospholipid metabolism		0.002519	0.042319	1.4051	Arginine and proline metabolism	0.002382	0.040027	0.19139
Glutathione metabolism		0.012023	0.16708	0.63816	Glycine, serine and threonine metabolism	0.003697	0.05176	0.35674
Taurine and hypotaurine metabolism		0.016455	0.16708	0.057143	Alanine, aspartate and glutamate metabolism	0.007553	0.087816	0.25155
Arginine and proline metabolism		0.017286	0.16708	0.10783	Pantothenate and CoA biosynthesis	0.008364	0.087816	0.025568
Alanine, aspartate and glutamate metabolism		0.017902	0.16708	0.16342	Cysteine and methionine metabolism	0.016897	0.1577	0.74161
Glycine, serine and threonine metabolism		0.029087	0.24434	0.66667	Taurine and hypotaurine metabolism	0.020936	0.17277	0.057143
HCC1937		Aminoacyl-tRNA biosynthesis	8.36E-09	7.03E-07	0	Aminoacyl-tRNA biosynthesis	6.05E-09	5.08E-07
	Glycine, serine and threonine metabolism	4.24E-05	0.001781	0.77013	Arginine biosynthesis	4.03E-06	0.000169	0.54769
	Arginine and proline metabolism	0.000156	0.004357	0.19275	Alanine, aspartate and glutamate metabolism	7.18E-05	0.002011	0.25692
	Alanine, aspartate and glutamate metabolism	0.000455	0.009555	0.26907	Glutamine and glutamate metabolism	0.000348	0.007318	0.055556
	Valine, leucine and isoleucine biosynthesis	0.00084	0.014109	0	Arginine and proline metabolism	0.000585	0.009829	0.19275
	Arginine biosynthesis	0.003289	0.046045	0.2	Valine, leucine and isoleucine biosynthesis	0.000774	0.010591	0
	Glyoxylate and dicarboxylate metabolism	0.005277	0.052485	0.043771	Glycine, serine and threonine metabolism	0.000883	0.010591	0.37754
	Glutathione metabolism	0.005277	0.052485	0.39739	Taurine and hypotaurine metabolism	0.002532	0.02658	0.085714
	Glutamine and glutamate metabolism	0.005623	0.052485	0.055556	Cysteine and methionine metabolism	0.004844	0.045211	0.67619
	Histidine metabolism	0.007034	0.05908	0.13548	Butanoate metabolism	0.022626	0.19004	0.12169

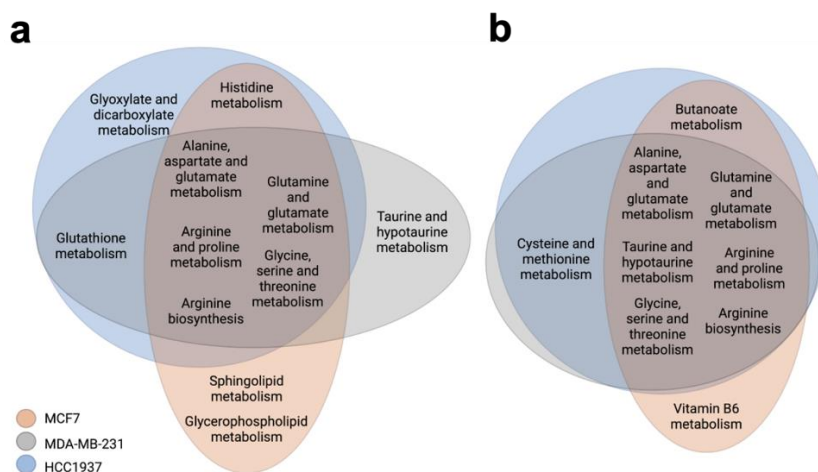


Figure S3. 10 Venn diagram representing the metabolic pathways in MCF7, MDA-MB-231 and HCC1937 cells .a) Baseline metabolic pathways and b) following a seven day treatment with olaparib at IC₅₀ doses.

Table S3. 9 Comparison analysis between MetaboAnalyst and Mummichog software. FDR = False discovery rate. Gamma = Gamma p-value. FET = Fisher's Exact test.

	MetaboAnalyst				Mummichog			
	Pathways	P-value	FDR	Impact	Pathways	Gamma	FET	Empirical
MCF7	Aminoacyl-tRNA biosynthesis	1.02E-10	8.57E-09	0	Biopterin metabolism	0.00589	0.073132	0.04
	Alanine, aspartate and glutamate metabolism	2.63E-05	0.001104	0.31879	Aspartate and asparagine metabolism	0.006205	0.22605	0.05
	Glutamine and glutamate metabolism	3.83E-03	0.072247	0.055556	Glycosphingolipid metabolism	0.007238	0.10342	0.02
	Histidine metabolism	3.94E-03	0.072247	0.11935	Arginine and Proline Metabolism	0.035136	0.50139	0.23
	Arginine and proline metabolism	4.30E-03	0.072247	0.13859	Hyaluronan Metabolism	1	0.18265	0.1
	Valine, leucine and isoleucine biosynthesis	0.006688	0.088594	0	N-Glycan biosynthesis	1	0.18265	0.1
	Glycine, serine and threonine metabolism	0.007382	0.088594	0.67221	Glycosphingolipid biosynthesis - ganglioseries	1	0.095694	0.08
	Arginine biosynthesis	0.012025	0.11847	0.14615	Sialic acid metabolism	1	0.18265	0.1
	Sphingolipid metabolism	0.012694	0.11847	0.78164	Linoleate metabolism	1	0.33331	0.15
	Glycerophospholipid metabolism	0.025021	0.20274	1.1815	Keratan sulfate degradation	1	0.18265	0.15
MDA-MB-231	Pathways	P-value	FDR	Impact	Pathways	Gamma	FET	Empirical
	Aminoacyl-tRNA biosynthesis	1.11E-07	9.31E-06	0	N-Glycan biosynthesis	0.041385	0.030525	0
	Glutamine and glutamate metabolism	0.000246	0.010315	0.055556	Glycosphingolipid metabolism	0.048443	0.10242	0.04
	Valine, leucine and isoleucine biosynthesis	0.000549	0.015362	0	Androgen and estrogen biosynthesis and metabolis	0.063099	0.31089	0.16
	Arginine biosynthesis	0.00201	0.042201	0.37538	Tryptophan metabolism	0.067861	0.39214	0
	Glycerophospholipid metabolism	0.002519	0.042319	1.4051	Aspartate and asparagine metabolism	0.071958	0.50513	0
	Glutathione metabolism	0.012023	0.16708	0.63816	Glycosphingolipid biosynthesis - ganglioseries	0.072898	0.17698	0.12
	Taurine and hypotaurine metabolism	0.016455	0.16708	0.057143	Keratan sulfate degradation	0.072898	0.17698	0
	Arginine and proline metabolism	0.017286	0.16708	0.10783	Glycosphingolipid biosynthesis - globoseries	0.072898	0.17698	0.12
	Alanine, aspartate and glutamate metabolism	0.017902	0.16708	0.16342	Glycosphingolipid biosynthesis - lactoseries	0.072898	0.17698	0.12
Glycine, serine and threonine metabolism	0.029087	0.24434	0.66667	Keratan sulfate biosynthesis	0.072898	0.17698	0.12	
HCC1937	Pathways	P-value	FDR	Impact	Pathways	Gamma	FET	Empirical
	Aminoacyl-tRNA biosynthesis	8.36E-09	7.03E-07	0	Beta-Alanine metabolism	0.01192	0.12328	0.04
	Glycine, serine and threonine metabolism	4.24E-05	0.001781	0.77013	Histidine metabolism	0.014179	0.16175	0.04
	Arginine and proline metabolism	0.000156	0.004357	0.19275	Tryptophan metabolism	0.016674	0.20218	0.08
	Alanine, aspartate and glutamate metabolism	0.000455	0.009555	0.26907	Aspartate and asparagine metabolism	0.047357	0.64926	0.32
	Valine, leucine and isoleucine biosynthesis	0.00084	0.014109	0	Tyrosine metabolism	0.072263	0.7102	0.1
	Arginine biosynthesis	0.003289	0.046045	0.2	Sialic acid metabolism	1	0.20095	0.06
	Glyoxylate and dicarboxylate metabolism	0.005277	0.052485	0.043771	Linoleate metabolism	1	0.28641	0.15
	Glutathione metabolism	0.005277	0.052485	0.39739	Keratan sulfate degradation	1	0.20095	0.07
	Glutamine and glutamate metabolism	0.005623	0.052485	0.055556	Biopterin metabolism	1	0.36314	0.13
Histidine metabolism	0.007034	0.05908	0.13548	Glycine, serine, alanine and threonine metabolism	1	0.87947	0.81	

Table S3. 10 Classification of the metabolites identified in MCF7, MDA-MB-231 and HCC1937 at all Olaparib doses (IC₁₀, IC₂₅ and IC₅₀) after seven days treatment. Class, name, Log₂ fold change, and the p-value (p) is represented for each compound. PC: phosphocholine; PE: phosphoethanolamine; PUFA: poly unsaturated fatty acid; SM: Sfingomyelin.

Class	Name	MCF7						MDA-MB-231						HCC1937					
		FC IC10	p	FC IC25	p	FC IC50	p	FC IC10	p	FC IC25	p	FC IC50	p	FC IC10	p	FC IC25	p	FC IC50	p
Amide	Nicotinamide	-0.5	0.1	-0.5	0.3	-0.1	0.3	-0.1	0.5	-0.2	0.1	-0.5	0	0.4	0.1	0.3	0	-0.1	0.3
Amine	N-Oleoylethanolamine	-1.5	0.1	-0.8	0.6	-0.1	0.6	-0.5	0.3	-3.2	0	-0.6	0.3	-1.6	0.2	-2.5	0	-1.2	0
Amine	Triethanolamine	1	0.6	-0.6	0	0.1	0.2	2.9	0.4	0.6	0.8	3.1	0.4	-0.5	0.5	0.4	0.1	0.4	0.5
Amino acid	3-Sulfinoalanine	-1.1	0.5	-1.8	0	-1.1	0.2	-	-	-0.7	0.3	-	-	0.3	0.7	-0.4	0.6	-0.7	0
Amino acid	4-Guanidinobutanoic acid	-1.3	0	-2	0	-1.1	0	-0.2	0.5	-0.3	0.6	-0.5	0.2	-1	0.1	-1.8	0	-1.8	0
Amino acid	4-Hydroxyproline	-1	0	-2.1	0	-1.1	0	-0.4	0.2	-	-	-0.4	0.1	-0.3	0.4	-0.3	0.3	-0.9	0
Amino acid	4-Oxoproline	-0.7	0.3	0.9	0	0.2	0.2	0.4	0.6	-0.3	0	0.8	0.1	0.6	0	1	0	1.5	0
Amino acid	Betaine	-	-	-0.8	0	0	0.7	0	0.3	-0.2	0.1	-0.4	0	-0.1	0.7	0	0.5	-0.4	0
Amino acid	Choline	-3.7	0.1	-2.1	0	-2.1	0.1	0.1	0.5	-1.3	0	-1.5	0	-2.1	0	-2.9	0	-3.7	0
Amino acid	Citrulline	-0.3	0.6	1.8	0	-0.4	0	-0.3	0.2	-0.3	0.1	-0.3	0	-0.1	0.5	0.3	0.5	0.1	0.9
Amino acid	Creatine	-0.3	0.6	-1.7	0	-0.5	0.1	-0.8	0	-0.4	0.2	-1.1	0	0.1	0.3	-0.4	0	-0.7	0
Amino acid	Creatinine	-	-	-0.1	0.2	0.1	0.7	-0.5	0	-0.4	0.1	-0.4	0.2	-0.1	0.4	0.3	0.4	-0.2	0.3
Amino acid	Gamma-Aminobutyric acid	-0.9	0	-1.8	0	-0.7	0	-0.2	0.1	-0.1	0.2	-0.2	0.1	-0.2	0.7	0	0.9	-0.5	0
Amino acid	Glycine	-1.3	0	-2.1	0	-1	0	-	-	-	-	-	-	-	-	-	-	-	-
Amino acid	Hypotaurine	0.3	0.3	-0.4	0.1	-0.6	0	0.3	0.6	-0.2	0.1	-0.5	0	-0.7	0	-0.6	0	-1.3	0
Amino acid	L-Alanine	-0.8	0	-1.7	0	-0.9	0	-	-	-	-	-	-	-	-	-	-	-	-
Amino acid	L-Arginine	6.7	0	-0.5	0	-0.1	0.6	-0.1	0.6	-0.1	0.7	0.3	0.4	0	0.5	0.3	0.1	-0.2	0.1
Amino acid	L-Asparagine	0.3	0.3	-0.4	0.2	1	0	-	-	-	-	-	-	0.9	0.2	1.1	0.1	1.3	0.1
Amino acid	L-Aspartic acid	-0.6	0	-2.2	0	-1.4	0	0.3	0.1	0.3	0.3	0.8	0	-0.1	0.9	-0.5	0	-1.6	0
Amino acid	L-Cystathionine	5.2	0	-2.1	0	-0.3	0.1	-0.1	0.9	1.2	0.4	0.8	0.6	-1.7	0	-2.2	0	-3.8	0
Amino acid	L-Glutamic acid	-1.3	0	-2.1	0	-1.3	0	-0.4	0.5	-0.7	0	-1.1	0	-0.4	0.1	-0.5	0	-2.1	0
Amino acid	L-Glutamine	-11.4	0	-1	0	-0.4	0.1	-0.1	0.2	0.2	0.4	-0.1	0.7	-0.2	0	-0.3	0	-0.5	0
Amino acid	L-Isoleucine	-	-	-1.5	0.3	-0.6	1	-1.4	1	1.5	0.3	-0.3	0.7	0.1	0.2	-0.6	0.7	0.1	1
Amino acid	L-Leucine	-	-	-1.4	0	-0.4	0.1	0.2	0.4	-	-	-0.5	0.1	-	-	-0.6	0	-1.3	0
Amino acid	L-Lysine	-1.1	0	-1	0	-0.4	0.3	-0.3	0.1	-0.4	0.1	0.1	0.5	0.2	0.3	0.3	0	-0.4	0
Amino acid	L-Methionine	-0.9	0	-2.3	0	-1	0	-0.1	0.2	-0.3	0	-0.4	0.1	0.1	1	-0.1	0.2	-0.9	0
Amino acid	L-Ornithine	-	-	-	-	-	-	-	-	-	-	-	-	0.2	0.6	0.3	0.1	-0.1	0.7

Amino acid	L-Phenylalanine	-1.3	0.7	-	-	-	-	-0.1	0.4	-0.4	0	-0.3	0.1	-0.2	0.9	-0.3	0.2	-0.7	0
Amino acid	L-Proline	-1.3	0	2	0.1	-0.3	0.5	0.1	0.6	-0.3	0.4	-0.4	0.1	-	-	-	-	-	-
Amino acid	L-Serine	2.2	0	2.5	0	2.1	0	0.3	0.2	0.3	0.5	0.9	0	-0.1	0.7	-0.3	0	-1	0
Amino acid	L-Tryptophan	-1.6	0	-2.4	0	-1.3	0	-0.3	0.1	-0.8	0	-0.9	0	-0.3	0.5	-0.8	0	-0.8	0
Amino acid	L-Tyrosine	0.1	0.7	-2.3	0	-1.3	0	-0.4	0	-0.5	0	-0.6	0	0.1	0	-0.4	0.1	-1	0
Amino acid	L-Valine	-1.2	0	-1.4	0	-0.6	0	0.1	0.6	0.1	0.9	0.4	1	0.1	0.8	0.2	1	0.6	0.4
Amino acid	N-a-Acetyl-L-arginine	-	-	-1.6	0	-0.6	0	0.5	0.5	-0.2	0.4	-0.6	0.1	-0.3	0.2	0	0.5	-0.4	0
Amino acid	N-Acetylaspartylglutamic acid	-0.5	0.1	-1.5	0	-0.7	0.1	0.2	0.7	-0.3	0.4	-0.1	0.2	-1.3	0	-0.8	0	-2.9	0
Amino acid	N-Acetylisoleucine	-0.1	0	0.3	0.1	-0.1	0.5	2.4	0.4	0.4	0.8	1.4	0.5	0	0.6	0.1	0	0.1	0.2
Amino acid	N-Acetylleucine	-	-	0.9	0.7	0.4	0.7	-	-	0.4	0.6	-	-	-	-	-	-	0.7	0.5
Amino acid	N-Acetyltaurine	-0.4	0.1	-0.8	0	-0.7	0	0.1	0.9	-0.2	0.2	-5.9	0	-0.7	0.1	-0.7	0	-1.1	0
Amino acid	Ornithine	4.8	0	-0.4	0.3	-0.2	0.2	-0.5	0.1	-0.6	0	-0.3	0.2	0.2	0.6	0.3	0.1	-0.1	0.7
Amino acid	Pyroglutamic acid	-10.3	0	-0.7	0	-0.2	0.5	-0.1	0.2	0.2	0.4	-0.3	0.6	-0.3	0	-0.3	0	-0.6	0
Amino acid	Taurine	-0.4	0.1	-0.8	0	-0.7	0	0.1	0.9	-0.2	0.2	-5.9	0	-0.7	0.1	-0.7	0	-1.1	0
Amino acid	Thiamine	5.4	0.4	-1.2	0	-0.9	0	-1.2	0	-0.4	0.1	-0.3	0.3	-0.3	0.5	-0.2	0.4	-1.1	0
Amino acid	Threonine	0.1	0.4	1.4	0.5	0.6	0.9	-1.9	0.6	-0.5	0.1	0.6	0.5	-0.2	0.7	-0.3	0.1	0.7	0.3
Benzenoid	Benzoic acid	0.6	0.9	0.3	0.4	0.1	0.4	0.4	0	0.1	0.6	0.3	0.4	-0.2	0.3	-0.2	0	0.8	0
Carbohydrate	D-Glucose	-0.2	0.9	1	0	0.2	0.2	-0.2	0.4	-0.4	0	0.1	0.2	1.1	0	0.9	0	0.8	0
Carbohydrate	Glyceraldehyde3-phosphate	-1.5	0	-2.3	0	-1.4	0	0.2	0.3	-0.2	0.2	-1.3	0	0.2	0.9	-0.3	0.3	-1.7	0
Carbohydrate	Mannose6-phosphate	-0.3	0.2	-0.7	0.1	-0.2	0.3	0.8	0	0	0.9	0.2	0.3	0.3	0	0.7	0	0.5	0
Carbohydrate	N-Acetyl-glucosamine 1-phosphate	-1.3	0	-2.4	0	-1.6	0	-0.1	0.1	-0.6	0	-1.2	0	-	-	-	-	-	-
Carbohydrate	Threonic acid	-0.7	0	-0.9	0	-0.3	0.7	-0.5	0	-0.3	0.1	-0.8	0	-0.5	0	-0.6	0	-1.6	0
Carboxylic acid	5-L-Glutamyl-taurine	2.2	0	1.2	0	2.1	0	-	-	-	-	-	-	-	-	-	-	-	-
Carboxylic acid	Citric acid	-0.4	0.1	-1.3	0	-0.3	0.2	0.1	0.8	-0.2	0.9	-	-	-	-	-	-	-0.9	0
Carboxylic acid	Dodecanedioic acid	0.4	0.7	0.7	0.1	0.5	0.1	1.8	0.4	0.1	0.7	-1.1	0.6	0.3	0.3	0.3	0.2	0.4	0.1
Carboxylic acid	Fumaric acid	-	-	-	-	-	-	-	-	-	-	-	-	0.3	0.2	0.1	0.1	-2.3	0
Carboxylic acid	L-Lactic acid	-0.6	0	-0.5	0.1	0.4	0.3	0.1	0.7	-0.4	0	-0.5	0.1	-0.1	0.8	0.1	0.3	-0.9	0

Carboxylic acid	Phthalic acid	-	-	-1.6	0	-0.7	0.5	-0.5	0.7	0.7	0.3	-	-	-	-	-	-	-	
Carboxylic acid	Pyruvic acid	-0.7	0	-1	0	-0.6	0	1.7	0.5	-0.3	1	0	0.1	-0.5	0	-0.6	0	-1.2	0
Carboxylic acid	Succinic acid	-0.9	0.1	-1.2	0.1	-0.6	0.3	-	-	-	-	-	-	-	-	-	-	-	
Carboxylic acid	Tetradecanedioic acid	-0.4	0.1	-0.2	0.3	-0.6	0	-	-	-	-	-	-	0.2	0.4	0.1	0.5	0.2	0.1
Carnitine	2-Methylbutyryl	-0.7	0	-2	0	-1.2	0	0.1	1	-0.4	0	-0.9	0	-0.3	0.1	-1.2	0	-3.3	0
Carnitine	Butenylcarnitine	-	-	1.1	0.3	-0.2	0.6	1.2	0	1.9	0	2.9	0	1.1	0.3	1.5	0	1.2	0
Carnitine	Decanoylcarnitine	0.4	0.8	-0.1	1	0.2	1	0	0.9	-1.4	0.3	1	0.9	-1.5	0.6	-0.9	0.6	-0.7	1
Carnitine	Dodecanedioyl carnitine	-1.3	0.4	0.6	0.1	0	1	2.9	0.5	0.9	0.6	-	-	1.2	0	1.1	0	1.8	0
Carnitine	Heptadecanoyl carnitine	-	-	-1.8	0.4	1.3	0	0.2	0.7	-1	0.1	-0.4	0.3	0.7	0.7	0.2	0.8	1.2	0
Carnitine	L-Carnitine	-0.2	0.8	0	0.5	-0.4	0.1	-0.4	0.4	0.4	0.8	1.7	0.6	1.1	0.1	0.5	0.1	1	0
Carnitine	L-Hexanoylcarnitine	0.6	0.6	1.4	0.3	0	1	-0.4	0.1	-1.3	0	-1.6	0	-0.9	0	1.8	0	1.7	0
Carnitine	L-Palmitoylcarnitine	-8.5	0.2	0.3	0.5	0.5	0.5	0.1	0.9	-0.9	0.1	-0.9	0.1	0.1	0.7	1.2	0.1	1.6	0
Carnitine	Pentadecanoyl carnitine	-1.6	0.2	-0.5	0.1	0	0.9	0.7	0.2	-	-	-1.2	0.8	-1.1	0.1	-2.7	0	-1.4	0
Carnitine	Propionylcarnitine	-15.4	0	-1.4	0.2	-0.7	0.6	0.1	0.9	0.2	0.9	-0.9	0	0.1	0.6	-0.9	0	-2.8	0
Carnitine	Stearoylcarnitine	-1.2	0.9	2	0	2.4	0.1	-0.4	0.9	-1	0.2	-0.7	0.2	1.1	0.2	1.6	0	2.1	0
Carnitine	Tiglylcarnitine	-0.4	0.1	-0.3	0	0.2	0.4	0	0.9	-0.2	0.1	-0.5	0	0.1	0.3	0.1	0.3	-1.9	0
Carnitine	trans-2-Dodecenoylcarnitine	-1	0.6	0.8	0.8	-0.5	0.2	-0.6	0.8	-0.4	0.1	0.3	0.3	-0.9	0	-0.5	0.1	-0.8	0
Carnitine	trans-Hexadec-2-enoyl carnitine	-	-	-0.7	0.1	0.4	0.9	0.2	0.8	-0.9	0.2	-0.5	0.3	-0.8	0.1	-1.2	0	-1.2	0
Ceramide	Cer(d18:1/16:0)	-0.6	0.2	-2.4	0	-0.7	0.1	0.4	0.9	-1.7	0.1	-1.3	0.2	-1.5	0	-	-	-2.7	0
Ceramide	Cer(d18:1/24:1(15Z))	-2.3	0.1	-2.7	0	-3	0.1	-	-	-	-	-	-	-1.5	0.1	-3.6	0	-3.7	0
Cholesterol ester	Cholesteryl acetate	-1.4	0.6	-0.9	0	-0.8	0.2	-0.1	0.2	-0.4	0.1	-1.3	0	-	-	-	-	-	-
Fatty acid	Glycerol 3-phosphate	-1	0	-1.6	0	-0.7	0	-0.6	0.1	-0.8	0.1	-2	0	-0.1	0.6	0	0.9	-0.8	0
Fatty acid	Linoleamide	-2.8	0.1	-1.5	0.6	-0.1	1	-0.1	0.6	-3	0	0	0.7	-1.2	0.4	-0.8	0.4	-1.2	0.3
Fatty acid	Stearic acid	-0.4	0.5	0.4	0.4	-0.3	0.6	0.2	0.8	0.7	0.8	0.7	0.7	0.3	0.5	0.3	0.1	0.7	0
Fatty acid	Stearoylethanolamide	-	-	-	-	-	-	-	-	-1.2	0	-1.3	0	-0.8	0.6	-1.3	0.2	-1.4	0.1
Fatty acid	Tetraglyme	-	-	0.7	0.1	-2	0	0.8	0.4	0.7	0.8	2.4	0.2	0.7	0.1	0.4	0	0.9	0
Fatty amide	Oleamide	-2.8	0.1	-1.5	0.6	-0.1	1	-0.1	0.6	-3	0	0	0.7	-1.2	0.4	-0.8	0.4	-1.2	0.3
Furanone	Ascorbic acid	0	1	-0.8	0	-0.2	0.2	1.3	0.5	-	-	1.4	0.3	-2.2	0	-1.6	0	-0.3	0.1

Inorganic compound	Pyrophosphate	0	0.3	0.9	0	0.5	0.2	0.6	0.3	0.6	0.2	0.9	0	0.9	0.1	1.5	0	1.7	0
Keto acid	Acetoacetic acid	7.7	0	-0.5	0	0	0.2	-0.1	0.4	-0.2	0.1	-0.7	0	-0.2	0.3	-0.4	0	-1.5	0
Keto acid	alpha-Ketoglutaric acid	-0.4	0	-1.4	0	0.4	0	0.5	0	0.1	0.2	-0.3	0.1	-0.6	0	-0.4	0	-0.6	0
Keto acid	Levulinic acid	-	-	-	-	-	-	-	-	-1.1	0	-0.6	0	-1.1	0.1	-0.8	0	-2.4	0
Nucleobase	Adenine	-1.2	0	-1.9	0	-0.8	0	-	-	-	-	-	-	-0.3	0.2	-1.6	0	-5.2	0
Nucleoside	2'-Deoxycytidine	-	-	-	-	-	-	-	-	-	-	-	-	-0.4	0.5	-0.1	0.7	-0.9	0
Nucleoside	5'-Methylthioadenosine	-1	0.2	-1.4	0	-0.8	0	-1.5	0.2	-0.4	0.6	-0.8	0.8	-0.6	0.1	-0.7	0	-0.9	0
Nucleoside	Adenosine	-1	0.2	0.9	0	1.1	0.1	-1.5	0.2	-0.4	0.6	-0.8	0.8	-0.6	0.1	-0.7	0	-0.9	0
Nucleoside	Thymidine	-	-	-	-	-	-	-	-	-	-	-	-	-0.3	0.2	0.2	0.9	-2.1	0
Nucleotide	3'-AMP	-	-	0.9	0	1.1	0.1	-	-	-	-	-	-	-	-	-	-	0.4	0.9
Nucleotide	CDP-ethanolamine	-	-	-	-	-	-	-	-	-	-	-	-	2.5	0	-	-	2.9	0
Nucleotide	Cytidine 5'-diphosphocholine	-	-	-	-	-	-	-	-	-	-	-	-	1.4	0	1.7	0	1.3	0
Nucleotide	NAD	4.7	0.3	-1.5	0	-0.6	0	0.5	0.2	0	0.2	-0.5	0	-0.3	0.2	-0.6	0	-1	0
Nucleotide	NADH	-0.5	0	-1.2	0	-0.5	0.1	-	-	-	-	-4.7	0	-	-	-	-	-	-
Nucleotide	Uridine	-0.8	0	-1.9	0	-1	0	0.4	0.4	-1.1	0.4	-2	0	-0.6	0.1	-0.7	0	-1	0
Nucleotide	Uridine 5'-diphosphogalactose	-	-	-	-	-	-	-0.1	0.2	-0.2	0.1	-0.8	0	-	-	-	-	-	-
Nucleotide	Uridine 5'- diphosphoglucuronic acid	-0.6	0	-1.4	0	-1	0	0.1	0.8	-	-	-	-	-0.5	0	-0.9	0	-1.9	0
Nucleotide	Uridine diphosphate-N-acetylglucosamine	-0.5	0	-2	0	-1.4	0	-0.9	0	-0.7	0	-1.7	0	-0.5	0	-1	0	-2	0
Nucleotide	Uridine diphosphategalactose	-0.9	0	-1.4	0	-0.6	0	-	-	-	-	-	-	-0.7	0	-1.1	0	-2.7	0
PC	1,2-Dipalmitoleoyl-sn-glycero-3-phosphocholine	-	-	-3.1	0	-2.8	0	0.5	0.3	-1.8	0.1	-1.3	0.1	-	-	-	-	-	-
PC	LysoPC(14:1(9Z)/0:0)	-1.7	0.6	-3.7	0	-2.4	0	-	-	-	-	-	-	-	-	-	-	-	-
PC	LysoPC(24:1(15Z))	-2.4	0.5	-2.1	0	-1.8	0.2	0.8	0.3	-1.4	0.2	-2.1	0.1	-2.6	0	-4.2	0	-4	0
PC	LysoPC(P-16:0/0:0)	-1.9	0.3	-1	0.1	-1.3	0.2	-	-	-	-	-	-	-1.9	0.1	-3.3	0	-3.3	0
PC	PC(16:0/18:1(9Z))	-	-	-0.8	0.2	-0.7	0.8	0.4	0.3	-1.5	0.3	-1.2	0.1	-0.6	0.1	-2.8	0	-2.9	0
PC	PC(16:0/18:3(9Z,12Z,15Z))	-4.2	0.3	-0.5	0.1	-1.2	0.1	0.5	0.2	-	-	-	-	-0.5	0.3	-1.3	0	-1.5	0
PC	PC(18:1(9Z)e/2:0)	-	-	-0.5	0.1	-1.5	0.1	0.5	0.5	-1.4	0.1	-1.9	0	-2.8	0	-4	0	-3.3	0
PE	1-oleoyl-2-linoleyl-sn-glycero-3-phosphoethanolamine	-0.8	0.1	-2.5	0	-1.8	0	-	-	-	-	-	-	-0.6	0.3	-1.6	0	-3.2	0
PE	1-Palmitoyl-2-linoleoyl PE	-0.8	0.1	-2.7	0	-1.6	0	0	0.9	-0.9	0.3	-0.3	0.5	-	-	-	-	-	-
PE	LysoPE(18:0/0:0)	-	-	-1.9	0.3	-1	0.4	-	-	-	-	-1.2	0.2	-2.1	0	-2.8	0	-1.4	0.1
PE	LysoPE(18:1(9Z)/0:0)	-1.2	0	-2.1	0	-1.1	0	0.8	0.1	-	-	-	-	-	-	-	-	-	-
PE	PE(16:0/22:6(4Z,7Z,10Z,13Z,16Z,19Z))	-0.1	0.7	-0.7	0	-0.1	0.3	-	-	-1.3	0.6	-	-	-	-	-	-	-	-

PE	PE(18:0/20:4(5Z,8Z,11Z,14Z))	-	-	-0.1	0.1	0.2	0.1	1.4	0.3	-0.5	0.4	0.2	0.6	2.1	0.4	1.7	0.7	1.6	0.4
PE	PE(P-16:0/20:4(5Z,8Z,11Z,14Z))	0.5	0.7	0	0.5	0.6	0.5	-	-	-0.3	0.2	-	-	-	-	-	-	-	-
Peptide	Carnosine	5.2	0	-0.2	0.4	0	0.8	-0.2	0.3	-0.4	0	-0.4	0	-0.9	0	-1.2	0	-1.5	0
Peptide	L-Glutathione(reduced)	-1	0	-3.3	0	-1.4	0	0	0.4	-0.3	0.1	-1.7	0	-0.6	0	-1.2	0	-1.7	0
Peptide	L-Glutathione(oxidized)	-	-	1.5	0	-	-	1.2	0.1	-	-	-	-	-0.2	0.6	-	-	-	-
Peptide	Ophthalmic acid	5.9	0.1	-2.2	0	0.2	0.4	0.4	0	0.5	0	0.8	0	1.6	0	1.6	0	1.5	0
Peptide	Pro-leu	8.4	0	-1	0	0.1	1	1	0	1.2	0	1.3	0	-0.2	0.7	-0.1	0.7	-0.5	0
Phenylketone	Kynurenine	-1.7	0.3	-	-	-	-	-	-	-0.3	0.4	1.2	0.1	-	-	-	-	-	-
Polyamine	N-Acetylputrescine	-1.3	0	-2.8	0	-2.4	0	-	-	-	-	-	-	-	-	-	-	-	-
Polyamine	N1,N12-Diacetyl spermine	1.8	0.4	3.1	0	5.7	0	3	0	3.7	0	4.5	0	4.8	0	4.4	0	5.4	0
Polyamine	N1,N8-Diacetyl spermidine	1	0	0.5	0	2.2	0	1.1	0	1.4	0	0.7	0	1.3	0	0.5	0	0.5	0
Polyamine	N8-Acetyl spermidine	8.4	0	0.7	0	2.7	0	1	0.3	1.2	0	0.8	0	1	0	0.6	0	0	0.8
PUFA	Alpha-Linolenic acid	-	-	0.6	0.9	2	0.4	-0.3	0.6	-1	0.8	0.3	0.6	-1.3	0.5	-1.3	0.6	-1.5	0.5
PUFA	Linolenelaidic acid	-	-	2.3	1	-1.9	0	0.1	0.5	-1.7	0.2	1	0.3	-1.4	0.6	-2.7	0.2	0	0.5
Pyridine	Pyridoxal	-	-	0.8	0.1	0.2	0.9	1.3	0.5	1	0.7	1	0.6	0.2	0.6	0.2	0.4	0.2	0.8
Pyridine	Pyridoxamine	-1.4	0.2	-2	0	-0.3	0.8	1.8	0.4	0	0.8	0.5	0.7	-0.1	0.4	0.1	0.7	-0.5	0.2
Pyridine	Pyridoxine	-0.7	0	-1.5	0	7	0	-	-	-	-	-1.1	0.7	0.6	0.9	1.4	0	-	-
Pyrrolidine	1-Methyl pyrrolidine	-	-	2.1	0	0.9	0.1	-0.3	0.2	0.9	0.6	0.2	0.9	0.9	0	1	0	1.5	0
Pyrrolidine	Pyrrolidine	-0.6	0.3	-0.9	0.6	-0.8	0.3	-1	0.7	-2.6	0.1	1.9	0.5	-2.1	0	-0.1	0.6	-0.3	0.2
SM	SM(d18:0/14:0)	-3.1	0.1	-2.3	0	-3.1	0.1	-	-	-	-	-	-	-2.3	0	-3.9	0	-4.1	0
SM	SM(d18:1/16:0)	-4	0.1	-5.2	0	-3.9	0	1.1	0.3	-1.3	0.3	-1.2	0.1	-2.3	0	-3.4	0	-4.3	0

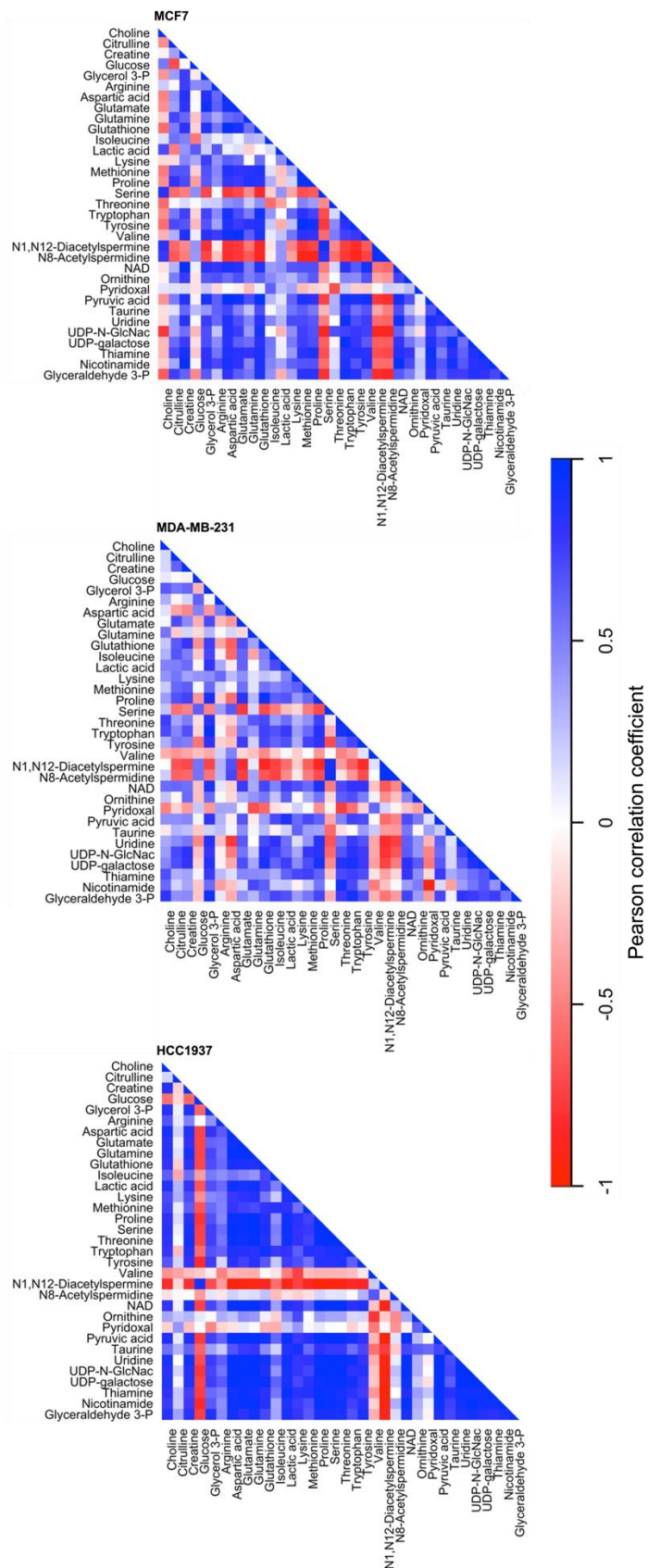


Figure S3. 11 Pearson's correlation analysis between the relevant metabolites identified within each different breast cancer cell line. Pearson's coefficient is set in a range of 1 to -1, indicative of a positive and negative correlation, respectively.

Table S3. 11 Effect scores of enriched metabolic genes in MCF-7, MDA-MB-231 and HCC1937 cells evaluated through the Dependency Map Portal (DepMap) database. Fitness effect score is based on the Chronos algorithm. Fitness Effect Score (FES).

PATHWAYS			MCF 7	MDA -MB- 231	HCC193 7
	FULL NAME	GENE	FES	FES	FES
Arginine biosynthesis					
	Glutamine synthetase	GLUL	-0.13	-0.05	-0.02
	Glutaminase 2	GLS2	-0.05	-0.11	-0.05
	Glutamic-oxaloacetic transaminase 1	GOT1	0.03	-0.06	-0.07
	Glutamic-Pyruvic Transaminase	GPT	0.04	0.11	-0.22
	Ornithine transcarbamylase	OTC	0.15	0.1	0.14
	Arginase 1	ARG1	0.23	0.09	0.02
	Nitric Oxide Synthase 1	NOS1	-0.02	-0.14	0
	Argininosuccinate Synthase 1	ASS1	-0.18	-0.4	-0.56
	Argininosuccinate Lyase	ASL	-0.11	-0.12	-0.05
Alanine, aspartate and glutamate metabolism					
	Succinate-semialdehyde dehydrogenase	SSDH	-0.15	-0.09	-0.24
	Aminobutyrate aminotransferase	ABAT	-0.05	-0.08	0.01
	Glutamate Decarboxylase 1	GAD1	-0.04	0	-0.1
	Glutamate Dehydrogenase 1	GLUD1	-0.02	-0.07	0.08
	Asparagine Synthetase	ASNS	-0.37	-0.56	-0.4
	Glycine Amidinotransferase	GATM	-0.05	-0.12	-0.18
Arginine and proline metabolism					
	Ornithine Decarboxylase 1	ODC1	-0.05	0.05	0.11
	Spermidine/Spermine N1-Acetyltransferase	SAT2	-0.19	0	-0.18
Taurine and hypotaurine					
	Glutamate Decarboxylase 1	GAD1	-0.04	0	-0.1
	Glutamate Decarboxylase Like 1	GADL1	0.08	-0.12	0.05
	Gamma-Glutamyltransferase 6	GGT6	-0.05	-0.09	-0.01
Glycine, serine and threonine metabolism					
	Serine Dehydratase	SDS	0.21	0.01	0.02
	Serine Hydroxymethyltransferase	SHMT	0.09	-0.11	-0.17

	Alanine-Glyoxylate Aminotransferase	AGXT	0	0.06	-0.09
	Guanidinoacetate Methyltransferase	GAMT	-0.07	0.02	0.04
	Antiquitin 1	ATQ1	-0.15	-0.08	0.02
	Arginine:glycine amidinotransferase	AGAT	-0.05	-0.12	-0.18
Vitamin B6 metabolism					
	Pyridoxine 5-prime-phosphate oxidase	PNPO	0	-0.06	0.04
Cysteine and methionine metabolism					
	Betaine-homocysteine methyltransferase	BHMT	-0.1	-0.08	0.04
	Glutathione Synthetase	GSS	-0.09	-0.01	0.17
	ChaC Glutathione Specific Gamma-Glutamylcyclotransferase 1	CHAC	0.1	-0.12	-0.19

6.4. Appendix 4

Received: November 6, 2020. Revised: June 6, 2022. Accepted: July 21, 2022. Published: August 16, 2022.

Cell Reports 40, 111198, August 16, 2022. DOI:
<https://doi.org/10.1016/j.celrep.2022.111198>.

Impact factor: 9.99

Cell Reports

CellPress
OPEN ACCESS

Article

Mitochondrial hyperfusion via metabolic sensing of regulatory amino acids

Mahmud O. Abdullah,¹ Run X. Zeng,² Chelsea L. Margerum,² David Papadopoli,³ Cian Monnin,⁴ Kaylee B. Punter,² Charles Chu,² Mohammad Al-Rofaidi,¹ Naser F. Al-Tannak,^{1,5} Domenica Berardi,¹ Zahra Rattray,¹ Nicholas J.W. Rattray,¹ Sheela A. Abraham,² Eeva-Liisa Eskelinen,⁶ David G. Watson,¹ Daina Avizonis,⁴ Ivan Topisirovic,³ and Edmond Y.W. Chan^{1,2,7,*}

¹Strathclyde Institute for Pharmacy and Biomedical Sciences, University of Strathclyde, Glasgow, Scotland

²Department of Biomedical and Medical Sciences, Queen's University, Kingston, Canada

³Lady Davis Institute, Gerald Bronfman Department of Oncology, Department of Biochemistry, Department of Experimental Medicine, McGill University, Montreal, Canada

⁴Metabolomics Innovation Resource, Rosalind and Morris Goodman Cancer Institute, McGill University, Montreal, Canada

⁵Department of Pharmaceutical Chemistry, Faculty of Pharmacy, Kuwait University, Kuwait City, Kuwait

⁶Institute of Biomedicine, University of Turku, Turku, Finland

⁷Lead contact

*Correspondence: eywc@queensu.ca

<https://doi.org/10.1016/j.celrep.2022.111198>

SUMMARY

The relationship between nutrient starvation and mitochondrial dynamics is poorly understood. We find that cells facing amino acid starvation display clear mitochondrial fusion as a means to evade mitophagy. Surprisingly, further supplementation of glutamine (Q), leucine (L), and arginine (R) did not reverse, but produced stronger mitochondrial hyperfusion. Interestingly, the hyperfusion response to Q + L + R was dependent upon mitochondrial fusion proteins Mfn1 and Opa1 but was independent of MTORC1. Metabolite profiling indicates that Q + L + R addback replenishes amino acid and nucleotide pools. Inhibition of fumarate hydratase, glutaminolysis, or inosine monophosphate dehydrogenase all block Q + L + R-dependent mitochondrial hyperfusion, which suggests critical roles for the tricarboxylic acid (TCA) cycle and purine biosynthesis in this response. Metabolic tracer analyses further support the idea that supplemented Q promotes purine biosynthesis by serving as a donor of amine groups. We thus describe a metabolic mechanism for direct sensing of cellular amino acids to control mitochondrial fusion and cell fate.

INTRODUCTION

Mitochondria display remarkably dynamic membrane remodeling that reflects their origin as autonomous bacteria (Dyall et al., 2004; Westermann, 2010). This enormous flexibility appears critical to sustain bioenergetics, particularly in metabolically demanding cells such as neurons, and may allow cancer cells to shift fuel utilization during starvation conditions (Nagdas et al., 2019). In normal contexts, new mitochondria are formed by expansion of existing organelles followed by fission to form progeny. Mitochondrial fission is promoted by dynamin-related protein 1 (Drp1), which localizes to the mitochondrial membrane via adaptor proteins to form ring structures that drive scission in a GTP-dependent manner (Lackner et al., 2009). Drp1 can be negatively regulated by phosphorylation at S637 via protein kinase A (PKA), which causes dissociation from mitochondria (Cereghetti et al., 2008; Cribbs and Strack, 2007). Other post-translational mechanisms include Drp1 SUMOylation and phosphorylation at S616, which are both associated with increased fission (Kashatus et al., 2015; Prudent et al., 2015; Serasinghe et al., 2015; Taguchi et al., 2007). Drp1-mediated fission is

essential at the cellular level for mitochondrial propagation during mitosis, as seen from knockout (KO) evidence during mammalian embryogenesis (Ishihara et al., 2009; Taguchi et al., 2007; Wakabayashi et al., 2009). Fission facilitates cytochrome c release from mitochondria and can therefore modulate levels of apoptosis (Frank et al., 2001; Prudent et al., 2015; Pyakurel et al., 2015; Wasiak et al., 2007). Importantly, Drp1-mediated fission is critical for quality control and homeostatic clearance via mitophagy (Kleele et al., 2021; Twig et al., 2008), potentially by directing specific capture of damaged mitochondrial regions by autophagosomes (Burman et al., 2017).

Counteracting fission, mitochondria constantly undergo fusion, leading to a dynamic interplay between the two opposing pathways (Nunnari et al., 1997). Fusion of the outer mitochondrial membrane is directed by mitofusin1 (Mfn1) together with mitochondria-endoplasmic reticulum tethering factor (Mfn2) (Chen et al., 2003; Naon et al., 2016), while inner membrane fusion is directed by optic atrophy 1 (Opa1) (Ishihara et al., 2006). Multiple mechanisms have been described to regulate these fusion factors, including phosphorylation or redox state (for Mfn1/2) (Chen and Dorn, 2013; Leboucher et al., 2012; Pyakurel et al.,

Received: October 14, 2021. Revised: June 13, 2022. Accepted: October 3, 2022.
Published: August 16, 2022.

Mol Cell 82(23):4537-4547.e7, December 1, 2022. DOI:
<https://doi.org/10.1016/j.molcel.2022.10.005>

Molecular Cell

CellPress
OPEN ACCESS

Article

Reversal of mitochondrial malate dehydrogenase 2 enables anaplerosis via redox rescue in respiration-deficient cells

Patricia Altea-Manzano,^{1,2,3} Anke Vandekerke,^{2,3,7} Joy Edwards-Hicks,^{4,7} Mar Roldan,¹ Emily Abraham,⁵ Xhordi Lleshi,⁴ Ania Naila Guerrieri,⁴ Domenica Berardi,⁴ Jimi Wills,⁴ Jair Marques Junior,⁴ Asimina Pantazi,⁴ Juan Carlos Acosta,^{4,8} Rosario M. Sanchez-Martin,¹ Sarah-Maria Fendt,^{2,3} Miguel Martin-Hernandez,^{1,6,*} and Andrew J. Finch^{4,5,9,*}

¹GENYO, Centre for Genomics and Oncological Research, Pfizer/Universidad de Granada, Junta de Andalucía, Granada 18016, Spain

²Laboratory of Cellular Metabolism and Metabolic Regulation, VIB-KU Leuven Center for Cancer Biology, VIB, Leuven 3000, Belgium

³Laboratory of Cellular Metabolism and Metabolic Regulation, Department of Oncology, KU Leuven and Leuven Cancer Institute (LKI), Leuven 3000, Belgium

⁴Cancer Research UK Edinburgh Centre, Institute of Genetics and Cancer, University of Edinburgh, Crewe Road, Edinburgh EH4 2XR, UK

⁵Centre for Tumour Biology, Barts Cancer Institute, Queen Mary University of London, Charterhouse Square, London EC1M 6BQ, UK

⁶Biochemistry and Molecular Biology I Department, School of Sciences, University of Granada, Avda Fuentenuova, 18071 Granada, Spain

⁷These authors contributed equally

⁸Present address: Instituto de Biomedicina y Biotecnología de Cantabria, IBBTEC (CSIC, Universidad de Cantabria), C/Albert Einstein 22, Santander 39011, Spain

⁹Lead contact

*Correspondence: miguelmartin@ugr.es (M.M.-H.), a.finch@qmul.ac.uk (A.J.F.)

<https://doi.org/10.1016/j.molcel.2022.10.005>

SUMMARY

Inhibition of the electron transport chain (ETC) prevents the regeneration of mitochondrial NAD⁺, resulting in cessation of the oxidative tricarboxylic acid (TCA) cycle and a consequent dependence upon reductive carboxylation for aspartate synthesis. NAD⁺ regeneration alone in the cytosol can rescue the viability of ETC-deficient cells. Yet, how this occurs and whether transfer of oxidative equivalents to the mitochondrion is required remain unknown. Here, we show that inhibition of the ETC drives reversal of the mitochondrial aspartate transaminase (GOT2) as well as malate and succinate dehydrogenases (MDH2 and SDH) to transfer oxidative NAD⁺ equivalents into the mitochondrion. This supports the NAD⁺-dependent activity of the mitochondrial glutamate dehydrogenase (GDH) and thereby enables anaplerosis—the entry of glutamine-derived carbon into the TCA cycle and connected biosynthetic pathways. Thus, under impaired ETC function, the cytosolic redox state is communicated into the mitochondrion and acts as a rheostat to support GDH activity and cell viability.

INTRODUCTION

Many key metabolic pathways occur within mitochondria, and thus mitochondrial metabolism is an attractive target for development of anticancer therapeutic agents. The efficacy of the widely used anti-diabetic drug metformin in reducing cancer incidence in patients with diabetes (Decensi et al., 2010) and the identification of complex I of the electron transport chain (ETC) as one of its key targets (El-Mir et al., 2000; Owen et al., 2000; Wheaton et al., 2014) indicate that partial inhibition of mitochondrial respiration may be a well-tolerated and effective therapy. However, tumors are metabolically heterogeneous, and clonal emergence of cells that have adapted to inhibition of respiration poses a problem for such therapies.

Despite the pivotal roles of mitochondria in cell metabolism, various models have demonstrated that complete inhibition of

respiration can be tolerated in cells. However, these models do reveal new metabolic dependencies caused by ETC disruption. For example, cells lacking mitochondrial DNA (termed “p⁰ cells”) have a requirement for pyruvate and uridine supplementation in their medium (King and Attardi, 1989). ETC-deficient cells need uridine to compensate for the activity of the pyrimidine biosynthesis enzyme dihydroorotate dehydrogenase (DHODH) that depends upon respiration (King and Attardi, 1989). The auxotrophic requirement for pyruvate in various ETC deficiency models was recently demonstrated to be due to its facilitation of aspartate biosynthesis (Birsoy et al., 2015; Cardaci et al., 2015; Lussey-Lepoutre et al., 2015; Sullivan et al., 2015). Indeed, supplementation of tissue culture medium with aspartate, in place of pyruvate, can rescue the viability of ETC-deficient cells. Thus, compensatory rewiring of cellular metabolism in